

NOVEL TECHNOLOGIES FOR CARDIOVASCULAR
MONITORING USING
BALLISTOCARDIOGRAPHY AND ELECTROCARDIOGRAPHY

A DISSERTATION

SUBMITTED TO THE DEPARTMENT OF ELECTRICAL ENGINEERING

AND THE COMMITTEE ON GRADUATE STUDIES

OF STANFORD UNIVERSITY

IN PARTIAL FULFILLMENT OF THE REQUIREMENTS

FOR THE DEGREE OF

DOCTOR OF PHILOSOPHY

Omer Tolga Inan

September 2009

UMI Number: 3382748

INFORMATION TO USERS

The quality of this reproduction is dependent upon the quality of the copy submitted. Broken or indistinct print, colored or poor quality illustrations and photographs, print bleed-through, substandard margins, and improper alignment can adversely affect reproduction.

In the unlikely event that the author did not send a complete manuscript and there are missing pages, these will be noted. Also, if unauthorized copyright material had to be removed, a note will indicate the deletion.

UMI[®]

UMI Microform 3382748
Copyright 2009 by ProQuest LLC
All rights reserved. This microform edition is protected against
unauthorized copying under Title 17, United States Code.

ProQuest LLC
789 East Eisenhower Parkway
P.O. Box 1346
Ann Arbor, MI 48106-1346

© Copyright by Omer T. Inan 2009
All Rights Reserved

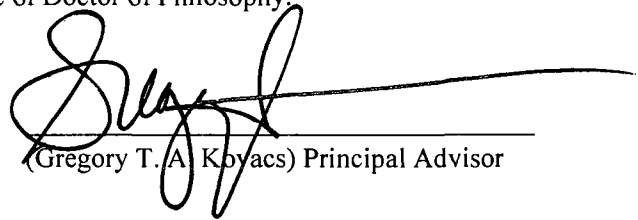
To my beautiful wife and children - your love is my elixir of life.



Mustafa, Ayşe (Memi), ve Mehmet İnan'ın unutulmaz fedakârlıklarına herşeyimi borçluyum.

I owe everything to the unforgettable sacrifices of
Mustafa, Ayşe (Memi), and Mehmet İnan.

I certify that I have read this dissertation and that, in my opinion, it is fully adequate in scope and quality as a dissertation for the degree of Doctor of Philosophy.



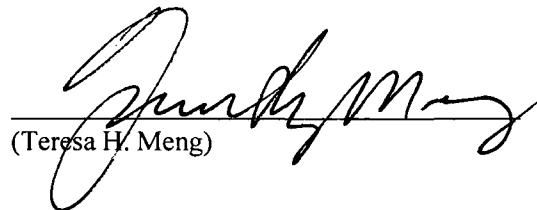
(Gregory T. A. Koyacs) Principal Advisor

I certify that I have read this dissertation and that, in my opinion, it is fully adequate in scope and quality as a dissertation for the degree of Doctor of Philosophy.



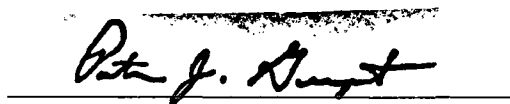
(Bernard Widrow) Associate Advisor

I certify that I have read this dissertation and that, in my opinion, it is fully adequate in scope and quality as a dissertation for the degree of Doctor of Philosophy.



(Teresa H. Meng)

Approved for the University Committee on Graduate Studies.



Abstract

More than 5,000,000 Americans suffer from heart failure, a progressive disorder where the heart cannot meet the metabolic demands of the tissues and organs. Approximately 1.5 million hospitalizations each year are related to heart failure in the US. After release from the hospital, the American Heart Association recommends monitoring heart failure patients at home by measuring body weight daily – upward trends of more than a few pounds could indicate edema, and the need for rehospitalization. Recently, in addition to simply monitoring weight, many researchers have investigated new devices for monitoring hemodynamics in the home to reduce unnecessary rehospitalizations.

This work proposes measuring both body weight and hemodynamics on the same device: a modified bathroom scale. Body weight measurement on a scale is straightforward; for hemodynamic monitoring, a combination of ballistocardiography and electrocardiography sensing technologies were developed.

When a patient stands on the scale, small fluctuations in body weight caused by the heartbeat – the ballistocardiogram (BCG) – are measured and related to the strength of cardiac contractions. Furthermore, while standing on the scale, a patient grips detachable handlebar electrodes, allowing simultaneous measurement of an electrocardiogram (ECG) signal. These two signals were fused using a novel estimation algorithm, and the BCG signal was reconstructed from the recorded waveform composed of both signal and measurement noise, such as motion artifacts.

To further improve robustness to motion, electromyogram (EMG) signals acquired from the subject's feet were recorded, and the correlation between the EMG power and the BCG noise was investigated. Floor vibrations represent another source of interference, and were mitigated by using a seismic sensor on the floor next to the scale and an adaptive algorithm. Using this approach, BCG recordings were obtained on a parked bus with the engine running – even under such extreme conditions the vibration interference was effectively eliminated.

With this system, normal standards at rest were established for 92 healthy subjects. The timing and amplitude features of the signal were found to be comparable to those measured using cumbersome bed- or table-based BCG measurement systems. Frequency domain features were also explored: the power spectral density of the BCG signal was estimated and characterized. A correlation analysis yielded that features of the BCG signal combined with height and weight were correlated to left ventricular mass ($R^2 = 0.60$, $p < 0.001$) and stroke

volume ($R^2 = 0.60$, $p < 0.01$), two important cardiovascular parameters estimated using echocardiography. The correlation to left ventricular mass is an especially encouraging result, as the system could potentially be used in large scale screening of athletes for hypertrophy.

After establishing standards at rest, the hemodynamics were modulated to determine the capability of the system to detect changes in cardiac output. For 10 trials involving nine healthy subjects, each subject exercised for 15 minutes then recovered while standing on the scale for 10 minutes. During the recovery, the gold standard for noninvasive cardiac output estimation – Doppler echocardiography – was used to measure this parameter repeatedly. The changes in cardiac output measured by Doppler were strongly correlated to the changes in root mean square (RMS) power of the BCG ($R^2 = 0.85$, $n = 275$ data points, $p < 0.001$). The prediction error, calculated based on Bland-Altman methods, was found to be lower than any other noninvasive method disclosed to date.

With this technology, heart failure patients could monitor both weight gain *and* cardiac output at home on the same device: an inexpensive, compact, modified commercial weighing scale. The subject compliance would be excellent, since the device is already a commonly-used household item and does not require anything to be attached to the body. By using the BCG/ECG-equipped weighing scale every day for less than 15 seconds at a time, unnecessary rehospitalizations could decrease, improving the quality of care for the large population of heart failure patients.

Acknowledgements

...And indeed there will be time
For the yellow smoke that slides along the street,
Rubbing its back upon the window-panes;
There will be time, there will be time
To prepare a face to meet the faces that you meet;
There will be time to murder and create,
And time for all the works and days of hands
That lift and drop a question on your plate;
Time for you and time for me,
And time yet for a hundred indecisions,
And for a hundred visions and revisions,
Before the taking of a toast and tea...

– T. S. Eliot, *The Love Song of J. Alfred Prufrock*

This work could never have been completed without the funding provided by the family of Gerald J. Lieberman (in the academic year 2008-'09) and the National Aeronautics and Space Administration's (NASA) National Center for Space Biological Technologies under cooperative agreement NNA04CC32A (in the year 2005). I would like to thank Helen Lieberman at Stanford and John Hines at NASA, particularly, for their support of my doctoral work.

Many people contributed technically to this work and personally to me during my studies at Stanford. The one who championed both forms of contribution was my advisor and dear friend, Gregory Kovacs. Greg has always allowed me to be creative in pursuing new ideas and new approaches to old ideas. He never rejected my ideas; he strongly challenged them. If convinced that they were right, he fought for them. Greg constantly promotes and defends his students, past and present. For this reason, having him by my side in any meeting tremendously boosted my confidence. I feel lucky to have taken a class from Greg, let alone to have spent years in his lab researching under his supervision. In those years, his influence on my life far surpassed what was learned on the second floor of the Paul Allen Building: just as I am a better scientist because of him, I am also a better father because of him. He is an outstanding mentor and a wonderful friend; a truly superb person that I look up to. I hope to continue working with him in any way that I can.

I would like to thank the other members of my reading committee, Bernard Widrow and Teresa Meng, and the members of my orals committee, Pierre Khuri-Yakub (orals chair) and Krishna Shenoy. They provided extremely helpful comments throughout this work, and their advice was much appreciated.

Professor Widrow has been a wonderful inspiration for my work and life. He is an outstanding person, and was more than willing to spend hours of his time working with me on this project; many of those hours were in the fishbowl at Packard, although some were enjoyed at the Faculty Club over good food. Professor Widrow embodies some of the best traits of academia: wisdom, curiosity, and an equal desire to both teach and learn. Regarding teaching, he is well-versed in a broad array of topics: he taught me everything I know about adaptive filtering, electrical modeling of mechanical circuits, and the Rodin sculpture garden at the Quad. Professor Widrow is an extremely generous and caring person (and has an equally generous and caring wife, Mrs. Ronna Lee Widrow). I feel privileged to have met them and hope our friendship continues after my graduation.

The Kovacs' lab is filled with wonderful people who have made my experiences at Stanford fun and fruitful. (I will mostly miss the multiple coffee breaks we shared as a lab every day.) It has been delightful to have worked with Laurent Giovangrandi, Mozzi Etemadi, Richard Wiard, Michael Chen, Hollis Whittington, Nadim Maluf, John Meador, Chris Storment, Tony Ricco, Bob Ricks, Joy Ku, Jonathan Sorger, Amy Droitcour, Janice Li, Matt Hills, Gaylin Yee, Mario Goins, David Burns, Keya Pandia, Shilpi Roy, Walt Wyman, Dirk Lange, Bernie Rihn, Jimmy Cassis, and Nicole Kerness. Sandy Plewa, at the beginning of my studies, and Claire Nicholas, in my final years, were both immensely helpful in making everything go smoothly at the office.

Laurent Giovangrandi is a wonderful friend and I will never forget the interesting and thought-provoking coffee breaks we had together. (We shared many, many espressos together.) His advice for my research was very helpful, and he asked the right questions to make sure I was considering all possibilities. He is a thorough and hard-working scientist, and I am thrilled I was able to work with him for all of my years in the Kovacs' lab. He also has a delightful family (Charlotte, Tomas, and Marco), and I thank them for their friendship to my family and me during our time at Stanford.

Mozzi Etemadi and I had some unforgettable times working on this project and others together. He is a colleague I have an extreme amount of respect for, and will be very successful in his continuing studies. I enjoyed our walks to the office together, opening the Kovacs' lab doors at very early hours of the morning; I am happy to say he was closing these doors *alone* at late hours of the night when I was already back with my family. He was the hardest worker in our group, and will likely be the hardest worker anywhere he ends up. (It should be noted that we also shared many coffees together, but his were decaf.)

I would like to thank Professor David Liang in the School of Medicine for supporting the echocardiography trials, and Allan Paloma for being such a superbly talented sonographer, and a very fun person to be around. The echocardiogram data used in Chapter 7 were measured and analyzed by Allan.

Professor Vic Froelicher and his team of researchers, particularly Dr. Jonathan Myers, Dr. Vy-Van Le, and the Cardiology Group, at the Palo Alto VA have also provided so much of their time and energy to helping this project. I am extremely grateful for everything they have done.

Professor Pierre Khuri-Yakub has been an inspiration to me during my years at Stanford. His course, E40, motivated me to pursue electrical engineering. Furthermore, my classmates and I used to joke that E40 covered everything one would learn in the entire EE core curriculum – this was a bit of a stretch, of course, but it shows how strong of a course Prof. Khuri-Yakub had developed, and I am extremely grateful for that as well as his delightful personality.

Professor Tony Fraser-Smith helped me in my undergraduate years to continue at Stanford for my graduate studies and I thank him for that.

The following professors have been instrumental to this work with their advice and technical discussions: Craig Heller, Teresa Meng, Bruce Darling, Euan Ashley, Harry Lemmens, and Ada Poon. Professor Heller, especially, provided very useful technical advice, and is an inspiring person to be around. Dr. Ashley helped edit the introductory text on heart failure in Chapter 1. Professor Poon helped with the presentation of the mathematical theory in Chapter 4.

I am indebted to Bob Ricks (NASA Ames Research Center) and Jim Williams (Linear Technology) for their extraordinarily helpful advice related to analog circuits. Every time I called either of them with circuit questions, regardless of how obvious or obscure, they immediately provided me with the precise answers I needed. I thank both of them for their valuable time.

Outside of Stanford, I have been fortunate to work with some wonderful people in Chris and Carolyn Countryman, Rosa Pimentel, and Alex Bullitt (Countryman Associates). They supported me in every way they could throughout this work, and it is much appreciated. Chris especially helped with mechanical prototyping, redrawing figures, and editing this text. Alex was also very helpful in his detailed and thorough edits of the text. I look forward to working with them in the future.

I am extremely grateful to Laurel Joyce, Reid Kovacs and Clark Kovacs, for their generosity and inspiring strength. They were unusually gracious and kind hosts when I visited them, making me feel like one of their own family, and are truly wonderful people.

Sharmila Bhattacharya, Oana Marcu, and Max Sanchez at NASA Ames Research Center were a pleasure to work with for my small-satellite-fruit-fly-monitoring side project. They are really fun people, and excellent scientists.

I am now left with the impossible task of properly thanking my family. For this, I must start with my father, who poured every ounce of himself into seeing me grow and be successful. He sacrificed for me in unparalleled ways. He taught me what I need to know about being a father and a selfless person in this life. I owe everything to his endless sacrifices and dedication; these are unforgettable.

Both of my grandparents gave up their retirement for raising me. They lived with me my whole life, including most of my years at Stanford. When I was very young, I used to love playing games with my grandmother. Now that I am older, and I see her playing these same games with my son – some things are truly timeless – I realize how instrumental she was in developing my curiosity. She is an angel to whom I am forever indebted.

Anything I say about my grandfather will sadly fall short. He is honest and hardworking, completely committed to fulfilling his goal: raising extremely well-educated children with strong moral values. He has always been my hero, and I dream to one day be as good of a family man as he was. Where I would be without his help is a discussion I am not brave enough to open.

I have a beautiful little boy named Omer Mustafa who is two years old as I write this. He's curious and good-natured, and overly gentle with animals and babies. He inspires me to try harder in everything, and my career has improved substantially since his birth. (No, Erin, this is not because I am trying to work more to avoid him.) So has my appreciation for this life. He is my joy.

I have a daughter who stole my heart at birth: Ayla Ceren. For most of the time I was writing this dissertation, she was in the womb – looking back now as I revise this section, I can't even remember life without her.

Finally, my Topkapi Diamond, Erin Inan, is the one I live for each day. Her sacrifices during this time of workaholicism known as "The PhD" allowed all of this work to be possible. Coming home to her at the end of my long days recharges my mind, body, and spirit

at once by experiencing her smiling face; not to mention her culinary expertise. She also spent many hours helping edit this document, as well as my journal papers.

Since I could never find my own words that would be strong enough, I quote Suleyman the Magnificent's words to his queen to describe my thanks to you, Erin:

*My very own queen, my everything,
my beloved, my bright moon;
My intimate companion, my one and all,
sovereign of all beauties, my sultan.*

*My life, the gift I own, my be-all,
my elixir of Paradise, my Eden,
My spring, my joy, my glittering day,
my exquisite one who smiles on and on...*

– *Sultan Suleyman the Magnificent,
writing to his wife, Hurem Sultan*

Finally, I must ask anyone I have forgotten to mention here to forgive me for overlooking you and please accept my humble thanks for all that you have helped me with.

– *Omer Tolga Inan, Fall 2009*

Table of Contents

Abstract	vii
Acknowledgements	ix
List of Tables.....	xxi
List of Figures	xxiii
1 Motivation and Potential Applications	1
1.1. Heart Failure.....	2
1.1.1. Pathophysiology of Heart Failure.....	3
1.1.2. Heart Failure Management at Home	4
1.1.3. Technologies for Monitoring Heart Failure Patients at Home.....	5
1.2. Ballistocardiography and Electrocardiography for Home Monitoring of Heart Failure	7
2 Ballistocardiography.....	9
2.1. Excitation-Contraction Coupling.....	9
2.2. Ventricular Mechanics.....	10
2.3. Cardiac Output.....	11
2.4. The Frank-Starling Law of the Heart	11
2.5. Brief History of the BCG	12
2.6. Diagnostic Value of the BCG.....	14
2.7. Absolute versus Relative BCG Measurements.....	16
2.8. Modern BCG Systems.....	17
2.8.1. Static-Charge-Sensitive Bed – Longitudinal and Transverse Forces	19
2.8.2. EMFi-Sensor-Based Chair – Longitudinal and/or Transverse Forces	19
2.8.3. Custom Force Plate for Lavatory Measurements – Longitudinal Forces.....	20

2.8.4.	Sternal Accelerometer – Longitudinal and Transverse Forces	20
2.8.5.	Modified Commercial Weighing Scale – Longitudinal Forces	21
2.9.	Value of Combining ECG and BCG	21

3 Instrumentation Design and Verification 23

3.1.	Standard ECG Amplifier	25
3.1.1.	Design Considerations and Circuit Schematic	25
3.1.2.	Electronic Characterization	28
3.1.3.	Practical Considerations	29
3.2.	Standard BCG Amplifier	29
3.3.	Sources of Noise and Interference in Standing BCG Recording	31
3.4.	Characterization of the BCG Sensor	31
3.4.1.	Static Characterization: Spring Constant, Force-to-Voltage Gain and Linearity	31
3.4.2.	Dynamic Characterization: Frequency Response, Distortion, Drift	32
3.5.	Lock-in BCG Amplifier	35
3.5.1.	Basic Lock-In Amplifier Theory	36
3.5.2.	Circuit Design	39
3.5.3.	Noise Measurements for Standard and Lock-In BCG Amplifiers	41
3.5.4.	BCG Measurements Using Standard and Lock-In Amplifier	43
3.5.5.	Discussion	44
3.6.	Novel Two-Electrode ECG Circuit Design	45
3.6.1.	Design Considerations and Objectives	46
3.6.2.	Mid-Band Gain and Frequency Response	47
3.6.3.	Input Impedance	51
3.6.4.	Common-mode-rejection ratio	51
3.6.5.	Experimental Results	53
3.6.6.	Integration of Two-Electrode Circuit in an Omron HBF-500 Scale	58
3.6.7.	Discussion	60
3.7.	Conclusions	61

4	BCG Signal Estimation.....	63
4.1.	Standard Signal Estimation Methods for Biomedical Signals	65
4.2.	Standard Approaches to BCG Signal Estimation.....	67
4.2.1.	R-Wave-Triggered Averaging of the BCG	68
4.2.2.	Reconstructing a BCG Signal from an Ensemble Averaged Beat	69
4.3.	BCG and ECG Pre-Processing	70
4.4.	Estimation of BCG Heartbeat Amplitudes	70
4.5.	Modified Ensemble Averaging Methods.....	74
4.6.	Reconstructing the BCG Signal.....	76
4.7.	Performance Evaluation Using Synthetic Signals.....	77
4.7.1.	Synthetic Signal Model	77
4.7.2.	Results of SNR Estimation.....	81
4.8.	Conclusions	83
5	External Interference Detection and Reduction: Motion Artifacts and Floor Vibrations	85
5.1.	Motion Artifact Detection Using Lower-Body Electromyogram Signals Acquired from the Feet.....	85
5.1.1.	Materials and Methods	86
5.1.2.	Statistical Analysis: Correlation Analysis	87
5.1.3.	Intra-Recording Analysis.....	89
5.1.4.	Noise Detection Example: Exercise Recovery.....	91
5.1.5.	Preliminary Evaluation of Body-Fat-Measurement Electrodes on Scale.....	92
5.2.	Adaptive Floor Vibration Cancellation Using a Seismic Sensor	93
5.2.1.	Theory of Adaptive Noise Cancellation	94
5.2.2.	Measurement Setup	96
5.2.3.	System Performance: Optimizing the Adaptive Filter Parameters.....	98
5.2.4.	Results for Simulated Vibrations.....	99
5.2.5.	Results from Recordings on a Parked (Idling) Bus.....	100

5.3.	Conclusions	101
6	Normal Standards for Resting BCG Recordings: Human Subjects Trials	103
6.1.	Materials and Methods	103
6.1.1.	Subject Population and Measurement Protocols	103
6.1.2.	Time Domain Features	105
6.1.3.	Frequency Domain Feature Extraction.....	106
6.1.4.	The L-N Waves of the BCG – Dispelling the Afterwaves Ambiguity	107
6.1.5.	Data Analysis.....	107
6.2.	Results and Discussion	108
6.2.1.	Normal Standards and Comparison to Previous Works	108
6.2.2.	The L-N Waves of the BCG.....	110
6.2.3.	Correlation Analysis (Subject Demographics).....	111
6.2.4.	Correlation Analysis (Echocardiogram Parameters).....	111
6.2.5.	Multi-Day Intra-Subject Variability	112
6.2.6.	Single-Day Intra-Subject Variability.....	113
6.3.	Preliminary Data from Subjects with Cardiovascular Conditions.....	115
6.4.	Conclusions	116
7	Effects of Hemodynamic Changes on the BCG.....	119
7.1.	Effects of Arrhythmias on the BCG: Ectopic Beats.....	120
7.1.1.	Pathophysiology of PVCs and PACs and the Associated ECG Waveforms	120
7.1.2.	BCG Recordings from Subjects with Ectopic Beats	121
7.2.	Effects of the Valsalva Maneuver	123
7.2.1.	Physiological Effects of the Valsalva Maneuver.....	123
7.2.2.	Expected Changes in the BCG Following Strain Release.....	124
7.2.3.	Study Details: Population and Procedure	124
7.2.4.	Digital Signal Processing and Feature Extraction	125

7.2.5.	Example Results from One Subject: Time Traces and Ensemble Averages	125
7.2.6.	Statistical Analysis for All Subjects	126
7.3.	BCG Measurements during Exercise Recovery	127
7.3.1.	Study Details: Subject Population	130
7.3.2.	Materials and Methods	131
7.3.3.	Measuring Changes in Cardiac Output from Doppler Recordings	132
7.3.4.	Measuring Changes in RMS Power from BCG Recordings	133
7.3.5.	Data Analysis	134
7.3.6.	Results	136
7.3.7.	Discussion	139
7.4.	Conclusions	140
8	Conclusions and Future Directions	143
8.1.	Conclusions	143
8.2.	Future Directions	145
8.3.	Final Remarks	145
	Glossary of Key Acronyms and Symbols	147
	References	151

List of Tables

Table 1-1	Concept of hemodynamic profiles for heart failure patients. Redrawn and adapted from [12].	4
Table 1-2	Comparison table of technologies for monitoring heart failure patients at home, ordered by degree of invasiveness.	6
Table 3-1	Measured electrical specifications for the standard ECG circuit.	28
Table 3-2	Measured electrical specifications for the standard BCG circuit.	30
Table 3-3	Measured electrical specifications for lock-in BCG amplifier.	40
Table 3-4	Measured electrical specifications for two-electrode ECG circuit	53
Table 6-1	Normal standards for subject demographics, time and frequency domain BCG features and combined ECG-BCG features (healthy subjects, n = 92).	108
Table 6-2	Summary of correlation coefficients for all statistically significant ($p < 0.05$) correlations between BCG features and subject demographics.	111
Table 6-3	Summary of correlation coefficients for all statistically significant ($p < 0.05$) correlations between BCG features, combined ECG-BCG features, subject demographics, and echocardiogram parameters.	111
Table 6-4	Summary of results from multi-day intra-subject variability trial (n = 50 recordings, one subject).	112
Table 6-5	Summary of results from single-day intra-subject variability trial (n = 8 recordings, one subject).	113
Table 7-1	Comparison of several studies on non-invasive cardiac output measurement for exercise and exercise recovery (healthy subjects)	129
Table 7-2	Characteristics and hemodynamic parameters for all subjects	130
Table 7-3	Correlation coefficient, slope, intercept, and standard deviation difference data for individually analyzed data from all subjects (sorted by R^2)	137

List of Figures

Figure 1.1	The projected effects of the growing elderly population on the incidence of heart failure (in the US), redrawn after [7]. Assuming a stable incidence in person age 65 and older, the number of new cases per year in the year 2040 is estimated to be one fifth of the US population.	2
Figure 1.2	Age-specific prevalence of heart failure hospitalizations per 1000 persons (US), redrawn after Center for Disease Control and Prevention, Division for Heart Disease and Stroke Prevention, Fact Sheet.	3
Figure 2.1	Force of contraction versus time for an isolated cardiac muscle for two cases: A, the control, and, B, increased contractility. In B, the peak force of contraction has heightened and the time to peak force is reduced.	9
Figure 2.2	Depiction of pressure-volume relationship for the left ventricular during a single cardiac cycle, adapted from [1].	10
Figure 2.3	PV loop showing the effects of compliance, preload, afterload, and contractility changes on stroke volume. The stroke volume is the horizontal width of the loop: end-diastolic volume minus the end-systolic volume	11
Figure 2.4	Illustration of the Frank-Starling law of the heart. Starling curves for a normal and failing heart are shown. For the normal heart, as preload increases, stroke volume increases as well. As contractility is increased, stroke volume increases much more with the same increase in preload. On the other hand, a failing heart cannot increase its output by simply increasing preload.	12
Figure 2.5	A typical BCG waveform for one heartbeat, redrawn after [9]. The arrow indicates the timing of the ECG R-wave.	13
Figure 2.6	Diagram illustrating relative timing of the BCG signal with respect to other more well known cardiovascular signals. Adapted from [2] and [13].	15
Figure 2.7	Illustration of longitudinal versus transverse BCG signals. The original Starr and Dock systems measured longitudinal forces; this is the true definition of the BCG. However, some of the modern systems do not differentiate between the two types of measurement and group both signals into the same category. For this reason, many of the 'BCG' signals shown in the modern literature do not resemble a true BCG waveform; they are more similar to a phonocardiogram	

	waveform, suggesting that the signal source is the heart valves.	17
Figure 2.8	Transverse ‘BCG’ signal, redrawn and adapted from [4]. The labeling of the ‘BCG’ waves appears to be arbitrary. Additionally, the ‘BCG’ has significantly greater high frequency content compared to the standard, longitudinally-measured waveform, as well as two compact pulses of energy rather than one. The signal is more similar to a phonocardiogram than a BCG.	18
Figure 2.9	BCG signal acquired using EMFi sensors redrawn from Fig. 4 of [14]. The ECG signal shown in the original figure has been replaced by arrows at each R-wave. The original caption reads, “ECG and BCG records of a filtered normal young subject using a band pass filter (1-45 Hz) for ECG and (1-10 Hz) for BCG. As can be seen, there are some motion artifacts in the BCG signal, which were not removed by filtering.”	20
Figure 2.10	Conceptual diagram of adaptive signal enhancement algorithm for averaging the BCG signal using the ECG as a reference. Adapted from [6].	22
Figure 3.1	Full schematic for standard ECG amplifier circuit. Note that the LT1014 integrated circuit is a quad package operational amplifier – accordingly, the powering is not shown separately for all four amplifiers (A-D). Decoupling capacitors are not shown in this schematic for convenience; 0.1 μ F ceramic capacitors were used next to all integrated circuit packages. The IC pin numbers are also shown next to the terminals.	25
Figure 3.2	Measured gain and phase response of the ECG amplifier.	27
Figure 3.3	Measured common-mode-rejection ratio (CMRR) versus frequency, using an SR780 signal analyzer. For measuring the common-mode gain, an input voltage of 2 V_{RMS} was used, and for differential gain, 1 mV_{RMS} . The CMRR was greater 130 dB for the bandwidth of the amplifier.	27
Figure 3.4	Input referred noise spectral density for the ECG amplifier. The thermal noise level was 15 $nV_{RMS} \sqrt{Hz}^{-1}$ and the noise corner frequency was approximately 2 Hz. The total noise integrated over the 0.1–200 Hz bandwidth was 2.4 μV_{RMS} .	27
Figure 3.5	Total harmonic distortion versus frequency.	28
Figure 3.6	BCG amplifier circuit schematic. Note that decoupling capacitors are not shown, and the fourth amplifier on the LT1014 integrated circuit (LT1014B) is unused. The IC pin numbers are also provided for convenience.	29

Figure 3.7	Block diagram showing sources of noise and interference in standing BCG recordings at the sensor input, due to the sensor, and due to the electronic amplifier.	30
Figure 3.8	Large-signal characterization of scale. The force-to-voltage transfer was shown to be linear ($R^2 = 1.00$).	32
Figure 3.9	Small-signal characterization of scale. The force-to-voltage transfer was shown to be linear ($R^2 = 1.00$).	32
Figure 3.10	Block diagram showing setup used for dynamic characterization of the BCG sensing scale.	33
Figure 3.11	Characterization of the drift in the BCG sensor: the loudspeaker was driven such that the output voltage of the BCG circuit was comparable to a typical BCG signal ($2 N_{pp}$). The RMS of the accelerometer and BCG waveforms are shown above after normalization and moving averaging (1 min. window). The BCG sensor drift was thus found to be negligible.	34
Figure 3.12	Standard lock-in amplifier modulation and demodulation procedure. The output consists of half the original signal plus half the signal shifted to twice the carrier frequency.	35
Figure 3.13	Phase-synchronous demodulation circuit used in this work, based on [3]. The switch is toggled in phase with the carrier.	35
Figure 3.14	Block diagram showing the stages of modulation and demodulation for signal, $s(t)$. An example of the waveforms that would be seen at points A–D is provided below.	38
Figure 3.15	Illustration of phase-synchronous demodulation scheme. The original signal is recovered with a scaling factor of approximately 0.64 after low-pass filtering (some of the signal amplitude is lost to the harmonics of the signal). The original signal is one quarter-cycle of a 0.01 Hz sine wave, and the modulation signal is a 1 Hz sine wave. The low-pass filter cutoff is 0.2 Hz.	38
Figure 3.16	Full schematic for lock-in BCG amplifier circuit. Note that the power supply connections for the LT1884A (in the feedback loop of the LT1167) are not explicitly shown since it is in the same package as the LT1884B to its side. Additionally, power supply decoupling capacitors ($0.1 \mu\text{F}$ at both supply pins of each IC) and the second op-amp in the relaxation oscillator package are not shown. The IC pin numbers are provided next to the packages for convenience.	39
Figure 3.17	Square-wave output from op-amp relaxation oscillator ($f_{osc} = 3.3 \text{ kHz}$).	41

Figure 3.18	Gain and phase response of input stage with an ac-coupled instrumentation amplifier. The mid-band voltage gain was 48 dB, and the low frequency cutoff (-3 dB) was 300 Hz.	41
Figure 3.19	Gain and phase response of the output stage. The mid-band voltage gain was 49 dB and the bandwidth was 0.3–12 Hz.	41
Figure 3.20	Input referred force noise density (in $mN_{RMS} \sqrt{Hz}^{-1}$) versus frequency for the lock-in and standard BCG amplifiers. The flicker noise is eliminated by the lock-in technique since the signal is modulated to a frequency beyond the corner frequency of the LT1167 before amplification. To convert the units to Volts, the force-to-voltage gain of the scale was used; then the thermal noise of the lock-in BCG amplifier was approximately $7.8 nV \sqrt{Hz}^{-1}$.	42
Figure 3.21	A BCG signal measured using the lock-in amplifier, after the standard digital filtering operations used for the BCG signal.	43
Figure 3.22	Ensemble average BCGs ($n = 45$ beats), with amplitude normalized to unity, and corresponding PSDs, computed for two sequentially taken recordings from the same subject. The variance of the residual of the two averages was less than 5% of the variance of the standard average, demonstrating that the BCGs were not distorted.	44
Figure 3.23	Omron HBF-500 bathroom scale with handlebar electrodes.	45
Figure 3.24	Block diagram describing the circuit topology. In this diagram, R_E represents the electrode-skin interface resistance, R_{CFB} represents the active current feedback series resistance, and R is the open-loop transimpedance gain of the amplifier. V_{DM} denotes the unloaded ECG voltage at the surface of the skin.	45
Figure 3.25	Full circuit schematic for two-electrode biosignal amplifier. Note that power supply decoupling capacitors are not shown. For both supply pins of the IC, $0.1 \mu F$ ceramic capacitors were connected to ground.	46
Figure 3.26	Transimpedance gain versus frequency for the first stage of the circuit with and without local feedback around amplifier 'A.' This feedback allows tight control of the second-order roll-off quality factor.	51
Figure 3.27	Equivalent model for common-mode inputs to the circuit. The node denoted by the asterisk (*) is considered a virtual ground in this model since the frequencies considered (typically 60 Hz) are beyond the cutoff frequency of the non-inverting integrator.	52

Figure 3.28	Gain and phase response of the circuit measured using an SR780 (Stanford Research Systems, Sunnyvale, CA) dynamic signal analyzer. An input voltage of 10mV_{RMS} through a source resistance of $300\text{k}\Omega$ was used for this measurement. Note that the gain is given in Ohms (dB).	53
Figure 3.29	Input referred current noise spectral density for transimpedance ECG amplifier. The thermal noise component was found to be $258\text{ fA}/\sqrt{\text{Hz}}$, and the noise corner frequency was below 1 Hz.	54
Figure 3.30	Performance comparison of this work to several other biosignal amplifiers from the literature: Input referred voltage noise (μV_{pp}), for a 200 Hz bandwidth, plotted versus power consumption (μW). To convert the input referred current noise density, measured as 23 pA_{pp} , to voltage, a typical low frequency skin-electrode resistance of $300\text{ k}\Omega$ was assumed. Designs using discrete components are shown by circles, and integrated designs are shown as squares. Note that all amplifiers in this figure, besides the amplifier shown in this work, require three electrodes on the subject; the circuit in this paper uses only two.	54
Figure 3.31	Sample ECG recordings taken from one subject with a standard (three electrodes, instrumentation amplifier input) and transimpedance ECG amplifier (two electrodes).	55
Figure 3.32	Ensemble averages for the proposed transimpedance amplifier and the standard amplifier taken simultaneously from a subject. Both signals were normalized to unity standard deviation. The residual is also shown for morphological comparison (note the difference in the vertical axis between the signals and the residual).	55
Figure 3.33	Amplitude spectra for the standard and transimpedance ECG amplifiers, and the residual. The frequency characteristics of the signal were accurately preserved by the new design.	56
Figure 3.34	(a) Handlebar electrodes from the Omron HBF-500 bathroom scale. These electrodes, combined with the footpad electrodes, are intended to be used for bioimpedance-based body fat measurements. (b) The handlebars were opened and a printed circuit board (PCB) version of the two-electrode ECG circuit was placed inside. The electrodes were soldered to the circuit and the output was connected to the cable. (c) A mini-XLR (TA-4F) connector was soldered to the end of the cable from the handlebars such signal, ground, and two supply voltages could be connected between the handlebars and the base of the scale (where the batteries were housed). (d) Screw terminals inside of the handlebars were used to fix	

	wires to the electrodes. These wires were connected to the input terminals of the circuit.	57
Figure 3.35	(Top) ECG signal acquired from the hands of a subject using the standard ECG amplifier and three gel electrodes. (Bottom) ECG signal acquired simultaneously using the transimpedance-based amplifier and the handlebar electrodes in the Omron scale. The QRS complexes could readily be extracted from both signals using standard detection algorithms.	59
Figure 3.36	Power spectral density ratio for amplitude-normalized ensemble averages from the handlebar and standard ECG circuits. At low frequencies, the ratio of the spectra exhibits a 10 dB/decade increasing slope, typical of differentiation. The frequency distortion introduced by the handlebar ECG is likely a result of the electrode-skin interface being capacitively coupled, rather than nearly dc-coupled as in Ag/AgCl gel-electrodes.	60
Figure 3.37	Standard ECG (gel-electrode) and handlebar ECG signals after digital high-pass filtering (20 Hz). While for the raw signals the cross-correlation maximum value, with the autocorrelations normalized to unity, was 0.66, after high-pass filtering it was increased to 0.91. This demonstrates that the handlebar electrodes affect the lower frequency components of the ECG, such as the P- and T-waves.	60
Figure 4.1	Illustration of baseline wander and EMG interference in the ECG signal. The noises and interferences in ECG recordings can be readily discerned from the cardiac-related 'signal.'	64
Figure 4.2	Spectrogram of a typical ECG signal. The P-, R-, and T-waves are separated in time and frequency, allowing approaches such as the wavelet transform and matched filtering to be effectively employed.	68
Figure 4.3	(a) Measured BCG signal. (b) Reconstructed signal using an ensemble averaged beat 'placed' at the R-wave locations of the ECG. Note that the amplitude variations in the original signal are lost, and there are clear discontinuities between various beats due to the limitation on the length of the ensemble average (the length must be, at most, the minimum R-R interval for the trace).	69
Figure 4.4	ECG signal, filtered to extract the QRS complexes, with peaks located using a simple automatic peak detection algorithm described in the text.	70

Figure 4.5	ECG, BCG, and respiration signals acquired from a subject at rest. The BCG amplitude modulates at the respiratory frequency.	71
Figure 4.6	Illustration of template matching and subtraction procedure for an example long-windowed BCG beat (a). The waveform shown in (b) was subtracted from (a), resulting in the interference-cancelled beat shown in (c).	73
Figure 4.7	(a) Conventional ensemble average taken over long-windowed BCG beat array. (b) Modified ensemble average of interference-cancelled and time aligned long-window beats. The artifacts are substantially reduced in this average, which is then considered the best estimate of the BCG pulse response.	73
Figure 4.8	Measured and estimated BCG signals from a subject with high signal quality. The amplitude variations in the signal are captured well by the estimate.	75
Figure 4.9	Measured and estimated BCG signals for the same subject as in Figure 4.8 zoomed in around $t = 30$ s into the recording. This demonstrates the morphological accuracy achieved by the signal estimation method. Additionally, note that although the same template function has been used for all beats, the beats in the resulting signal are not identical and, in fact, preserve the original features of the measured waveform. For example, the afterwaves of the first beat are larger than the second for both traces.	76
Figure 4.10	Measured and estimated BCG traces for a subject with lower signal quality. The reconstructed BCG signal tracks the overall amplitude variations that are not due to noise. Note that the envelope of these amplitude variations appears to be periodic, at a frequency approximately four times slower than the heart rate. This suggests that the respiratory amplitude variation of the BCG has been accurately reconstructed by the algorithm.	77
Figure 4.11	(Top left): Template function used for generating synthetic signal. (Top right): Synthetic BCG signal, generated using equations (4.13–4.16). (Bottom left): Power-spectral density (PSD) estimate for synthetically generated, band-limited white noise. The estimate was computed by Welch’s method, with a Hamming window, 2000 sample segment length, and 50% overlap. (Bottom right): Synthetically generated BCG signal with additive noise (SNR = 0.5).	79
Figure 4.12	Synthetically generated BCG, synthetic BCG plus additive band-limited white noise, and reconstructed BCG – using the methods described in this chapter – for four combinations of	

	parameters. The SNR estimates for this method, maximum likelihood (ML) and the cross-correlation method (R) are also provided for comparison.	80
Figure 4.13	Error in SNR estimate versus mean heart rate (bpm) for synthetically generated data. The results are compared to maximum likelihood (ML) and correlation coefficient (Corr Coef) based SNR estimation methods from the literature [15, 16]. At each heart rate, the SNR is estimated in twenty separate trials for eight different values (SNR = 0.1–20), and the average ($\pm\sigma$) SSE are shown. The algorithm described here outperforms both other methods at all heart rates.	81
Figure 4.14	Error in SNR estimate versus BCG amplitude scaling factor standard deviation (σ_A), with heart rate fixed at 60 bpm, for synthetically generated data. The algorithm described here outperforms both other methods at all values of σ_A at this heart rate.	81
Figure 4.15	Error in SNR estimate versus BCG amplitude scaling factor standard deviation (σ_A), with heart rate fixed at 100 bpm. The algorithm described here outperforms both other methods at all values of σ_A , except when σ_A is 0.05 and the heart rate is 100 bpm. There, ML outperforms the other two methods. This is as expected since with no overlapping beats, and no amplitude variation, ML would be the ideal estimator of SNR.	82
Figure 4.16	Illustration of effects of overlapping beats on the beat-by-beat morphology of the BCG. Although the same template function is used for each beat, and no noise is added to the signal, the afterwaves from one beat interfere with the next due to the length of the template function being longer than one cardiac cycle.	83
Figure 5.1	Block diagram showing setup for evaluating lower-body EMG as a motion noise reference for standing BCG measurements.	86
Figure 5.2	BCG, ECG, and lower-body EMG signals acquired from two subjects. (a) One subject with high SNR BCG signals and low EMG RMS power throughout the recording. (b) One subject with lower SNR BCG signals and higher EMG RMS power.	87
Figure 5.3	Left: Correlation plot showing BCG noise-to-signal ratio (NSR) versus lower-body EMG variance (in units of $V^2 \times 1000$, for convenience). Right: Correlation plot showing BCG NSR versus multiple linear regression NSR estimate derived from EMG variance and subject demographics. The correlation is much stronger when height, weight, and age are	

	taken into account. Note that the error bars indicate standard error in computing the NSR and EMG.	88
Figure 5.4	ECG, BCG, moving RMS of the BCG noise, BCG baseline wander, and EMG traces for one subject. BCG noise and baseline wander increase substantially around $t = 30$ seconds, and EMG power increases simultaneously, indicating that the subject is correcting his balance.	88
Figure 5.5	Moving RMS EMG power and moving RMS BCG noise power, both with a 10 second moving average length, plotted versus time for six subjects from the trial. Visually, the RMS EMG power tracks the BCG noise power closely in time, indicating that it could be used for automatically detecting segments of the BCG signal with elevated noise.	89
Figure 5.6	Exercise recovery used as an example of an application where EMG gating could improve BCG analysis. As discussed in Chapter 7, changes in the RMS power of the BCG measured on the bathroom scale were shown to be highly correlated with changes in cardiac output measured by Doppler echocardiography. However, for the first 20–30 seconds of recording immediately following exercise, the BCG trace is usually corrupted by artifacts due to motion of the subject on the scale. The RMS power of the lower-body EMG effectively tracks this elevated noise at the start of the trace, and can be used to gate the signal accordingly.	90
Figure 5.7	Simultaneously acquired EMG signals from the top (gel electrodes) and bottom (footpad electrodes of scale) of the feet for two subjects. For both recordings, the upper plot shows the high-pass filtered ($f_c = 20$ Hz) EMG signals for a subject swaying on the scale. Note that the signals are artificially offset (but not scaled) for convenience. The lower plots show moving RMS power (5 second window) of both EMG signals, demonstrating that the relative changes in the two track closely in time. This preliminary data suggests that in future implementations, the footpad electrodes built into the scale could be used for providing an index of motion.	92
Figure 5.8	Adaptive noise canceller, adapted from Widrow, <i>et al.</i> [8]	94
Figure 5.9	Block diagram of measurement setup used for floor vibration cancellation. The subject stands on the scale while the force of cardiac ejection, F_h , and floor vibrations, F_v , are sensed by the scale. Simultaneously, the floor vibrations are sensed by the geophone. The scale and geophone signals are inputted to an adaptive noise canceller, and the system output is the best least-squares estimate of the cardiac signal.	96

Figure 5.10	(a) Primary input (weighing scale output) and filtered output using the optimum parameters for the adaptive filter (Length = 250 taps, Misadjustment = 1%, Delay in desired response = 62 samples). The noise reduction was 12 dB. (b) Frequency response of the adaptive filter after convergence. The response dips at the resonant frequency of the geophone (10 Hz) and peaks at the resonant frequency of the scale with a 40 kg load (27 Hz).	97
Figure 5.11	Top trace: geophone signal output of amplifier. Middle trace: measured BCG signal with vibration induced artifacts. Bottom trace: filtered BCG output of noise canceller. The vibration artifacts are substantially eliminated in the filtered signal, without distorting the morphology of the BCG.	99
Figure 5.12	BCG recordings taken from a subject standing in a parked bus. Top trace: geophone output of the amplifier. Middle trace: raw BCG signal output of amplifier with significant vibration induced artifacts. These artifacts were caused by the engine of the bus as well as other vehicles driving on the road. Bottom trace: filtered BCG output of the noise canceller. The artifacts due to vibrations have been significantly reduced from the recording.	100
Figure 5.13	(a) Residual computed from the raw and filtered BCG signals, recorded on the bus, from Figure 5.12. (b) Power spectral density estimate of this residual. The frequency content of the noise has higher frequency peaks which could be reduced by linear filtering, but also contains significant low frequency content that overlaps with the bandwidth of the BCG (1–10 Hz). The adaptive noise canceller effectively eliminates these artifacts from the signal.	101
Figure 6.1	Modified ensemble averaged BCG beat with labeled features. The correlation analysis was performed for these time-domain features.	104
Figure 6.2	Rectified integral of the BCG pulse response: the magnitude of the momentum change. The maximum value of the integral is shown here, and was used in the correlation analysis.	104
Figure 6.3	ECG, PPG, and BCG signals from a subject at rest. The PPG was used as the trigger for ensemble averaging the BCG in the multi-day intra-subject variability trial.	105
Figure 6.4	Top: BCG pulse response (computed as described in Chapter 4). Bottom: PSD estimates for the BCG signal computed using the periodogram method from the pulse response (solid black line) and the modified covariance method from the signal itself (dashed black line). The model order for the	

	modified covariance estimate was set at 17 based on the Akaike information criterion (AIC) [5].	106
Figure 6.5	Relationship of the ECG P-waves to the R-wave for an array of beats taken from one recording of a healthy subject at rest. The segmented P-waves are overlaid onto the ensemble averaged ECG beat for the recording (shown in gray). The P-waves on the left side are well-correlated to the R-wave in time, but the waves on the right side are not. This demonstrates that the P-waves are a diastolic event, which is well-known.	109
Figure 6.6	Relationship of the ECG T-waves to the R-wave for an array of beats taken from one recording of a healthy subject at rest. The segmented T-waves are overlaid onto the ensemble averaged ECG beat for the recording (shown in gray). The T-waves on the right side are well-correlated to the R-wave in time, but the waves on the left side are not. This demonstrates that the T-waves are a post-systolic event, which is well-known.	109
Figure 6.7	Illustrative results for one subject, demonstrating that the L-O waves of the BCG, similarly to the T-waves of the ECG, are well correlated to the right of the main systolic peak (J-wave) and uncorrelated to the left. The beats, which were aligned using the J-wave peak, are overlaid on the ensemble averaged BCG. This suggests that the waves are not related to diastole; rather, they are post-systolic events.	110
Figure 6.8	Ensemble averages for fifty recordings from the same subject taken at random times during the day for a three-week period. Amplitudes are not normalized, though the signals are aligned in time using the J-wave.	113
Figure 6.9	BCG pulse responses, estimated using methods described in Chapter 4, for eight recordings taken throughout the same day for one subject. The timing intervals and RMS power of the BCG signals showed minimal variability among the measurements.	114
Figure 6.10	Ensemble averaged BCG from a subject with heart failure. The amplitude and RMS power of the BCG were significantly lower and the R-J interval was longer than for the normal population. Additionally, the beat has two I-waves, marked as <i>I</i> and <i>I'</i> in the figure.	114
Figure 6.11	Ensemble averaged BCG beat from a subject with cardiomyopathy, heart block, and an implanted pacemaker. The amplitude and RMS power of the BCG were significantly lower than for the normal population, and the morphology of the beat was unusual.	115

Figure 6.12	Ensemble averaged BCG taken from a subject with a 4.8 cm abdominal aortic aneurysm. The R-J interval and the IJK width are much shorter than the minimum values for all healthy subjects in the trials. Visually, the response seems to be much more resonant than the typical traces, suggesting that the mechanical properties of the vasculature may be related to the afterwaves of the signal.	116
Figure 7.1	ECG recording showing normal ('N') and premature ventricular contraction ('V') beats.	120
Figure 7.2	ECG recording showing normal ('N') and premature atrial contraction ('A') beats.	120
Figure 7.3	ECG and BCG recordings from a subject with PVCs. For both the ECG and BCG, the normal beats are annotated 'N' and the PVC beats 'V'. The BCG IJ amplitude of the PVC beats is lower than for the normal beats.	121
Figure 7.4	ECG and BC65G recordings from a subject with PACs. For both the ECG and BCG, the normal beats are annotated 'N', the PAC beats 'A', and the compensatory beat 'C'. The BCG J-amplitude of the PAC beats is lower than for the normal beats, and the amplitudes of the compensatory beats are higher.	122
Figure 7.5	Correlation of BCG J-amplitude to the R-R interval preceding the premature beat, consistent with the literature: stroke volume was shown to be correlated with the preceding R-R interval due to the modulation of the diastolic time interval [10]. The bars show mean ($\pm\sigma$) normal and compensatory J-amplitudes; the x-location and width of the bars correspond to the mean ($\pm\sigma$) R-R intervals for these beats.	123
Figure 7.6	ECG and BCG time traces showing the response of one subject to the Valsalva maneuver. The BCG amplitude is reduced during the period of intrathoracic strain and then overshoots above the resting value after release. The time-series R-J interval plot is also shown and the response is remarkably similar to the expected pre-ejection period (PEP) responses reported in the literature. The Valsalva response suggests that changes in BCG amplitude are correlated to changes in stroke volume and that the R-J interval is modulated by changes in ventricular contractility.	125
Figure 7.7	Ensemble averaged BCG waveforms from the resting, strained (Valsalva), and post-release periods of the traces shown in Figure 7.6. R-J interval increased during the strained segment and decreased after release when the sympathetic tone was elevated.	126

Figure 7.8	Periodogram-based power spectral density estimates for the ensemble averages shown in Figure 7.7. The high frequency content decreased during the period of strain when blood pressure decreased, and increased transiently following release when blood pressure was elevated.	126
Figure 7.9	Ratio of post-release to resting values for all subjects (mean \pm standard deviation). A paired t-test was used to determine p-values (* indicates $p < 0.01$ and **, $p < 0.001$).	127
Figure 7.10	Block diagram depiction of measurement setup. The iE-33 [®] Ultrasound System (Philips Healthcare, Andover, MA) was used to acquire Doppler ultrasound, and the CASE [®] Exercise ECG Testing System (GE Healthcare, Chalfont St. Giles, United Kingdom) was used to acquire the ECG.	131
Figure 7.11	Image of sample ECG, BCG and Doppler ultrasound recordings taken from a subject at rest. Note that the ECG and BCG signals have been digitally band-pass filtered for this image, as described in the text. The P-T waves of the ECG and the I-L waves of the BCG are annotated. The velocity time integral (VTI) of the Doppler trace is used to calculate stroke volume.	131
Figure 7.12	Demonstrative exercise recovery results from one subject. (A) Raw BCG waveform during recovery. The spikes in the waveform were caused by sudden movements of the subject on the scale. (B) Percentage change in RMS power (moving averaged over a ten second window) of the BCG waveform and cardiac output measured using Doppler echocardiography. (C) Correlation plot showing percentage change in cardiac output versus RMS power of the BCG. The correlation was high ($R^2 = 0.89$) and the null hypothesis of zero slope was rejected ($p < 0.01$). The slope of the regression line was 0.84 and the intercept was 8.1%. The equal value line (dashed line with unity slope) is also shown. (D) Bland-Altman plot showing agreement between the two methods. The mean difference was 2% with a standard deviation of 17%.	135
Figure 7.13	(A) Correlation plot showing percentage changes in cardiac output measured by Doppler echocardiography versus percent changes in the RMS power of the BCG ($R^2 = 0.85$, $n = 275$ data points, $p \ll 0.001$). The solid black line is the best least squares regression line for the data ($y = 0.67x + 27$) and the two parallel grey lines are the 95% prediction bands. The dashed black line shows the line of equal value. (B) Bland-Altman plot showing agreement of the methods (Mean Difference: -0.5%, Standard Deviation Difference: 37%). The percent changes in RMS BCG tended to exceed those of cardiac output measured by Doppler, resulting in an upward	

trend in this difference plot. This skews the data, causing an exaggerated standard deviation difference between the methods. When the data is calibrated based on the regression line slope by a single scaling operation, the standard deviation difference is 24%.

1

Motivation and Potential Applications

Now there are more overweight people in America than average-weight people. So overweight people are now average. Which means you've met your New Year's resolution.

– Jay Leno, *The Tonight Show*

The most prevalent health monitoring device used in the home today is the weighing scale. Approximately \$200 million are spent by Americans to purchase seven million scales each year [30, 31]; over 80% of all households have at least one scale [30]. While in the past, scales only measured body weight, modern devices can also estimate body fat percentage, store results, and compare these results to the normal healthy ranges.

In addition to increasing the available features, manufacturers have also improved the technical specifications of weighing scales significantly over the years. Many modern scales have a resolution of 45 g, and a maximum capacity exceeding 150 kg. Although the scale is not considered a 'medical device' by a majority of the population, there are four key motivating factors for further improving the measurement capability of the device for health monitoring:

1. The device has already penetrated such a large percentage of households.
2. The frequency of use is generally very high: most people weigh themselves at least monthly or, in many cases, weekly or even daily.
3. The scale is already the primary means for monitoring heart failure patients at home.
4. When a subject stands on a scale, many physiologically relevant signals can be measured unobtrusively.

The last point may not be obvious, and should partly be enabled by the work described in this dissertation. The third point is a major motivation for pursuing cardiovascular monitoring on a weighing scale: the population of heart failure patients needs an improved monitoring strategy, due to the disturbingly-high prevalence, mortality, and health care costs, and significant emotional burden of the disorder.

1.1. Heart Failure

Heart failure is a progressive disorder in which the heart cannot supply enough blood to the tissues [32, 33]. In the U.S., it claims nearly 300,000 lives each year, and an estimated 5,700,000 Americans suffer from the syndrome; among the elderly population (65 and older), nearly one in 100 are afflicted [34]. The incidence of heart failure exceeds half a million cases, and this number is growing rapidly due to the increasing percentage of the population that is 65 and older (see Figure 1.1, redrawn after [7]).

Since 1972, heart failure mortality has increased by 103.2% [35], rendering it the third leading cause of death in the US, following other diseases of the heart and malignant neoplasms [36]. Hospitalizations due to the disorder have increased more than 155% [37] in the past three decades. The age-specific breakdown of the prevalence of heart failure hospitalizations per 1000 population (US) is shown in Figure 1.2 from 1979–2004. In 2008, 1,100,000 Americans were hospitalized with heart failure [34].

In addition to burdening these Americans with chronic disease, heart failure encumbers all tax-paying Americans in terms of its staggering health care costs: the 2009 costs are estimated to be \$37 billion. More Medicare dollars are spent for the diagnosis and treatment of this condition than any other. An estimated \$20.1 billion will be spent on direct hospital costs in

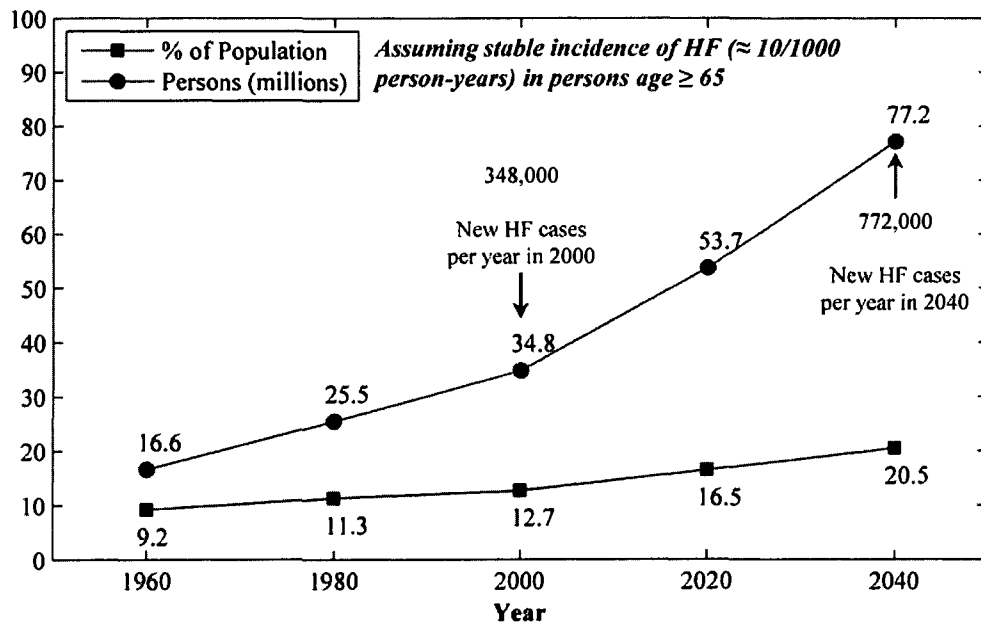


Figure 1.1 The projected effects of the growing elderly population on the incidence of heart failure (in the US), redrawn after [7]. Assuming a stable incidence in person age 65 and older, the number of new cases per year in the year 2040 is estimated to be one fifth of the US population.

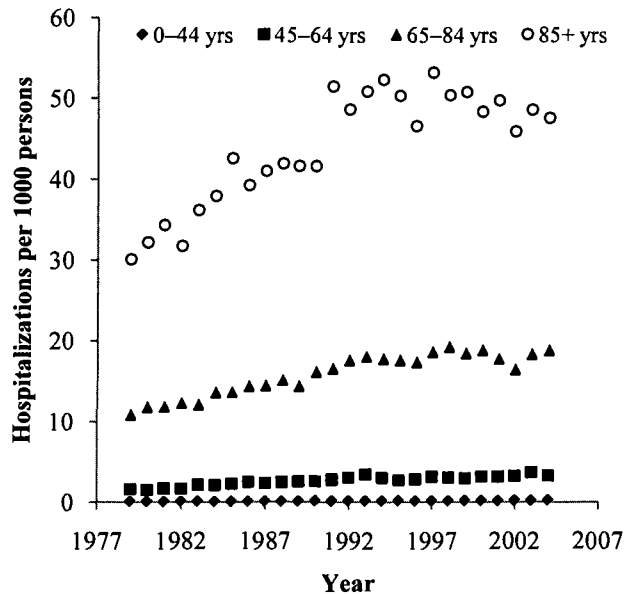


Figure 1.2 Age-specific prevalence of heart failure hospitalizations per 1000 persons (US), redrawn after Center for Disease Control and Prevention, Division for Heart Disease and Stroke Prevention, Fact Sheet.

2009 [38] – these hospital costs alone rival the *total* costs in 1999, \$21 billion [39].

Improving home monitoring technologies for these patients could reduce the number of heart failure hospitalizations and decrease the healthcare costs of the disorder. If the care at home is adequate and affordable, the patients will avoid returning to the hospital – most importantly, this will greatly improve the quality of their lives.

This section discusses the pathophysiology of heart failure

and describes some of the technologies that have been developed for monitoring the disorder at home.

1.1.1. Pathophysiology of Heart Failure

A failing heart is unable to adequately pump blood to the body. In terms of hemodynamic parameters this translates to low cardiac output – or the volumetric flow rate of blood from the heart. In the early stages of heart failure, resting cardiac output is the same as for the healthy population. However, during exercise the heart is unable to increase its output to meet the elevated demands of the body. In later stages, the heart is unable to pump enough blood to the tissues even at rest. The condition is progressive due to the inability of the compensatory mechanisms of the body to sustainably increase cardiac output.

One of the compensatory mechanisms is fluid retention, a result of increased circulating vasopressin. Normally, the heart can increase its output by increased ventricular filling, or preload, according to the Frank-Starling relationship [32] (described in Chapter 2, below). However, with chronically elevated vasopressin levels, intravascular volume and ventricular preload increase beyond the optimal level for cardiac efficiency. Elevated filling pressures reduce subendocardial flow and promote pulmonary edema and shortness of breath.

Table 1-1 Concept of hemodynamic profiles for heart failure patients. Redrawn and adapted from [12].

	No Congestion	Congestion
Adequate Perfusion	<i>“Warm-Dry”</i> Quadrant A Optimal profile: focus on preventative measures.	<i>“Warm-Wet”</i> Quadrant B Administer diuretic and continue therapy.
	<i>“Cold-Dry”</i> Quadrant L Limited further options for therapy.	<i>“Cold-Wet”</i> Quadrant C Administer diuretic and majorly redesign oral regimen.

Another compensatory mechanism is the activation of the sympathetic nervous system, resulting in beta adrenergic receptor activation. Increased sympathetic tone in a normal heart will lead to higher contractility and, thus, higher cardiac output for a given preload. In the short term, for a failing heart, this increase in beta adrenergic receptor stimulation will lead to higher cardiac output and improved state. However, long-term elevated beta receptor activation leads to adverse remodeling.

In the clinic, physicians can assign heart failure patients to one of four hemodynamic profiles based on the assessment of congestion (wet vs. dry) and perfusion (warm vs. cold) at rest. These profiles were shown to be predictive of the heart failure outcome, and are visually depicted in Table 1-1, redrawn and adapted from [12]. Perfusion is assessed by measuring cardiac output; congestion by measuring the pulmonary capillary wedge pressure (PCWP). PCWP, measured with a balloon-tipped catheter inserted in the pulmonary artery, provides an estimate of the left atrial pressure (LAP) – elevated LAP is associated with overfilling of the ventricles, or ‘congestion.’

The optimal profile is A, where the perfusion of the tissues is adequate and the filling pressures are not elevated. The highest risk of death is for profiles B and C. This results from the fact that excess fluid retention can overload the ventricle and cause elevated filling pressures, reducing coronary flow.

1.1.2. *Heart Failure Management at Home*

In the clinic, excess fluid volume is monitored by a pressure sensor on a catheter, and, if there is congestion, diuretics are administered [40]. Outside the clinic, to indirectly monitor fluid retention, daily body weight monitoring is used. Studies have shown that monitoring body weight at home can decrease mortality and hospitalization rates significantly for heart

failure patients [41]. Chaudhry, *et al.*, showed that, for the cardiac-related hospitalizations, a marked increase in body weight of 2–5 pounds was apparent one to two weeks preceding the hospitalization [42].

However, body weight monitoring is less reliable in the long-term: the *non-fluid* weight could also increase or decrease, compromising the specificity of the measurement [43, 44]. Decrease in body weight is regularly observed in patients with chronic disorders, due to loss of appetite, anemia, or metabolic abnormalities (cachexia) [45].

Additionally, even increasing trends in fluid weight represent the compensatory efforts of the body in *reaction* to worsening cardiac performance, not the worsening performance itself. By monitoring cardiac hemodynamics directly, an earlier warning of worsening condition may be obtained. Furthermore, by combining cardiac hemodynamic information *and* subsequent increases in body weight, the assessment of the patient's condition may be more accurate and specific.

1.1.3. *Technologies for Monitoring Heart Failure Patients at Home*

Recently, many studies have attempted to reduce hospitalizations for heart failure using modern diagnostic tools [46]. These approaches include monitoring external [47] or internal [48, 49] thoracic impedance, heart rate variability [50, 51], and intracardiac pressures [52, 53]. They are discussed below, in order of invasiveness, and the operation principle and level of invasiveness are summarized in Table 1-2.

External, trans-thoracic impedance cardiography (ICG) is a technique for estimating the flow of blood through the thorax using impedance changes. The physical basis is that the impedance of the thoracic volume changes as blood flows in or out of the volume. This change, usually on the order of tens to hundreds of milliohms, is measured and inputted to an empirically-defined model, including height, weight, and age, which then estimates stroke volume [54, 55].

The effectiveness of ICG measurements has yet to be conclusively demonstrated for heart failure management [44, 46]. Some studies have shown that, when measured at regular intervals, external impedance cardiography can predict the risk of acute decompensation [47]. The obvious disadvantages of this approach are that it requires frequent hospital visits (every two weeks) and is highly sensitive to electrode positioning on the thorax [56]. For most commercial instruments, four to eight electrodes must be positioned on the body: one (or two) on each side of the neck, and one (or two) at the xiphoid level on the sides of the chest. The

Table 1-2 Comparison table of technologies for monitoring heart failure patients at home, ordered by degree of invasiveness.

Technology	Operation Principle	Invasive or Noninvasive
Weighing Scale	Daily bodyweight measurements are used to estimate fluid volume status.	Noninvasive
External Impedance	Four-point impedance measurement of thorax; cardiac output is estimated by empirical equation.	Noninvasive, but obtrusive
Heart Rate Variability	Heartbeat intervals are measured using an implanted pacemaker or external sensors.	Noninvasive, but obtrusive (external) Invasive (pacemaker)
Internal Impedance	Impedance measurement is taken internally to estimate stroke volume and cardiac output.	Invasive
Intracardiac Pressure	Left atrial pressure is measured directly using the lead of an implanted pacemaker.	Invasive

distance between electrodes on the same side of the neck or chest must be fixed at a few centimeters, precisely, for the measurement to be accurate.

Heart rate variability, an indirect assessment of autonomic control, has been demonstrated to be a promising predictor of mortality in heart failure patients [50]. Heart rate variability quantifies an individual's normal sinus arrhythmia due to respiration (respiratory sinus arrhythmia [57]). Continuous long-term heart rate variability measurement, using an implanted pacemaker, has been shown to be useful in clinical management of heart failure patients, providing early warning of decompensation [51]. Although these trials have been limited to invasive measurements of heart rate variability, noninvasive methods using textile or chest-strap electrodes are also available, and may be used in future studies to provide an effective platform for home monitoring. The success of this approach may be limited by patient compliance, since the sensors must be attached to the body. Furthermore, motion artifacts could degrade the accuracy of the extracted heartbeats, particularly during daytime measurements. On the other hand, for invasive measurements of heart rate variability, while intervals can be robustly extracted continuously throughout the day and night, the applicability is limited and the cost effectiveness must be addressed. Additionally, whether heart rate

variability can lead to improved outcomes or reduced acute decompensation incidents is not yet conclusively demonstrated [44].

Internal impedance measurements have also demonstrated reasonable results in providing early warning of decompensation [48, 49]. For these measurements, a special pacemaker is implanted in the left pectoral region and a defibrillator lead is inserted into the right ventricle. The impedance between this defibrillator lead and the pacemaker case is recorded to detect fluid overload prior to heart failure related hospitalization. Unfortunately, the data supporting these measurements are limited [46], and a cost analysis has not yet been attempted. Additionally, the method is disadvantaged since other factors besides volume overload can change intrathoracic impedance, and measurements taken in the first 30 days after implantation are unreliable due to changes in the soft tissue surrounding the pacemaker generator [44, 56].

Another promising technology is continuous intracardiac pressure management using an implantable hemodynamic monitor. This technology hinges on estimating fluid status by measuring LAP – fluid overload should lead to elevated LAP. While devices capable of accurately measuring LAP have been manufactured, the clinical trials to date have not yet demonstrated the clinical benefit of the device [46, 52]. Heart failure events were not significantly reduced in these trials, with complications related to the device being a major source of problems.

1.2. Ballistocardiography and Electrocardiography for Home Monitoring of Heart Failure

This work proposes a new technology for monitoring heart failure at home: ballistocardiography and electrocardiography acquired on a modified electronic weighing scale. A commercial weighing scale is utilized as the sensor for acquiring these signals, resulting in an integrated solution capable of unobtrusively measuring body weight *and* cardiovascular health parameters from a patient. This allows the estimate of both perfusion and congestion, providing a full assessment of the patient's hemodynamic profile that could not be obtained by any other device alone.

Furthermore, the device is compact, inexpensive and easy to use. From the patient's perspective, the monitoring apparatus and procedure appears not to change – every morning before breakfast he or she steps on a bathroom scale for 5-10 seconds. However, since that same scale would now provide an early warning of declining cardiac output, the end result may change drastically: fewer visits to the hospital translate to a higher quality of life;

confidence in the care at home allows the patient psychological freedom from the constant burden of a chronic disease. Ultimately, a direct measure of cardiac performance will likely provide a more specific and accurate assessment of cardiac condition than the indirect measurement of body weight alone. This would also allow a more controlled titration of cardioactive drugs and diuretics, eventually enhancing the quality of life of the patient.

To meet this important clinical need, the engineering objectives of this thesis were set as follows:

1. To devise methods for enabling robust measurements on this simple platform
2. To fully characterize the system in terms of noise, interference, and measurement repeatability
3. To establish normal standards for the measured BCG signals
4. To find features of the measured signals that relate to important cardiovascular parameters, particularly cardiac output changes.

With these objectives met, the next step would be to design a large clinical trial to use this system in managing heart failure at home, and determine the extent to which it could improve the state-of-the-art in heart failure management.

2

Ballistocardiography

Our ignorance of history causes us to slander our own times.
– Gustave Flaubert

Even in the valley of the shadow of death, two and two do not make six.
– Leo Tolstoy

Ballistocardiography is a non-invasive measurement for monitoring the health of the heart and vasculature [9, 58]. As the heart contracts and forces blood into the aorta, an equal but opposite reaction force is experienced by the body. This force can be measured externally by placing the body on a compliant platform, and connecting a force sensor to the platform or the body. This chapter describes the relevant physiological background, history and diagnostic value of the BCG, and provides an overview of some modern BCG measurement systems.

2.1. Excitation-Contraction Coupling

Cardiac muscle cells – cardiomyocytes – contract mechanically as a result of the electrical inflow of ionic currents [1]. A local increase in the extracellular potential causes voltage-gated sodium channels to open, resulting in a rapid inrush of sodium ions into the cell. After this spike of sodium influx, and a rapid increase in intracellular potential, an influx of calcium ions causes an amplified release of more calcium from the sarcoplasmic reticulum. By binding to troponin-C, calcium prevents troponin-I from inhibiting the actin-myosin interaction, and the myocyte contracts. This process linking the electrical to the mechanical event is generally referred to as

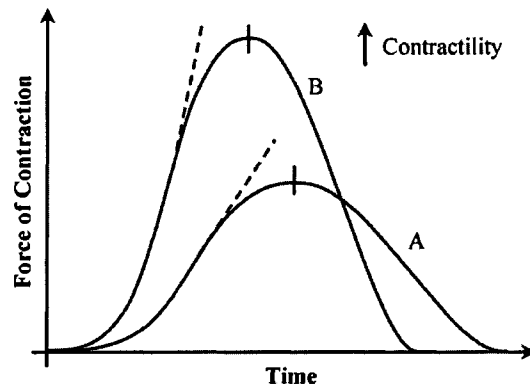


Figure 2.1 Force of contraction versus time for an isolated cardiac muscle for two cases: A, the control, and, B, increased contractility. In B, the peak force of contraction has heightened and the time to peak force is reduced.

excitation-contraction coupling. Note that there is also some reciprocal effect – mechanical stimulation can lead to electrical depolarization. For a thorough description, the reader is referred to the literature, e.g. [1].

Since the mechanical contraction is caused by the electrical depolarization of the cell, there is a time delay between the two; the length of this delay is related to the strength of the ensuing contraction. As the contractile state of the cell, or muscle, is elevated,

this period of time between electrical influx of ions and mechanical contraction of the cell shortens, and the force of contraction increases. This is illustrated diagrammatically in Figure 2.1.

2.2. Ventricular Mechanics

These basic concepts developed at the cellular level can be extrapolated to describe the mechanics of the ventricles: the force-length relationships for isolated cardiac muscle correspond to pressure-volume relationships for the ventricle. A tool commonly used for visualizing these relationships is the pressure-volume (PV) loop, as shown in Figure 2.2.

The PV loop illustrates the pressure-volume relationships for the left ventricle during one cardiac cycle. Point A represents the opening of the mitral valve, which allows blood to begin filling the left ventricle (phase 1). As the ventricle continues filling with blood, the pressure increases to the point where it rises above the left atrial pressure – at this point (B), the mitral valve closes. Then, the ventricle begins its isovolumetric contraction, phase 2, against the closed aortic valve, increasing the left-ventricular pressure. At point C, when this pressure increases above the pressure in the aorta, the aortic valve opens, beginning the third phase of the cycle: ventricular ejection. Finally, at point D, the aortic valve closes, and the ventricle begins the isovolumetric relaxation phase (4).

The ventricular volume at point B is referred to as the end diastolic volume (EDV); at point A is the end-systolic volume (ESV). Stroke volume (in milliliters), which is defined as the volume of blood ejected in each beat, is simply the difference between the EDV and ESV. The

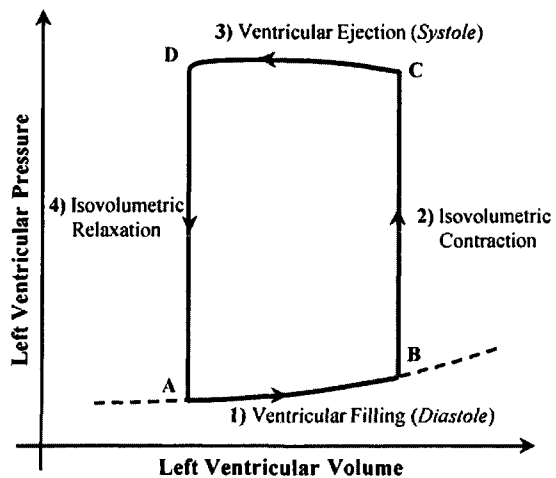


Figure 2.2 Depiction of pressure-volume relationship for the left ventricular during a single cardiac cycle, adapted from [1].

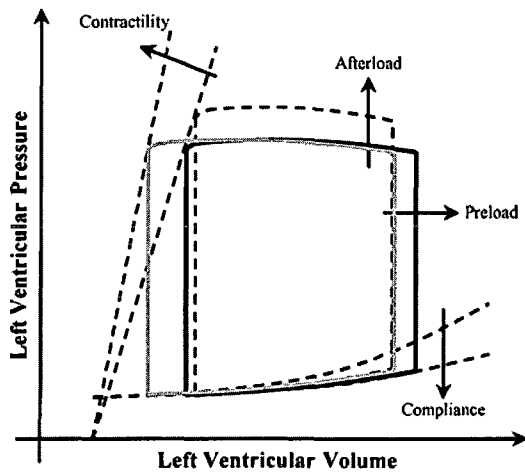


Figure 2.3 PV loop showing the effects of compliance, preload, afterload, and contractility changes on stroke volume. The stroke volume is the horizontal width of the loop: end-diastolic volume minus the end-systolic volume

product of stroke volume (converted to liters) and heart rate (in beats per minute) is cardiac output (in liters per minute), the average volumetric flow rate of blood pumped by the heart in a minute.

2.3. Cardiac Output

Cardiac output is one of the most important parameters used in clinical settings to evaluate a patient's cardiovascular health [1]. As described in Chapter 1, it is crucial for directing therapeutic decisions for heart failure

patients. To change cardiac output, one can either vary heart rate or stroke volume, or both, as described below.

Stroke volume is controlled by three factors: left ventricular EDV (preload), the resistance presented to the heart by the vasculature (afterload), and the contractile state of the heart (contractility). The effects of changing preload, afterload, and contractility on stroke volume are shown visually in Figure 2.3. Effects of changing the compliance of the ventricle on the PV loop is also shown, as this factor will determine the achievable preload for a given end diastolic pressure. The direction of the arrows in this figure indicates the effect increasing each of these parameters has on the boundary conditions for the loop. As shown in this figure, stroke volume increases with elevated preload and contractility, and decreases with a higher afterload.

2.4. The Frank-Starling Law of the Heart

The effects of preload on the heart are described in detail by the Frank-Starling Law of the heart. The Frank-Starling curve, illustrated in Figure 2.4, defines how stroke volume should increase as preload increases. As shown in this figure, if contractility is increased, a much larger change in stroke volume results from a fixed change in preload compared to the normal state. In contrast, for a failing heart, increasing preload by the same amount would lead to a much smaller change, or no change, in stroke volume. This implies that the ejection fraction, defined as the ratio of stroke volume to EDV (or preload), decreases with increased preload

for a failing heart. Eventually, excess fluid in the ventricles can lead to pulmonary edema and shortness of breath. Unfortunately, one of the body's standard compensation mechanisms for raising cardiac output is to increase preload – hence the unstable positive feedback loop discussed in Chapter 1.

One main hypothesis of this dissertation is that the combination of the BCG, which measures cardiac ejection force, and the ECG, which measures electrical depolarization of the heart, can provide a measure of both cardiac output changes and contractility changes. The human subjects trials used to test this hypothesis are discussed in Chapter 7. If both cardiac output and contractility changes could be estimated, it would be possible to determine if a subject

were moving to a different Starling curve compared to his/her normal state. For example, during exercise both preload and contractility should increase compared to rest. If the BCG does not show an increase in stroke volume as a result, the subject may be at risk of developing heart failure, or may already have a weakened ventricular state. This form of assessment – tracking relative changes in a person's cardiovascular health – is different from the diagnostic applications for which the BCG was historically used. These applications targeted making absolute diagnoses based on a subject's recording compared to a population norm.

2.5. Brief History of the BCG

The phenomenon of body movement in response to the heartbeat was first discovered by Gordon in 1877 [59]. While standing on a weighing scale, he noticed that the display needle oscillated synchronously with his heartbeat. In 1905, Henderson first recorded these movements of the body in response to the heart's contractile force using a "swinging table" with a set of levers [60]. He also suggested that the amplitude of these deflections might be related to cardiac output. Eight years later, Douglas developed a simplified version of

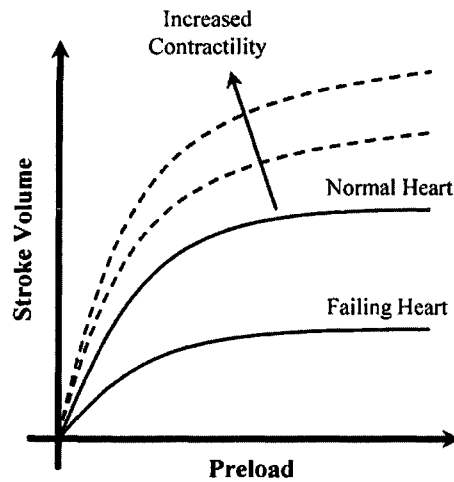


Figure 2.4 Illustration of the Frank-Starling law of the heart. Starling curves for a normal and failing heart are shown. For the normal heart, as preload increases, stroke volume increases as well. As contractility is increased, stroke volume increases much more with the same increase in preload. On the other hand, a failing heart cannot increase its output by simply increasing preload.

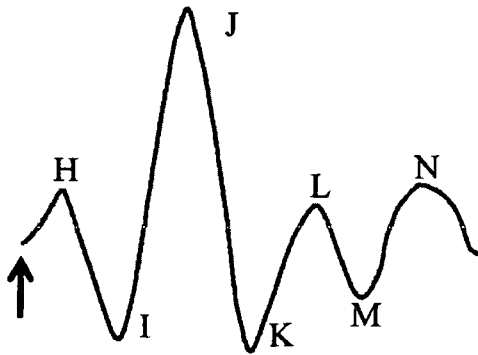


Figure 2.5 A typical BCG waveform for one heartbeat, redrawn after [9]. The arrow indicates the timing of the ECG R-wave.

Henderson’s apparatus and postulated the effects of altitude on cardiac output on the Pike’s Peak expedition [61]. For the next twenty-five years, several other researchers strived to create instrumentation capable of acquiring robust and repeatable measurements of this heart-induced body movement. Finally, in 1939, Starr’s research group succeeded with the invention of a precise, table-based measurement system [9].

Starr, *et al.* constructed a mechanical table with a steel spring opposing its lateral motion. The subject would lie supine, fixed to this table, and displacements were recorded mechanically. The signal measured on their innovative apparatus was named the ballistocardiogram (BCG), derived from the Greek words *ballein* (to throw), *kardia* (the heart), and *grafein* (to write). They then proceeded to conduct the first correlation study, linking features of this signal to stroke volume measured by the ethyl iodide method: the correlation was relatively strong ($R^2 = 0.74$).

According to Starr, *et al.*, mechanical displacements resulted mainly from five events in healthy subjects: isovolumetric contraction at the onset of systole, ventricular ejection of blood, reversal of direction at the aortic arch, deceleration of blood at the abdominal aorta, and diastolic filling. These physiological events were linked to reproducible waves in the BCG recordings: H, I, J, K, L, M, and N, respectively. (Some of these ascriptions of the waves to physiological events of the cardiac cycle are disputed in this work – in particular, waves L-N are believed to be mechanical resonances following the cardiac ejection impulse. This is discussed more in Chapters 4 and 6.)

Figure 2.5 shows a typical BCG beat, redrawn after [9]. In this figure, the arrow denotes the timing of the corresponding ECG R-wave peak. While the Starr, *et al.*, system of 1939 accurately captured the events of the cardiac cycle, it introduced some errors into the BCG signal due to in-band mechanical resonance [62-64]. The frequency content of the BCG signal was shown to lie between 1–10 Hz, but the resonant frequency of the Starr, *et al.*, apparatus was 9 Hz [65].

Additionally, the Starr, *et al.*, system was expensive (\approx \$25,000 in 2007 dollars [66]) and could not easily fit in a doctor’s office (2 x 0.75 x 0.75 meters in size [58]). This limited its

use to research settings where it was used extensively. To introduce the BCG into clinical settings, some researchers attempted more practical approaches. One of these approaches succeeded [67]: the Dock direct-body ballistocardiograph of 1949 [68].

For this method, the subject would lie freely on any rigid surface (such as a bed or table) and the portable BCG recorder was connected to the lower legs. The recorder consisted of an electromagnet set on the surface between the subject's legs, and coils attached to the lower legs. The current generated in the coils resulting from displacements of the body was amplified into a voltage signal with amplitude on the order of a raw ECG. This voltage signal, the BCG, was fed into an existing ECG instrument where it was displayed to the physician.

This apparatus was highly practical: portable, less expensive (\approx \$1,000 in 2007 dollars [66]), and interfaced directly to already-existing ECG instruments. This practicality immediately allowed the Dock ballistocardiograph to become a widely used clinical tool. Unfortunately, within a decade, many physicians realized the relative unreliability of the signals obtained using this apparatus compared to the Starr, *et al.*, table [69-71]. The Dock instrument provided inconsistent and distorted BCG traces which were shown to be much less valuable in clinical settings, leading to a decline in its clinical use.

2.6. Diagnostic Value of the BCG

Both the Starr and Dock BCG recorders were used extensively in clinical trials to understand the diagnostic capabilities of the BCG signal. First, the relative timing of the BCG with respect to the healthy cardiac cycle was established by using a simultaneous ECG as a reference [71]. Based on the findings of these studies, the BCG (for healthy subjects) is shown in Figure 2.6 alongside several other well known signals of the cardiac cycle [2, 13]. In this figure, the BCG and ECG are the top two traces, the phonocardiogram (PCG) – representing the acoustic signals generated by the valve closures – is the third trace, the aortic pressure is the fourth trace, and the left ventricular pressure and volume are the final two traces. The cardiac cycle has been segmented into diastole and systole, and the valve openings and closures have been noted by grey dashed vertical lines.

As shown in this figure, the BCG follows the QRS complex of the ECG. The maximum peak of the BCG (J-wave) occurs 200–250 ms after the ECG R-wave peak, synchronous with maximal aortic and ventricular pressure. The width of the main complex (IJK) of the BCG is approximately 250 ms [72], corresponding to the average duration of ventricular systole.

After establishing the timing of the BCG for healthy subjects, researchers studied the BCG waveforms from diseased patients to link timing and morphological variations in the signal to

specific cardiovascular pathologies. They found the BCG to be highly effective in evaluating the strength of the myocardium [73-80].

To show that weak cardiac contractions resulted in abnormal BCG recordings, several studies were conducted from 1940–1960 on patients with coronary artery disease (CAD) [74, 78, 79, 81]. In these works, simultaneous BCG and ECG signals were recorded from a total of 1,019 patients of ages 20–80: 618 with CAD and 401 healthy. BCG and ECG signals were classified as normal or abnormal for each subject. The results from these papers are summarized and quantified here in terms of sensitivity and specificity.

The BCG was more sensitive than the ECG in

detecting CAD, but less specific. The sensitivity to CAD of the BCG was 89% and of the ECG was 72.9%; the corresponding specificities were 80.9% and 95.8%, respectively. Specificity of the BCG was shown to be highly dependent on age [74]. For patients under 50,

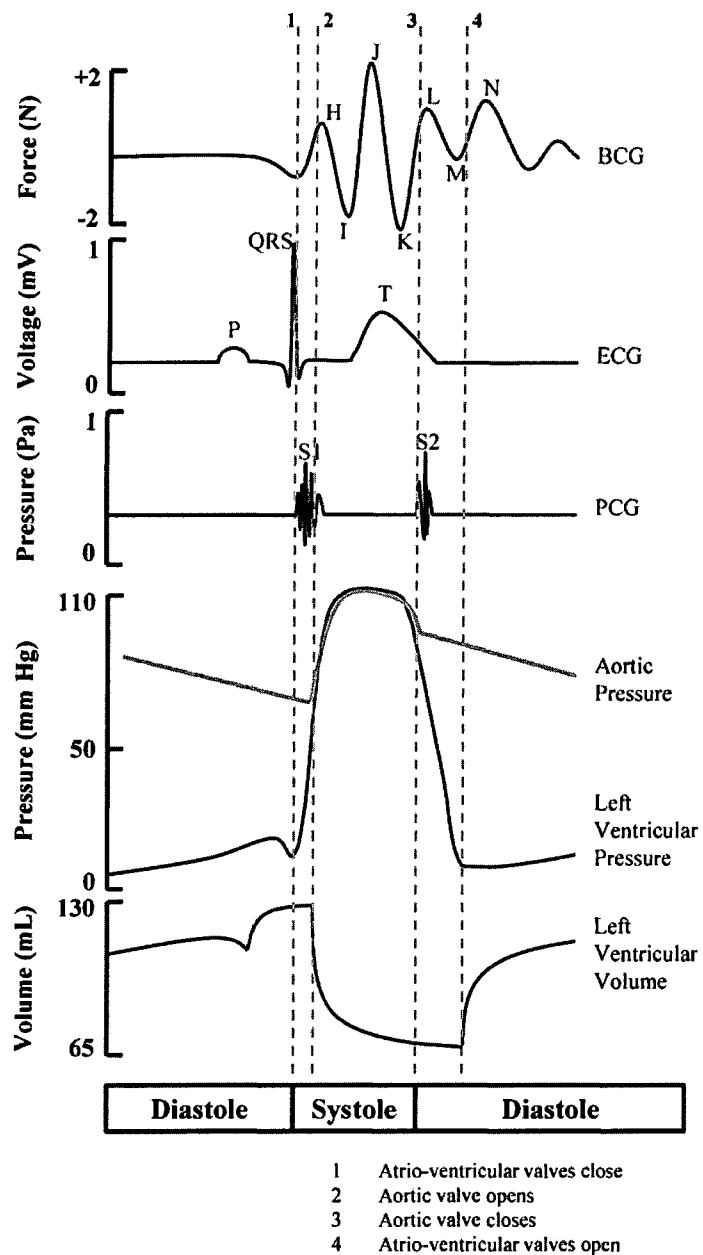


Figure 2.6 Diagram illustrating relative timing of the BCG signal with respect to other more well known cardiovascular signals. Adapted from [2] and [13].

the specificity of BCG was comparable to the ECG. For patients over 50, it decreased as age of the patients increased. The high occurrence of abnormal BCG readings from elderly patients resulted from the sensitivity of the signal to properties of the aorta [82-84].

Aging generally lowers the ratio of elastin to collagen in the aortic walls, resulting in decreased aortic compliance and increased caliber. Consequently, there was a higher prevalence of abnormal BCG recordings in elderly patients. However, for patients under 50, the BCG sensitivity was higher than and specificity was comparable to that of the ECG, rendering it an effective non-invasive tool for evaluating myocardial strength.

2.7. Absolute versus Relative BCG Measurements

As the volume of blood ejected by the heart increases, so does the force imparted by the heart on the blood. Consequently, for a given subject, increasing the stroke volume should increase the amplitude of the measured BCG signal. However, the capability of the BCG to provide information about the *absolute* output of the heart is now in question [85]. The waveform morphology is significantly dissimilar among healthy populations, rendering the amplitudes of the various peaks difficult to analyze.

The variability in BCG morphology most likely results from anatomical differences. The BCG signal represents the reaction force of the whole body to the cardiac event that occurs at the heart and the aortic arch. For absolute measurements this results in potential errors – the force imparted by the heart and the aortic arch propagates through an inhomogeneous medium, the body, to the sensor. The precise manner in which the anatomical structure will impact the waveform morphology, and amplitude, is still unknown, and is a subject of future research.

While large anatomical variations can be expected from person to person, such variations are greatly reduced when considering the same person over time, resulting in highly reproducible waveform morphologies. Thus, serial BCG measurements could be used to accurately estimate *relative changes* in cardiac output, or contractility, for one subject, as shown in Chapter 7.

Notably, in 1953, Mandelbaum and Mandelbaum measured the BCG signals of one hundred recovering heart attack patients during clinic visits over 18 months and concluded that the BCG was a valuable prognostic indicator of functional recovery [80]. The degree of restoration of the BCG signal to normal was correlated to the patient's recovery, judged by the ability of the patient to return to regular work duties as well as the occurrence or absence of further heart-related episodes. Of the patients whose BCGs improved to a higher grade of

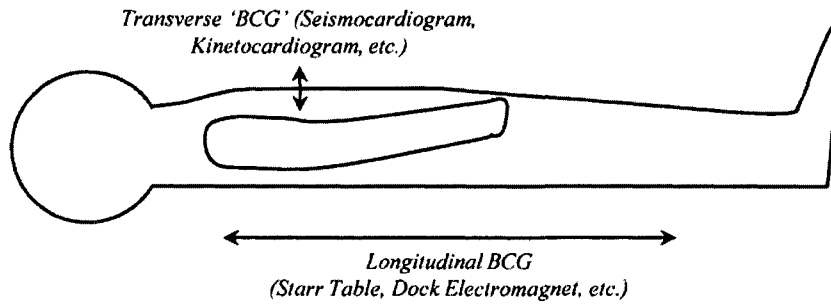


Figure 2.7 Illustration of longitudinal versus transverse BCG signals. The original Starr and Dock systems measured longitudinal forces; this is the true definition of the BCG. However, some of the modern systems do not differentiate between the two types of measurement and group both signals into the same category. For this reason, many of the ‘BCG’ signals shown in the modern literature do not resemble a true BCG waveform; they are more similar to a phonocardiogram waveform, suggesting that the signal source is the heart valves.

normalcy, 85% recovered well and returned to their homes. Of the patients whose BCGs continued to be abnormal or worse, 31% died and 55% were cardiac invalids.

Another longitudinal study confirmed that decreasing BCG amplitude over time was an accurate sign of degrading cardiac health [86]. Starr followed 211 healthy subjects for 17–23 years, measuring their BCG waveforms once in the late 1930s, then a second time in the late 1950s. The subjects with lower BCG amplitude in the first test had far higher incidence of heart disease and mortality than those with normal or higher BCG amplitude. For many subjects, the BCG prognosis preceded other clinical evidence of heart disease by years.

2.8. Modern BCG Systems

In the past thirty years, several research groups have developed new systems for acquiring the BCG. For many of these groups, the goal was to facilitate BCG measurement in the home, an ideal setting for taking serial measurements over a long period of time. As a result, the efforts have focused on improving the practicality of the instrumentation – reducing hardware costs, miniaturizing the system, improving usability, and eliminating the need for a medical professional to administer the test. The most notable of these systems have been static-charge-sensitive beds (SCSBs) [87], piezoelectric strain sensors (EMFi) [88], custom force plates [89], accelerometers [90], and modified commercial weighing scales [91, 92].

Before discussing these approaches, one important clarification is needed regarding the axis along which the ‘BCG’ is measured: the BCG, as described by Starr, represents the heart-induced body movements along the *longitudinal axis* (headward-to-footward) [9]. In contrast,

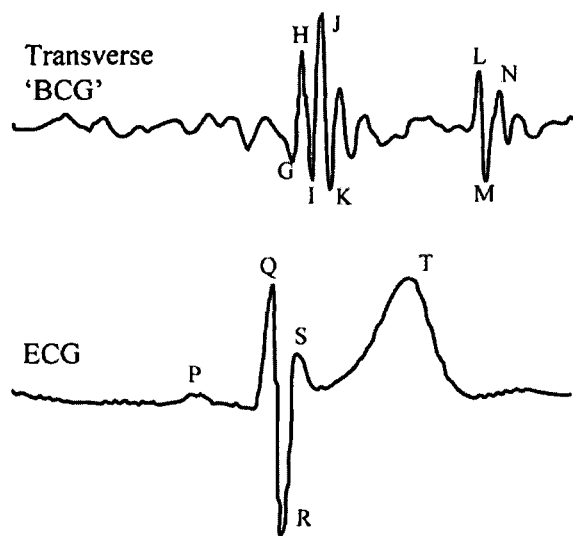


Figure 2.8 Transverse ‘BCG’ signal, redrawn and adapted from [4]. The labeling of the ‘BCG’ waves appears to be arbitrary. Additionally, the ‘BCG’ has significantly greater high frequency content compared to the standard, longitudinally-measured waveform, as well as two compact pulses of energy rather than one. The signal is more similar to a phonocardiogram than a BCG.

some of these modern ‘BCG’ measurement systems are measuring the deflections along the *transverse axis* (sternal vibrations). This is illustrated in Figure 2.7.

In the broadest definition of the signal as, ‘body movements caused by the heart,’ it would still be technically accurate to name this transverse signal the BCG. However, the physical phenomenon measured along this axis is quite different from the original measurements taken by Starr: While the longitudinal BCG results from the reaction force of the body to *cardiac ejection*, these

transverse deflections of the chest wall are likely associated with the acoustic pressure waves generated by the *valves*. As a result, changes in cardiac output will have vastly different effects on these two signals – thus, the longitudinal BCG will increase in RMS power proportional to the changes in cardiac output while the transverse signal will not. To complicate the issue further, some systems acquire a combination of both forces, longitudinal and transverse, and have yet to be characterized to determine the degree to which each couples into the sensor.

For these reasons, some authors prefer to name the transverse signal the kinetocardiogram (KCG) [93] or the seismocardiogram (SCG) [94], thus explicitly differentiating it from the BCG; unfortunately, a majority simply refer to it as a BCG [90, 95]. Visually, the signals are quite different: the transverse signals, being related to valve action, have two main peaks whereas the longitudinal BCG has one. Additionally, the transverse signals have significantly more high frequency content than the longitudinal BCG. Figure 2.8, redrawn after [4], shows a transverse ‘BCG’ beat with a corresponding ECG to illustrate the differences between this signal, and the signal measured by Starr, *et al.* [9] (Figure 2.5). Furthermore, the naming of the waves seems somewhat arbitrary in this figure as there are two or three deflections following

the K-wave that could easily be named L-N; instead, these deflections are unnamed, and the waves in the second complex are named L-N.

Accordingly, in this section describing the various modern methods for BCG acquisition, the direction along which the signal is measured has explicitly been noted in the title of each sub-section. If the researchers measured a combination of longitudinal and transverse forces, without differentiating between the two signals, the sub-section title reads, “Longitudinal *and* Transverse Forces.” If both were measured separately and independently, the title reads, “Longitudinal *and/or* Transverse Forces.”

2.8.1. *Static-Charge-Sensitive Bed – Longitudinal and Transverse Forces*

The static-charge-sensitive bed (SCSB) was the first modern BCG measurement system, developed in the early 1980s by researchers in Finland [96]. The apparatus involved a mattress with a large, built-in metal-insulator-metal capacitor, with the subject lying flat on top. Vertical movements of the body in response to sternal vibrations generate static charges on the top plate, which are then amplified by a conventional circuit. Longitudinal movements also generate static charges, however, since the body depresses into the soft mattress, the movements along this axis are dampened. The extent to which these movements are dampened would most likely depend on both body mass and composition – this issue has not been discussed in the literature, and certainly has not been quantitatively characterized.

Nevertheless, with this apparatus, high-quality recordings were demonstrated from subjects at rest and recovering from exercise. Additionally, a preliminary study was conducted to evaluate the effect of changes in contractility on the BCG. Exercise and isoprenaline, an inotropic agent, were used to increase the contractile state of the heart, and under these conditions the interval between the ECG R-wave and the BCG J-wave peaks (R-J interval) was shown to decrease significantly compared to rest for three subjects. To decouple these changes from heart rate variations alone, atropine, a chronotropic agent with no positive inotropic effects, was also administered – in this test, while there was a significant difference in heart rate, no significant difference was observed in the R-J interval [97]. The authors suggested that this system would be most suitable for sleep studies or patient monitoring, where long-term recordings are required.

2.8.2. *EMFi-Sensor-Based Chair – Longitudinal and/or Transverse Forces*

In 2004, Koivistoinen, *et al.*, introduced an ElectroMechanical-Film-equipped BCG measurement chair [88]. ElectroMechanical Film (EMFi) is a pressure sensor which consists of a plastic film coated with permanently polarized electronically conductive layers [98]. Their

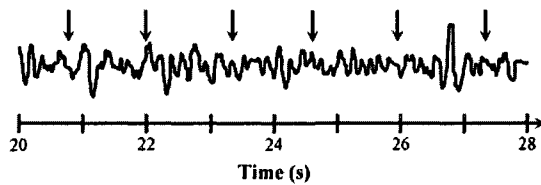


Figure 2.9 BCG signal acquired using EMFi sensors redrawn from Fig. 4 of [14]. The ECG signal shown in the original figure has been replaced by arrows at each R-wave. The original caption reads, “ECG and BCG records of a filtered normal young subject using a band pass filter (1-45 Hz) for ECG and (1-10 Hz) for BCG. As can be seen, there are some motion artifacts in the BCG signal, which were not removed by filtering.”

BCG chair used two layers of EMFi sensors: one on the seat, and one on the backrest. With this setup, both the transverse and longitudinal forces could be measured separately.

While the apparatus is inexpensive, compact, and capable of independently measuring both BCG and SCG signals, the signal quality is relatively low, as shown in Figure 2.9. The resulting BCG signal varies significantly from one

heartbeat to the next, even for data taken from healthy subjects, without any cyclic features that are synchronized to the heart rhythm. Additionally, the consistency of multiple recordings taken from one subject has not been quantitatively addressed. Thus, a majority of the work surrounding EMFi-sensor-based BCG measurement has been focused on automatic beat detection and classification; in contrast, the clinical relevance of the signals obtained by this method has not been adequately assessed.

2.8.3. *Custom Force Plate for Lavatory Measurements – Longitudinal Forces*

In the mid-1990s, Japanese researchers developed a custom force plate for measuring excreta weight in the lavatory [89]. This force plate was designed with a capacity of 2000 N (200 kg mass) and a sensitivity of less than 50 mN. With this apparatus, body weight and urine weight were unobtrusively recorded daily for several months at a time. In their efforts to measure excreta weight, these authors noticed the BCG, measured along the longitudinal axis, as a noise in their measurement, and presented it as an incidental finding in their work. Unfortunately, no quantitative characterization of the frequency response, signal-to-noise ratio (SNR), or consistency of the measured BCG was presented in this work.

2.8.4. *Sternal Accelerometer – Longitudinal and Transverse Forces*

An accelerometer was attached to the chest of subjects lying supine, and the deflections of the body caused by the heartbeat were recorded [90, 95]. In one study, conducted by McKay, *et al.*, where only the accelerations along the longitudinal axis of the body were recorded [90], the information from the BCG and ECG were combined and correlated to stroke volume measured simultaneously by a pulmonary artery catheter: the correlation was strong ($R^2 = 0.76$) for 30 subjects.

Recently, another group has developed a similar system for BCG acquisition [95]; for this work, the primary direction sensed by the accelerometer is transverse, resulting in significantly different waveforms compared to McKay, *et al.* Regardless of the measurement axis selected on the accelerometer, both of these setups would record a combination of transverse and longitudinal forces, since the body is lying supine on an immovable platform – a mattress or the floor. The relationship between sternal acceleration and BCG measurements is a subject of future research.

2.8.5. *Modified Commercial Weighing Scale – Longitudinal Forces*

In 1990, the idea of measuring the BCG from a modified commercial weighing scale was first disclosed by Jim Williams in a Linear Technology Application Note on bridge circuits (AN-43) [91]. In designing a circuit capable of precise body weight sensing – 4.5 gram resolution at 135 kg full scale – Williams noticed the heart-induced fluctuations of the weight signal as a noise in the measurement. He noted that these fluctuations were, in fact, the BCG and showed that, after exercising, their amplitudes increased.

Five years after Williams' AN-43, Sepponen disclosed the idea of non-invasively estimating heart rate and cardiac output by measuring the BCG on a modified weighing scale [99]. Unfortunately, no results were provided in his disclosure, and this idea was never revisited in the patent or academic literature.

Part of the work described in this dissertation focuses on assessing the robustness and repeatability of weighing-scale-based BCG measurements, including the quantification of frequency response, SNR, sources of noise and interference, and methods for reducing these noises. These subjects are discussed in the following chapters, particularly Chapters 3–5.

2.9. **Value of Combining ECG and BCG**

There are multiple advantages to combining both the ECG and BCG for diagnostic purposes. The signals are synchronized in time, but corrupted by independent noise sources, allowing the use of one to improve the signal quality of the other. The most direct application of this is R-wave triggered ensemble averaging of BCG beats, as described in Chapter 4. Similar results can also be achieved by feeding the signals into an adaptive signal enhancement algorithm, as shown in Figure 2.10, adapted from Ferrara, *et al.* [6].

In addition to improving signal quality, acquiring both signals simultaneously can enhance the diagnostic power of the measurement. The ECG and BCG represent complementary physiological information: electrical depolarization of the myocytes versus cardiac force

imparted on the aorta. The timing interval between the two signals, as discussed in Chapter 7, is modulated by changes in the contractile state of the heart. Furthermore, by combining the morphological features of the ECG with the amplitude of the BCG, arrhythmia detection could be improved. Preliminary data

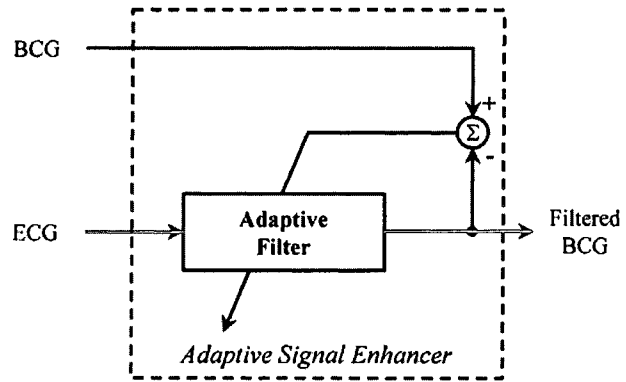


Figure 2.10 Conceptual diagram of adaptive signal enhancement algorithm for averaging the BCG signal using the ECG as a reference. Adapted from [6].

showing the effects of two arrhythmias on the signals are also provided in Chapter 7.

These advantages demonstrate the need for measuring both signals simultaneously, since more robust and informative diagnostic results can be obtained. This work provides novel instrumentation approaches to facilitate simultaneous and unobtrusive ECG and BCG measurement on a modified weighing scale. It also describes new methods for fusing the information from the two signals to lower the measurement error, and extract clinically relevant diagnostic features from the signals.

3

Instrumentation Design and Verification

The aim of every artist is to arrest motion, which is life, by artificial means and hold it fixed so that a hundred years later, when a stranger looks at it, it moves again, since it is life.

– William Faulkner

Sometimes the questions are complicated and the answers are simple.

– Theodor Seuss Geisel (*Dr. Seuss*)

The first ECG instrument was made in 1901: Willem Einthoven developed a string galvanometer for measuring electrical currents flowing through the body caused by the heartbeat. While initially this instrument was used primarily for research, it soon found a place in the clinic as a tool for diagnosing heart disease [100]. Since then, major advances in both analog and digital electronics have improved ECG instrumentation tremendously. As a result, it is now one of the most prevalent tools used for evaluating cardiovascular health: ECG recorders can be found in nearly all hospitals and clinics in the US.

Until the 1970s, it seemed that the BCG would follow a similar trajectory as the ECG, and become the mechanical complement to its electrical counterpart as a cardiovascular diagnostic. In 1939, Isaac Starr's revolutionary instrumentation for measuring the BCG – the Starr BCG Table – pioneered its use in research and clinical settings [9]. For the following thirty years, the BCG was investigated in both settings, and encouraging results were obtained; however, by the mid-1970s existing BCG instruments were growing obsolete, and few scientists were pursuing research in the field. Perhaps the strongest driver for the decline of the BCG was the cumbersome instrumentation required for accurately measuring the signal.

In the past ten years, there has been a gradual resurgence of BCG research. Interestingly, instrumentation is, again, the major driver. There is a need today for low-cost, simple medical instrumentation usable outside the clinic; specifically, as-needed cardiovascular monitoring in the home. The application requires a new class of BCG instruments: practical devices capable of acquiring high fidelity waveforms. And, in the past decade, several attempts have been made at developing such an instrument. In this work, a modified commercial bathroom scale combined with custom electronics and secondary sensors was used for BCG measurement.

This chapter describes the design and verification of this instrumentation. Specifically, it focuses on the design of the analog circuits used for amplifying and filtering the signals, and the characterization of the BCG sensor. Initially, the circuits were implemented using standard topologies, with high-fidelity, commercially available, discrete components. Then, novel circuits for BCG and ECG measurement were developed, and compared to the standard circuits in terms of electronic performance and physiological accuracy. The chapter is organized as follows: first, the design and verification of the standard circuits is presented; then, the new tools, and techniques for characterizing the BCG sensor are discussed; finally, novel circuits for ECG and BCG acquisition are described.

These new circuits were needed in this research for two main reasons: reducing the electronic noise in BCG measurement, and enabling low-power, low-noise ECG recording with only two electrodes contacting the body (the handlebars of a commercial bathroom scale). For the BCG, lower electronic noise was required to increase the electronic signal-to-noise ratio (SNR). The sources of noise and interference in BCG recordings are discussed in this chapter, in Section 3.3. As discussed in Section 3.3, sources of interference, such as motion artifacts and floor vibrations, are generally more pronounced than the electronic noise in BCG measurements – nevertheless, as these interferences are mitigated or eliminated by the solutions discussed in Chapter 5, the electronic noise will set the sensitivity of the instrument. To reduce electronic noise, a lock-in BCG amplifier was designed, as described in Section 3.5.

These noises interferences would further be reduced by the addition of an ECG sensor to the apparatus, thus enabling triggered averaging of the BCG. In particular, the innovative methods for averaging described in Chapter 4 leverage the timing information of the ECG to provide a full reconstruction of the BCG signal from a recording corrupted by noise and interference.

For integrating ECG sensing into the scale, the handlebar electrodes of an existing commercial scale were used, with a novel two-electrode ECG amplifier, described in Section 3.6. Note that all analog circuits were interfaced to a data acquisition card (USB6218, National Instruments, Austin, TX) and stored on a laptop computer using dedicated software written by Dr. Laurent Giovanrandi and adapted by Mozziyar Etemadi, both at Stanford University.

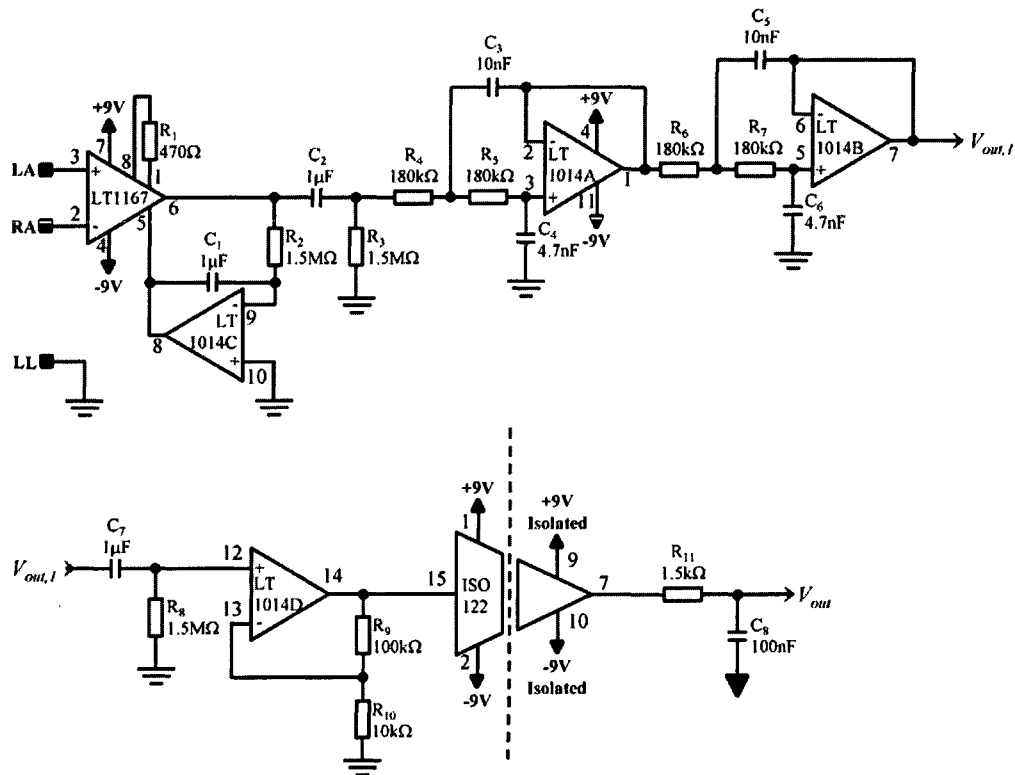


Figure 3.1 Full schematic for standard ECG amplifier circuit. Note that the LT1014 integrated circuit is a quad package operational amplifier – accordingly, the powering is not shown separately for all four amplifiers (A-D). Decoupling capacitors are not shown in this schematic for convenience; 0.1μF ceramic capacitors were used next to all integrated circuit packages. The IC pin numbers are also shown next to the terminals.

3.1. Standard ECG Amplifier

3.1.1. Design Considerations and Circuit Schematic

The ECG is a biopotential with amplitude on the order of 0.5–4 mV_{pp}, and frequency content spanning 0.01–250 Hz [101]. For reliable heartbeat (R-wave) detection, the bandwidth can be narrowed to 5–15 Hz, where the energy of the QRS complex is maximized [102]. The ECG is generally sensed on the surface of the skin using gel-based electrodes which are then connected to an electronic amplifier for conditioning; the output of this amplifier is sampled using an analog-to-digital converter (ADC) and stored in memory or transmitted to a remote location.

Standard ECG amplifiers use a low-noise instrumentation amplifier as the front-end, followed by band-pass filtering and, in some instances, a subsequent gain stage. The most important considerations in voltage-mode ECG sensing are generally high common-mode-

rejection ratio (CMRR) and low input-referred voltage noise density (e_{ni}); both are primarily set by the first stage. Accordingly, the selection of the instrumentation amplifier is crucial in determining the performance of the overall amplifier. The importance of filtering should also not be overlooked: as in any other sensing application followed by an ADC, the filtering must be of high enough order to significantly reduce aliasing of higher frequencies in the subsequent sampling stage.

In this work, a standard ECG amplifier was developed using discrete components. The main purpose of this amplifier was to enable highly-accurate R-wave detection; as a result the full 0.05–250 Hz bandwidth was not targeted in the design. The design objectives were as follows:

1. Differential voltage gain of 1,000 (60 dB).
2. Frequency response spanning 0.2–100 Hz.
3. Greater than 50 dB attenuation at Nyquist rate of the ADC.
4. Electrical isolation for patient safety.
5. Greater than 100 dB CMRR at 60 Hz.
6. Less than 15 nV $\sqrt{\text{Hz}^{-1}}$ of input referred voltage noise density.
7. Less than 1 μV_{pp} of input referred voltage noise at low frequencies (0.1–10 Hz).

The full schematic is shown in Figure 3.1. An LT1167 was used as the front-end instrumentation amplifier, due to its high CMRR (greater than 120 dB), low e_{ni} (approximately 7.5 nV $\sqrt{\text{Hz}^{-1}}$), and low total low-frequency voltage noise (0.28 μV_{pp} from 0.1–10 Hz) at a differential voltage gain of 40 dB. The gain of the front-end was set at 40 dB rather than the total desired differential gain of 60 dB to avoid saturation due to low-frequency baseline wander and motion artifacts. The remaining 20 dB of gain was provided by the final amplification stage of the circuit, a non-inverting amplifier.

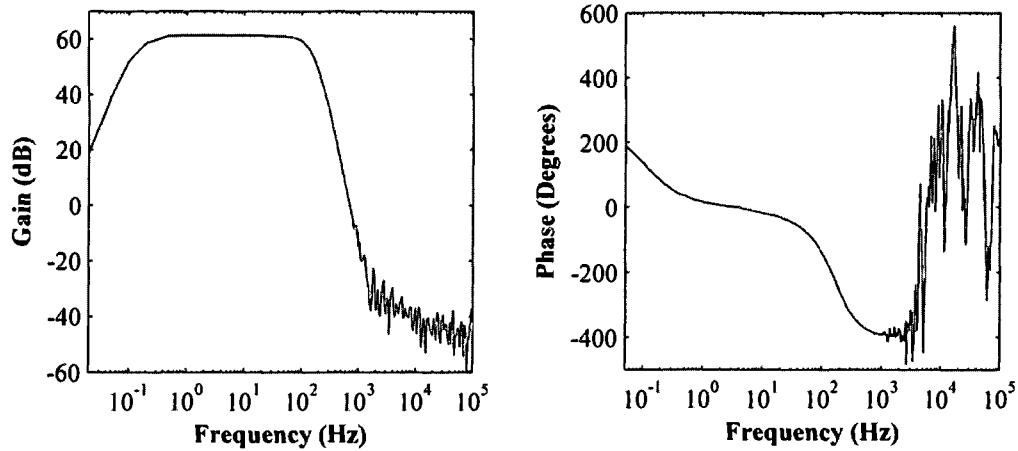


Figure 3.2 Measured gain and phase response of the ECG amplifier.

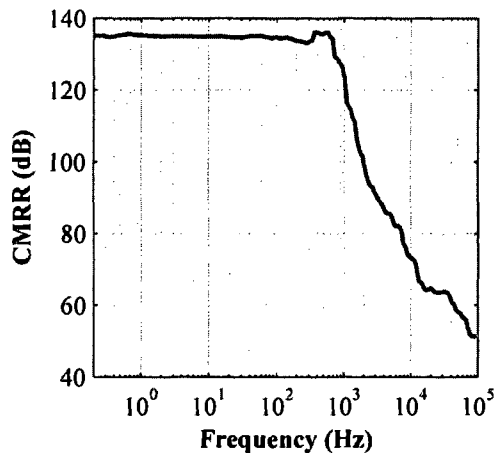


Figure 3.3 Measured common-mode-rejection ratio (CMRR) versus frequency, using an SR780 signal analyzer. For measuring the common-mode gain, an input voltage of $2 V_{RMS}$ was used, and for differential gain, $1 mV_{RMS}$. The CMRR was greater 130 dB for the bandwidth of the amplifier.

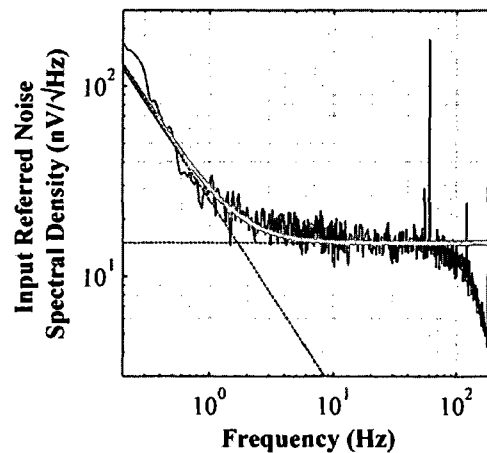


Figure 3.4 Input referred noise spectral density for the ECG amplifier. The thermal noise level was $15 nV_{RMS} \sqrt{Hz}^{-1}$ and the noise corner frequency was approximately 2 Hz. The total noise integrated over the 0.1–200 Hz bandwidth was $2.4 \mu V_{RMS}$.

To reduce the baseline wander in the first stage, an integrator was used in the feedback loop of the LT1167. This forced the output voltage of the LT1167 to zero at low frequencies (< 0.2 Hz), providing an overall high-pass filtering effect. Subsequent high-pass filtering was achieved by ac-coupling between stages; for low-pass filtering, two cascaded second-order Sallen-and-Key low-pass filters were used, with an overall cutoff frequency ($-3dB$) of 100 Hz.

The output of the final gain stage was fed into an analog isolation amplifier (ISO122). This integrated circuit provides a 1 kV isolation barrier to protect the patient from the equipment

used for storing the signal – in this work, a laptop computer. The ISO122 was powered on both the isolated and non-isolated side by $\pm 9V$. Additionally, since it introduced a 500 kHz ripple voltage of 20 mV_{pp} onto the output signal, a simple 1 kHz cutoff frequency first-order-RC filter was used on the output prior to inputting the signal to the ADC.

3.1.2. *Electronic Characterization*

The ECG amplifier was fully characterized and the electronic specifications are summarized in Table 3-1. First, the gain and phase of the amplifier were measured versus frequency, and are shown in Figure 3.2. The mid-band gain was measured as 61 dB and the frequency response spanned from 0.2–104 Hz (-3 dB cutoff). At 500 Hz, the attenuation was 50 dB with respect to the mid-band gain, and at 1 kHz it was 78 dB – as a result, 8-bit accuracy could be

obtained at a 1 kHz sampling rate, and 13-bit accuracy at 2 kHz sampling. The common-mode gain was measured by inputting a sine wave, 2 V_{RMS}, into the two differential inputs (tied together) and measuring the transfer function on the SR780 (Stanford Research Systems, Sunnyvale, CA). The ratio of common- to differential-mode gain (CMRR) was then calculated at various frequencies, and is shown in Figure 3.3 (after moving averaging over 10 points). The CMRR was greater than 130 dB for the full bandwidth of the amplifier (0.2–104 Hz).

The output noise spectral density was measured using the SR780, and the input referred voltage noise spectral density is shown in Figure 3.4. The thermal noise level was 15 nV $\sqrt{\text{Hz}}^{-1}$

Table 3-1 Measured electrical specifications for the standard ECG circuit.

Specification	Measured Value	Units/Comments
Supply Voltage	18	V
Supply Current	13.5	mA
Bandwidth (-3dB)	0.2 - 104	Hz
Mid-Band Voltage Gain	61.2	dB
CMRR	> 130 > 50	dB/0.2–104 Hz dB/0.2 Hz–100 kHz
Input-Referred Voltage Noise	2.4	μV_{RMS}
Total Harmonic Distortion	< -60	dB/0.5–100 Hz

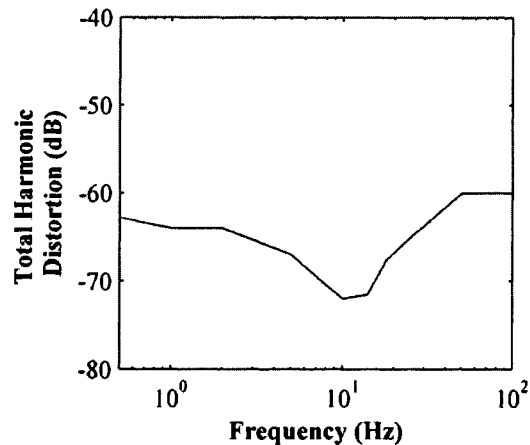


Figure 3.5 Total harmonic distortion versus frequency.

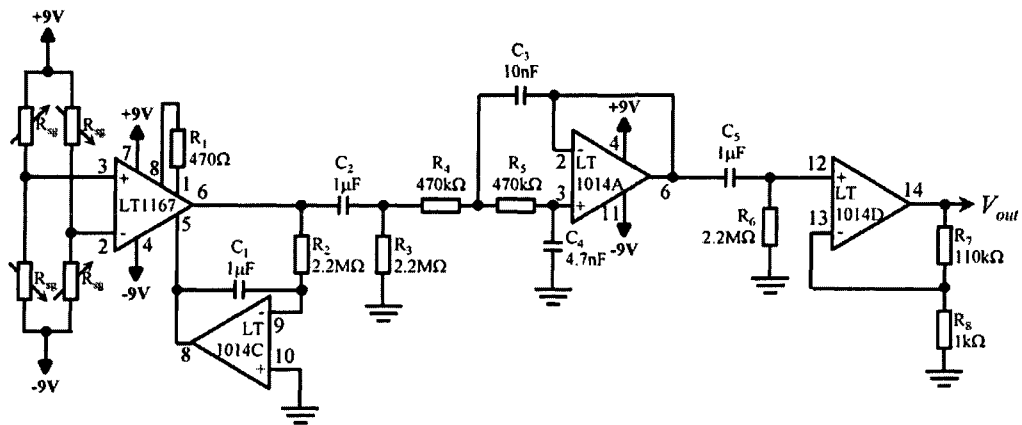


Figure 3.6 BCG amplifier circuit schematic. Note that decoupling capacitors are not shown, and the fourth amplifier on the LT1014 integrated circuit (LT1014B) is unused. The IC pin numbers are also provided for convenience.

and the noise corner frequency was 2 Hz; the total input referred noise integrated over the amplifier bandwidth was $2.4 \mu\text{V}_{\text{RMS}}$.

The total harmonic distortion (THD) versus frequency was also measured using the SR780, and is shown in Figure 3.5. The THD was less than -60 dB (0.1%) for the amplifier bandwidth. The THD at 10 Hz was less than -70 dB (0.03%).

3.1.3. Practical Considerations

In practice, the internal noise of the electronic amplifier will generally be overwhelmed by the interferences in ECG recording: electromyogram (EMG) interference caused by the contraction of muscles around the electrode site [103], motion artifacts due to the stretching of the stratum corneum layer of the skin under the electrode [104], microphonics due to cable motion, and electromagnetic interference coupling to the body [8]. The latter can be mitigated substantially by using shielded cables, where the shield is connected to the ground of the amplifier at the circuit, or driven actively by the sensed common-mode voltage at the input.

3.2. Standard BCG Amplifier

The BCG represents a force along the longitudinal axis of the body. The bathroom scale used for BCG sensing (BC-534, Tanita Corporation, Tokyo, Japan) consisted of a glass platform mounted on four strain gauges, one at each corner of the device, which varied in resistance proportional to the vertical force that loaded the platform. The strain gauges were assembled in a Wheatstone bridge configuration such that the resistors on the complementary

Table 3-2 Measured electrical specifications for the standard BCG circuit.

Specification	Measured Value	Units/Comments
Supply Voltage	18	V
Supply Current	16	mA
Bandwidth (-3dB)	0.15 – 24	Hz
Mid-Band Voltage Gain	90	dB
CMRR	> 130	dB/1–10 Hz
Input-Referred Voltage Noise	140	nV _{RMS}
Total Harmonic Distortion	< -65	dB/1–10 Hz

arms of the bridge varied in opposite direction due to a downward force on the platform. The details of characterizing the BCG sensor are described below.

Vertical forces on the scale generate a differential voltage across the strain gauge bridge; this voltage was sensed using a similar circuit to the ECG amplifier, with a much narrower bandwidth and higher gain. As a result, the design objectives were similar, with the relevant bandwidth of the BCG signal being

1–10 Hz [65, 105], and the signal being on the order of tens of microvolts at the input of the circuit. The circuit used for sensing the BCG is shown in Figure 3.6.

Similarly to the ECG amplifier, the LT1167 instrumentation amplifier was used as the input stage, with integrator feedback to the reference terminal reducing the low frequency drift in the output. Since the sampling rate used for the BCG was always the same as for the ECG, while the bandwidth was ten times narrower, one Sallen-and-Key filter (2nd order) was sufficient for reducing aliasing. The low-pass cutoff frequency (-3 dB) was set at 24 Hz by this

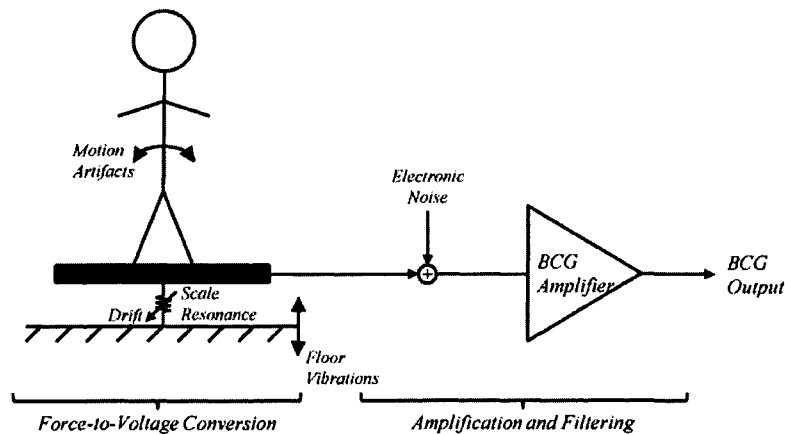


Figure 3.7 Block diagram showing sources of noise and interference in standing BCG recordings at the sensor input, due to the sensor, and due to the electronic amplifier.

filter, and the high-pass filtering resulting from the integrator feedback in the first stage and the ac-coupling throughout had a cutoff frequency of 0.15 Hz.

The measured electrical specifications for the BCG circuit are summarized in Table 3-2. The gain and frequency response of this circuit were found to be 90 dB and 0.15–24 Hz, respectively. The CMRR was greater than 100 dB over the full BCG bandwidth. Using an oscilloscope (TDS3012, Tektronix, Beaverton, OR), the output voltage noise was found to be 1.5 mV_{RMS}; when referred to the input, this corresponds to a voltage noise of 140 nV_{RMS}. The measurement was repeated using a 5½-digit digital multimeter (34401A, Agilent Technologies, Santa Clara, CA): the output voltage noise was found to be 0.9 mV_{RMS} which, referred to the input, corresponds to a voltage noise of 82 nV_{RMS}. The THD was less than -65 dB for the bandwidth of the amplifier.

3.3. Sources of Noise and Interference in Standing BCG Recording

Noise and interference can be introduced into standing BCG measurements at various stages of the acquisition process. The word ‘standing’ is used here to highlight the fact that if the measurements were taken from a prone subject – such as on a table- or bed-based system – some of these effects would be much less pronounced or not present at all. The block diagram in Figure 3.7 shows the signal path and details each significant source of noise or interference that can corrupt standing BCG measurements.

In general, there are two classes of noises and interferences that corrupt the recordings: those inherent to the sensors or amplifiers, such as voltage noise, distortion, and drift, and those caused by external sources, such as motion artifacts or floor vibrations. The former can be minimized by the proper selection and design of the sensor and amplifier. In this work, the sensor was a commercial product – as a result, the majority of the work was focused on characterizing the sensor to understand and mitigate its shortcomings. These methods are discussed below in the following section. In addition, various new techniques were implemented to reduce the effects of external interferences, as discussed in Chapters 4 and 5.

3.4. Characterization of the BCG Sensor

3.4.1. Static Characterization: Spring Constant, Force-to-Voltage Gain and Linearity

The modified weighing scale was statically characterized as a force sensor to determine the gain factor and linearity in translating input force to output voltage across the strain gauge bridge.

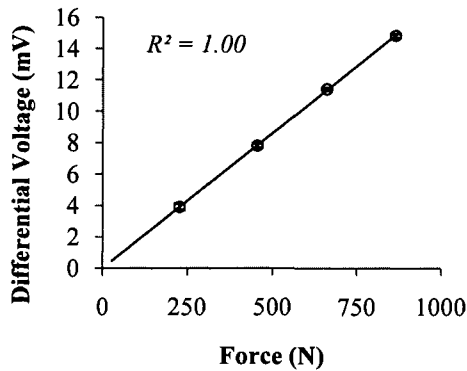


Figure 3.8 Large-signal characterization of scale. The force-to-voltage transfer was shown to be linear ($R^2 = 1.00$).

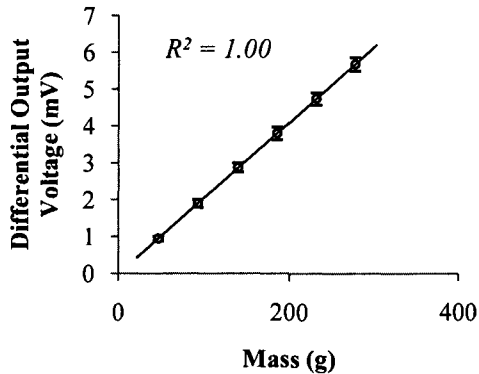


Figure 3.9 Small-signal characterization of scale. The force-to-voltage transfer was shown to be linear ($R^2 = 1.00$).

The gain and linearity of the scale were measured for both large and small forces by loading the scale with several weights and measuring the differential voltage across the bridge. The bridge was biased at $\pm 9V$ for all experiments, and the unloaded resistance of each strain gauge was $1.49 \text{ k}\Omega \pm 0.01 \text{ k}\Omega$. To test large signal linearity, iron plates of known mass were loaded onto the scale in increments of 4.5 kg from zero to 102.5 kg. At each weight, the differential voltage across the bridge was measured using a 5½-digit multimeter (34401A, Agilent Technologies, Santa Clara, CA). To test small signal linearity, the scale was biased with 65.9 kg and several calibrated 45 g masses were consecutively loaded from zero to 270 g. For each weight, the differential voltage across the bridge was amplified using a dc-coupled instrumentation amplifier and measured with the same multimeter.

The results are shown in Figure 3.8 for the large-signal characterization and Figure 3.9 for the small-signal characterization. The scale was shown to be linear (R^2 of 1.00) as a transducer from force to differential voltage across the bridge for both large and small loads. The force to differential voltage gain factor was $19.1 \mu\text{V N}^{-1}$. Since the expected amplitude of the BCG was on the order of a few Newtons peak-to-peak, this corresponded to an input voltage on the order of tens of microvolts at the input of the amplifier, as discussed in Section 3.2 above.

3.4.2. *Dynamic Characterization: Frequency Response, Distortion, Drift*

For testing the dynamic response of the scale-circuit system, the test setup shown in Figure 3.10 was used. The scale was loaded by iron weights of known mass and a loudspeaker – with an accelerometer attached to its cone – was set on top. With this setup, the frequency response, distortion, and drift of the system were measured.

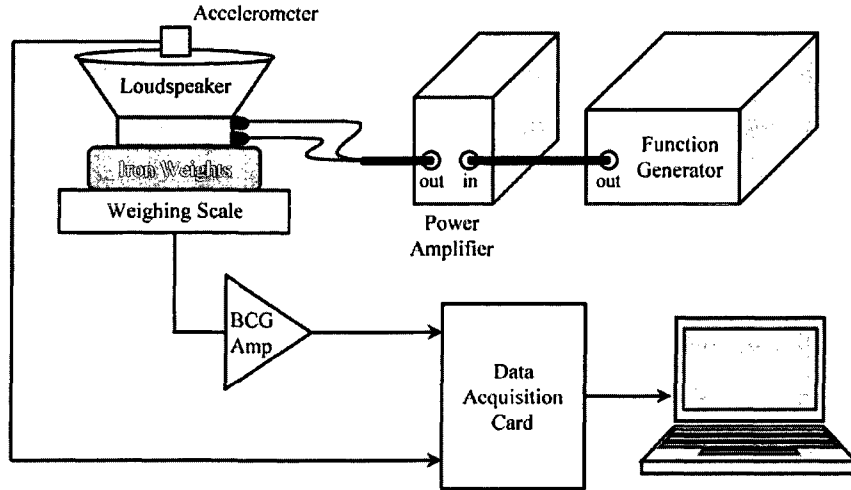


Figure 3.10 Block diagram showing setup used for dynamic characterization of the BCG sensing scale.

The frequency response of the scale-circuit system was measured indirectly by analyzing the step response of the system in the frequency domain. The scale was modeled as a second-order mechanical system – where the glass scale platform with the human body on top was considered to be a spring loaded by a mass – with resonant frequency given by:

$$f_{res} = \frac{1}{2\pi} \sqrt{\frac{k}{m}} \quad (3.1)$$

where f_{res} is the resonant frequency (in Hz), k is the spring constant (in N m^{-1}), and m is the mass loading the spring (in kg). The mass on the scale was varied and the resonant frequency was computed at each load; a best least-squares fit was then used to estimate the spring constant of the scale.

To measure the step response, the loudspeaker was driven by square waves generated by a bench-top function generator fed through an HP467A power amplifier (Hewlett-Packard Company, Palo Alto, CA). The voltage output of the BCG amplifier was recorded simultaneously as the signal from the accelerometer mounted on the speaker cone. The total mass loading the scale was varied and the step response was measured repeatedly at each load.

The accelerometer data was used as a trigger to ensemble average the step responses of the scale output for each load. At each load, the peaks of the accelerometer signal were manually located and an ensemble of step responses was formed from the scale output. The ensemble

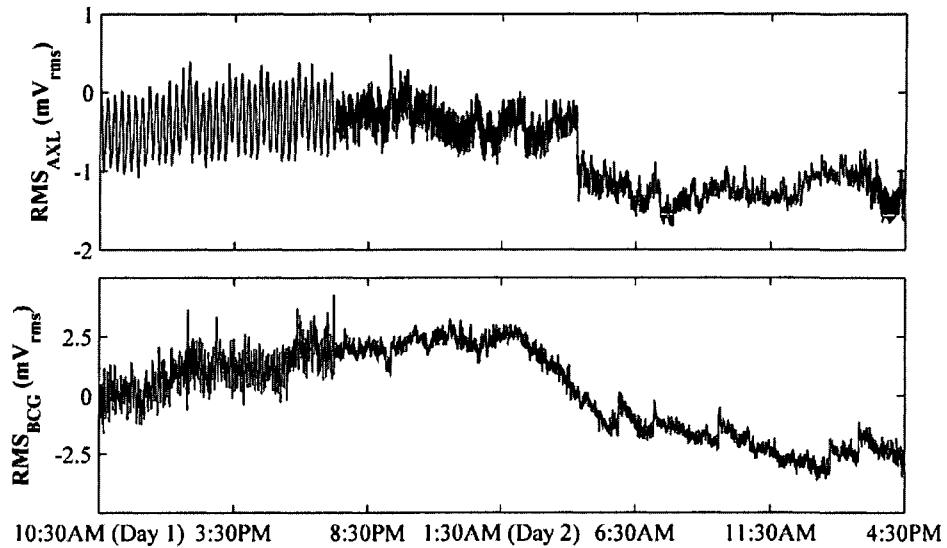


Figure 3.11 Characterization of the drift in the BCG sensor: the loudspeaker was driven such that the output voltage of the BCG circuit was comparable to a typical BCG signal ($2 N_{pp}$). The RMS of the accelerometer and BCG waveforms are shown above after normalization and moving averaging (1 min. window). The BCG sensor drift was thus found to be negligible.

average over all responses for a given load was then computed; the periodogram, computed as the fast Fourier transform (FFT) of the autocorrelation sequence for this average response, was then found to estimate the power spectral density (PSD).

The peak frequency of this estimated PSD was manually located and recorded as the resonant frequency of the scale for each load mass. This process was then repeated for all masses, providing the resonant frequency of the scale as a function of load mass. As described above, this data was then used to find the spring constant of the scale: $1.19 \text{ N } \mu\text{m}^{-1}$, within 6% of the spring constant determined statically by Richard Wiard (Stanford University), as described in Inan, *et al.* [92]. With this spring constant, body masses up to 300 kg could theoretically be tolerated on the scale without lowering the resonant frequency below the upper end of the BCG bandwidth, 10 Hz – in reality, the capacity of the scale was 150 kg, which is adequate for the majority of the population.

The total harmonic distortion (THD) introduced by the scale in converting vertical force-to-voltage was investigated: this would directly influence the morphological accuracy of the measured BCGs. The scale was biased at 40 kg and the speaker cone was loaded by small masses, attached by adhesive to the cone, such that a 10 Hz sine-wave excitation of the cone produced a low distortion $2 N_{pp}$ mechanical force on the scale. (Note that this force was measured using the force-to-voltage gain factor of the scale computed above.) The signal from

the accelerometer was monitored simultaneously as the output signal from the BCG amplifier, and the THD of both were computed from the first five harmonics and compared.

For the accelerometer signal, the THD was measured as 0.5%, or -46 dB; for the scale amplifier output, the THD was 0.76%, or -42.4 dB. The difference was considered to be the excess distortion introduced by the scale-circuit combination: 0.26%, or -51.7 dB. For a force input of amplitude $2 N_{pp}$, on the order of a BCG signal, this corresponds to a distortion level on the order of $5 mN_{pp}$; this is comparable to the input referred voltage noise of the amplifier which was found to be 4–7 mN_{pp} (80–140 nV_{pp}).

The drift was determined by monitoring the ac force-to-voltage gain of the scale was monitored continuously for a 30-hour period to determine the drift. For this measurement, the same 10 Hz, $2 N_{pp}$ sine wave was used to mechanically excite the scale, and the accelerometer and scale amplifier outputs were recorded continuously. The results of this characterization are shown in Figure 3.11. As shown in this figure, the ac gain trended similarly for both signals for this period of time.

As a result, for BCG measurements taken over recording periods on the order of five to ten minutes, the drift in sensor gain was not considered to be a confounding variable. This result is important for the data analysis presented in Chapter 7, below, where the RMS power of the

BCG was monitored for ten minutes continuously during exercise recovery.

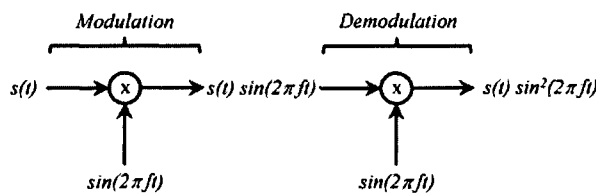


Figure 3.12 Standard lock-in amplifier modulation and demodulation procedure. The output consists of half the original signal plus half the signal shifted to twice the carrier frequency.

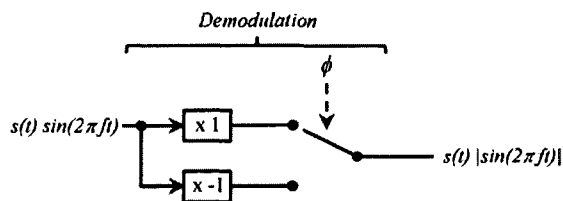


Figure 3.13 Phase-synchronous demodulation circuit used in this work, based on [3]. The switch is toggled in phase with the carrier.

3.5. Lock-in BCG Amplifier

With the BCG sensor fully characterized, a lock-in BCG amplifier was designed to lower the electronic noise in BCG measurements. The predominant component of electronic noise in BCG measurements is flicker noise in the first stage of the amplifier. The lower end of the BCG spectrum can extend below 1 Hz, which is less than the noise corner frequency

of most commercial instrumentation amplifiers – for example, the LT1167 instrumentation amplifier used in this work has a corner frequency of 7 Hz (at a voltage gain greater than 100).

For a lock-in amplifier, the signal to be measured is modulated up to a higher frequency than the signal bandwidth, amplified, and demodulated. By boosting the *modulated* version of the signal, the amplifier operates well beyond its noise corner frequency. Then, since the noise is mainly thermal, the noise density is less than it would be at lower frequencies (around dc). Several implementations of lock-in amplifiers can be used depending on the requirements of the system in terms of performance and complexity. In this work, a square-wave modulation signal is used, followed by differential amplification and synchronous demodulation, as described by Horowitz and Hill [3]. This chapter briefly discusses the theory of lock-in amplification, describes the circuit design and characterization of the lock-in BCG amplifier, and shows recordings obtained using this approach.

3.5.1. *Basic Lock-In Amplifier Theory*

The simplest lock-in amplifier, in terms of theoretical analysis, modulates a signal with a sine wave then multiplies the signal by the same sine wave for demodulation (see Figure 3.12). The bandwidth of the signal must be much lower than the frequency of modulation for this technique to be effective. The output of the demodulator can be expressed as

$$\begin{aligned}
 v_{out}(t) &= s(t)\sin^2(2\pi ft) \\
 &= s(t)\left(\frac{1 - \cos(2\pi(2f)t)}{2}\right) \\
 &= \frac{1}{2}s(t) - \frac{1}{2}s(t)\cos(2\pi(2f)t)
 \end{aligned} \tag{3.2}$$

This output, $v_{out}(t)$, is then passed through a low-pass filter, which is assumed to be ideal in this analysis, resulting in the original signal, $s(t)$ (with half the original amplitude lost).

In this work, the simple demodulator was replaced by a phase-synchronous demodulation circuit, shown in Figure 3.13, based on the Horowitz and Hill text [3] and Williams' AN-43 [91]. Although the waveform used for modulation in this work was a square wave, the theory presented here is for sine wave excitation; this analysis could then be extended for square waves by using a Fourier series representation of the square wave as a sum of sine waves.

For this demodulation scheme, the switch toggles the gain between positive and negative one in phase with the original carrier. This effectively sets the output as the absolute value of the carrier sine wave, with amplitude modulated by the signal:

$$\begin{aligned}
v_{out}(t) &= s(t)|\sin(2\pi ft)| \\
&= s(t)\sqrt{\sin^2(2\pi ft)} \\
&= \frac{s(t)}{\sqrt{2}}\sqrt{1 - \cos(2\pi(2f)t)}
\end{aligned} \tag{3.3}$$

The statement in the radical, which will always be nonnegative, can be expanded by a Taylor series taken about zero as follows:

$$\begin{aligned}
v_{out}(t) &= \frac{s(t)}{\sqrt{2}} \left[1 - \frac{1}{2} \cos(2\pi(2f)t) - \frac{1}{8} \cos^2(2\pi(2f)t) \right. \\
&\quad - \frac{1}{16} \cos^3(2\pi(2f)t) - \frac{5}{128} \cos^4(2\pi(2f)t) \\
&\quad \left. - \frac{7}{256} \cos^5(2\pi(2f)t) - \frac{21}{1024} \cos^6(2\pi(2f)t) - \dots \right]
\end{aligned} \tag{3.4}$$

Again, assuming that this output signal will be passed through an ideal low-pass filter, and that the bandwidth of $s(t)$ is much less than f , this expression can be greatly simplified. Note that only the even powers of the cosine function will have frequency components at dc. On the other hand, the odd powers of cosine will only have frequency components at and above the fundamental modulation frequency, f .

As a result, the odd powers in equation (3.4) can be excluded from the analysis. The Fourier transforms of the even powers, \cos^2 , \cos^4 , etc., will include impulses at dc with the following magnitudes: $[1/2, 3/8, 5/16, \dots]$. Note that these magnitudes can be calculated directly by using the convolution property of the Fourier transform. All other frequency components of the even powers of cosine will be greater than or equal to twice the fundamental modulation frequency ($2f$), and thus will be substantially attenuated by the low-pass filter operation.

Accordingly, when low-pass filtered, the output can be approximated as:

$$\begin{aligned}
v_{out}(t) &= \frac{s(t)}{\sqrt{2}} \left[1 - \left(\frac{1}{8}\right)\left(\frac{1}{2}\right) - \left(\frac{5}{128}\right)\left(\frac{3}{8}\right) - \left(\frac{21}{1024}\right)\left(\frac{5}{16}\right) \dots \right] \\
&\approx 0.648 s(t)
\end{aligned} \tag{3.5}$$

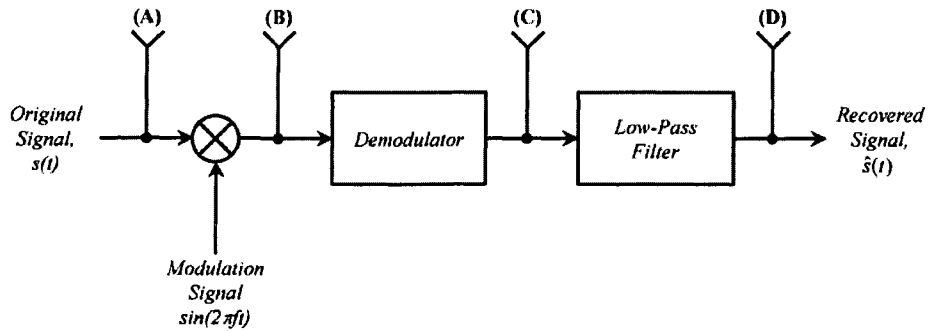


Figure 3.14 Block diagram showing the stages of modulation and demodulation for signal, $s(t)$. An example of the waveforms that would be seen at points A–D is provided below.

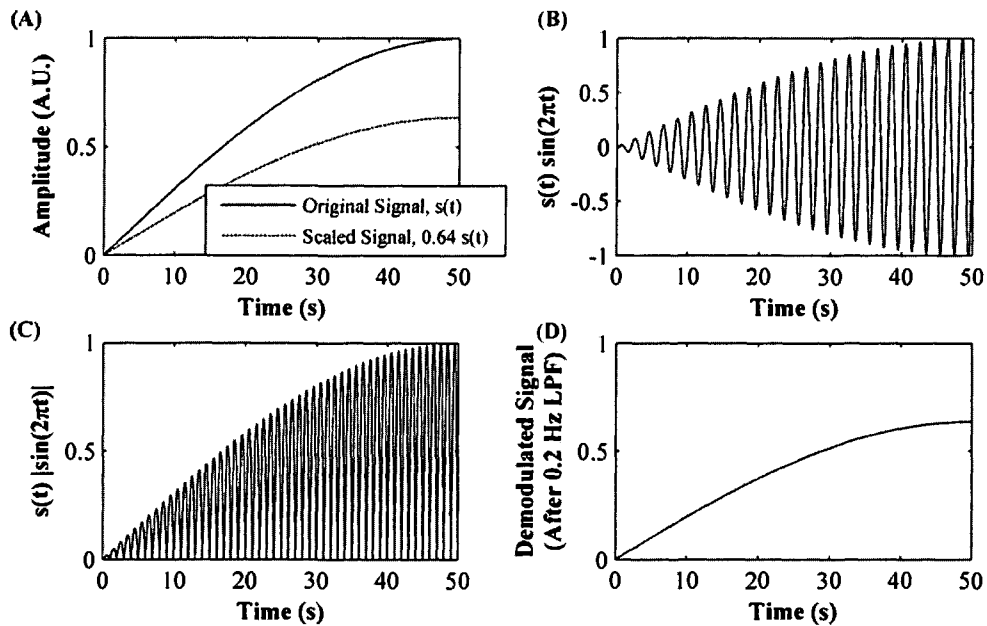


Figure 3.15 Illustration of phase-synchronous demodulation scheme. The original signal is recovered with a scaling factor of approximately 0.64 after low-pass filtering (some of the signal amplitude is lost to the harmonics of the signal). The original signal is one quarter-cycle of a 0.01 Hz sine wave, and the modulation signal is a 1 Hz sine wave. The low-pass filter cutoff is 0.2 Hz.

Considering these first four terms of the series yields a scaling factor of 0.648; with all of the terms considered, the scaling factor converges to 0.637.

The principle of operation for this demodulation scheme is shown visually in Figure 3.14 and Figure 3.15. In this example, the original signal was a quarter-cycle of a 0.01 Hz sine wave, and the modulation carrier was a 1 Hz sine wave. The upper-right plot in Figure 3.15 shows the modulated version of the original signal; the bottom-left, the output of the phase-synchronous demodulator. When the demodulated signal is low-pass filtered with a cutoff

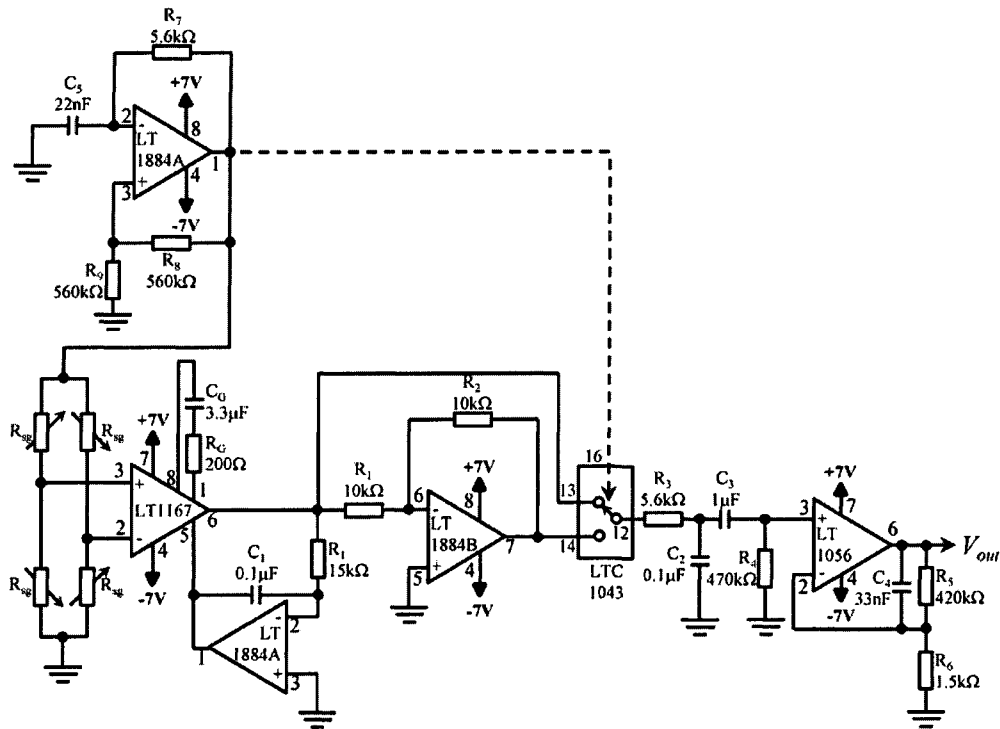


Figure 3.16 Full schematic for lock-in BCG amplifier circuit. Note that the power supply connections for the LT1884A (in the feedback loop of the LT1167) are not explicitly shown since it is in the same package as the LT1884B to its side. Additionally, power supply decoupling capacitors (0.1 μF at both supply pins of each IC) and the second op-amp in the relaxation oscillator package are not shown. The IC pin numbers are provided next to the packages for convenience.

frequency of 0.2 Hz, the original signal is recovered with a scaling factor of 0.637. As a result, the demodulation is successfully achieved with approximately one third of the signal amplitude lost.

3.5.2. Circuit Design

The full circuit schematic is shown in Figure 3.16. An op-amp relaxation oscillator was designed to excite the strain gauge bridge of the scale. The op-amp (LT1884, Linear Technology, Milpitas, CA) was selected based on a smooth large signal step response, rail-to-rail output swing capability, and an adequate slew rate for the application (approximately $1 \text{ V } \mu\text{s}^{-1}$ to facilitate high quality 10 V_{pp} , 3 kHz pulses). The frequency of oscillation, f_{osc} (in Hz), was set using the following equation:

$$f_{osc} = \frac{1}{2 \ln(2) R_7 C_5} \quad (3.6)$$

With R_7 set at 5.6 k Ω , and C_5 at 22 nF, the oscillator frequency was designed to be 3.7 kHz. The square wave output of this oscillator is shown in Figure 3.17 – the measured oscillation frequency was 3.3 kHz.

An ac-coupled differential amplifier was designed for boosting the voltage generated across the strain gauge bridge. For this purpose, a commercial instrumentation amplifier (LT1167, Linear Technology, Milpitas, CA) was used with a series RC combination in place of the gain-setting resistor: R_G and C_G in Figure 3.16. The voltage gain of the instrumentation amplifier input stage of the circuit, $A_{v1}(j\omega)$, can then be written as:

$$A_{v1}(j\omega) = 1 + \frac{49.9 \text{ k}\Omega}{R_G} (1 + j\omega R_G C_G) \quad (3.7)$$

where the 49.9 k Ω value is given in the LT1167 datasheet.

To set the mid-band gain at 250, R_G was selected to be 200 Ω ; for a low-end cutoff frequency of 100 Hz, the capacitor was then selected to be 3.3 μ F. To provide another order of high-pass filtering, an inverting op-amp integrator was used from the output to the reference terminal of the instrumentation amplifier. The gain and phase response of this amplifier, measured using the SR780 signal analyzer (Stanford Research Systems, Sunnyvale, CA), are shown in Figure 3.18. For this measurement, an input level of 10 mV_{RMS} was used.

This differential amplifier was followed by the synchronous demodulation stage as described above. The LTC1043 switched capacitor building block, with built-in charge injection cancellation circuitry, was used for the switching. Although in this implementation the op-amp oscillator was directly connected to the clock input of the LTC1043, in some instances some phase compensation may be required at this input [91]. For this purpose, a simple RC low-pass filter with a potentiometer in parallel with the

Table 3-3 Measured electrical specifications for lock-in BCG amplifier.

Specification	Measured Value	Units/Comments
Supply Voltage	10	V
Supply Current	12	mA
Bandwidth (-3dB)	0.2–12	Hz
Mid-Band Voltage Gain	97	dB
Input-Referred Voltage Noise	21	nV _{RMS} /BW: 0.3–10 Hz
Input-Referred Force Noise	0.97	mN _{RMS} /BW: 0.3–10 Hz

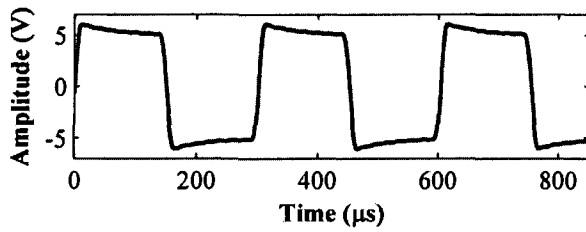


Figure 3.17 Square-wave output from op-amp relaxation oscillator ($f_{osc} = 3.3$ kHz).

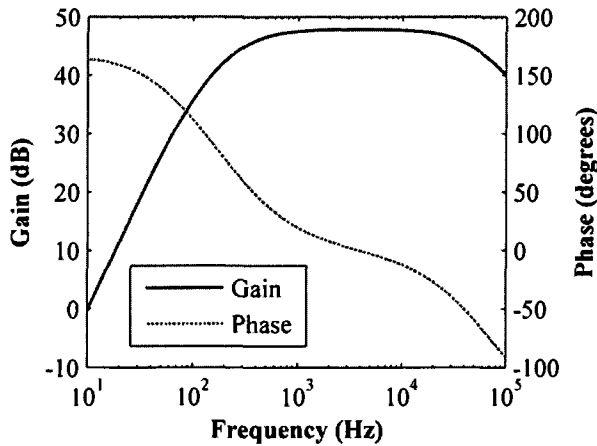


Figure 3.18 Gain and phase response of input stage with an ac-coupled instrumentation amplifier. The mid-band voltage gain was 48 dB, and the low frequency cutoff (-3 dB) was 300 Hz.

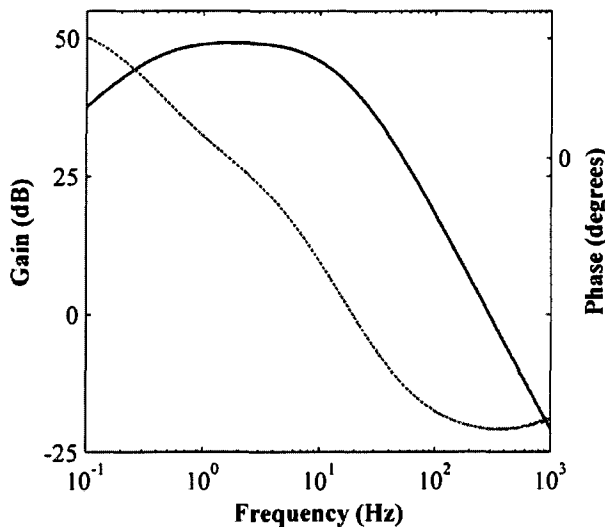


Figure 3.19 Gain and phase response of the output stage. The mid-band voltage gain was 49 dB and the bandwidth was 0.3–12 Hz.

capacitor would suffice for adjusting the phase.

The output of the synchronous demodulation stage was fed into a band-pass filter block with a gain of 280 and a bandwidth (-3 dB) from 0.3–12 Hz. The gain and phase response of this stage are shown in Figure 3.19. The attenuation at the clock frequency was greater than 80 dB with this filtering. At 500 Hz, the Nyquist frequency for the sampling rate typically used in this work, the attenuation was approximately 60 dB, corresponding to 10 bits of dynamic range before the aliasing limit. The electronic specifications are summarized in Table 3-3.

3.5.3. Noise Measurements for Standard and Lock-In BCG Amplifiers

The output voltage noise density was measured as a function of frequency for the standard BCG amplifier described in 3.2 and the lock-in amplifier. For this measurement, the unloaded BCG scale was connected to

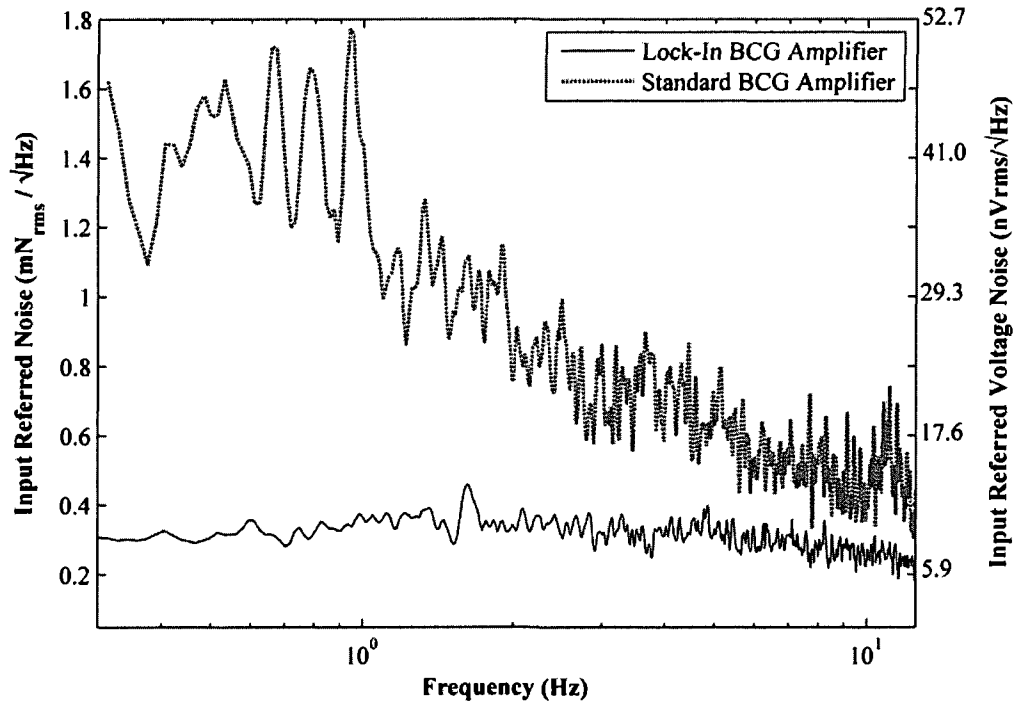


Figure 3.20 Input referred force noise density (in $\text{mN}_{\text{RMS}} \sqrt{\text{Hz}}^{-1}$) versus frequency for the lock-in and standard BCG amplifiers. The flicker noise is eliminated by the lock-in technique since the signal is modulated to a frequency beyond the corner frequency of the LT1167 before amplification. To convert the units to Volts, the force-to-voltage gain of the scale was used; then the thermal noise of the lock-in BCG amplifier was approximately $7.8 \text{ nV} \sqrt{\text{Hz}}^{-1}$.

the input of each amplifier, and the output voltage spectrum was recorded using the SR780. Both circuits were battery operated and placed in a Faraday cage to reduce external interference. The spectra were averaged ($N = 50$) using the RMS averaging feature of the signal analyzer.

To refer the output voltage noise density to the input, the force-to-voltage gain of the entire system was used for both circuits. Accordingly, the input referred force noise densities for both circuits are shown in Figure 3.20. As shown in this figure, the flicker noise has been eliminated from the spectrum in the lock-in amplifier: while the standard BCG amplifier noise density has a typical inverse relationship to frequency, the lock-in noise density is relatively constant in frequency.

To find the total noise for both circuits, the square of the noise density was integrated over the desired bandwidth (0.3–10 Hz) and the square root was taken:

$$F_{ni,tot}(N_{rms}) = \sqrt{\int_{f=0.3 \text{ Hz}}^{10 \text{ Hz}} F_{ni}(f)^2 df} \quad (3.8)$$

where $F_{ni,tot}$ (in Newtons, RMS) is the total force noise taken over the 0.3–10 Hz bandwidth, and $F_{ni}(f)$ (in $\text{N} \sqrt{\text{Hz}^{-1}}$) is the force noise density as a function of frequency. The total noise for the standard BCG circuit was found to be $2.4 \text{ mN}_{\text{RMS}}$ ($52 \text{ nV}_{\text{RMS}}$), and, for the lock-in circuit, $0.97 \text{ mN}_{\text{RMS}}$ ($21 \text{ nV}_{\text{RMS}}$), corresponding to a total noise reduction of 7.7 dB.

3.5.4. BCG Measurements Using Standard and Lock-In Amplifier

A BCG measurement taken using the lock-in amplifier is shown in Figure 3.21. The signal-to-noise ratio is sufficiently high to detect the heartbeat peaks, and the morphology of the BCG appears undistorted. Unfortunately, simultaneous recordings with both the standard and lock-in BCG amplifiers could not be made: stacking two scales vertically would alter the mechanical frequency response of the setup and placing them side-by-side with one foot on each may not equally distribute the BCG forces to the two scales.

Nevertheless, to ensure that the lock-in amplifier was not distorting the measured BCG waveform, BCG recordings were acquired from one subject using both circuits sequentially. The ECG was recorded simultaneously such that the ensemble averages using both circuits could be compared in the time and frequency domains.

The ensemble averages, and the corresponding PSDs, using both circuits are shown in Figure 3.22. Visually, the averages look similar in both the time and frequency domain. The residual was also computed for the averages, and the variance of this residual was less than

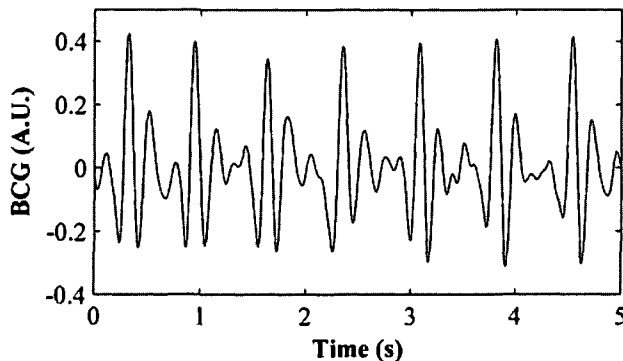


Figure 3.21 A BCG signal measured using the lock-in amplifier, after the standard digital filtering operations used for the BCG signal.

5% of the variance of the ensemble averaged BCG acquired by the standard BCG circuit. The cross-correlation of the two averages, with the auto-correlation of each normalized to unity, was found to be 0.98. Accordingly, the lock-in

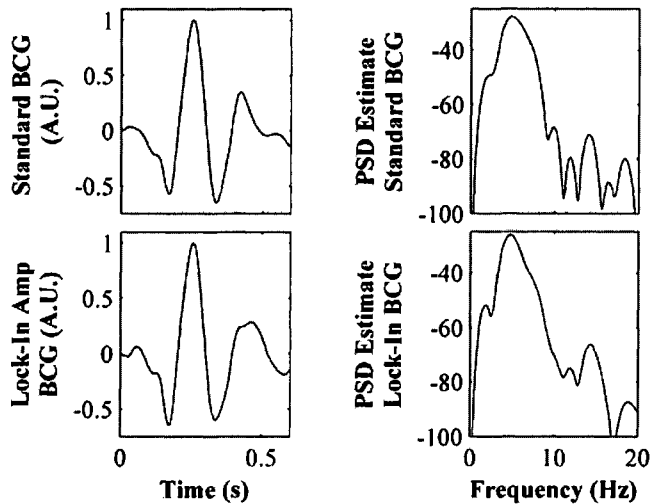


Figure 3.22 Ensemble average BCGs ($n = 45$ beats), with amplitude normalized to unity, and corresponding PSDs, computed for two sequentially taken recordings from the same subject. The variance of the residual of the two averages was less than 5% of the variance of the standard average, demonstrating that the BCGs were not distorted.

amplifier was not significantly distorting the measured BCG signal.

3.5.5. Discussion

The circuit described in this section could be used to significantly reduce the electronic noise in BCG measurement. In practice, electronic noise is typically not the dominant source of error in standing BCG recordings – motion artifacts and floor vibrations are usually most prominent.

However, as the technology for reducing these interferences improves, the electronic noise will be the next limiter of achievable SNR. At that point, by using a lock-in approach rather than a standard amplifier, an extra 7.7 dB of headroom can be attained.

It should be noted that the electronic noise for the lock-in amplifier described here is also significantly lower than a BCG amplifier circuit disclosed in the recent literature [106]. In this paper, the noise floor of the BCG acquisition system was $3.9 \text{ mN}_{\text{RMS}}$. This value takes into account power supply rails of $\pm 9\text{V}$, and the highest sensitivity scale described in their work. For the other scales discussed in their study, the force noise would be higher proportional to the decrease in sensitivity of the scale.

Additionally, if the scale is used in other measurement conditions, such as on a chair under a seated subject, the effects of motion and floor vibrations would be significantly reduced, rendering the electronic noise a much more significant portion of the overall noise and interference corrupting the recording. Finally, since the noise reduction is most effective at lower frequencies, the slowly-varying heartbeat amplitudes of the lock-in signal may track respiration more accurately than the standard circuit.

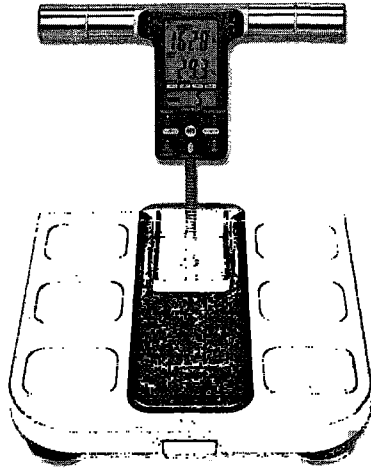


Figure 3.23 Omron HBF-500 bathroom scale with handlebar electrodes.

3.6. Novel Two-Electrode ECG Circuit Design

In some settings, applying electrodes to the subject for simultaneously acquiring ECG alongside BCG signals is impractical. However, simultaneous ECG acquisition is the best option for robust BCG recording, since the timing of the ECG can be used for signal estimation (as described in Chapter 4). For this reason, a scale with handlebar electrodes – originally intended for use in body fat analysis via impedance measurements – was investigated: the Omron HBF-500 (Omron Healthcare Inc., Bannockburn, IL), shown in Figure 3.23. The handlebar electrodes,

attached by a phone cable to the scale base, were disconnected from the internal circuitry and interfaced to an ECG amplifier.

Unfortunately, since there were only two electrodes available for ECG recording, the

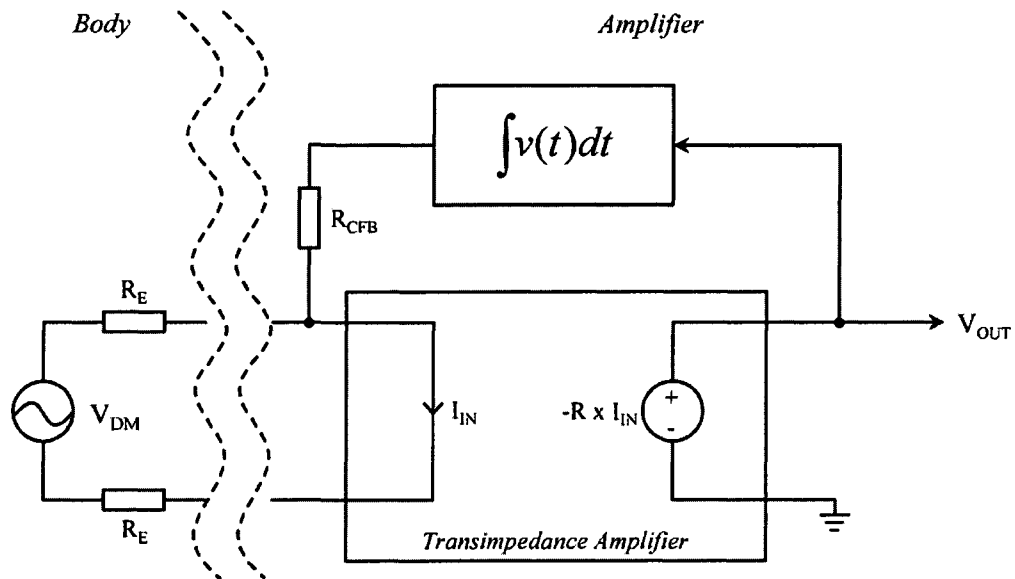


Figure 3.24 Block diagram describing the circuit topology. In this diagram, R_E represents the electrode-skin interface resistance, R_{CFB} represents the active current feedback series resistance, and R is the open-loop transimpedance gain of the amplifier. V_{DM} denotes the unloaded ECG voltage at the surface of the skin.

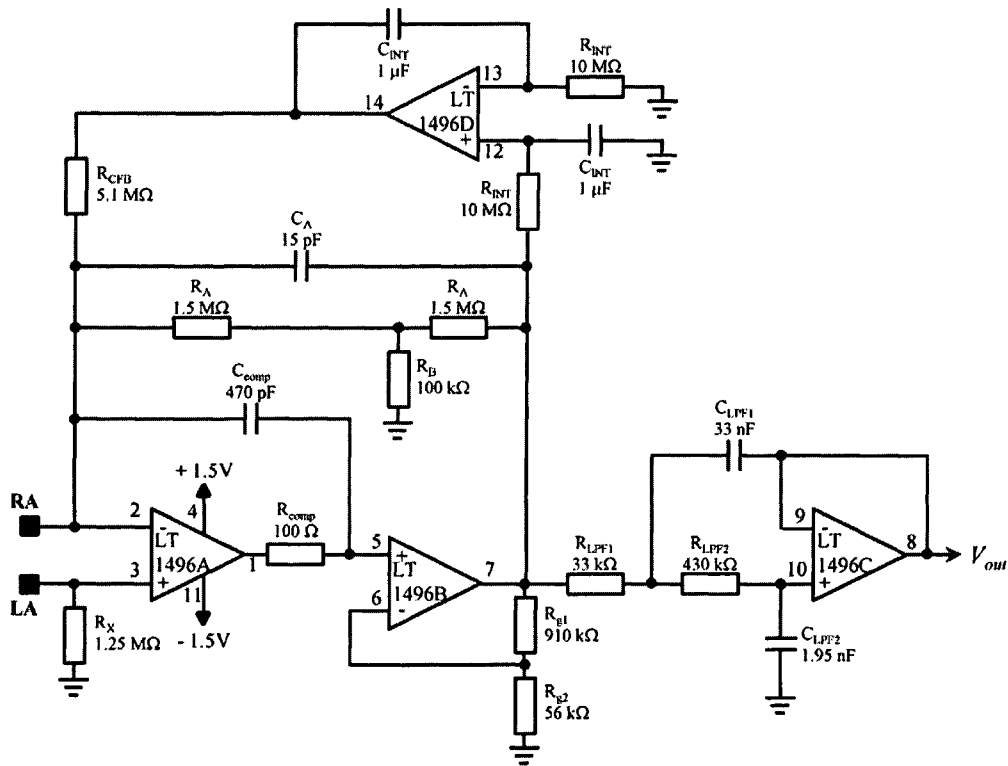


Figure 3.25 Full circuit schematic for two-electrode biosignal amplifier. Note that power supply decoupling capacitors are not shown. For both supply pins of the IC, 0.1 μF ceramic capacitors were connected to ground.

standard three-electrode amplifier described above would not provide stable results in this application. Standard ECG circuits depend on having a third connection to the body which is either passively coupled or actively driven to the ground of the circuit. Without this third ‘ground’ electrode, the common-mode input voltage can drift outside the allowable range of the amplifier, causing intermittent saturation problems where the signal is lost. Additionally, the common-mode-rejection of the circuit degrades significantly without this third electrode, causing an intolerably high level of power-line interference overwhelming the quality of the measured ECG. As a result, a new ECG amplifier was designed specifically for use in two-electrode systems. This section describes the design and verification of this amplifier.

3.6.1. Design Considerations and Objectives

The goal was to design an ultra-low power, low noise ECG amplifier capable of stable operation with only two electrodes connected to the body. These objectives would need to be met without compromising the signal quality of the measured ECGs.

To achieve an ultra-low quiescent power, the circuit uses a composite transimpedance topology to circumvent the low gain-bandwidth-product (GBWP) of commercially available micro-power operational amplifiers. Additionally, the active current feedback stabilized the common-mode input voltage of the amplifier to reduce electrode drift and amplifier saturation problems that can be present in typical two-electrode systems.

A block diagram of the circuit is shown in Figure 3.24. The differential ECG voltage at the skin is denoted V_{DM} . This voltage sources current through the resistance of the skin-electrode interface, R_E , into the transimpedance stage, which provides an amplified voltage output proportional to the current input. A non-inverting integrator filters the slowly varying components of the output voltage and feeds back a current to the electrode at the input. Since the amplifier has inverting open-loop gain, this has an overall negative feedback effect, driving the average low frequency variations in output voltage to zero.

The fundamental difference between this circuit and standard biosignal amplifiers is that it amplifies current rather than voltage. The input stage presents low differential input impedance to the body, which reduces cable noise and interference without the need for shielding or guarding.

The full circuit schematic is shown in Figure 3.25. The two electrodes are connected to the positive and negative inputs. While the discussion of this circuit here is primarily focused on ECG acquisition, the same topology could readily be adapted for electroencephalogram (EEG), electrooculogram (EOG), and electromyogram (EMG) acquisition as well.

A composite amplifier topology is used to allow a micro-power (low GBWP) operational amplifier, such as the LT1496 (Linear Technology Inc., Milpitas, CA), to be used without compromising the full medically-relevant bandwidth required for an ECG amplifier. This operational amplifier has a quiescent current of less than 1 μA per amplifier, at the expense of very low GBWP (2.7 kHz). For an ECG amplifier, where a gain of at least 100 to 1000 and a bandwidth exceeding 150 Hz is necessary, this gain bandwidth product is insufficient. The composite amplifier extends the bandwidth such that the ECG amplifier requirements are met with the lowest power operational amplifiers that are available. An alternate solution to the composite amplifier would be cascaded gain stages, resulting in higher output noise.

3.6.2. *Mid-Band Gain and Frequency Response*

The amplifier was designed such that the mid-band *voltage* gain would be approximately 40 dB at electrode-to-skin interface resistances of 250 k Ω – this requires a transimpedance gain of approximately 50 M Ω . To achieve this high transimpedance gain, a T-network was

used in the feedback loop, simulating a higher valued resistance without introducing high Johnson noise. The equivalent resistance, $R_{f,eq}$, of a T-network consisting of two larger resistors, R_A , and a smaller resistor to ground from the T-junction, R_B , is:

$$R_{f,eq} = 2R_A + \frac{R_A^2}{R_B} \quad (3.9)$$

For the values used in this circuit ($R_A = 1.5 \text{ M}\Omega$, $R_B = 100 \text{ k}\Omega$) this corresponds to an equivalent feedback resistance of $25.5 \text{ M}\Omega$. Note that the transimpedance gain of the circuit is further boosted by R_X and R_{CFB} , as shown in the closed-loop transfer function given below. Nevertheless, $R_{f,eq}$ is explicitly defined here to simplify the presentation of the following equations.

Including the effects of these resistors, the mid-band transimpedance gain of the circuit, in Ohms, can be written as:

$$A_{mb} = -\left(R_{f,eq} \left(1 + \frac{R_X}{R_{CFB}}\right) + R_X \left(1 + \frac{R_A}{R_B}\right)\right) \quad (3.10)$$

Including the effects of the electrode-to-skin interface, the mid-band differential *voltage* gain of the circuit can then be written as:

$$A_{Vdm,mb} = \frac{A_{mb}}{2R_E + \Delta_{RE}} \quad (3.11)$$

In this equation, R_E is the electrode-to-skin interface resistance for each electrode, and the imbalance in electrode-to-skin resistance between the two electrodes is denoted Δ_{RE} . Furthermore, assuming ideal operational amplifiers, the closed-loop transfer function for the circuit, excluding the output low-pass filter stage, can then be written as follows:

$$A_{cl}(s) = A_{mb} \frac{s \frac{R_{CFB} R_{INT} C_{INT}}{R_{f,eq}} \left(1 + s \frac{C_A R_X R_{f,eq}}{A_{mb}}\right)}{\left(1 + s \frac{R_{CFB} R_{INT} C_{INT}}{R_{f,eq}}\right) \left(1 + s R_{f,eq} C_A\right)} \quad (3.12)$$

Here, the effects of the non-inverting integrator have also been incorporated. This integrator feedback sets the high-pass cutoff frequency of the circuit at:

$$f_{hpf} = \frac{R_{f,eq}}{2\pi R_{CFB} R_{INT} C_{INT}} \quad (3.13)$$

The low-pass cutoff frequency is set by the equivalent T-network resistance in parallel with the feedback capacitor, C_A .

$$f_{lpf} = \frac{1}{2\pi R_{f,eq} C_A} \quad (3.14)$$

Since the LT1496 has a relatively low gain-bandwidth product, this ideal operational amplifier transfer function should be extended to include the effects of the dominant pole of the amplifier. Accordingly, a single-pole model for the amplifier's open-loop transfer function is introduced here:

$$A_{op}(s) = \frac{A_o}{1 + s\tau} \quad (3.15)$$

With this equation, the voltage gain of the second stage of the composite amplifier can then be written as:

$$A_{V,2}(s) = \frac{A_{o,2}}{1 + s\tau_2} \quad (3.16)$$

where

$$A_{o,2} = \frac{A_o(R_1 + R_2)}{(A_o + 1)R_1 + R_2} \quad (3.17)$$

and

$$\tau_2 = \frac{\tau(R_1 + R_2)}{(A_o + 1)R_1 + R_2} \quad (3.18)$$

Note that as $A_{o,2}$ approaches infinity, this voltage gain becomes $(1 + R_2/R_1)$, as expected. Without considering the effects of R_{comp} and C_{comp} temporarily (these are discussed below), the closed-loop transfer function in equation (3.12) can be expanded as follows:

$$A_{cl,exp}(s) = A_{mb} \frac{s \frac{R_{CFB}R_{INT}C_{INT}}{R_{f,eq}} \left(1 + s \frac{C_A R_X R_{f,eq}}{A_{mb}}\right)}{\left(1 + s \frac{R_{CFB}R_{INT}C_{INT}}{R_{f,eq}}\right) \left(-\frac{1}{A_{op}A_{V,2}} \left(\frac{R_{f,eq}}{R_{CFB}}\right) + \left(\frac{A_{op}A_{V,2} - 1}{A_{op}A_{V,2}}\right) (1 + sR_{f,eq}C_A)\right)} \quad (3.19)$$

As expected, as the open-loop voltage gain of the amplifiers approach infinity, this expression converges to equation (3.12).

For fine-tuning the roll-off of the input stage, the $R_{comp}C_{comp}$ pair was placed in the local feedback loop of amplifier 'A' from the negative input terminal to the output. Taking these components into account, and considering only amplifier 'B' to be a non-ideal operational amplifier, the closed-loop transfer function can be further expanded as follows:

$$A_{cl,full}(s) = A_{mb} \frac{s \frac{R_{CFB}R_{INT}C_{INT}}{R_{f,eq}} \left(1 + s \frac{(C_A + C_{comp})R_X R_{f,eq}}{A_{mb}}\right) \left(\frac{A_{o,2}}{R_{f,eq}\tau_2 C_{comp}}\right)}{\left(1 + s \frac{R_{CFB}R_{INT}C_{INT}}{R_{f,eq}}\right) \left(\frac{A_{o,2}}{R_{f,eq}\tau_2 C_{comp}} + s \frac{1}{\tau_2} \left(1 + \frac{A_{o,2}C_A}{C_{comp}}\right) + s^2\right)} \quad (3.20)$$

By adjusting the value of C_{comp} , the quality factor, Q , of the second-order roll-off can be set as follows:

$$Q = \sqrt{\frac{C_{comp}\tau_2}{R_{f,eq}A_{o,2}} \frac{1}{C_A + \frac{C_{comp}}{A_{o,2}}}} \quad (3.21)$$

The effect of this local feedback pair on the overall closed-loop transfer function is shown visually in Figure 3.26. In this figure, the transimpedance gain of the first stage is plotted versus frequency with and without R_{comp} and C_{comp} . These curves illustrate the sharper roll-off

achieved by including these components, with Q set at 0.77. Including the Sallen-and-Key filter output stage of the amplifier, the overall low-pass cutoff (-3 dB) frequency of the circuit is set at 200 Hz.

3.6.3. Input Impedance

The magnitude of the differential-mode input impedance, $|Z_{in,DM}(s)|$, is given below for frequencies greater than the high-pass filter cutoff of 0.05 Hz:

$$|Z_{in,DM}(s)| = \frac{-A_{mb}}{1 + \frac{R_A}{R_B} + \frac{R_{f,eq}}{R_{CFB}} - |A_{op}(s)A_{V,2}(s)|} \quad (3.22)$$

As $|A_{op}(s)|$ approaches infinity (as is the case for an ideal operational amplifier), the differential input impedance approaches zero. Using the component values shown in Figure 3.25, and equations (3.15—3.18) with the electronic specifications for the LT1496 ($A_o = 250$ V/mV, $\tau = 14.7$ s), the magnitude of the differential input impedance at low frequencies (1 Hz) is calculated to be 1.1 k Ω . This hand calculation was confirmed by the simulation result: 1.1 k Ω .

3.6.4. Common-mode-rejection ratio

While in a standard transimpedance amplifier configuration the positive terminal of the input operational amplifier is grounded, in this circuit it is connected via a 1.25 M Ω resistor to ground. This resistor increases the common-mode-rejection-ratio (CMRR) of the amplifier by matching the single-ended transimpedance gain of the circuit looking into the positive and negative input terminals of the amplifier.

Figure 3.27 shows an equivalent circuit model for the body-amplifier interface for common-mode inputs at mid-band. In this model, R_{CFB} is shorted to ground since the non-

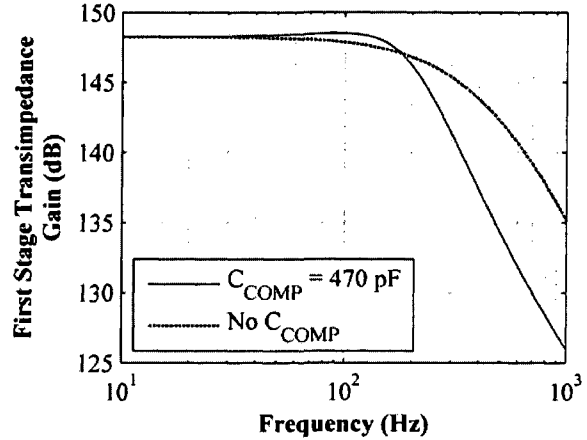


Figure 3.26 Transimpedance gain versus frequency for the first stage of the circuit with and without local feedback around amplifier 'A.' This feedback allows tight control of the second-order roll-off quality factor.

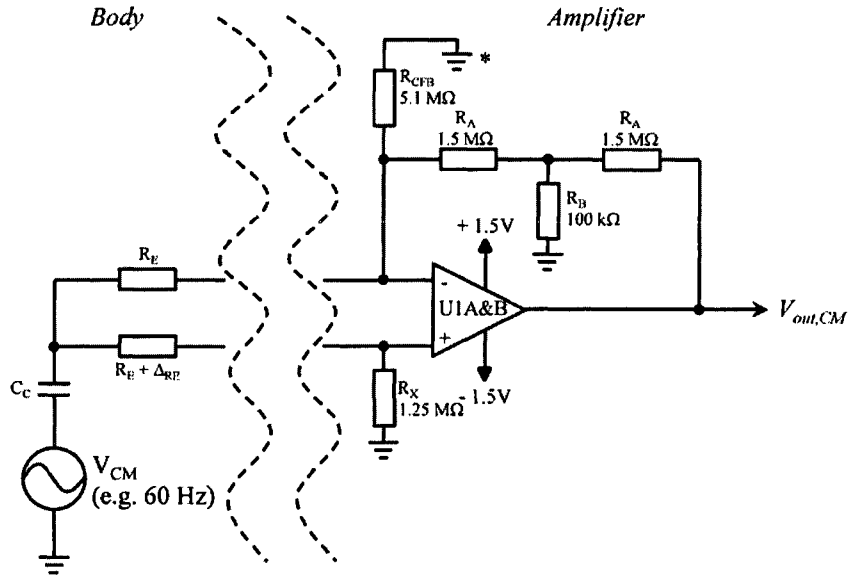


Figure 3.27 Equivalent model for common-mode inputs to the circuit. The node denoted by the asterisk (*) is considered a virtual ground in this model since the frequencies considered (typically 60 Hz) are beyond the cutoff frequency of the non-inverting integrator.

inverting integrator is beyond its cutoff frequency and the low-pass filtering capacitors are open-circuited. Based on this equivalent circuit, the value of R_X can be tuned to maximize the CMRR of the circuit.

For perfectly balanced electrode-skin resistances (R_E), the CMRR can theoretically be infinite. However, in reality, the two electrodes will have some finite imbalance, represented in Figure 3.27 as Δ_{RE} . The mid-band common-mode voltage gain of the circuit is:

$$A_{V_{cm,mb}}(V/V) = \frac{1}{R_X + R_E} \left(R_X \left(1 + \frac{R_A}{R_B} \right) - R_{f,eq} \left(\frac{R_E}{R_E + \Delta_{RE}} - \frac{R_X}{R_{CFB}} \right) \right) \quad (3.23)$$

Considering the case where $R_A \gg R_B$ and $\Delta_{RE} = 0$, the common-mode gain can be minimized by selecting an R_X value as follows:

$$R_X|_{A_{cm,MB}=0} \approx \frac{1}{\frac{1}{R_{CFB}} + \frac{1}{R_A}} = R_{CFB} \parallel R_A \quad (3.24)$$

Table 3-4 Measured electrical specifications for two-electrode ECG circuit

Specification	Measured Value	Units/Comments
Supply Voltage	3	V
Supply Current	3.5	μA
Bandwidth (-3dB)	0.05 - 200	Hz
Mid-band Voltage Gain	48	dB/Measured with $R_E = 100\text{k}\Omega$
CMRR	50	dB/Measured with $R_E = 100\text{k}\Omega$
Input-referred Current Noise	23	pA_{pp}
Output Noise Voltage	1.2	mV_{pp} /Open-circuit input
Total Harmonic Distortion	-74	dB/Measured with $V_{in} = 10\text{mV}_{RMS}$, $f_{in} = 2\text{Hz}$, $R_E = 300\text{k}\Omega$

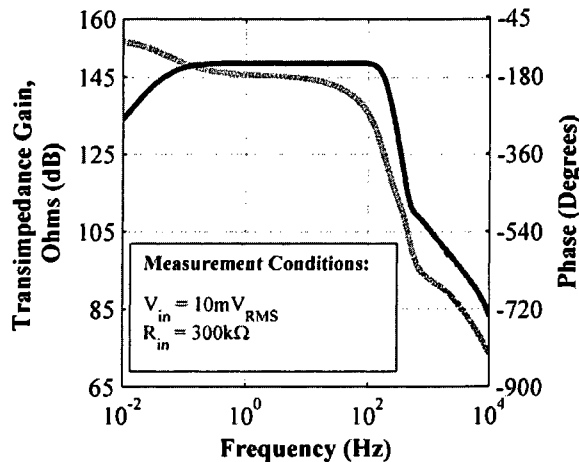


Figure 3.28 Gain and phase response of the circuit measured using an SR780 (Stanford Research Systems, Sunnyvale, CA) dynamic signal analyzer. An input voltage of 10mV_{RMS} through a source resistance of $300\text{k}\Omega$ was used for this measurement. Note that the gain is given in Ohms (dB).

the peak-to-peak output voltage was measured using an oscilloscope. Then, the output noise spectral density was measured using the SR780. The output noise voltage was found to be 1.2mV_{pp} , corresponding to an input referred current noise of 23pA_{pp} . For a typical low-frequency

For the component values used in this work, and assuming realistic R_E and Δ_{RE} values of $100\text{k}\Omega$ and $5\text{k}\Omega$, respectively, the theoretical common-mode gain of the circuit is 3.3 dB . Using Equation (7.5), the differential-mode gain under the same conditions is 48 dB , resulting in a theoretical CMRR of 44.7 dB .

3.6.5. Experimental Results

The amplifier was built and the electrical specifications were measured. The key specifications are summarized in Table 3-4. The gain and phase response of the circuit, measured using an SR780 dynamic signal analyzer (Stanford Research Systems, Sunnyvale, CA), are shown in Figure 3.28. The SR780 was operated in swept-sine mode, with an output signal level of 10mV_{RMS} input through a $300\text{k}\Omega$ resistor to the circuit. For typical skin-electrode resistances, this gain corresponds to an ECG output voltage of approximately 1V_{pp} .

For the noise measurement, the input terminals were left open and

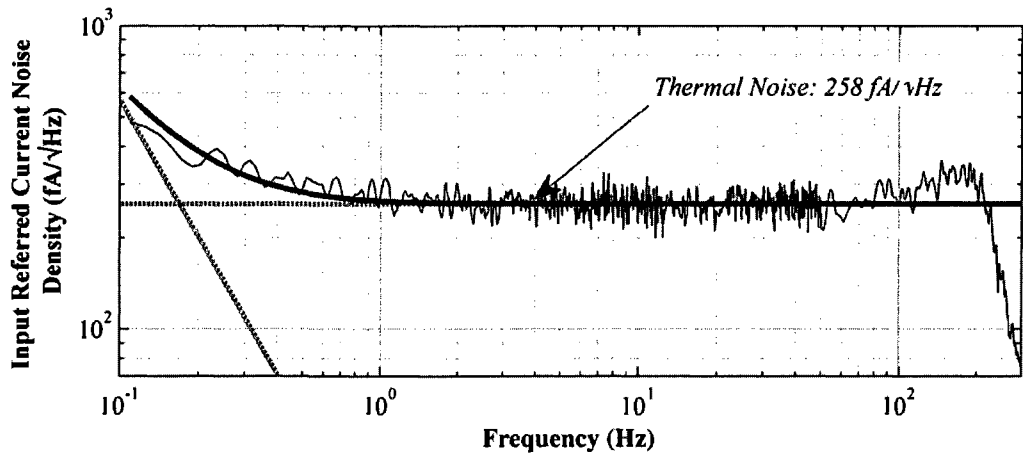


Figure 3.29 Input referred current noise spectral density for transimpedance ECG amplifier. The thermal noise component was found to be 258 fA/√Hz, and the noise corner frequency was below 1 Hz.

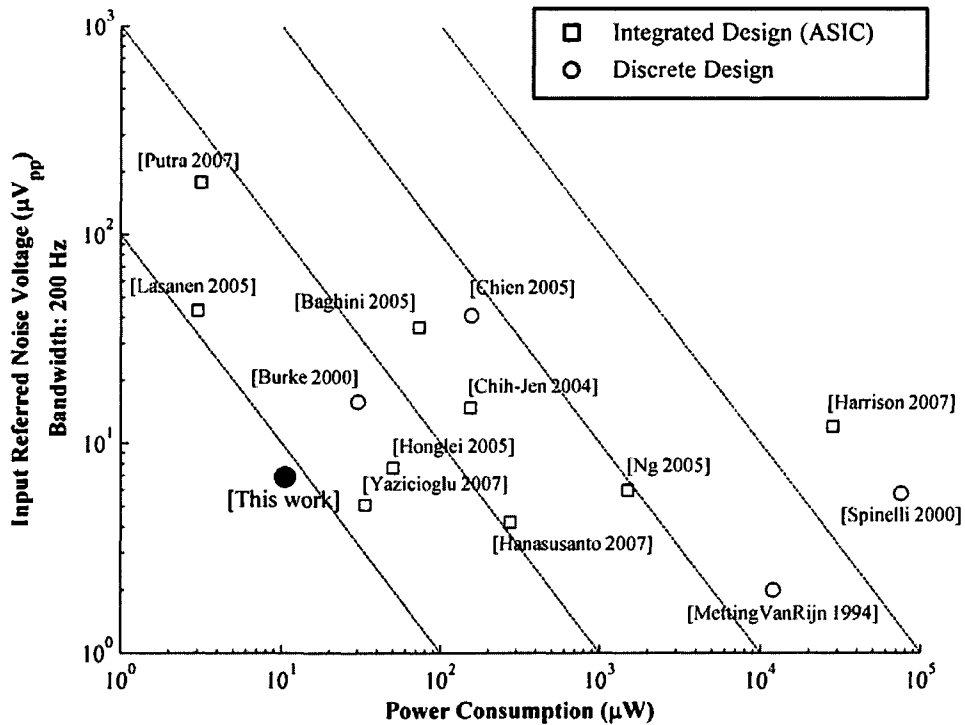


Figure 3.30 Performance comparison of this work to several other biosignal amplifiers from the literature: Input referred voltage noise (μV_{pp}), for a 200 Hz bandwidth, plotted versus power consumption (μW). To convert the input referred current noise density, measured as 23 pA_{pp}, to voltage, a typical low frequency skin-electrode resistance of 300 k Ω was assumed. Designs using discrete components are shown by circles, and integrated designs are shown as squares. Note that all amplifiers in this figure, besides the amplifier shown in this work, require three electrodes on the subject; the circuit in this paper uses only two.

skin resistance of $300\text{ k}\Omega$, this corresponds to an input referred voltage noise of $6.9\ \mu\text{V}_{pp}$. The noise spectral density, referred to the input, is shown in Figure 3.29. The total noise, integrated over the bandwidth $0.1\text{--}200\text{ Hz}$, was found to be $4.3\ \text{pA}_{RMS}$.

Figure 3.30 shows input referred voltage noise (in μV_{pp}), for a 200 Hz noise bandwidth, versus power consumption (in μW) for the circuit from this work compared to several other biosignal amplifiers from the literature. Designs using discrete components [107-110] are shown as circles, and integrated designs [111-119] are shown as squares. It should be noted that in addition to comparing favorably to these other amplifiers, the circuit from this work uses only two electrodes, without the need for a third ‘ground’ connection to the body. For this figure, to achieve a fair comparison of electrical performance, all RMS values were converted to peak-to-peak values by a factor of six multiplication and bandwidths were normalized by multiplying the reported noise voltage by the square-root of the ratio of 200 Hz to the bandwidth specified in the work.

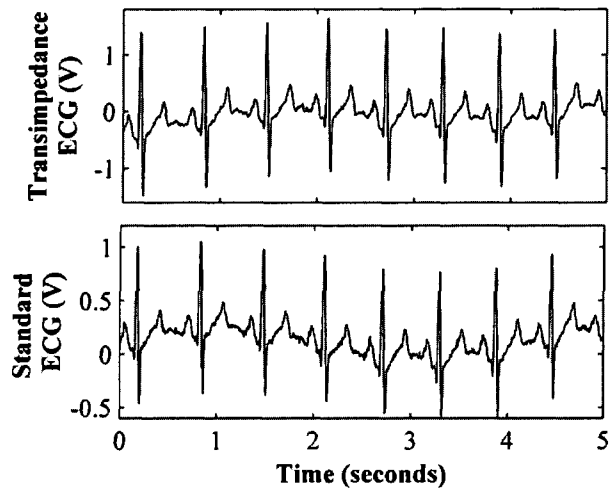


Figure 3.31 Sample ECG recordings taken from one subject with a standard (three electrodes, instrumentation amplifier input) and transimpedance ECG amplifier (two electrodes).

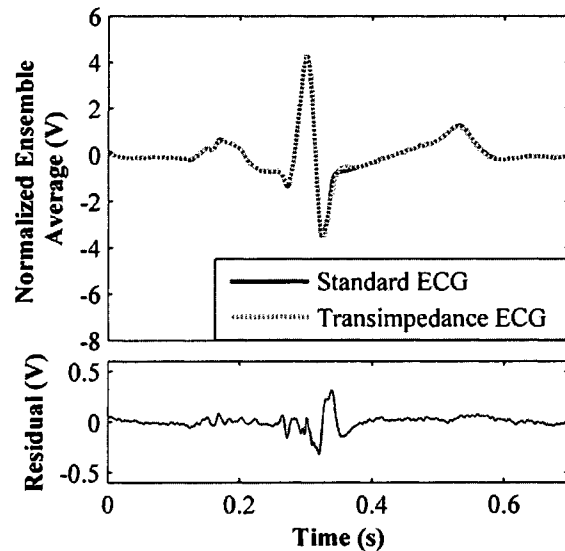


Figure 3.32 Ensemble averages for the proposed transimpedance amplifier and the standard amplifier taken simultaneously from a subject. Both signals were normalized to unity standard deviation. The residual is also shown for morphological comparison (note the difference in the vertical axis between the signals and the residual).

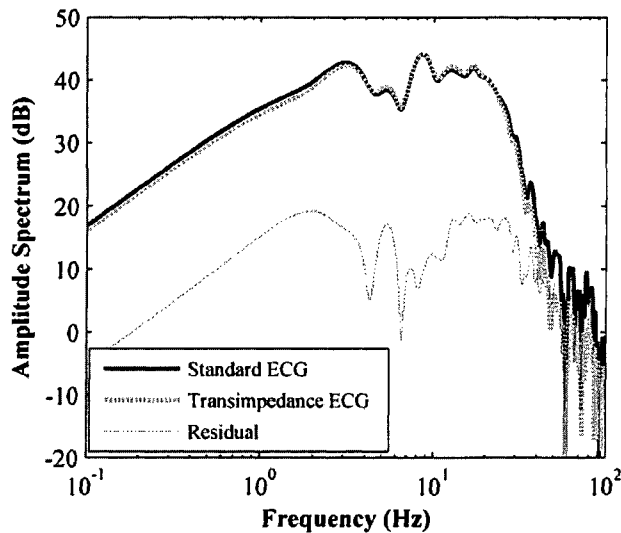


Figure 3.33 Amplitude spectra for the standard and transimpedance ECG amplifiers, and the residual. The frequency characteristics of the signal were accurately preserved by the new design.

The total-harmonic-distortion (THD) was measured on the signal analyzer: with a 2Hz, 10 mV_{RMS} amplitude, sine wave through a source resistance of 300k Ω , the THD was -74 dB (0.02%). At input frequencies of 25 and 50 Hz, the THD was measured to be -70 dB (0.03%) and -53 dB (0.2%), respectively. The source resistance was chosen to be on the higher end of normal electrode-skin resistances such that the worst case THD would be measured.

In addition to the electronic characterization, the morphological accuracy of the measured ECG signals was verified using the standard ECG circuit discussed above, with the bandwidth increased to 180 Hz rather than 104 Hz.

ECG signals were measured from one subject simultaneously using both circuits. Five electrodes – two for the transimpedance, and three for the standard amplifier – were attached to the subject, and both amplifiers were operated on separate power supplies (batteries) with separate isolation amplifiers approved by Stanford Clinical Engineering. Figure 3.31 shows raw ECG signals, with no digital filtering, measured simultaneously using the two-electrode amplifier and the standard three-electrode amplifier. The subject provided written consent for participating in the study (Stanford IRB Protocol #6503).

To quantitatively compare the morphological accuracy of the transimpedance based recording, the ECG signals were processed digitally to remove baseline wander, normalized to zero mean and unity standard deviation, and ensemble averaged using the ECG R-waves as a trigger. The residual was also computed for the normalized averages and is shown alongside the averages in Figure 3.32. The variance of this residual was less than 0.54% of the variance of the standard ECG, demonstrating the morphological accuracy of the transimpedance measurement. The amplitude spectra of the averages were also computed and analyzed to ensure that the frequency information of the ECG was accurately preserved. These are shown

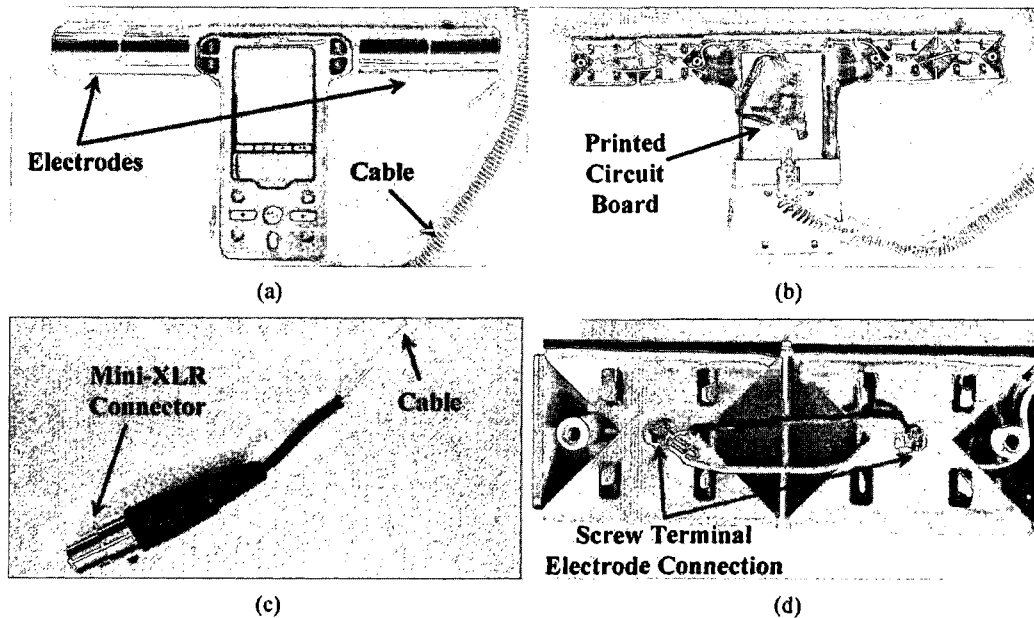


Figure 3.34 (a) Handlebar electrodes from the Omron HBF-500 bathroom scale. These electrodes, combined with the footpad electrodes, are intended to be used for bioimpedance-based body fat measurements. (b) The handlebars were opened and a printed circuit board (PCB) version of the two-electrode ECG circuit was placed inside. The electrodes were soldered to the circuit and the output was connected to the cable. (c) A mini-XLR (TA-4F) connector was soldered to the end of the cable from the handlebars such signal, ground, and two supply voltages could be connected between the handlebars and the base of the scale (where the batteries were housed). (d) Screw terminals inside of the handlebars were used to fix wires to the electrodes. These wires were connected to the input terminals of the circuit.

in Figure 3.33. The frequency characteristics of the ECG were accurately preserved by the new design.

It should be noted that the amplitude of the transimpedance ECG will not necessarily match that of the standard ECG, since the *voltage* gain of the circuit is not fixed, but rather dependent on the electrode-to-skin resistance (see equation (3.13), above). In some instances, where ECG amplitude is an important feature for the diagnosis, this is a shortcoming of the approach. However, in many instances, such as arrhythmia detection, amplitude is much less relevant than morphology and timing, which are accurately preserved in the transimpedance configuration. For the work described in this thesis, the most important objective of ECG acquisition was to acquire a strong R-wave for triggering the BCG averaging methods described below in Chapter 4. The integration of the transimpedance ECG circuit into the handlebars of the Omron scale is described below.

Another limitation of the circuit is that the bandwidth can also, to some extent, be compromised at low values of R_E (higher values of voltage gain) due to the limited gain-bandwidth product of the LT1496. If R_E is less than 50 k Ω , the circuit bandwidth will fall below the acceptable bandwidth for standard clinical ECG recorders, 100 Hz [101, 120]. The circuit was optimized for typical ranges of electrode-to-skin resistance for surface electrodes – several tens to hundreds of k Ω cm⁻² [121, 122] – for which the bandwidth is more than adequate for ECG acquisition. In situations where lower electrode-to-skin resistance is expected, as is the case with skin preparation for example, the voltage gain of the circuit can readily be decreased by increasing the value of R_B to 200 or 500 k Ω to mitigate the problem.

3.6.6. *Integration of Two-Electrode Circuit in an Omron HBF-500 Scale*

The handlebar electrodes of the HBF-500 scale are shown in Figure 3.34 (a). In Figure 3.34 (b), the handlebars have been opened, and the two-electrode transimpedance circuit placed inside. A printed circuit board (PCB) layout was completed with a 2.5 x 4.5 cm footprint for the circuit using dual in-line (DIP) package integrated circuits and through-hole discrete components.

The batteries (4 x AA) for powering the circuit were contained in the base of the scale, and were connected via two free conductors in the original phone cable to the ECG circuit in the handlebars. For interfacing the phone cable to the base of the scale, a low profile, mini-XLR (TA-4M/F) connector was used (Figure 3.34 (c)). The scale originally had wires connected to the handlebar electrodes via screw terminals (Figure 3.34 (d)); these wires were de-soldered from the commercial PCB, which was removed, and soldered to the input terminals of the custom ECG circuit PCB. The output from the ECG circuit was passed via the existing cable to the base of the scale, where it was then interfaced to a panel-mount BNC connector fixed on the back side of the scale (behind where the heels are placed). When reassembled and packaged, the scale was visually unchanged from its original state, aside from the BNC cable output.

ECG signals were then measured using this apparatus, and an example trace is shown in Figure 3.35 alongside a standard ECG taken from the hands with three gel electrodes. Note that both signals have been digitally band-pass filtered (0.5–55 Hz), to remove baseline wander and power-line interference. In this figure, the handlebar signal appears to be distorted compared to the standard measurement. The R-wave amplitude is much higher relative to the T-wave, indicative of a high-pass filtering effect which is likely due to the non-ideal electrode-skin interface.

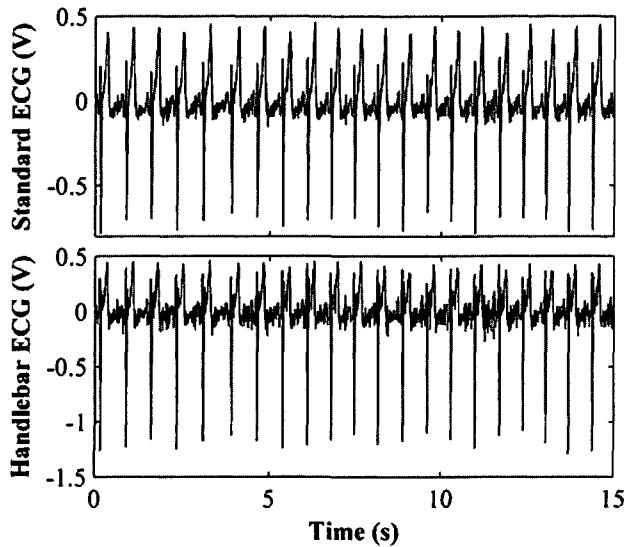


Figure 3.35 (Top) ECG signal acquired from the hands of a subject using the standard ECG amplifier and three gel electrodes. (Bottom) ECG signal acquired simultaneously using the transimpedance-based amplifier and the handlebar electrodes in the Omron scale. The QRS complexes could readily be extracted from both signals using standard detection algorithms.

While for the standard ECG the electrodes are adhered to the skin with an Ag/AgCl gel which effectively increases the electrode-skin contact capacitance (low impedance), the handlebar electrodes are simply metal pads touching the surfaces of the palms, a much smaller capacitance. As a result, the lower frequency components of the signal are suppressed by the handlebar measurement.

The periodogram-PSDs for ensemble averages taken from both signals were computed to quantify the frequency distortion introduced by the handlebars. After the ensemble averages were found for both signals, they were normalized to unity R-wave magnitude, and the PSDs were found. The ratio of the handlebar PSD to the standard ECG circuit PSD is shown in Figure 3.36. At low frequencies, the ratio of the PSDs exhibits a 10 dB/decade increasing slope, typical of a derivative operation.

To further verify that the distortion was mostly at low frequencies, the maximum cross-correlation between the two signals, with the autocorrelation of each normalized to unity, was found for the raw signals, and for the signals passed through a digital high-pass filter ($f_c = 20$ Hz). The filtered signals are shown in Figure 3.37. The maximum cross-correlation was found to be 0.66 for the raw signals and 0.91 for the signals after high-pass filtering. This further supports the theory that a majority of the distortion is at the lower frequencies.

In addition to the frequency distortion introduced by the handlebar electrodes, both ECG signals exhibit elevated levels of EMG interference due to the hands gripping the handlebars. The finer morphological features of both signals are corrupted by these EMG signals; however, the QRS complexes could readily be extracted from either trace using standard

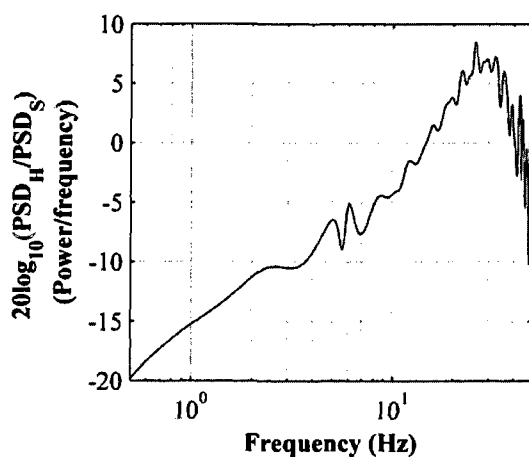


Figure 3.36 Power spectral density ratio for amplitude-normalized ensemble averages from the handlebar and standard ECG circuits. At low frequencies, the ratio of the spectra exhibits a 10 dB/decade increasing slope, typical of differentiation. The frequency distortion introduced by the handlebar ECG is likely a result of the electrode-skin interface being capacitively coupled, rather than nearly dc-coupled as in Ag/AgCl gel-electrodes.

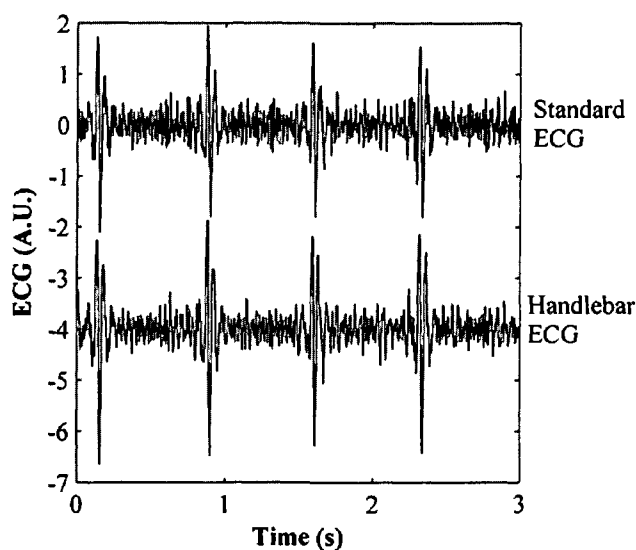


Figure 3.37 Standard ECG (gel-electrode) and handlebar ECG signals after digital high-pass filtering (20 Hz). While for the raw signals the cross-correlation maximum value, with the autocorrelations normalized to unity, was 0.66, after high-pass filtering it was increased to 0.91. This demonstrates that the handlebar electrodes affect the lower frequency components of the ECG, such as the P- and T-waves.

methods [102]. Most importantly for this application, as shown below in Chapter 6, this method of ECG measurement was used for nearly 100 subjects without any instances of amplifier saturation, demonstrating the effectiveness of the active current feedback approach.

3.6.7. Discussion

The ECG circuit described in this section has several advantages over existing ECG amplifiers both in terms of electrical specifications and practicality for portable applications, for discrete or integrated (ASIC) implementations. For ECG amplifiers using discrete components, the quiescent current of this circuit is the lowest reported in the literature, allowing for long continuous use without battery replacement. Additionally, the relatively low differential input impedance ($k\Omega$ versus $G\Omega$ for a typical instrumentation amplifier input stage) of the circuit allows for unshielded, lightweight cables to be used

without significant cable noise and interference – in the integrated scale implementation, this is crucial since the handlebar electrodes are in a plastic case and will move around in the subject's hands during signal acquisition. The use of active feedback to suppress electrode drift enables robust two-electrode ECG recording without intermittent problems due to amplifier saturation.

3.7. Conclusions

This chapter presented the instrumentation designs used in this research for ECG and BCG measurement. Standard circuits were developed, capable of acquiring high fidelity measurements. These circuits were thoroughly characterized in terms of gain, frequency response, distortion, and noise. In addition to these standard topologies, novel circuit designs were conceived to achieve state-of-the-art electronic specifications – for the BCG, the lock-in amplifier reduced the electronic noise floor by 7.7 dB; for the ECG, the transimpedance amplifier jointly optimized noise and power consumption, producing better results than any design disclosed in the existing literature. Furthermore, the ECG amplifier was designed to accommodate two-electrode recordings, such that a handlebar-equipped bathroom scale could be used for combined ECG and BCG measurements. For all new designs, the physiological accuracy was benchmarked against the standard topologies to ensure that the diagnostic quality of the signals was not compromised by the new designs. The next chapter describes how the robust dual ECG and BCG acquisition could be used for improving BCG measurement robustness.

4

BCG Signal Estimation

A toothache, or a violent passion, is not necessarily diminished by our knowledge of its causes, its character, its importance or insignificance.

– T. S. Eliot

Estimating a biomedical signal from a recording consisting of both the ‘signal’ and noise is an important, yet not straightforward, problem. If properly estimated, the reconstructed signal can provide access to otherwise obscured, diagnostically relevant features. Furthermore, by estimating the *signal* one can readily estimate the *noise* – the two of these together can provide an estimate of the signal-to-noise ratio (SNR) for the entire recording *and* various parts of the recording.

In the case of the BCG, the estimated noise trace can be used for evaluating auxiliary noise sensors, to determine whether accurate and time-synchronous indices of BCG noise could be obtained without the use of a simultaneous ECG. For example, in Chapter 5, the electromyogram (EMG) signal acquired from the subject’s feet is evaluated as a noise reference for standing BCG measurements – for assessing this approach, the BCG noise is estimated using methods described here, and correlated to features of the EMG.

The SNR estimate can also be used to quantitatively compare various sensors, algorithms, and measurement setups: for example, the SNR of standing BCG measurements can be compared to seated; or weighing-scale-BCG measurements to EMFi recordings. However, many researchers – for the BCG as well as other biosignals – choose to specify only the *electronic* SNR of their measurements. For this, they measure the electronic noise of the circuit (and, in some cases, the sensor as well) and compare this noise to the peak amplitude of the signal.

Alihanka, *et al.* claim an SNR of 20 for their static charge-sensitive bed (SCSB) system, providing only the explanation that this is “based on the BCG amplitude” [96]. Schwerdt, *et al.* disclose SNR estimates of 15–30, again based on the peak amplitudes of the BCG [123]. Gonzalez-Landaeta, *et al.* assert that their SNR is 27–38 dB (22–79), depending on the type of electronic weighing scale used (the different strain gauge resistances cause the thermal noise

to differ among the scales) [106]. For this calculation, they compute the ratio of the peak signal amplitude to the combined RMS noise voltage of the circuit and scale. This is a somewhat nonstandard method since, usually, the peak signal amplitude is compared to the peak noise amplitude, or both are analyzed as RMS values. Regardless, even the approaches that are incontestably valid for computing electronic SNR inappropriately ignore the other sources of noise and interference that corrupt the recordings: motion artifacts, floor vibrations, and beat-to-beat interference. Since these other noise sources are usually more prominent than the electronic noise, the *real* SNR of the measured signal is never known.

Some authors even describe new algorithms for improving the quality of the BCG signal and claim SNR improvement without any quantitative evidence. For example, Postolache and Girao report an ‘adaptive neuronal network’ for improving the SNR of BCG recordings; however, the SNR of the recordings were not estimated before, nor after, the processing [124].

A method for estimating the real SNR of BCG recordings – beyond simply considering the electronic noise – is lacking in the existing literature. The most likely reason is that, unlike the ECG and other more prevalent biomedical signals, the physiological origin of the BCG is not fully understood. For a normal ECG recording, it is relatively straightforward to visually discern which components of the signal are cardiac-related, and which are artifacts due to noise or interference (see Figure 4.1). (Although, it should be noted that even for the ECG,

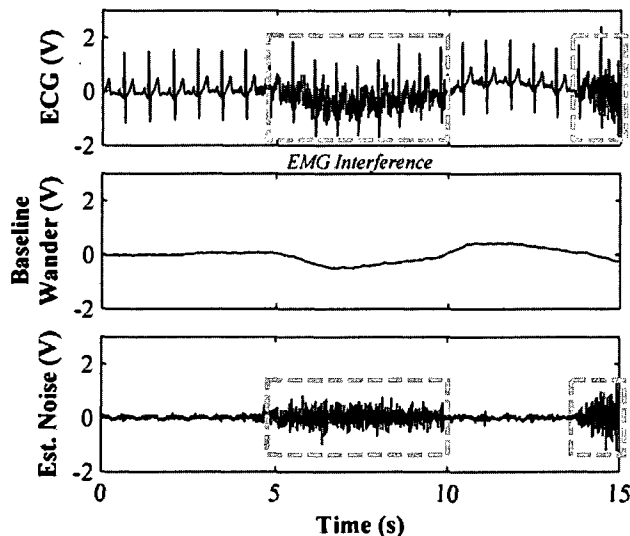


Figure 4.1 Illustration of baseline wander and EMG interference in the ECG signal. The noises and interferences in ECG recordings can be readily discerned from the cardiac-related ‘signal.’

some of the most basic characteristics, such as amplitude, are still fervently being researched today (e.g., [125, 126]).) On the other hand, for BCG recordings this is not necessarily the case. Other than the main peak (J-wave) which is clearly synchronized to the heart rhythm, the definitions of what parts of BCG recordings are cardiac-related ‘signal’ and which components are mainly due to noise are somewhat ambiguous.

This ambiguity could be resolved by implementing one, or a combination, of the following approaches: empirical studies, mechanical modeling, or statistical estimation techniques. Of these three, empirical approaches have dominated the literature. In fact, mechanical modeling has scarcely been applied, and the statistical treatment of the BCG has been limited to ensemble averaging the signal over several beats. In this thesis, Chapters 6 and 7 present hypothesis-driven empirical studies designed to establish important correlations between BCG features and cardiovascular parameters. Mechanical modeling is left as a subject for future work, and is currently being pursued by Richard Wiard at Stanford University.

Statistically estimating the BCG ‘signal’ from a measurement composed of both signal and noise is addressed in this chapter. First, some assumptions are made regarding the BCG signal and the characteristics of the noise based on physiological considerations and observations in the recorded BCGs. Second, the amplitudes of each BCG beat are estimated using the timing information provided by the ECG, and first-order statistical methods. Third, an ensemble averaged BCG beat is computed using standard methods. Fourth, the amplitude information is combined with this ensemble average to compute a modified ensemble averaged BCG beat. Finally, this beat is used to reconstruct the BCG time trace. The reconstruction is applied to two BCG signals with significantly different SNRs for visual comparison, and a synthetic model is used to quantitatively validate the estimate, and compare the results to the existing methods in the literature. Before describing this new algorithm for BCG signal estimation, the standard methods for signal estimation in the existing literature are described below.

4.1. Standard Signal Estimation Methods for Biomedical Signals

Many signal (or, similarly, SNR) estimation algorithms have been developed for biomedical signals in the existing literature, mainly for ECGs [127, 128] and evoked potentials [128, 129]. Some of the most notable algorithms are described in this section.

For ECGs, SNR estimation is rather straightforward for three reasons: first the signal is compact in time, yielding segments between the beats where the ‘signal’ goes to zero; second, the amplitude variations from beat-to-beat are rather minimal; third, the signal level is relatively high, allowing the peaks to (usually) be reliably detected. The ECG SNR could be estimated by comparing the power of the ECG R-wave to the power of the segment between the T- and P-waves, where the ECG ‘signal’ is essentially zero. Alternatively, an ensemble averaged ECG beat can be subtracted from each beat of the signal, rendering an estimate of the measurement noise – the ratio of the variance of the ensemble average to the variance of this noise estimate can then be considered the SNR [127].

For evoked potentials, electrical potentials recorded from the body in response to stimuli, signal averaging techniques are used to increase the signal level above the noise floor of the recording system. These potentials are usually only a few microvolts in amplitude. Since they are responses to the external stimuli, the stimuli can directly be used as timing references for triggered averaging. Furthermore, the time interval between successive stimuli can be set longer than the expected duration of the evoked response, eliminating any possibility of signal-to-signal interference in the averaging. The averaging methods range from the simplest – ensemble averaging – to more complex methods such as maximum likelihood (ML) or SNR-based weighted averaging [129]. Two of the most commonly-used SNR estimators are described below.

The evoked potentials can be arranged in a matrix, X , such that each i^{th} row contains a measurement composed of both signal (the evoked potential) and additive noise:

$$x_i = s + n_i \quad (4.1)$$

where x_i is the i^{th} row of X , s is the desired evoked potential signal, and n_i is the additive noise for the i^{th} waveform. The ensemble average over all M recorded waveforms can then be taken directly as follows:

$$\hat{s} = \sum_{i=1}^M x_i \quad (4.2)$$

where \hat{s} represents the ensemble averaged evoked potential. As described by Sornmo and Laguna [128], the SNR of this ensemble average can then be estimated by separating the data set into two equally sized subsets, computing two sub-ensemble averages (\hat{s}_1 and \hat{s}_2), then using an ML SNR estimator [15]:

$$SNR_{ML} = \frac{2 \sum_{k=1}^L \hat{s}_1[k] \hat{s}_2[k]}{\sum_{k=1}^L (\hat{s}_1[k] - \hat{s}_2[k])^2} \quad (4.3)$$

Alternatively, the two sub-ensemble averages can be compared using a cross-correlation [16] SNR estimator, which first requires the correlation coefficient to be computed between the averages:

$$r = \frac{\sum_{k=1}^L \hat{s}_1[k] \hat{s}_2[k]}{\sqrt{\sum_{k=1}^L \hat{s}_1[k]^2 \hat{s}_2[k]^2}} \quad (4.4)$$

The SNR estimate, SNR_r , is then given by:

$$SNR_r = A \frac{r}{1-r} + B \quad (4.5)$$

where the constants

$$A = \exp\left(\frac{-2}{N-3}\right) \quad (4.6)$$

and

$$B = -\frac{1}{2} \left(1 - \exp\left(\frac{-2}{N-3}\right) \right) \quad (4.7)$$

cause the estimate to be unbiased for large values of N .

These SNR estimators can also be used over the entire ensemble of waveforms to determine the SNR of the overall *recording* rather than of just the *ensemble average*. For this estimate, the equations above would be applied to each combination of two waveforms from the recording, and the average over all pairs would be considered the SNR of the recording.

4.2. Standard Approaches to BCG Signal Estimation

The BCG signal presents more challenges than the ECG and evoked potentials in terms of signal estimation for the following reasons: the signal is not compact in time, thus no segments exist in the recording where the BCG ‘signal’ has gone to zero; the beat-to-beat amplitude variations are quite significant, usually 5 or 10 times greater than for a typical ECG; and, although a trigger may be available for averaging (the ECG R-wave, as described below), the time interval between successive beats is shorter than the length of each beat’s pulse response, causing signal-to-signal interference. This last point is known since the ensemble averaged BCG does not decay to zero within the time frame of one cardiac cycle.

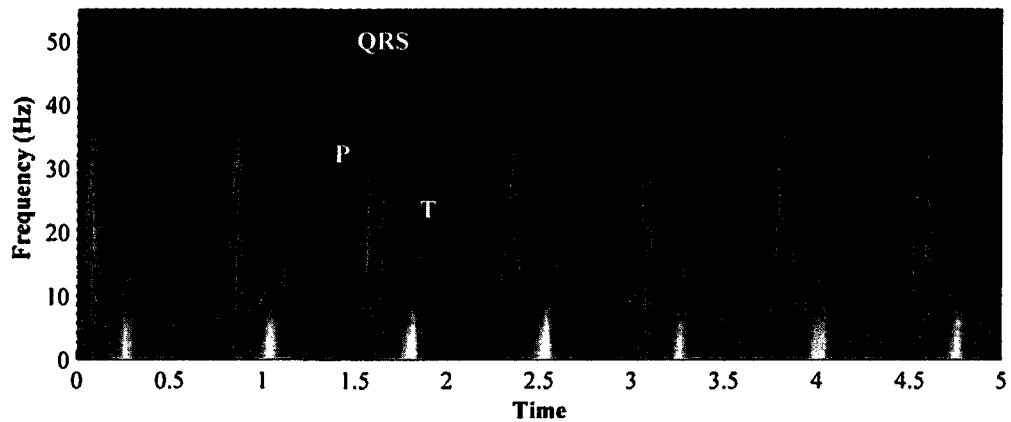


Figure 4.2 Spectrogram of a typical ECG signal. The P-, R-, and T-waves are separated in time and frequency, allowing approaches such as the wavelet transform and matched filtering to be effectively employed.

The standard approaches to BCG estimation leverage the fact that the ECG (from a resting subject) provides a reliable timing reference to be used for triggered averaging of the BCG. Specifically, the ECG R-wave is an excellent fiduciary point since it is readily discernable from its surrounding waves both in the time and frequency domains: in the time domain, the R-wave is generally larger than the surrounding waves, and its energy is compact; accordingly, in the frequency domain, the R-wave contains more high-frequency content than its counterparts. This is illustrated in an example spectrogram – or short-time Fourier transform (STFT) – of a typical resting ECG signal shown in Figure 4.2. The P-wave, which occurs first in time, contains frequency content between 5–25 Hz; the R-wave, occurring next, from 5–40 Hz; and the T-wave, occurring last, from 1–10 Hz. As a result, combined time-frequency approaches, such as the wavelet transform, or simple matched-filtering algorithms, are well-suited for detecting these peaks, and have been utilized successfully in dozens of works in the literature, e.g. [130, 131].

4.2.1. *R-Wave-Triggered Averaging of the BCG*

The most straightforward method for estimating the BCG signal from a recording involves first computing an ensemble averaged BCG using R-wave-triggered averaging. To generate a beat ensemble, the BCG waveform is segmented into an array of beats, with each ensemble member beginning at the ECG R-wave, and having a fixed length. This length must be less than the length of the minimum R-R interval for the recording to ensure that the beats do not overlap. The average is computed over all beats in the array, and this ensemble averaged BCG is then considered the best statistical estimate of one beat of the overall signal.

This approach has three main limitations: first, any beat-to-beat variations of the signal will be lost in the averaging process; second, the length of the average is confined to the minimum R-R interval, such that if the beat extends beyond that length, some of the information will be lost; and, third, changes in the signal over time are lost in the averaging.

4.2.2. *Reconstructing a BCG Signal from an Ensemble Averaged Beat*

While the first and second limitation listed above cannot be addressed using standard methods, the third can, to some extent, be mitigated using the following approach. Since the timing of each BCG beat is known based on the R-wave peaks of the ECG, the ensemble averaged BCG can simply be ‘placed’ at each R-wave to reconstruct an estimated BCG signal. Mathematically, this ‘placement’ can be described as follows: first, a train of unity amplitude impulses is generated, with each impulse occurring at the R-wave peaks of the ECG; then, the ensemble averaged BCG is convolved with this impulse train to reconstruct the entire waveform. The output of such a process is shown in Figure 4.3, with the measured BCG signal on top (a), and the reconstructed signal on the bottom (b).

In addition to the limitations listed above, this process results in discontinuities (gaps) in the resultant waveform since most of the R-R intervals are longer than the minimum interval. Namely, there will be segments of the original BCG signal that would not be reconstructed by this process. Note that the amplitude variations of the original signal are also not addressed using this standard technique.

The new methods for BCG signal estimation described below address these limitations by combining the ECG timing information with a statistical model for the BCG. These methods are validated using a synthetically generated BCG signal with additive white Gaussian noise, as described below.

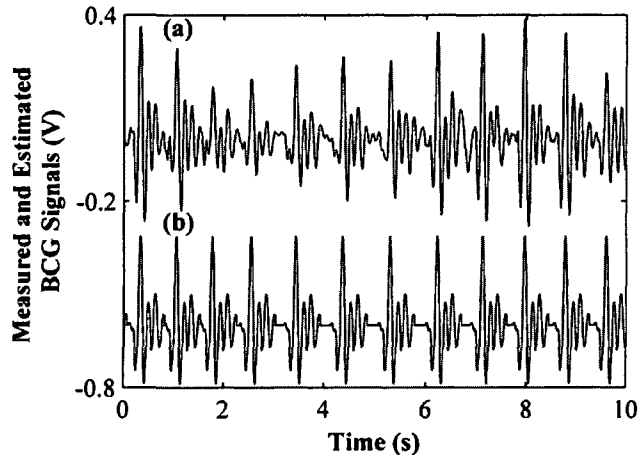


Figure 4.3 (a) Measured BCG signal. (b) Reconstructed signal using an ensemble averaged beat ‘placed’ at the R-wave locations of the ECG. Note that the amplitude variations in the original signal are lost, and there are clear discontinuities between various beats due to the limitation on the length of the ensemble average (the length must be, at most, the minimum R-R interval for the trace).

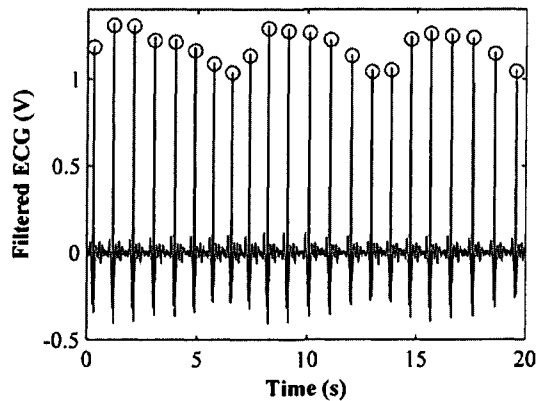


Figure 4.4 ECG signal, filtered to extract the QRS complexes, with peaks located using a simple automatic peak detection algorithm described in the text.

4.3. BCG and ECG Pre-Processing

The first steps in processing the recorded BCG (and ECG) to obtain an estimate of the cardiac-related BCG ‘signal’ are described here. First, the BCG was digitally band-pass filtered using an FIR filter (Kaiser window) with a bandwidth of 0.5–15 Hz (-3 dB) and a length of 4,467 samples. Next the low-frequency baseline wander in the BCG was eliminated by polynomial

subtraction. The same steps were then applied to the ECG signal, except that the band-pass filter spanned a bandwidth of 10–45 Hz with a length of 727 samples. This bandwidth was chosen to optimally extract the QRS complexes of the signal for the ensuing simple peak detection algorithm described below.

For peak detection, first the derivative of the filtered and baseline-wander-removed ECG signal was computed. Then, the signum function of the ECG derivative was computed. The locations at which the absolute value of the derivative of this function’s output was unity were then considered the possible peak locations. For all such indices within the trace, those that **1** corresponded to ECG amplitude higher than the user defined threshold (usually half the maximum amplitude of the rectified ECG signal), and **2** did not occur within the user defined time interval (usually 300 ms) of the previous peak, were considered to be detected peaks of the ECG signal. An example filtered ECG signal with detected peaks (shown as circles above the R-waves) is provided in Figure 4.4. With these pre-processed ECG and BCG signals, and the located ECG R-wave peaks, the following algorithm was applied to estimate the BCG ‘signal’ and the SNR of the recording.

4.4. Estimation of BCG Heartbeat Amplitudes

The simple statistical model developed for the BCG uses the following assumptions:

1. The system was assumed to be linear.
2. The BCG signal was assumed to be morphologically identical from beat-to-beat, except for slow amplitude variations.

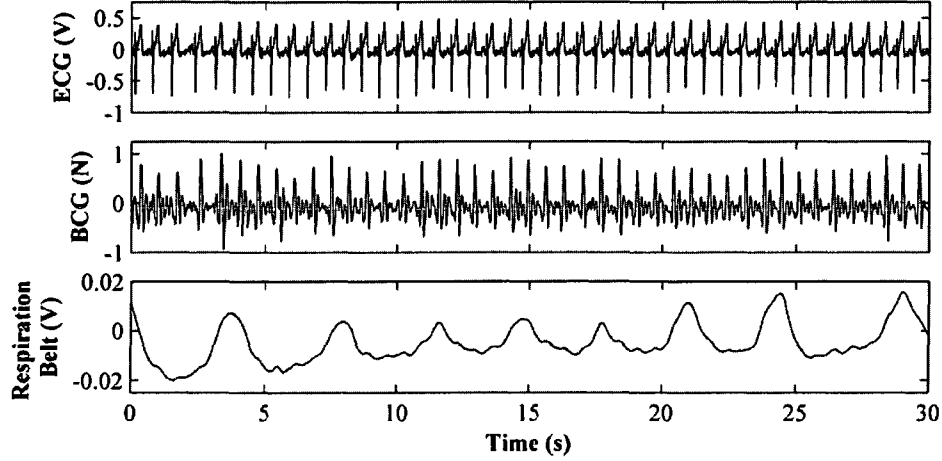


Figure 4.5 ECG, BCG, and respiration signals acquired from a subject at rest. The BCG amplitude modulates at the respiratory frequency.

3. These amplitude variations were considered to be slower than the heart rate.
4. The timing of the beats was assumed to be deterministic.
5. The noise was assumed to be uncorrelated to the BCG and zero mean.

It is important to briefly note that the slow amplitude variations in the BCG are not noise; rather, BCG amplitude is known to modulate due to respiration (see Figure 4.5). In 1946, Starr and Friedland investigated the causes of this variation, determining that it was due to cardiac filling and not to changes in heart position [132]. As a result, accurate estimation of this amplitude envelope could be used for respiration sensing as well.

Using the four assumptions listed above, the measured BCG signal, $x[k]$, was written as N repetitions – or heartbeats – of a template function, $h[k]$, with a slowly varying amplitude component, a_n , as follows:

$$x[k] = \sum_{n=1}^N a_n h[k - \tau_n] + z[k] \quad (4.8)$$

The template function is the pulse response of the BCG: the mechanical forces resulting from the ejection of blood in each heartbeat. As shown in this equation, the template is repeated at times τ_n . Additionally, there is an additive noise component, $z[k]$, which could, for example, represent the electronic noise of the circuit, motion artifact, or floor vibrations. The period between successive occurrences of $h[k]$, was then defined as follows:

$$T_n = \tau_n - \tau_{n-1} \quad (4.9)$$

where T_n represents the heart period for the n^{th} beat.

Similarly to the standard methods of estimating the BCG signal, the first step in finding the full length pulse response consisted of computing a truncated ensemble averaged BCG. This truncated average was then used to determine the amplitude estimates for each beat, as well as to cancel the overlapping beats in the full length average, as discussed below.

To compute a truncated ensemble average, a windowing function was used:

$$w_n[k] = \Pi \left[\frac{k - \tau_n}{T_{min}} \right] \quad (4.10)$$

where T_{min} is the minimum heart period, or R-R interval, for the given recording. By using the minimum heart period for the recording, the signal-to-signal interference in the windowed beats was minimized.

For purposes of convenience, the $\Pi[k]$ function was defined as follows:

$$\Pi \left[\frac{k}{A} \right] = \begin{cases} 1, & 0 \leq k \leq A \\ 0, & \text{else} \end{cases} \quad (4.11)$$

An ensemble of N heartbeats was then generated by windowing the measured BCG, $x[k]$, with this windowing function:

$$x_n[k] = x[k]w_n[k] \quad (4.12)$$

From this ensemble of beats, a truncated estimate of $h[k]$ was directly computed by shifting each windowed beat to the origin and averaging over all N beats:

$$s[k] = \frac{1}{N} \sum_{n=1}^N x_n[k + \tau_n] \quad (4.13)$$

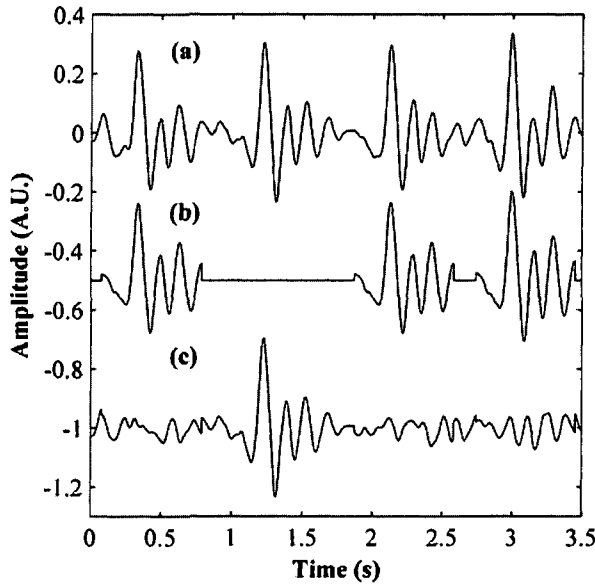


Figure 4.6 Illustration of template matching and subtraction procedure for an example long-windowed BCG beat (a). The waveform shown in (b) was subtracted from (a), resulting in the interference-cancelled beat shown in (c).

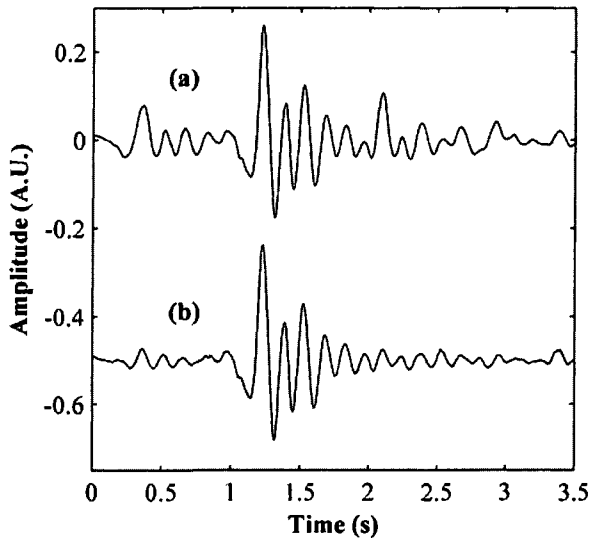


Figure 4.7 (a) Conventional ensemble average taken over long-windowed BCG beat array. (b) Modified ensemble average of interference-cancelled and time aligned long-window beats. The artifacts are substantially reduced in this average, which is then considered the best estimate of the BCG pulse response.

where $s[k]$ is the truncated estimate of $h[k]$. Note that the weighting vector was considered to be unity mean. This simply implies that the amplitude vector represents the relative magnitudes of each BCG beat with respect to the average of all beats, without any loss of generality.

These methods, to this point, describe the standard ensemble averaging techniques for the BCG, using the ECG R-wave trigger. Using this ensemble averaged beat, the amplitude scaling factor for each heartbeat, \hat{a}_n , was computed using first-order statistics: the ratio of the cross-correlation between the ensemble average and a given beat evaluated at τ_n , normalized to the autocorrelation at zero lag for the ensemble average,

$$\hat{a}_n = \frac{R_{x_n s}[\tau_n]}{R_{ss}[0]} \quad (4.14)$$

where R_{xy} is defined as the cross-correlation sequence for x and y . This addresses the first limitation described above for signal estimation since, with the ensemble averaged beat and the

estimated scaling factors, the BCG signal could be reconstructed with beat-by-beat amplitude variations included. However, the other limitations remain: the ensemble average is still limited in length to the minimum heart period for the recording, and, as a result, the reconstructed signal would have gaps between the beats. Note that these discontinuities would artificially lower the SNR for the trace, since the signal components coinciding with these gaps would incorrectly be considered to be noise by the estimator.

4.5. Modified Ensemble Averaging Methods

The amplitude estimates were then used in the following modified ensemble averaging procedure to cancel overlapping beats and acquire a full-length ensemble average. This average could then be used to reconstruct the BCG trace without any gaps between beats. The truncated estimate of $h[k]$ and the estimated amplitudes of each heartbeat were used to find the full-length estimate of $h[k]$. First, a longer windowing function was defined:

$$\tilde{w}_n[k] = \Pi \left[\frac{k - \tau_n + T_{max}}{4T_{max}} \right] \quad (4.15)$$

This function was then used to generate an ensemble of $N - 3$ quadruplets, as shown in Figure 4.6 (a), including one heartbeat, the preceding heartbeat, and the two following heartbeats:

$$\tilde{x}_n[k] = x[k] \tilde{w}_n[k] \quad (4.16)$$

The conventional ensemble average of these quadruplets was then computed to estimate the full-length template function, $h[k]$, using a similar approach as in equation (4.6):

$$\hat{h}_{con}[k] = \frac{1}{N} \sum_{n=1}^{N-3} \tilde{x}_n[k + \tau_n - T_{max}] \quad (4.17)$$

This conventional ensemble average, $\hat{h}_{con}[k]$, is shown in Figure 4.7 (a). Since there is a significant amount of overlap between beats, this approach does not yield an adequate estimate of $h[k]$: the preceding and following heartbeats manifest as artifacts in the average.

As a result, the following modified averaging approach was implemented to reduce these artifacts, producing a more accurate average BCG pulse response. Since the best estimate of

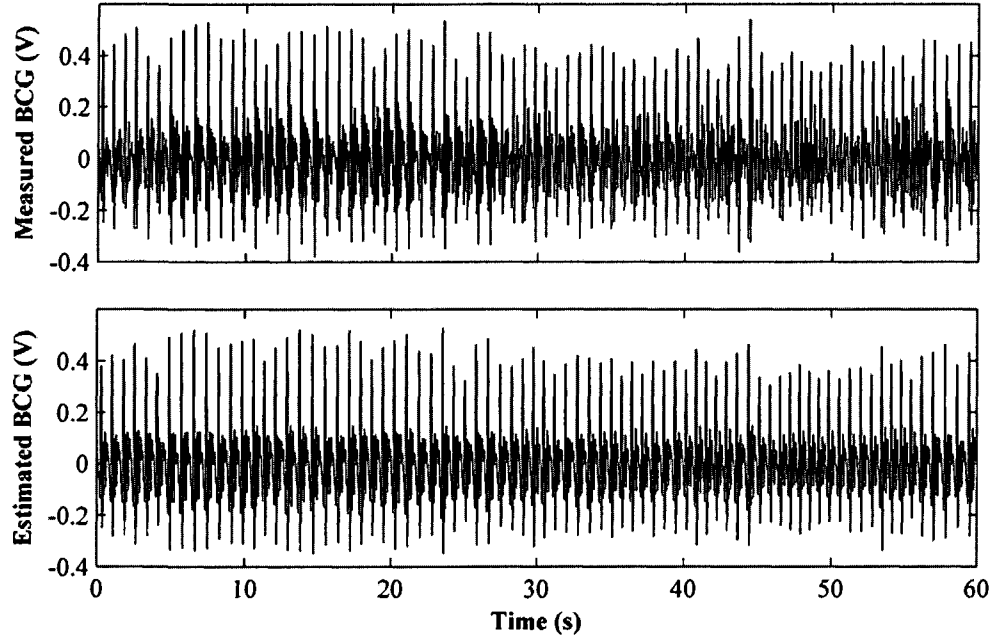


Figure 4.8 Measured and estimated BCG signals from a subject with high signal quality. The amplitude variations in the signal are captured well by the estimate.

each n^{th} heartbeat is the ensemble average, $s[k]$, weighted by the corresponding amplitude estimate, \hat{a}_n , and shifted in time by a known delay, τ_n , the full-length estimate of $h[k]$ was:

$$\begin{aligned} \hat{h}[k] = \frac{1}{N} \sum_{n=2}^{N-2} & \tilde{x}_n[k + \tau_n - T_{max}] - \hat{a}_{n-1}s[k + T_n - T_{max}] \\ & - \hat{a}_{n+1}s[k - T_{n+1} - T_{max}] \\ & - \hat{a}_{n+2}s[k - T_{n+2} - T_{max}] \end{aligned} \quad (4.18)$$

Here, the best estimates of the previous and following beats were subtracted prior to averaging the windowed beats. This process is depicted in Figure 4.6 (b) and (c).

The resulting estimate of the template function, $\hat{h}[k]$, after the time-alignment procedure, is shown in Figure 4.7 alongside the conventional ensemble average, $\hat{h}_{con}[k]$. The artifacts caused by the interfering beats are substantially reduced in the modified average.

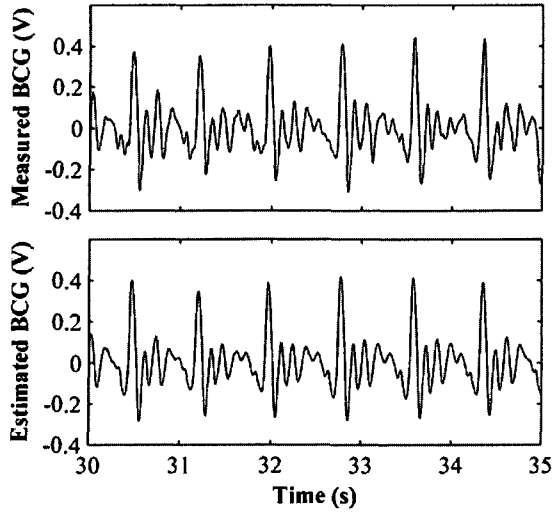


Figure 4.9 Measured and estimated BCG signals for the same subject as in Figure 4.8 zoomed in around $t = 30$ s into the recording. This demonstrates the morphological accuracy achieved by the signal estimation method. Additionally, note that although the same template function has been used for all beats, the beats in the resulting signal are not identical and, in fact, preserve the original features of the measured waveform. For example, the afterwaves of the first beat are larger than the second for both traces.

4.6. Reconstructing the BCG Signal

This modified ensemble averaged BCG was considered to be the best estimate of the full BCG pulse response given the measured data. It was then used to reconstruct an estimate of the BCG signal and, thus, provide an estimate of the SNR.

An impulse train was generated, with each impulse occurring at each R-wave peak, and the amplitude of each impulse being the estimated BCG amplitude for each beat. The pulse response was then convolved with this impulse train and the resulting trace was the best estimate of the BCG signal:

$$\widehat{BCG}[k] = \hat{h}[k] * \sum_{n=1}^N \hat{a}_n \delta[k - \tau_n] \quad (4.19)$$

The measured and estimated BCG signals are shown in Figure 4.8 for a high SNR BCG trace – this demonstrates that the estimator can properly track the amplitude variations in the BCG signal. Figure 4.9 shows the same signals, zoomed in around $t = 30$ s into the recording.

The measured and estimated waveforms are shown in Figure 4.10 for a low SNR BCG recording. In this recording, the noise has been substantially reduced in the estimated signal: most prominently, the respiratory amplitude modulation is apparent in the estimated signal, but obscured by the noise in the original trace.

For both of these recordings, the estimated BCG signal qualitatively fits the data well, with no discontinuities between beats. Accordingly, all of the limitations of the standard methods were addressed by this new approach.

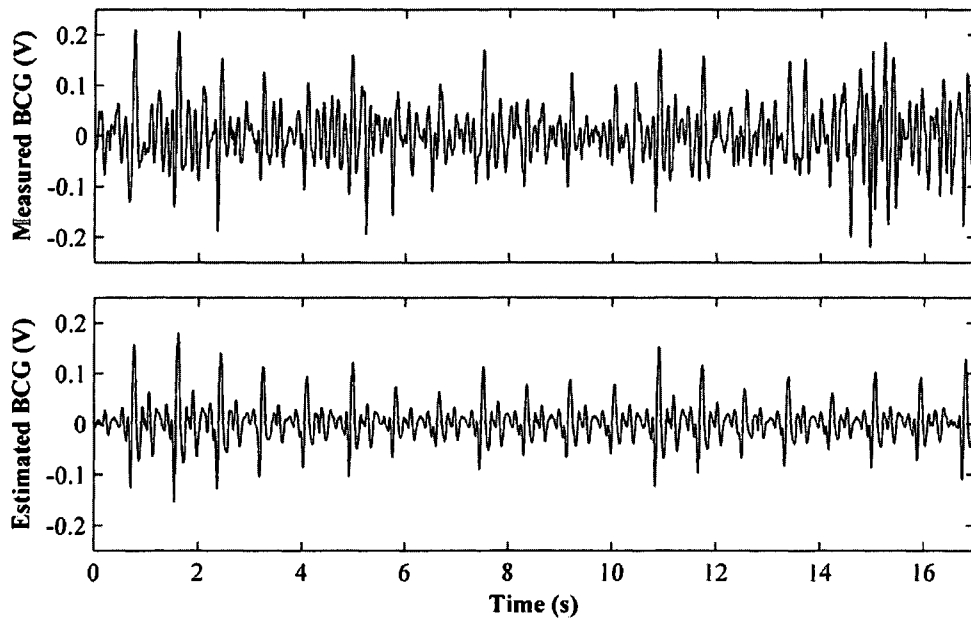


Figure 4.10 Measured and estimated BCG traces for a subject with lower signal quality. The reconstructed BCG signal tracks the overall amplitude variations that are not due to noise. Note that the envelope of these amplitude variations appears to be periodic, at a frequency approximately four times slower than the heart rate. This suggests that the respiratory amplitude variation of the BCG has been accurately reconstructed by the algorithm.

Note that although the same template function is used for each beat, the resulting signal does not look identical from beat-to-beat. This is a result of the longer pulse response interfering from one beat to the next; due to normal sinus arrhythmia, this interference is sometimes constructive and other times destructive. This is consistent with the hypothesis that the underlying template function does not vary beat-to-beat. Furthermore, the afterwaves may likely be mechanical resonances of the body-scale combination, or the vasculature within the thorax, that are underdamped and extend beyond the length of a single BCG beat.

4.7. Performance Evaluation Using Synthetic Signals

4.7.1. Synthetic Signal Model

If the morphology of the BCG did not vary significantly from person to person, a subject with bradycardia could be found to directly measure the real pulse response of the BCG. This measured pulse response could then be compared to the estimated pulse response to evaluate the methods. Alternatively, if infinite recording times were feasible, a conventional long-windowed ensemble average could be taken over the infinite number of beats, yielding the true pulse response of the BCG. However, since the BCG signal morphology does vary

significantly from person to person, can never be acquired with *no* noise or interference, and recording times are practically limited by subject compliance, the validity of these methods can best be assessed using synthetic signals. For these synthetic traces, the signal, noise and SNR will be known and used to assess the accuracy of the estimated BCGs.

Accordingly, a synthetic model was developed for the BCG based on the assumptions developed above, the existing literature, and observations made in this and previous works about the characteristics of the signal. Mathematically, the signal was written as follows:

$$Y[k] = \sum_{i=1}^M h[k - \tau_i]A_i + V[k] \quad (4.20)$$

$$A_i \sim N(1, \sigma_A) \quad (4.21)$$

$$T_i = \tau_i - \tau_{i-1} \\ \sim N(\mu_T, \sigma_T) \quad (4.22)$$

$$V \sim N(0, \sigma_V) \quad (4.23)$$

where $h[k]$ is the template function of the BCG; T_i is a normally distributed random variable, representing the heart periods, with μ_T mean and σ_T standard deviation; A_i is a normally distributed random variable, representing the amplitudes of the beats, with unity mean and σ_A standard deviation; $V[k]$ is a normally distributed random variable, representing the additive noise, with zero mean and σ_V standard deviation; and $Y[k]$ is the resulting synthetic BCG.

For a template function, the waveform in Figure 4.11 (a) was used, with unity standard deviation, σ_h . The locations of the heartbeats, given by τ_i , were considered to be deterministic for this analysis. The SNR of the traces was set as follows, by varying σ_V appropriately:

$$SNR = \frac{\sigma_h^2}{\sigma_V^2} = \frac{1}{\sigma_V^2} \quad (4.24)$$

As shown in equations (4.13–4.16), there are three parameters that can take on various different values depending on the physiology and the measurement conditions:

1. Mean inter-beat interval, μ_T .
2. Standard deviation amplitude scaling factor, σ_A .
3. Standard deviation of the noise, σ_V .

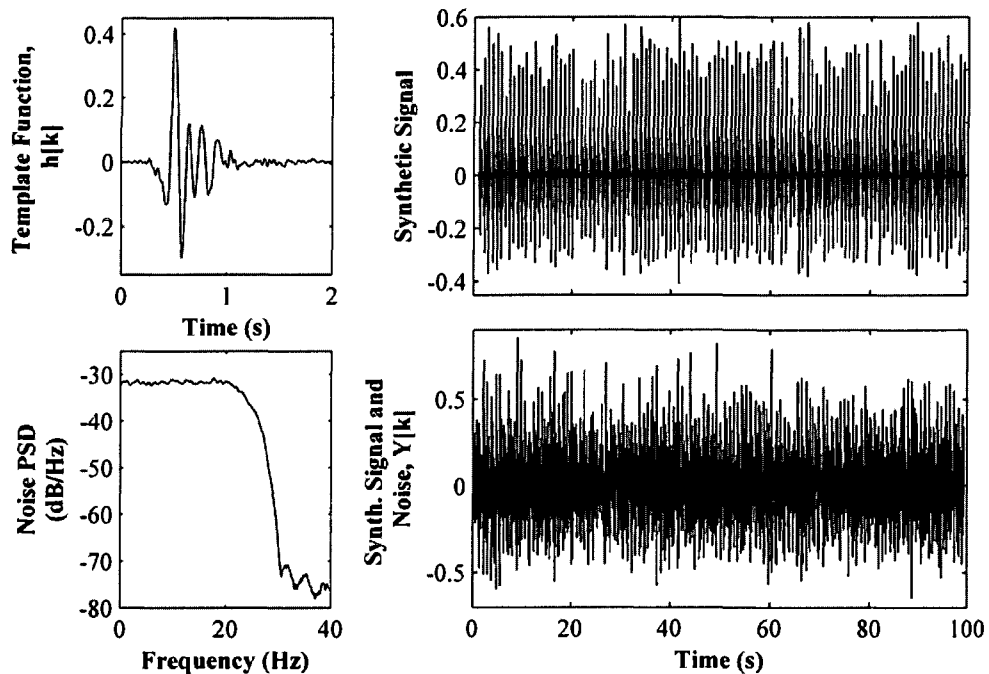


Figure 4.11 (Top left): Template function used for generating synthetic signal. (Top right): Synthetic BCG signal, generated using equations (4.13–4.16). (Bottom left): Power-spectral density (PSD) estimate for synthetically generated, band-limited white noise. The estimate was computed by Welch’s method, with a Hamming window, 2000 sample segment length, and 50% overlap. (Bottom right): Synthetically generated BCG signal with additive noise (SNR = 0.5).

Note that the standard deviation inter-beat interval, σ_T , was always considered to be 7.5% of the mean inter-beat interval based on observations from real data. The effects of different mean inter-beat intervals – or heart periods – on the SNR estimation was investigated first by holding σ_A constant at 0.25. Then, the effects of different σ_A values on the SNR estimation was quantified by holding the mean heart period constant at 1 s (heart rate of 60 bpm) and at 0.6 s (100 bpm). For all three experiments, SNR values of 0.1, 0.2, 0.5, 1, 2, 5, 10, and 20 were used, corresponding to σ_V values of 10, 5, 2, 1, 0.5, 0.2, 0.1, and 0.05, respectively.

In each case, the sum of the square errors (SSE) in SNR estimation was defined as follows:

$$SSE = \sum_{i=1}^K |SNR_{est,i} - SNR_{actual,i}|^2 \quad (4.25)$$

The experiment was iterated twenty times to quantify the standard deviation over multiple trials. For each iteration, data were generated randomly from the distributions shown in

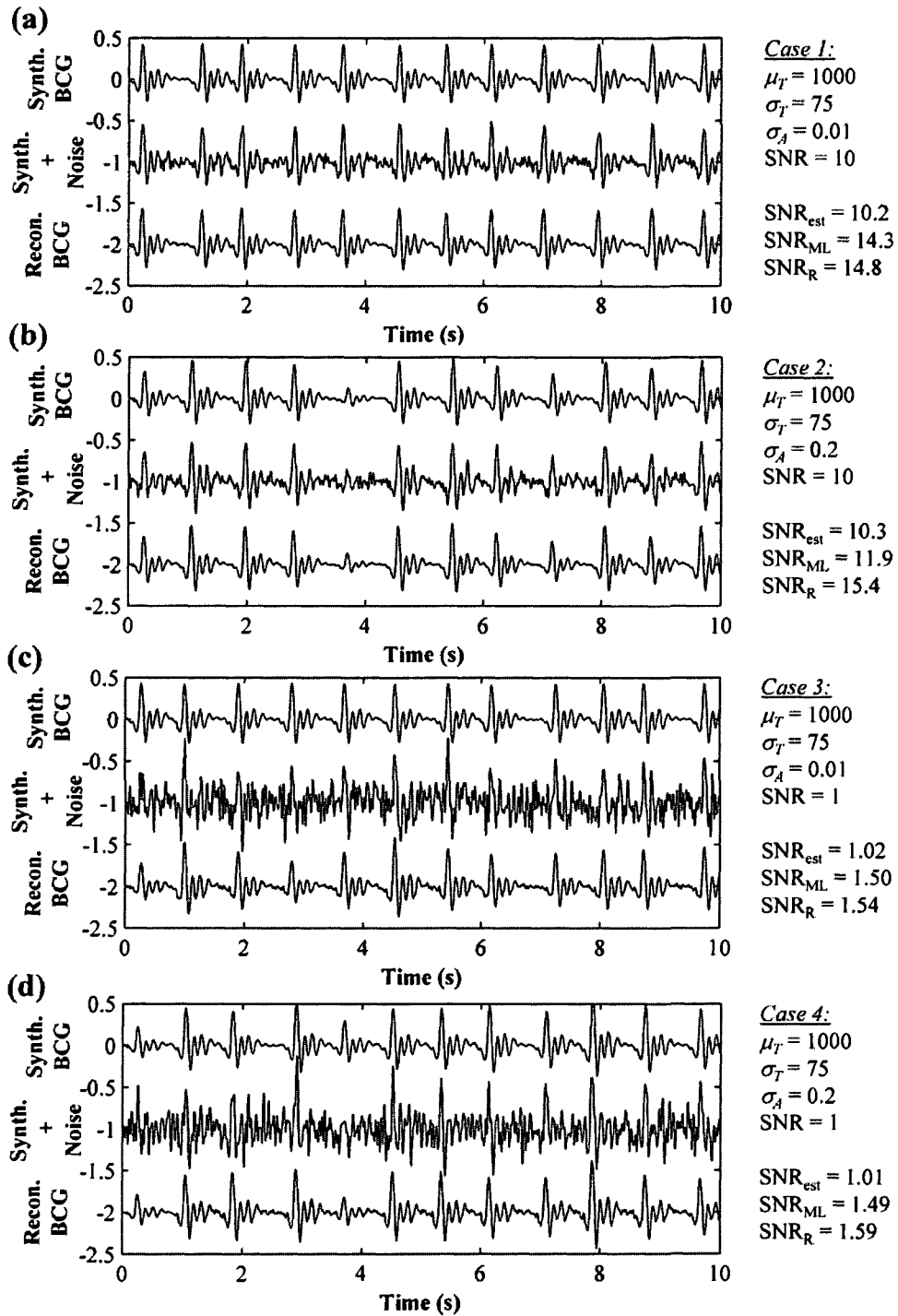


Figure 4.12 Synthetically generated BCG, synthetic BCG plus additive band-limited white noise, and reconstructed BCG – using the methods described in this chapter – for four combinations of parameters. The SNR estimates for this method, maximum likelihood (ML) and the cross-correlation method (R) are also provided for comparison.

equation (4.20–4.23). The template function, synthetically generated signal, noise spectral density, and synthetic signal with additive noise are shown in Figure 4.11.

4.7.2. Results of SNR Estimation

The SNR estimates, computed using the novel signal estimation algorithm, were compared to the ML and cross-correlation methods for all of the estimation trials. Figure 4.12 shows the synthetically generated BCG, the synthetic signal with band-limited additive white noise, and the reconstructed signal – using methods described here – for four combinations of the various parameters of the synthetic model. The SNR estimates are also shown for the three methods for comparison. For each case, the SNR estimation method described in this chapter outperforms the other methods.

This analysis was rigorously performed for multiple trials using various combinations of the synthetic model parameters.

The SSE versus mean heart rate (bpm) – with σ_A fixed at 0.25 and σ_T fixed at 7.5% of the mean heart period (μ_T) – is shown in Figure 4.13 for synthetically generated data. Each data

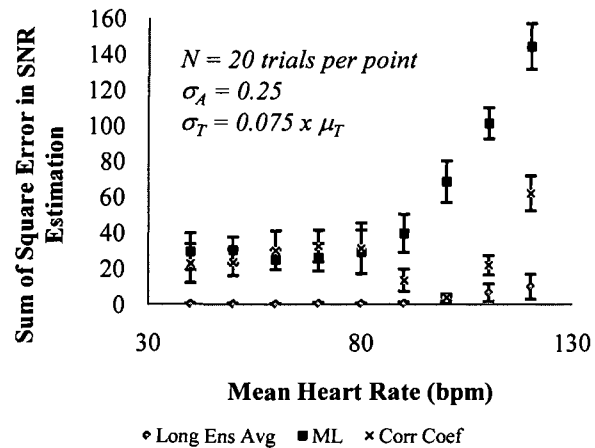


Figure 4.13 Error in SNR estimate versus mean heart rate (bpm) for synthetically generated data. The results are compared to maximum likelihood (ML) and correlation coefficient (Corr Coef) based SNR estimation methods from the literature [15, 16]. At each heart rate, the SNR is estimated in twenty separate trials for eight different values (SNR = 0.1–20), and the average ($\pm\sigma$) SSE are shown. The algorithm described here outperforms both other methods at all heart rates.

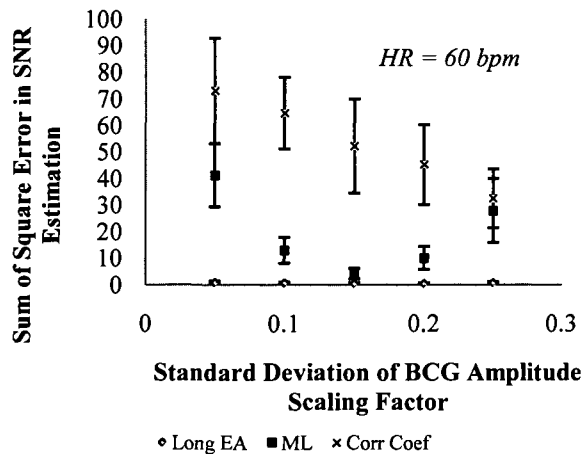


Figure 4.14 Error in SNR estimate versus BCG amplitude scaling factor standard deviation (σ_A), with heart rate fixed at 60 bpm, for synthetically generated data. The algorithm described here outperforms both other methods at all values of σ_A at this heart rate.

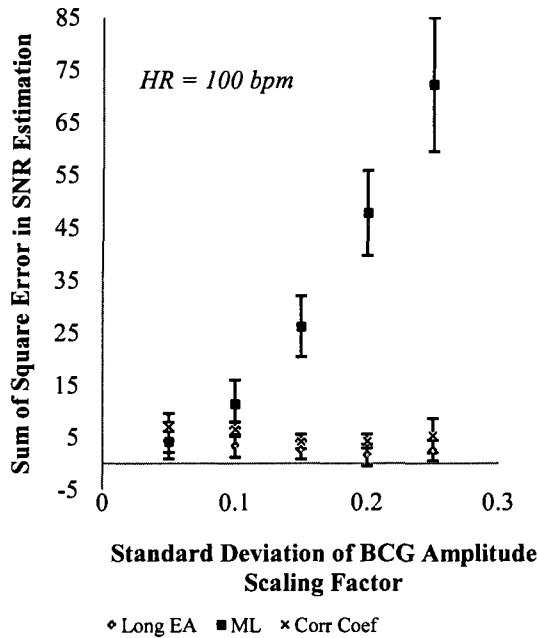


Figure 4.15 Error in SNR estimate versus BCG amplitude scaling factor standard deviation (σ_A), with heart rate fixed at 100 bpm. The algorithm described here outperforms both other methods at all values of σ_A , except when σ_A is 0.05 and the heart rate is 100 bpm. There, ML outperforms the other two methods. This is as expected since with no overlapping beats, and no amplitude variation, ML would be the ideal estimator of SNR.

point represents the mean ($\pm\sigma$) values over 20 separate trials for eight different values of SNR (0.1–20). The algorithm presented here outperformed both other methods at all heart rates.

This result illustrates two major advantages of the methods described here over ML and correlation coefficient estimators of BCG SNR: first, these other two methods do not take amplitudes variations into account, and, second, they cannot differentiate interferences due to overlapping beats from random noise.

The errors of these two methods at low heart rates are due to the inability to account for amplitude variations. At higher heart rates, the beat-to-beat interference becomes stronger, leading to the sharp rise in SSE for both ML and correlation coefficient estimators. The correlation coefficient method performs optimally when the width of the beat is approximately equal to width of the template function: at this point, the successive beats are most correlated to each other.

The effects of different σ_A values on SNR estimation are shown in Figure 4.14 for a constant heart rate of 60 bpm, and in Figure 4.15 for a constant rate of 100 bpm. The method described here outperformed both other methods at all values of σ_A , except when σ_A was 0.05 and the heart rate was 100 bpm. With these settings, since the beats were not overlapping significantly, and the amplitude variation was negligible, ML was the minimum square error estimator of SNR, by definition.

Finally, Figure 4.16 illustrates the effects of overlapping beats on the morphology of the BCG. A synthetically generated BCG is shown, *with no added noise*, but with the heart rate set at 120 bpm ($\mu_T = 500$). The other parameters used were as follows: $\sigma_A = 0.2$ and $\sigma_T = 37.5$.

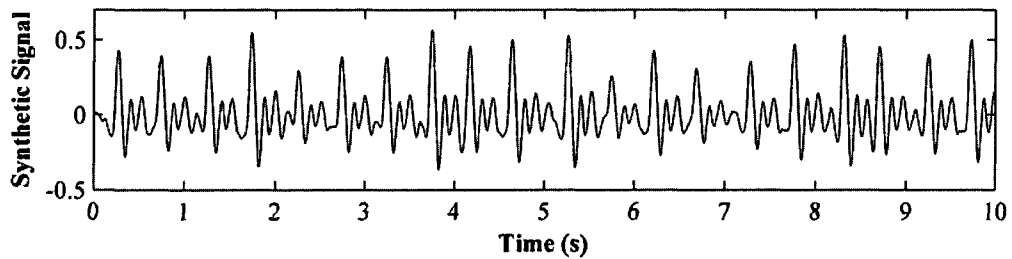


Figure 4.16 Illustration of effects of overlapping beats on the beat-by-beat morphology of the BCG. Although the same template function is used for each beat, and no noise is added to the signal, the afterwaves from one beat interfere with the next due to the length of the template function being longer than one cardiac cycle.

Note that although no noise is added to the signal, and the same template function is used for each heartbeat, there is significant beat-to-beat variation in the morphology of the signal. This is simply due to the constructive and destructive interferences of the afterwaves, due to the fact that the template function is longer than a single cardiac cycle, and that the heart rhythm is aperiodic.

4.8. Conclusions

This chapter presented methods for BCG signal (and SNR) estimation that overcome the main limitations of the standard methods. The amplitude variations were accurately captured by first-order statistical techniques. Furthermore, the length of the ensemble average was not limited to the minimum R-R interval of the trace, due to the modified-averaging procedure with interfering-beat-subtraction. As a result, the entire signal was reconstructed without any discontinuities between the beats, enabling a more accurate SNR estimate for the recording. Note that the noise was estimated for all times in the recording; furthermore, there was no requirement that the noise be stationary for this procedure to be effective. Transient changes in the noise level, such as those caused by motion artifacts, can thus be captured, as shown in the next chapter.

Additionally, the methods presented here for BCG estimation could enhance the fundamental understanding of the physical origin of the signal. For example, the fact that the afterwaves of the signal following the IJK complex do not attenuate within a cardiac cycle suggest that these waves could be resonances of an underdamped mechanical system. This opposes the accepted interpretation of these waves as diastolic waves [62]. Finally, the same methods described here could be applied to other biomedical signals, such as the phonocardiogram, impedance cardiogram, or photoplethysmogram, in signal estimation problems, to improve feature extraction or SNR estimation.

5

External Interference Detection and Reduction: Motion Artifacts and Floor Vibrations

But did thee feel the earth move?
– Ernest Hemingway, *For Whom the Bell Tolls*

As mentioned in Chapter 2, BCG measurement on a commercial weighing scale has several practical advantages over the alternatives – tables [9], beds [96], electromagnets [67], chairs [88], and custom force plates [89] – in terms of compactness, ease of use, and long-term reliability. As a result, this modality is well suited for home monitoring applications. However, one disadvantage of using a weighing scale for BCG measurement is the increased susceptibility to motion artifacts and floor vibrations.

Motion artifacts are pronounced in these measurements since the user stands on the device rather than sitting or lying prone. Floor vibrations affect the signal since the measurement axis is parallel to the primary direction of the vibrations. To increase measurement robustness, a second sensor, indicative of the motion or floor vibration, can be used as a noise reference for artifact detection and cancellation. This chapter describes methods that were used in this work to increase the robustness of the weighing-scale-based BCG instrumentation to external interferences – specifically, these methods targeted the detection of motion, and cancellation of floor vibrations.

5.1. Motion Artifact Detection Using Lower-Body Electromyogram Signals Acquired from the Feet

For motion artifact detection, a novel noise reference was proposed: the lower-body electromyogram (EMG) signal measured from the feet of the subject [133]. Motion of the subject on the scale would result in a reactive contraction of the muscles in the feet and legs to stabilize the body, thus increasing the lower-body EMG power. The correlation between BCG noise and EMG power was investigated to determine if it was a viable reference for detecting motion noise in standing BCG measurements.

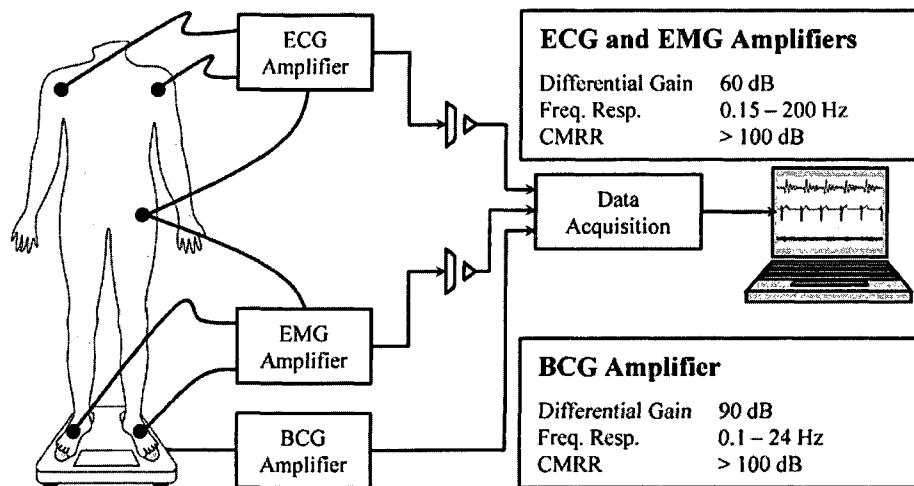


Figure 5.1 Block diagram showing setup for evaluating lower-body EMG as a motion noise reference for standing BCG measurements.

5.1.1. *Materials and Methods*

Fourteen healthy adults – eight males and six females – participated in this study. Their demographics were as follows (min-max): height (1.57–1.88 m), weight (57.5–95.5 kg), age (21–37 years). All subjects provided written consent before participating in the Stanford Institutional Review Board approved study (Protocol Number 6503).

BCG, lower-body EMG, and electrocardiogram (ECG) signals were acquired from all subjects for 60 seconds as they stood on the scale (see Figure 5.1). The recording period was chosen to be long enough for averaging a high number of beats, but not so long that the subject would have difficulty standing still. Subjects were not instructed how to stand on the scale during data collection; they were only guided to fix their eyes on a focal point positioned approximately two meters in front of them on the wall. The standard BCG and ECG amplifiers were used for BCG and ECG acquisition, and the ECG amplifier was also used for EMG acquisition. All signals were sampled at 1 kHz.

For ECG recording, each subject was asked to attach electrodes to their chest and hip in the standard Lead I configuration. For EMG recording, the electrode placement was not standard: rather than placing a local electrode pair on the muscle of interest, an electrode was attached to the top of each foot, and the differential voltage across the feet was measured. The electrodes were attached to the *top* of each foot since, if attached to the bottom, the weight of the person would sandwich the electrode between the foot and scale; this was found to cause large motion artifacts and intermittent amplifier saturation. Since the primary objective was to test the hypothesis – that EMG signals from the feet could provide a noise reference for standing BCG

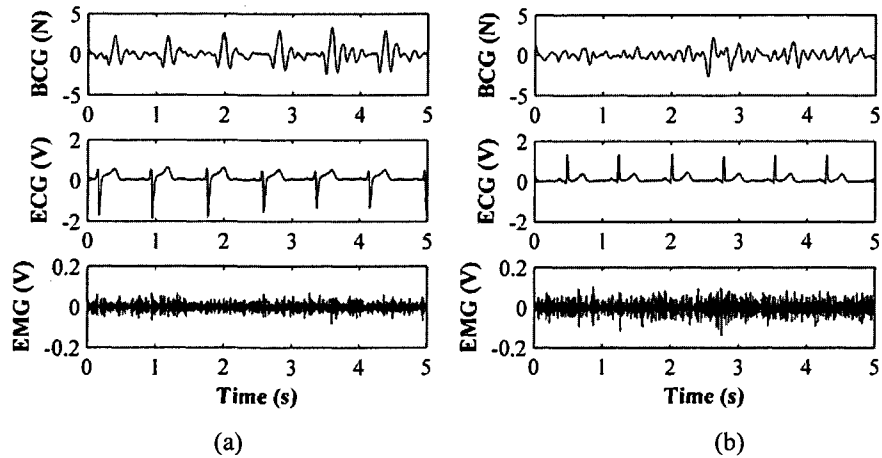


Figure 5.2 BCG, ECG, and lower-body EMG signals acquired from two subjects. (a) One subject with high SNR BCG signals and low EMG RMS power throughout the recording. (b) One subject with lower SNR BCG signals and higher EMG RMS power.

recordings – these motion artifacts would be confounding variables in the experiment. Nevertheless, preliminary EMG recordings were acquired from the bottom of the feet, as described below, using the electrodes on the bathroom scale.

With this setup, the electrical signals from any of the muscles in the legs and feet between the electrodes were integrated to provide an aggregate lower-body EMG signal. This electrode placement was selected over the standard placement – a pair of electrodes placed locally on a given muscle – since the objective was to detect the presence of motion rather than to locally probe the contractile strength of a specific muscle.

5.1.2. Statistical Analysis: Correlation Analysis

The lower-body EMG variance was plotted against the BCG noise-to-signal ratio (NSR), calculated using the methods described in Chapter 4, for all subjects. Although the data were found to be correlated, the correlation coefficient was found to be relatively weak ($R^2 = 0.33$, F-statistic p-value < 0.05). The correlation plot is shown in Figure 5.3 (left) for all 14 subjects. Note that the error bars show the standard error in each measurement.

Since the linear correlation was not strong, a multiple linear regression analysis was used to determine if height, age, or body weight combined with the lower-body EMG variance would yield a higher correlation: this was, in fact, the case as the coefficient of multiple determination (R^2) was relatively high at 0.73 and the F-statistic p-value, 0.01, confirmed the statistical significance. The coefficients providing the best correlation were as follows (for convenience, the units for each parameter are also given in *italics*): 6.12 (constant), -0.049 (height, *cm*), 0.033 (weight, *kg*), 0.015 (age, *years*), and 0.34 (variance of EMG, $1000 \times V^2$).

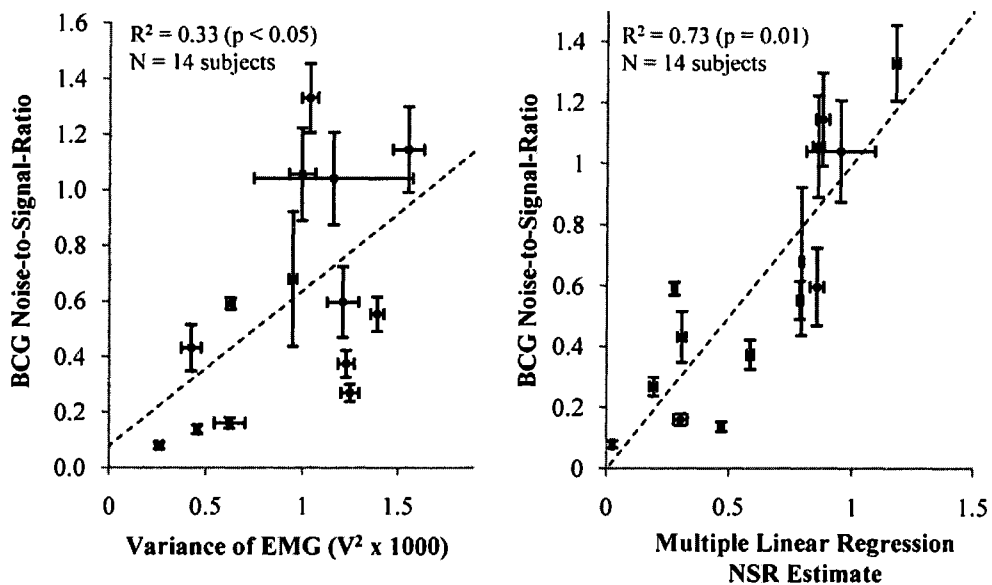


Figure 5.3 Left: Correlation plot showing BCG noise-to-signal ratio (NSR) versus lower-body EMG variance (in units of $V^2 \times 1000$, for convenience). Right: Correlation plot showing BCG NSR versus multiple linear regression NSR estimate derived from EMG variance and subject demographics. The correlation is much stronger when height, weight, and age are taken into account. Note that the error bars indicate standard error in computing the NSR and EMG.

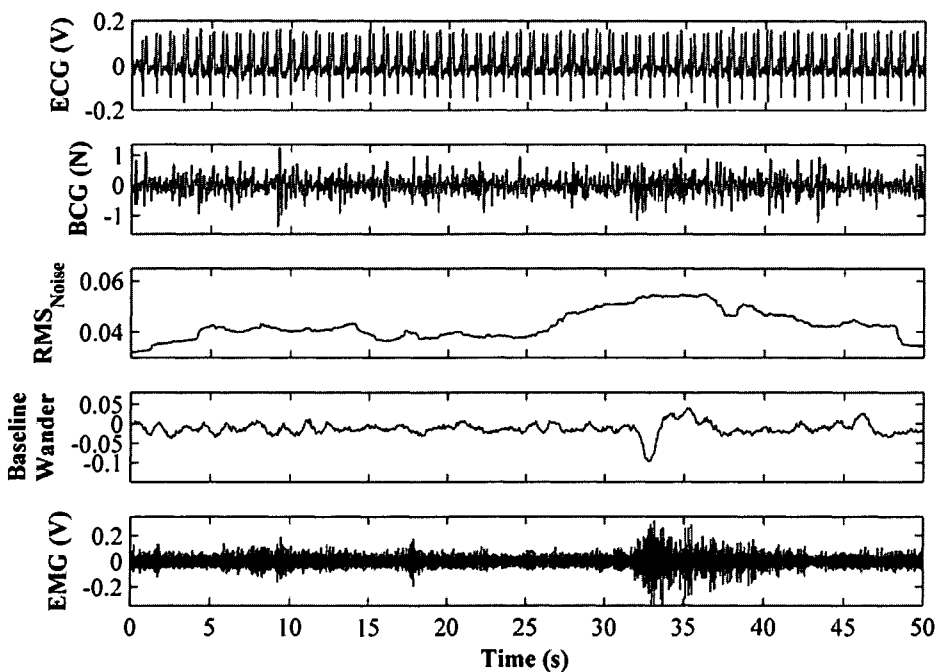


Figure 5.4 ECG, BCG, moving RMS of the BCG noise, BCG baseline wander, and EMG traces for one subject. BCG noise and baseline wander increase substantially around $t = 30$ seconds, and EMG power increases simultaneously, indicating that the subject is correcting his balance.

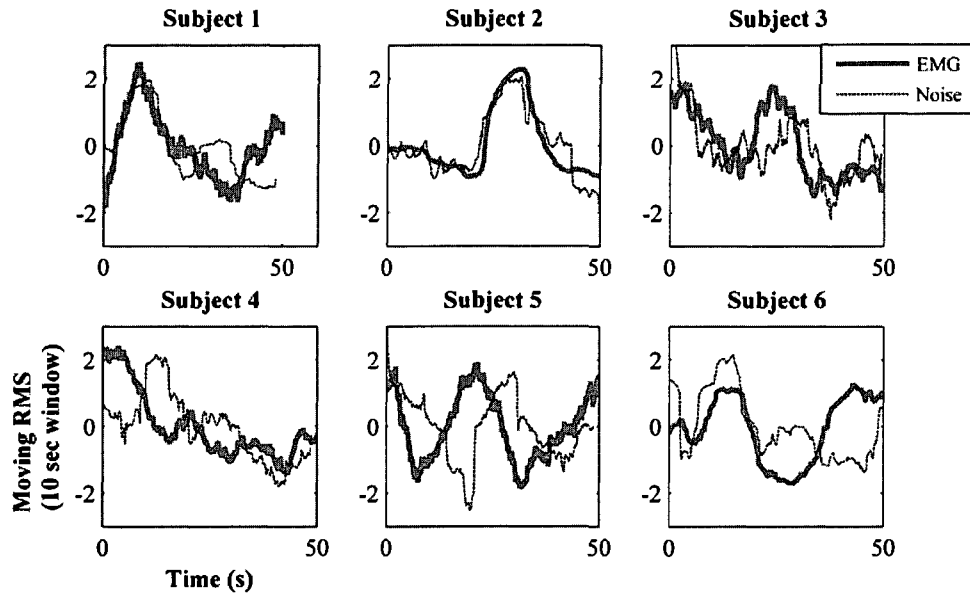


Figure 5.5 Moving RMS EMG power and moving RMS BCG noise power, both with a 10 second moving average length, plotted versus time for six subjects from the trial. Visually, the RMS EMG power tracks the BCG noise power closely in time, indicating that it could be used for automatically detecting segments of the BCG signal with elevated noise.

The resulting correlation plot is shown in Figure 5.3. To visually illustrate the difference in signal quality between subjects with lower EMG variance and those with higher EMG variance, two example time traces are shown in Figure 5.2.

5.1.3. *Intra-Recording Analysis*

In addition to the comparison among subjects, the correlation between EMG power and BCG noise *within* a recording was investigated. For this intra-recording analysis, the moving RMS power of the BCG noise – computed as described in Chapter 4 – and the moving RMS power of the lower-leg EMG were found using a 10 second moving average window. Both moving RMS traces were then normalized to zero mean and unity standard deviation.

Figure 5.4 shows the ECG, BCG, moving RMS of BCG noise, baseline wander, and EMG traces for one subject. The noise and baseline wander of the BCG signal were both significantly elevated approximately 30 seconds into the recording. The EMG power increased as well at this event, as shown in the bottom trace, suggesting that it could be used to flag regions of high motion artifact.

Figure 5.5 shows the moving RMS of BCG noise and lower-leg EMG for six subjects. In some instances, the RMS EMG power tracked the BCG noise power closely in time, indicating that it could readily be used in an automatic motion noise detection algorithm in

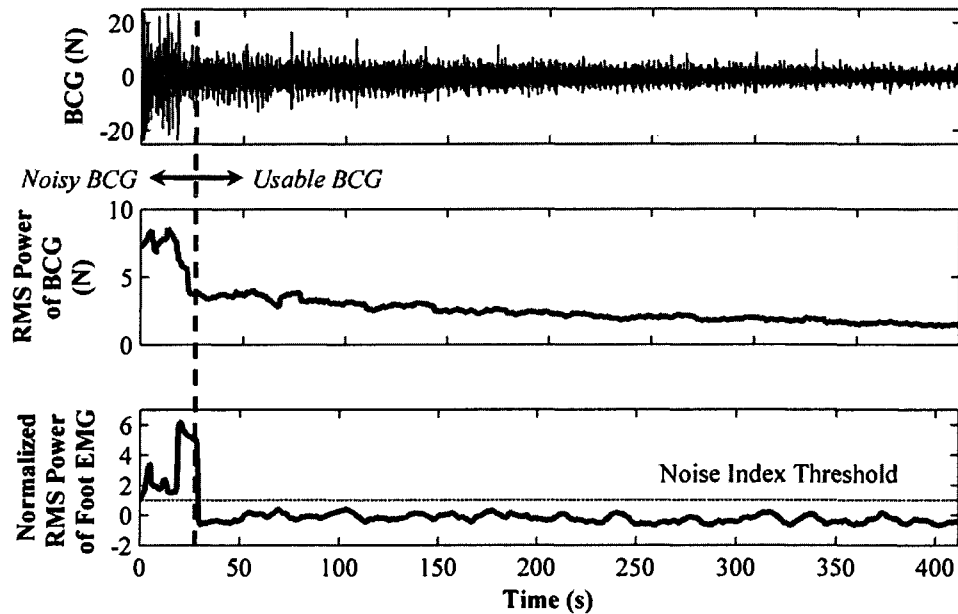


Figure 5.6 Exercise recovery used as an example of an application where EMG gating could improve BCG analysis. As discussed in Chapter 7, changes in the RMS power of the BCG measured on the bathroom scale were shown to be highly correlated with changes in cardiac output measured by Doppler echocardiography. However, for the first 20–30 seconds of recording immediately following exercise, the BCG trace is usually corrupted by artifacts due to motion of the subject on the scale. The RMS power of the lower-body EMG effectively tracks this elevated noise at the start of the trace, and can be used to gate the signal accordingly.

future work. In other instances, there was a delay in time between the onset of BCG noise and the increase in EMG power; this is likely a result of the reaction time of the body in response to movement on the scale. The delay complicates the analysis of the temporal correlation between the two measurements since it can vary significantly among subjects and even among different movements for the same subject, ranging from one to almost ten seconds. For example, if the body begins to slowly drift off-balance in one direction, the stabilizing action from the leg muscles may not immediately take effect until the body senses that it is off-balance. Additionally, it is likely that normal postural shifting is responsible for some of these movements. In the case as well, the body would need several seconds before realizing that the posture has changed, and recovering to the original position.

While in this study this information presents an obstacle for analyzing and interpreting the data, in some applications – such as rehabilitation or physical therapy – it could be useful for understanding the neuromuscular control system of the body. For example, in monitoring the recovery of stroke patients, this neuromuscular information could be coupled with the

cardiovascular parameters measured from the BCG; this data, representing the rehabilitation progress of the patient, could be obtained simply by using a modified bathroom scale equipped for BCG and EMG recording. Future work should include investigating applications where the fusion of these parameters could provide clinically relevant information.

For simple BCG noise detection algorithms, this delay can be circumvented using the following approach: a fixed window can be taken around the region with elevated EMG power, and considered an area of high motion-related noise in the BCG. These regions of high motion noise can then be further analyzed by other algorithms to determine if they should be discarded from the overall dataset.

5.1.4. *Noise Detection Example: Exercise Recovery*

One subject was asked to exercise for 30 minutes on a treadmill then stand on the scale during recovery. While exercising, he was wearing surface electrodes on the feet and, immediately following exercise, snap-on leads were connected to these electrodes to begin recording lower-body EMG signals. The subject then stood on the scale for the duration of the recovery period; during this period, certain segments of the BCG signal were corrupted by motion noise.

By using the RMS power of the lower-body EMG signal as a reference, the corrupted segments of the BCG signal were automatically gated as follows: first, the RMS power of the lower-body EMG was normalized to zero mean and unity standard deviation, then, the segments of the trace where this normalized RMS power exceeded unity were considered time periods of elevated motion.

The results are illustrated in Figure 5.6. Since it is more difficult than normal to stand still immediately following exercise, there were significant motion artifacts in the first 20–30 seconds of the BCG recording. These artifacts corrupted the RMS power measurement from the BCG signal, which, as discussed below in Chapter 7, was shown to be correlated to changes in cardiac output [11]. Considering these corrupted regions in the analysis would result in an inaccurate prediction of cardiac output changes induced by exercise. Using the EMG, these segments were gated, and the resulting gating signal – named “Noise Index” in Figure 5.6 – is shown overlaying the RMS power of the BCG. Note that for real time applications, other approaches would be used that do not require the normalization of the EMG power; one such approach could take EMG recordings from the feet over several measurements and use the statistics from these recordings as the baseline value.

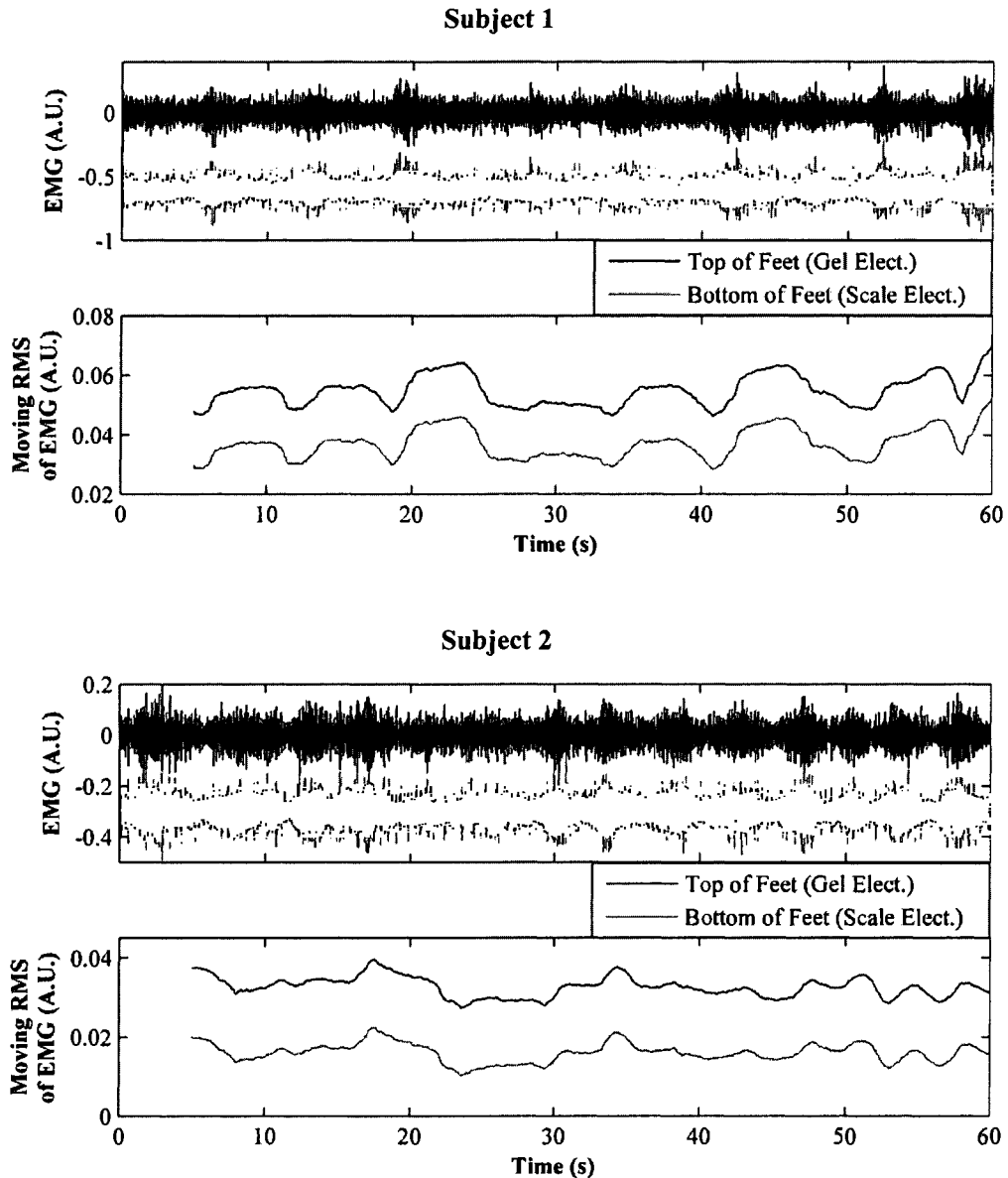


Figure 5.7 Simultaneously acquired EMG signals from the top (gel electrodes) and bottom (footpad electrodes of scale) of the feet for two subjects. For both recordings, the upper plot shows the high-pass filtered ($f_c = 20$ Hz) EMG signals for a subject swaying on the scale. Note that the signals are artificially offset (but not scaled) for convenience. The lower plots show moving RMS power (5 second window) of both EMG signals, demonstrating that the relative changes in the two track closely in time. This preliminary data suggests that in future implementations, the footpad electrodes built into the scale could be used for providing an index of motion.

5.1.5. Preliminary Evaluation of Body-Fat-Measurement Electrodes on Scale

Some modern bathroom scales use large electrodes contacting the soles of the feet for impedance-based body-fat measurements. These scales generally have at least four electrodes

to facilitate a four-point-probe impedance measurement. By connecting the two opposing heel electrodes to the positive and negative input terminals of the amplifier, and one toe electrode to the ground terminal, EMG measurements can be acquired without the need for gel-based surface electrodes on top of the feet.

With this setup, a preliminary study was conducted to evaluate these electrodes for lower-leg EMG measurements. Two subjects of significantly different body types were chosen for this study: a large subject (Height: 201 cm, Weight: 143 kg) and a smaller subject (Height: 165 cm, Weight: 61 kg). Each subject stood barefoot on the scale, with the electrode footpads connected to one channel of the EMG amplifier, and surface electrodes on top of the feet connected to the second channel; accordingly, the lower-leg EMG was recorded simultaneously from the top (gel electrodes) and bottom (footpad electrodes) of the feet. The purpose was to provide a preliminary assessment of whether these electrodes could be used in a future implementation in place of the gel-electrodes, thus further reducing the obtrusiveness of the method.

The recordings from these subjects are shown in Figure 5.7. Note that both signals were filtered using the same high-pass filter ($f_c = 20$ Hz) used in the other data analysis steps of this chapter. Additionally, the signals were artificially offset (but not scaled) in this figure for convenience. The signals taken from the top and bottom of the feet are very comparable for both subjects – the variance of the residual is less than 10% of the variance of the gel electrode trace. There is no apparent delay in time or significant difference in amplitude between the two. Most importantly, as shown in the lower plots of this figure, the moving RMS power for both signals also tracks closely in time, and the relative magnitudes of the maxima and minima are consistent between the two. The qualitative comparisons were verified quantitatively: the correlation coefficient, calculated on a point-by-point basis, was found to be 0.996 for the first subject, and 0.922 for the second. This preliminary data suggests that, in future implementations, the footpad electrodes built into the scale for body-fat analysis could be modified for providing an index of motion for BCG recordings.

5.2. Adaptive Floor Vibration Cancellation Using a Seismic Sensor

To eliminate the effects of floor vibrations from the BCG signals, a seismic sensor was placed next to the scale on the floor and used as a noise reference for an adaptive noise canceller [134]. While in this work a geophone was used as the seismic sensor, a low-noise accelerometer could also be used with the same algorithm, provided that the accelerometer was firmly coupled to the floor next to the scale. The system with adaptive vibration

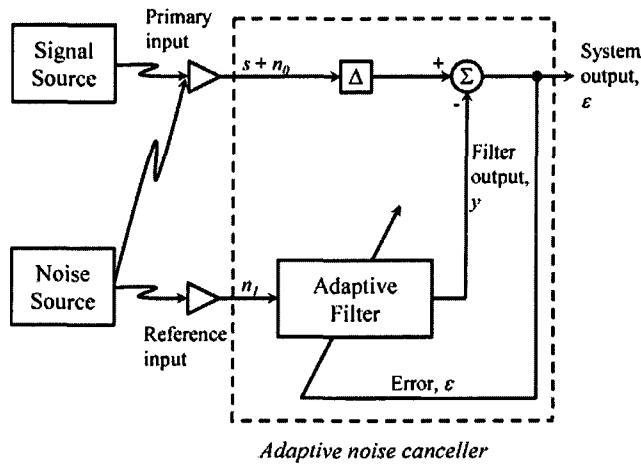


Figure 5.8 Adaptive noise canceller, adapted from Widrow, *et al.* [8]

cancellation could increase the robustness of BCG recording in the home, as well as enable measurements on transport vehicles, such as ambulatory settings. This section discusses the theory of adaptive noise cancellation, the procedures used for tuning the algorithm, and the results obtained in two settings: one where floor vibrations were simulated, and a second on board

a parked bus with the engine running.

5.2.1. Theory of Adaptive Noise Cancellation

The basic adaptive noise cancellation architecture is shown in Figure 5.8, after Widrow, *et al.* [8] The noise canceller has two inputs, the primary and the reference inputs, and one output, the system output. One sensor at the primary input receives some signal of interest, s , combined with an uncorrelated noise, n_0 . A second sensor at the reference input receives a noise, n_1 , which is correlated to n_0 by some unknown transfer function. The noise at the reference input is then filtered adaptively to match the noise component of the primary input, as shown below. For a more detailed treatment of the theory of adaptive noise cancellation, the reader is referred to the literature [8, 135].

Assume that s , n_0 , n_1 , and y are statistically stationary and have zero means; s is uncorrelated with n_0 and n_1 ; and n_0 is correlated with n_1 . Using an adaptive algorithm, as discussed below, the filter will adjust its weights, at each iteration, to minimize the mean-square error. The error signal, ϵ , is also the system output, and can be written as:

$$\epsilon = s + n_0 - y \tag{5.1}$$

The square of the error is then:

$$\epsilon^2 = s^2 + (n_0 - y)^2 + 2s(n_0 - y) \tag{5.2}$$

The expected value of both sides of this equation can then be computed to find the mean-square error:

$$\begin{aligned} E[\varepsilon^2] &= E[s^2] + E[(n_0 - y)^2] + 2E[s(n_0 - y)] \\ &= E[s^2] + E[(n_0 - y)^2] \end{aligned} \quad (5.3)$$

The $E[s(n_0 - y)]$ term goes to zero since s is uncorrelated with n_0 and n_l , and y is a filtered version of n_l . Since the filter cannot affect the signal power, $E[s^2]$, the minimum mean-square error will be achieved when $E[(n_0 - y)^2]$ is minimized. The filter output, y , is thus the best least-squares estimate of the primary noise, n_0 . Finally, when $E[(n_0 - y)^2]$ is minimized, $E[(\varepsilon - s)^2]$ is also minimized since

$$(\varepsilon - s) = (n_0 - y) \quad (5.4)$$

As a result, the system output, ε , is the best least-squares estimate of the primary signal.

In this work, the LMS algorithm [135] was used to update the weights of the adaptive filter:

$$\mathbf{W}_{k+1} = \mathbf{W}_k + 2\mu\varepsilon_k\mathbf{X}_k \quad (5.5)$$

where \mathbf{W}_k is a $1 \times L$ vector of weights at a given iteration, k ; μ is the learning rate of the filter that controls speed and stability of the adaptation; ε is the error signal fed back to the filter; \mathbf{X}_k is the vector of input samples to the filter; and \mathbf{W}_{k+1} is the vector of weights to be used in the next iteration. With this algorithm, the misadjustment – or the normalized excess mean-square error – will be given by:

$$M = \mu \operatorname{tr}[R] \quad (5.6)$$

where M is the misadjustment, and $\operatorname{tr}[R]$ is the trace of the autocorrelation matrix, R , for the input vector, \mathbf{X} . The general expression for the time constant of the learning curve, τ_{MSE} , assuming equal eigenvalues of the R matrix, is given by:

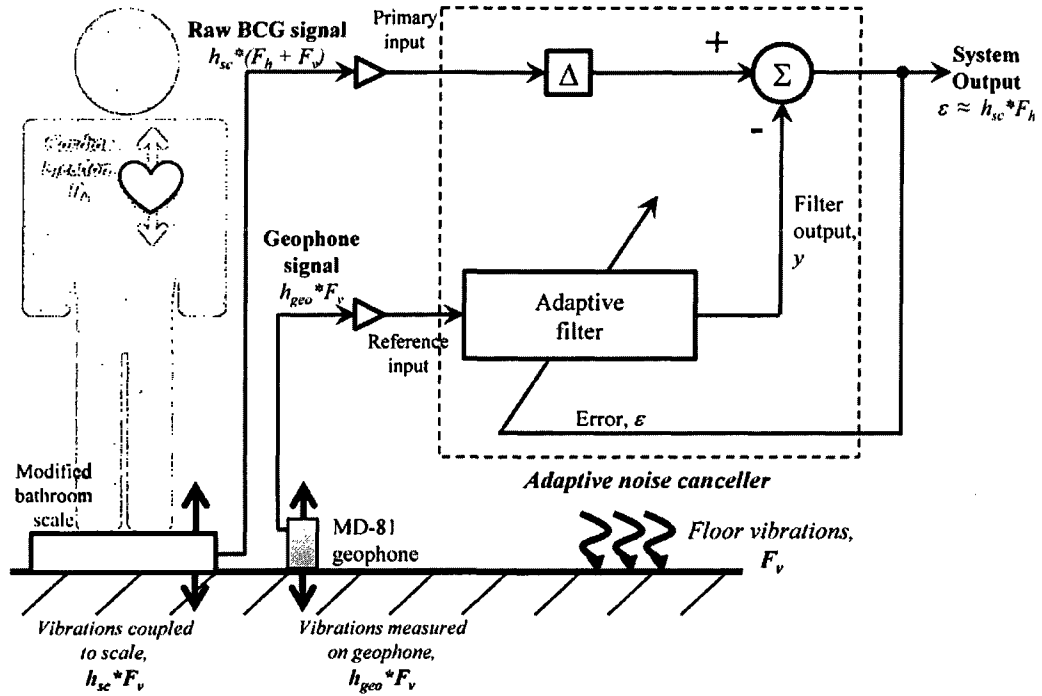


Figure 5.9 Block diagram of measurement setup used for floor vibration cancellation. The subject stands on the scale while the force of cardiac ejection, F_h , and floor vibrations, F_v , are sensed by the scale. Simultaneously, the floor vibrations are sensed by the geophone. The scale and geophone signals are inputted to an adaptive noise canceller, and the system output is the best least-squares estimate of the cardiac signal.

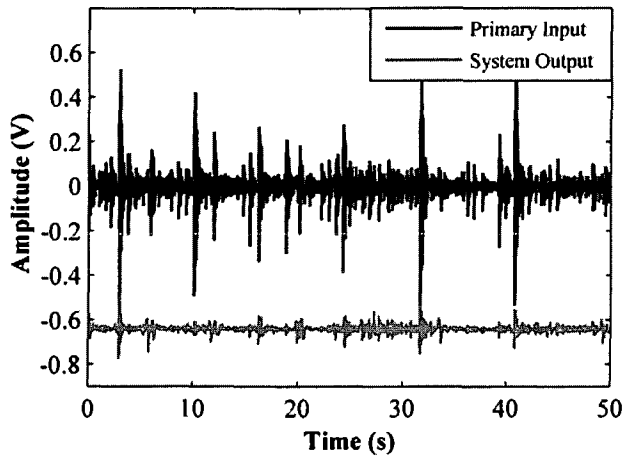
$$\tau_{MSE} \approx \frac{L + 1}{4M} \quad (5.7)$$

In many cases, this is also a good approximation when the eigenvalues of R are unequal [135]. The process used for selecting the optimum parameters for the filter is described below.

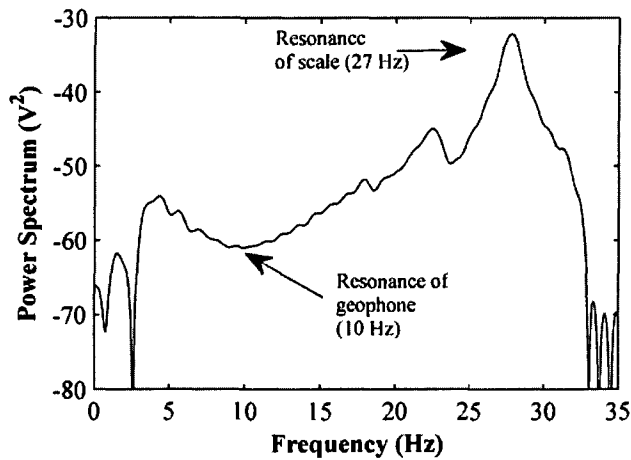
5.2.2. Measurement Setup

The measurement setup is shown in Figure 5.9. During the BCG measurement, the subject stands on the BCG measurement scale. With each heartbeat, a contractile force, F_h , is exerted by the heart on the blood and an equal but opposite force is experienced by the body. This causes vertical body motion synchronized with the beating heart.

In addition to the forces due to cardiac ejection, forces due to floor vibrations, F_v , are also coupled to the scale through this same transfer function, h_{sc} . These vibrations can corrupt the signal quality of the BCG, reducing the robustness of the recording. To attenuate the artifacts caused by these vibrations in the BCG signal, an adaptive noise canceller was implemented with a seismic sensor (MD-81 Geophone, Geosource Inc., Houston, TX) placed on the floor



(a)



(b)

Figure 5.10 (a) Primary input (weighing scale output) and filtered output using the optimum parameters for the adaptive filter (Length = 250 taps, Misadjustment = 1%, Delay in desired response = 62 samples). The noise reduction was 12 dB. (b) Frequency response of the adaptive filter after convergence. The response dips at the resonant frequency of the geophone (10 Hz) and peaks at the resonant frequency of the scale with a 40 kg load (27 Hz).

next to the scale as the noise reference. This geophone sensed the same floor vibrations, F_v , through a different transfer function, h_{geo} . The circuit used for amplifying and filtering the geophone signal was a simple non-inverting amplifier stage ac-coupled to a Sallen-and-Key low-pass filter – the overall gain was 101 and the bandwidth was 0.1–24 Hz. Both the BCG and geophone signals were sampled at 1 kHz using a data acquisition card (6024E, National Instruments, Austin, TX) and stored on a laptop computer using software (Matlab®, Version 2007b, The Mathworks, Natick, MA). The signals were downsampled to 200 Hz prior to the filtering operations.

If the transfer function of the scale, h_{sc} , and of the geophone, h_{geo} , were time invariant, and could be measured prior to the BCG recording, the noise could be cancelled using a

straightforward approach: the geophone signal could be passed through an optimum filter composed of the inverse of the geophone transfer function cascaded with the transfer function of the scale. The resulting output would, in theory, be exactly equal to $h_{sc} * F_v$, where $*$ is the convolution operator.

Unfortunately, the transfer function of the scale, h_{sc} , can vary significantly based on the properties of the scale and the mass and other physical characteristics of the subject, and can be quite different from person to person. As a result, an adaptive noise cancelling architecture was implemented, with the raw BCG signal as the primary input and the geophone signal as the reference input. With this approach, the adaptive filter automatically, and continually, adjusted its impulse response to best map the geophone signal to the floor vibrations component of the measured BCG to achieve cancellation of these vibrations.

5.2.3. *System Performance: Optimizing the Adaptive Filter Parameters*

The setup shown in Figure 5.9, where the person on the scale was replaced by iron weights, was used to tune the parameters of the adaptive filter: length (L), misadjustment (M), and delay (Δ) in the desired response path. The delay in the desired response is necessary in practice to allow the adaptive filter response to approximate a two-sided impulse response [135]. The iron weights on the scale were of mass, $m = 40$ kg, and the scale output and geophone output were recorded while a person stomped around the scale to create significant floor vibrations. With this setup, the BCG signal source was set to zero since no subject was standing on the scale.

The adaptive filter weights were initialized at zero and the parameters were varied to maximize the noise reduction, ΔN , defined as the ratio of the variances of the scale output and the system output, expressed in dB:

$$\Delta N = 10 \log_{10} \left(\frac{\text{var}(h_{sc} * F_v)}{\text{var}(\epsilon)} \right) \quad (5.8)$$

A maximum noise reduction of 12 dB was achieved with a filter length, L , of 250 taps, a misadjustment of 1%, and a desired response delay of 62 samples ($L/4$). Using equation (5.7), these parameters correspond to a convergence time constant, τ_{MSE} , of 6,275 samples, or approximately 31 seconds. For real-time implementations, this convergence time constant could be reduced by increasing the misadjustment with a slight decrease in noise reduction.

The recorded signal and the system output of the canceller using these parameters are shown in Figure 5.10 (a). Figure 5.10 (b) shows the frequency response of the adaptive filter after convergence. Interestingly, the response of this filter has a dip at the resonant frequency of the geophone (10 Hz) and a peak at the resonant frequency of the scale (27 Hz), calculated based on the spring constant of the scale measured in Chapter 3 ($1.19 \text{ N } \mu\text{m}^{-1}$).

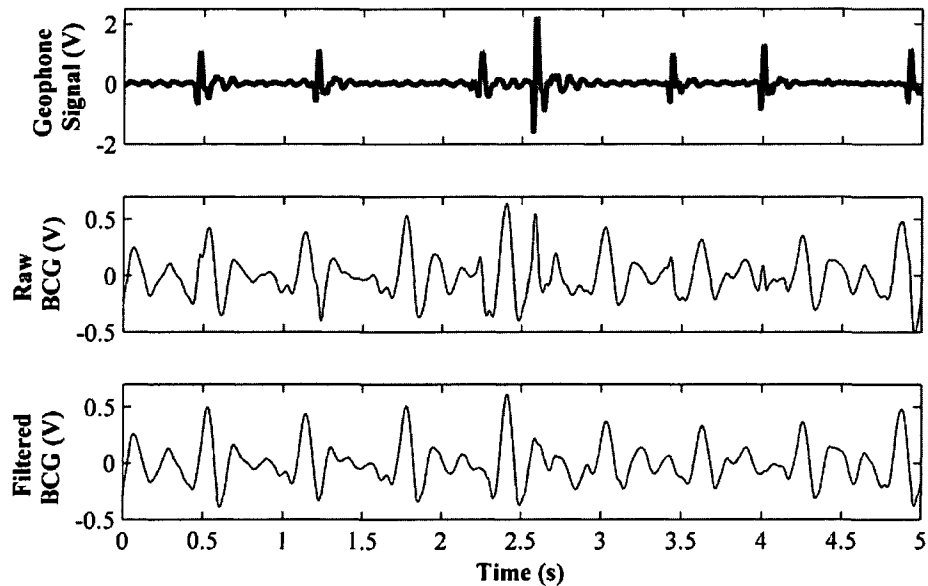


Figure 5.11 Top trace: geophone signal output of amplifier. Middle trace: measured BCG signal with vibration induced artifacts. Bottom trace: filtered BCG output of noise canceller. The vibration artifacts are substantially eliminated in the filtered signal, without distorting the morphology of the BCG.

This frequency response is consistent with the expected response of the optimum filter discussed above: the adaptive filter response is the inverse transfer function of the geophone cascaded with the transfer function of the scale. With loads on the scale other than 40 kg, the same results are obtained by the noise canceller, as soon as the adaptive filter converges. With a filter length of 250 taps and a delay of 62 samples, a 1% misadjustment was achieved with a 31 second convergence time constant.

5.2.4. *Results for Simulated Vibrations*

The BCG and geophone signals were recorded from a healthy subject standing on the scale while another person (140 kg in weight) stomped around the scale to cause significant floor vibrations. The subject on the scale was 1.65m in height, 54kg in weight, and 22 years of age. The adaptive filter parameters determined in Section 5.2.3 were used, and a filtered BCG signal was obtained by using the noise canceller. The results are shown in Figure 5.11. The top trace is the geophone signal from the amplifier. The middle trace is the measured BCG waveform, with vibration artifacts. The bottom trace is the filtered BCG output of the adaptive noise canceller, where these artifacts have been removed by the adaptive filter.

In some instances, the artifacts appear as distortions in the morphology of the signal, such as the first artifact at the time $t = 0.5\text{s}$ into the recording. These types of artifacts could lead to

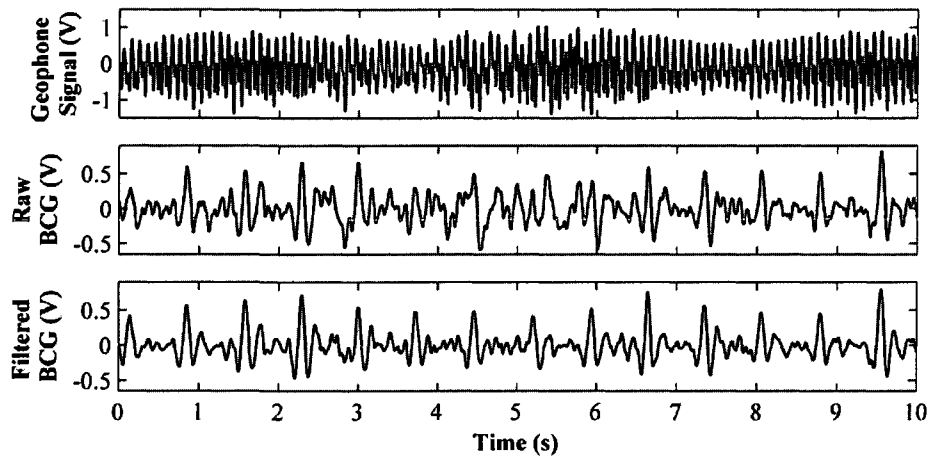


Figure 5.12 BCG recordings taken from a subject standing in a parked bus. Top trace: geophone output of the amplifier. Middle trace: raw BCG signal output of amplifier with significant vibration induced artifacts. These artifacts were caused by the engine of the bus as well as other vehicles driving on the road. Bottom trace: filtered BCG output of the noise canceller. The artifacts due to vibrations have been significantly reduced from the recording.

a misinterpretation of the signal, resulting in a misdiagnosis of the cardiovascular health of the subject. In other instances, the artifacts appear as extra peaks in the signal, such as the artifact at the time $t = 2.6\text{s}$ into the recording. These types of artifacts could lead to errors in heartbeat and arrhythmia detection.

To ensure that the output of the noise canceller did not distort the average signal morphology of the BCG, the ensemble average of both the raw signal and the filtered signal were computed and compared. A residual was computed by subtracting the average filtered signal from the average raw signal. The variance of this residual was 0.09% of the variance of the original signal average, demonstrating that the signal morphology was adequately preserved in the filtering.

5.2.5. *Results from Recordings on a Parked (Idling) Bus*

The signals were acquired from another healthy subject while standing inside of a bus. The subject was 1.75m in height, 63.6kg in weight, and 25 years of age. When the bus was in motion, the BCG and geophone amplifier outputs railed, preventing the use of adaptive noise cancelling for removing the vibrations. However, when the bus was parked, the signals were acquired successfully without railing the amplifier. In these recordings, the vibrations due to the engine and the other vehicles driving on the road corrupted the signal quality of the BCG significantly. The noise cancellation algorithm was used to eliminate the vibrations from the measured BCG. The results are shown in Figure 5.12.

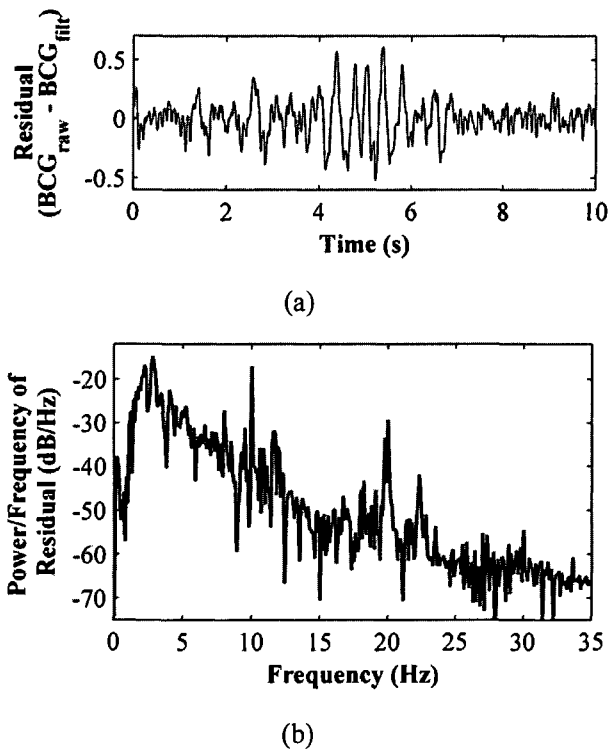


Figure 5.13 (a) Residual computed from the raw and filtered BCG signals, recorded on the bus, from Figure 5.12. (b) Power spectral density estimate of this residual. The frequency content of the noise has higher frequency peaks which could be reduced by linear filtering, but also contains significant low frequency content that overlaps with the bandwidth of the BCG (1–10 Hz). The adaptive noise canceller effectively eliminates these artifacts from the signal.

The top trace shows the geophone amplifier output. The middle trace shows the measured BCG waveform. Many of the BCG beats are completely obscured by the vibration noise from the bus – in fact, with the exception of a few beats at the end, the signal is relatively unusable. The bottom trace shows the filtered BCG waveform, where the vibration artifacts have been effectively eliminated.

The residual of the raw and filtered BCG signals of Figure 5.12 was computed to analyze the nature of the vibration noise, and is shown in Figure 5.13 (a). Figure 5.13 (b) shows the power spectral density (PSD) estimate for this residual. The PSD was

estimated by taking the fast Fourier transform (FFT) of the autocorrelation sequence of the residual. While some of the noise power appears to be outside of the useful bandwidth of the BCG (1 – 10 Hz), a majority of the power overlaps in frequency with the BCG and, thus, could not be removed by simple linear filtering operations; all components were, however, removed quite effectively by the adaptive noise cancellation algorithm. Nevertheless, future work should focus on developing other algorithms for cancelling these vibration artifacts from the BCG as well, including possibly using parametric spectral estimation techniques for determining the optimum filter described in Section 5.2.2.

5.3. Conclusions

The methods presented in this chapter would increase the robustness of BCG measurements in real settings, where the subject compliance and environmental conditions

may be non-ideal. For motion artifacts, the lower-body EMG was shown to be a viable estimate of BCG noise – this includes both motion due to high frequency involuntary twitches and slower swaying on the scale. In future implementations, as suggested by the preliminary results provided in Section 5.1.5, the lower-body EMG can be acquired directly from the footpad electrodes of some bathroom scales, resulting in an unobtrusive, self-contained BCG acquisition system capable of automatic motion artifact detection. Note that the performance of these electrodes for a variety of foot sizes and types would first need to be verified experimentally.

For floor vibrations, the seismic sensor provides substantial improvement in terms of signal quality with the use of an adaptive noise canceller. As a result, high fidelity BCG recording is possible in nearly all settings, including ambulances or other transport vehicles, provided that the vibrations are not so significant as to saturate the amplifier or cause a distorted version of the BCG forces to be coupled to the scale. Additionally, while in this work a geophone was used as the seismic sensor, in future work other sensors – such as accelerometers – could also be used with the same approach. The methods could also be applied to other BCG measurement modalities such as chair- or bed-based systems, where the seismic sensor could even be implanted into the structure of the measurement system itself.

6

Normal Standards for Resting BCG Recordings: Human Subjects Trials

The best of all medicines is resting and fasting.
– Benjamin Franklin

This chapter describes two human subjects trials of a large healthy population and a few subjects with cardiovascular diseases. For the first trial, multiple subjects were enrolled, and a single measurement was taken from each subject. The purposes of this first trial were as follows:

1. To compare features of the BCG measured on a weighing scale to features (from the existing literature) measured on bed- and table-based systems.
2. To determine whether the L-N waves of the BCG were diastolic or post-systolic components.
3. To correlate features of the BCG to subject demographics and echocardiogram parameters.

For the second trial, multiple measurements were taken serially from the same subject. The main purpose of this trial was to evaluate the repeatability of the measurements. In addition to these two trials, some preliminary data were recorded from subjects with various cardiovascular conditions, including heart failure.

6.1. Materials and Methods

6.1.1. Subject Population and Measurement Protocols

For the inter-subject analysis trial, the data were collected from 92 healthy subjects – all provided informed consent for participating in the Stanford IRB approved trial (Protocol No. 6503). The HBF-500 scale (Omron Healthcare Inc., Bannockburn, IL) was used such that both ECG and BCG signals could be obtained without the need for surface electrodes. Each subject was instructed to hold the handlebar electrodes firmly while standing still on the scale for one minute. The length of the recording was chosen to be high enough to be able to average a large number of beats, but not so high that the subject would have difficulty remaining still on the

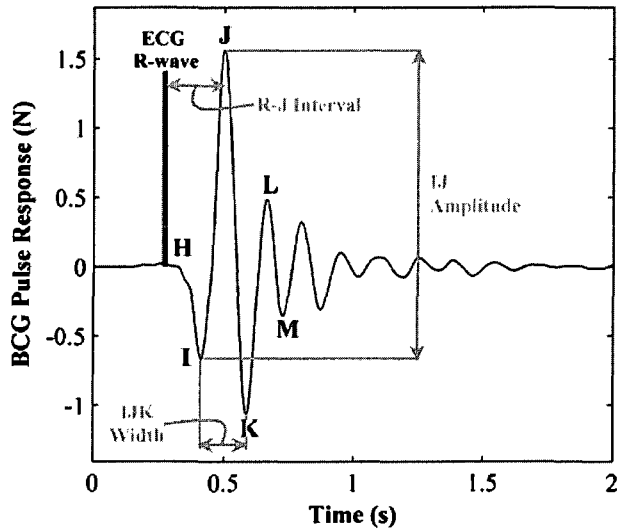


Figure 6.1 Modified ensemble averaged BCG beat with labeled features. The correlation analysis was performed for these time-domain features.

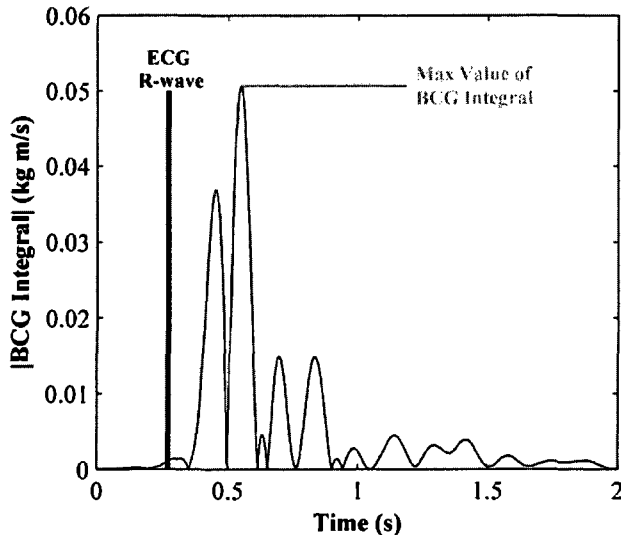


Figure 6.2 Rectified integral of the BCG pulse response; the magnitude of the momentum change. The maximum value of the integral is shown here, and was used in the correlation analysis.

scale. For 26 subjects, echocardiogram data were also available. These data were measured by Dr. Victor Froelicher's research group on the same day as the BCG trial and analyzed by Dr. Vy-Van Le (both from the Palo Alto VA).

For the intra-subject analysis trial, data were collected from two subjects: from the first subject, 50 recordings were taken randomly over a three week period (multi-day intra-subject variability trial); from the second subject, eight recordings were taken throughout a single day (single-day intra-subject variability trial). Both subjects provided informed consent for the IRB approved protocol (6503). Each recording was 30–45 seconds long to allow enough beats to be recorded for signal averaging. Note that for the multi-day intra-subject variability trial, for convenience, a photoplethysmograph (PPG) signal was used rather than the

ECG for triggered averaging. The PPG was measured using the analog output of a commercial pulse oximeter (N-200, Nellcor Corporation, Pleasanton, CA). This output was recorded simultaneously as the BCG on the same data acquisition card.

6.1.2. Time Domain Features

For all trials where simultaneous ECGs were recorded, the BCG and ECG signals from each subject were processed and ensemble averaged using the methods described in Section 4.3. Figure 6.1 shows an example modified ensemble averaged BCG pulse response for one subject, with labeled features. The pulse response represents the mechanical response of the vessels and body to a pulse of blood being ejected from the heart into the aorta, and was calculated using the methods described in Chapter 4. The J-wave was located as the maximum peak of the BCG response within a window of 150–400 ms following the ECG R-wave. The other waves were located by finding the successive local minima (or maxima) of the pulse response within 200 ms of the preceding wave. For example, if the K-wave was located at $t = 600$ ms, the L-wave was considered to be the local maximum of all points from $t = 600$ to 800 ms. Using this information, the wave amplitudes were then computed as shown in the figure (for the IJ amplitude). The RMS power of the BCG, computed over the pulse response, was included in the analysis. The rectified integral of the BCG pulse response, corresponding to the change in momentum, was also computed, and is shown in Figure 6.2. The maximum value of this BCG integral was another feature examined in the analysis. Finally, combined ECG-BCG features, such as the R-J interval, were also extracted and analyzed.

The PPG signal, used in the multi-day intra-subject variability trial, was digitally band-pass filtered (1.5–10 Hz) to reduce noise. A simple peak detection algorithm with a constant threshold – half the maximum amplitude of the PPG – was used to find the fiduciary points

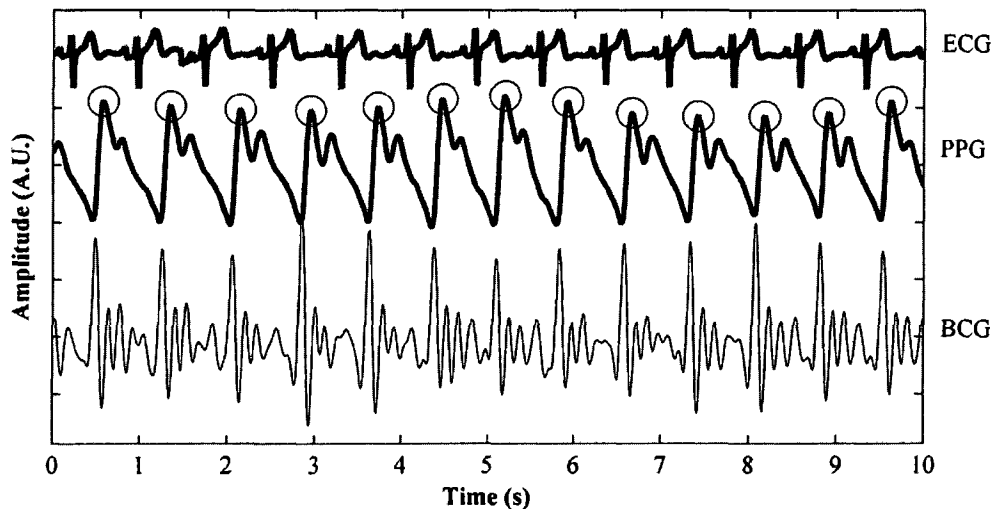


Figure 6.3 ECG, PPG, and BCG signals from a subject at rest. The PPG was used as the trigger for ensemble averaging the BCG in the multi-day intra-subject variability trial.

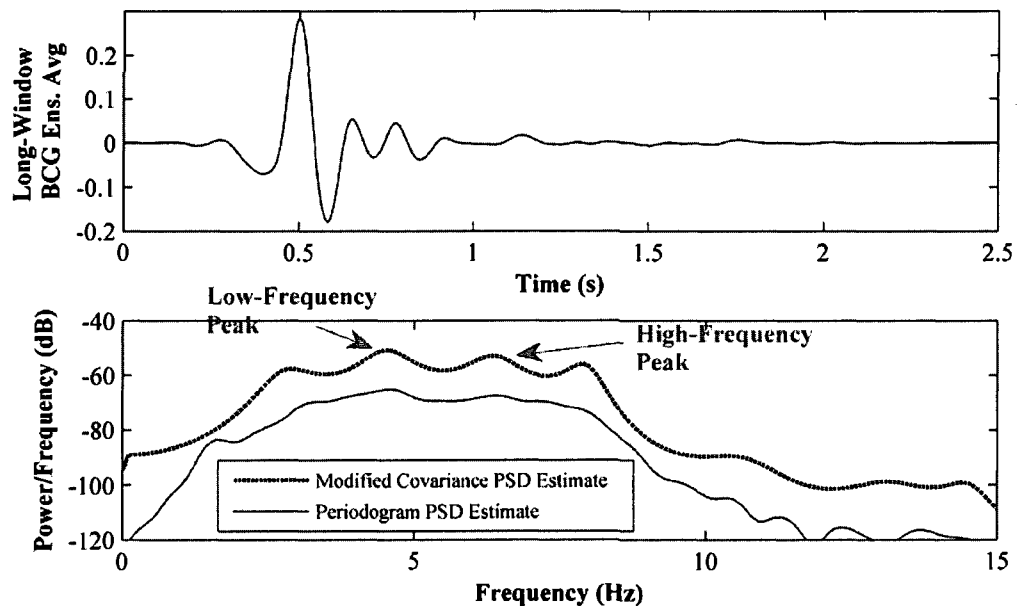


Figure 6.4 Top: BCG pulse response (computed as described in Chapter 4). Bottom: PSD estimates for the BCG signal computed using the periodogram method from the pulse response (solid black line) and the modified covariance method from the signal itself (dashed black line). The model order for the modified covariance estimate was set at 17 based on the Akaike information criterion (AIC) [5].

necessary for ensemble averaging the BCG signal. A sample recording of ECG, PPG and BCG signals from one subject at rest is shown in Figure 6.3. Using the peaks of the PPG, one ensemble averaged BCG waveform ($n = 30$ beats) for each of the 50 recordings was computed and used for feature extraction. Since an ECG waveform was not available, combined ECG-BCG features were not analyzed for the multi-day intra-subject variability trial. In the single-day intra-subject variability trial, the ECG signal was available, and blood pressure was also measured before each BCG recording.

6.1.3. Frequency Domain Feature Extraction

The power spectral densities (PSDs) of the BCG signals were computed using the modified covariance method, with a model order selected based on the Akaike information criterion (AIC) [5]. An example BCG PSD is shown in Figure 6.4 (bottom) alongside the PSD computed using the periodogram of the estimated pulse response. The maximum normalized cross-correlation between the two PSDs was found to be 0.98, and, in terms of practicality, the modified covariance estimate is faster to implement. Accordingly, it was used for calculating the frequency domain features of the BCG for all subjects. The two largest peaks in the BCG

PSD were found for each subject, as shown in Figure 6.4. The relative amplitudes of these peaks were also examined.

6.1.4. *The L-N Waves of the BCG – Dispelling the Afterwaves Ambiguity*

For the past 70 years, researchers have ambiguously referred to the L-N (or L-O) waves of the signal as ‘diastolic deflections’ [136, 137], ‘diastolic waves’ [62, 97, 138-141], the ‘diastolic part’ [142] or the ‘diastolic phase’ [4] of the BCG. In this work, a simple study was conducted showing that these ‘diastolic’ waves of the BCG are not associated with diastole. The approach was to show statistically that these waves do not *cause* the systolic waves of the BCG; they are *caused by* the systolic waves. Thus rather than naming them the ‘diastolic’ waves, a new nomenclature is suggested: ‘post-systolic’ waves.

In a healthy heart, the time interval between diastole and systole is relatively constant in resting conditions. On the other hand, the interval between successive heartbeats is known to fluctuate due to respiration (respiratory sinus arrhythmia) [57]. Accordingly, the time interval between one beat’s systole and the next beat’s diastole will also fluctuate due to respiration. These simple relationships were used to determine if parts of a signal are diastolic or post-systolic.

6.1.5. *Data Analysis*

Normal standards were established for the time and frequency domain features. The time domain features were compared to values from the existing literature (for table- and bed-based systems). Since the frequency domain analysis of the BCG in the literature is very limited, these findings could not be compared to table- and bed-based systems.

The L-N (or L-O) waves of the BCG were analyzed in depth to understand their relationship, if any, to diastole. First, for one subject, some visual comparisons were made to the ECG P- and T-waves, to determine if the BCG L-N waves were associated with diastole, or were post-systolic features. Then, for all subjects, the time intervals were statistically analyzed to quantitatively validate these visual observations.

Correlations between BCG, and combined ECG-BCG features, and subject demographics were established. For the subset of subjects with echocardiogram data, parameters extracted from the echocardiogram were also correlated to these features. Specifically, correlations to stroke volume (SV), left ventricular mass (LVM), and ejection fraction were investigated.

Table 6-1 Normal standards for subject demographics, time and frequency domain BCG features and combined ECG-BCG features (healthy subjects, n = 92).

	Feature	Mean	Standard Dev.	Min	Max
Subject Demographics	Height (cm)	174.0	9.14	157.5	200.7
	Weight (kg)	69.6	13.2	45.9	107.3
	Age (years)	18	-	18	21
	Syst. Blood Pressure (mmHg)	122	12	95	164
	Diast. Blood Pressure (mmHg)	73	10	54	94
	Heart Rate (bpm)	67	13	45	98
Echocardiogram Parameters (n = 26 subjects)	Stroke Volume (mL)	55	16	30	87
	Ejection Fraction (%)	60.1	6.0	50.0	76.5
	Left Ventricular Mass (g)	131.7	32.7	88.3	200.8
Time Domain BCG Features	RMS BCG (N_{RMS})	1.31	0.48	0.55	3.59
	IJ Amp. (N)	4.06	1.53	0.63	10.95
	JK Amp. (N)	5.09	1.90	1.27	13.25
	Max Value BCG Integral (g m/s)	92.2	33.0	22.8	240.1
	IJ Int. (ms)	94.7	21.2	42.0	174.0
	JK Int. (ms)	98.4	14.5	55.0	175.0
	IJK Width (ms)	252.4	23.2	205.0	339.0
Frequency Domain BCG Features	Low Freq. Peak (Hz)	4.08	0.79	2.1	6.3
	High Freq. Peak (Hz)	5.99	1.23	3.9	13.1
Combined ECG-BCG Feature	R-J Int. (ms)	244.9	18.8	203.0	290.0

For the multi-day intra-subject variability trial, the features taken over the multiple recordings were compared. The correlations between various BCG time intervals and heart rate were investigated. For the single-day intra-subject variability trial, the features were compared and the correlations between blood pressure and BCG features were investigated. For both intra-subject variability trials, all ensemble averages were plotted for visual comparison.

6.2. Results and Discussion

6.2.1. Normal Standards and Comparison to Previous Works

The normal standards for subject demographics, BCG time and frequency domain features, and combined ECG-BCG features are summarized in Table 6-1.

For BCG amplitude, Starr, *et al.*, provides data that can be used for comparison. With the calibration factor (28 g static force per mm) given for converting millimeters on the readout to force in Newtons, the mean ($\pm\sigma$) BCG IJ-amplitude found by Starr, *et al.*, was 3.7 N (± 0.53 N), for seven subjects [9]. In this work, using the modified weighing scale, the BCG IJ-amplitude was found to be 4.06 N (± 1.53 N), well within the expected range based on the Starr, *et al.* study.

For timing information, Deuchar, *et al.*, provides Q-I and Q-J interval data, which can be used to find the average I-J interval for healthy subjects: 70 ms (no standard deviation given) [143]. In this work, the corresponding interval was 94.7 ms (± 21.2 ms), slightly higher than

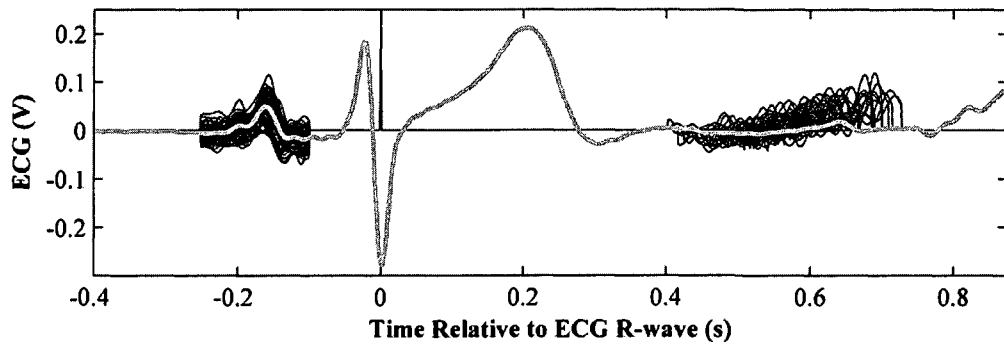


Figure 6.5 Relationship of the ECG P-waves to the R-wave for an array of beats taken from one recording of a healthy subject at rest. The segmented P-waves are overlaid onto the ensemble averaged ECG beat for the recording (shown in gray). The P-waves on the left side are well-correlated to the R-wave in time, but the waves on the right side are not. This demonstrates that the P-waves are a diastolic event, which is well-known.

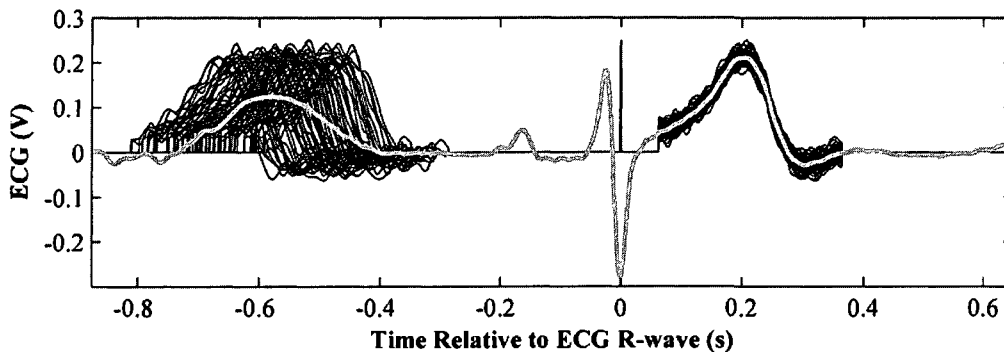


Figure 6.6 Relationship of the ECG T-waves to the R-wave for an array of beats taken from one recording of a healthy subject at rest. The segmented T-waves are overlaid onto the ensemble averaged ECG beat for the recording (shown in gray). The T-waves on the left side are well-correlated to the R-wave in time, but the waves on the right side are not. This demonstrates that the T-waves are a post-systolic event, which is well-known.

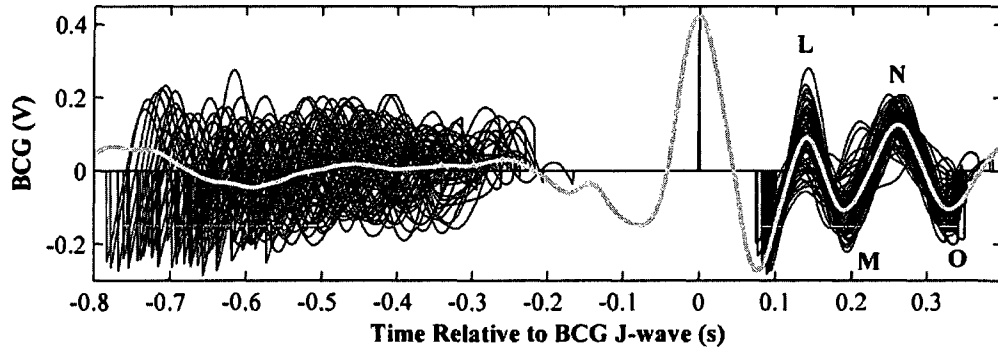


Figure 6.7 Illustrative results for one subject, demonstrating that the L-O waves of the BCG, similarly to the T-waves of the ECG, are well correlated to the right of the main systolic peak (J-wave) and uncorrelated to the left. The beats, which were aligned using the J-wave peak, are overlaid on the ensemble averaged BCG. This suggests that the waves are not related to diastole; rather, they are post-systolic events.

Deuchar's values. Tannenbaum, *et al.*, provides J-K interval data [144]: 90 ms (± 15 ms); in this work, this interval was 98.4 ms (± 14.5 ms), well within the expected range. The mean ($\pm \sigma$) R-J interval reported by Deuchar, *et al.*, for the Q-J interval was 210 ms (no standard deviation given) [143]. In this work, the interval was found to be 244.9 ms (± 18.8 ms).

6.2.2. *The L-N Waves of the BCG*

For the ECG, it is well known that the P-wave is associated with diastole and the T-wave is post-systolic. If several ECG beats from a recording are aligned using the R-wave peaks, with a window large enough to view more than one beat, the P-waves would be well correlated temporally on the left side of the R-wave, but uncorrelated on the right. Each R-wave is preceded by a P-wave, with a relatively consistent time interval in between. However, although each P-wave is preceded by the previous beat's R-wave, the timing interval in between varies with respiration. This is illustrated visually in Figure 6.5. On the other hand, the T-waves would be well correlated temporally on the right side of the R-wave, but not on the left side, since they always follow the R-wave, as shown in Figure 6.6.

This same basic analysis was performed on the BCG signal to determine visually if the L-O waves are diastolic, or post-systolic, components of the waveform. The BCG beats were segmented from the recording and aligned to the J-wave, which denotes peak systole. If the L-O waves were diastolic components, they would be aligned on the left side of the following J-wave; if aligned on the right, then they would be post-systolic.

The results are shown in Figure 6.7. Clearly, the L-O waves of the BCG are aligned to the right of the J-wave peak, indicating that they are post-systolic events unrelated to diastole. To

Table 6-2 Summary of correlation coefficients for all statistically significant ($p < 0.05$) correlations between BCG features and subject demographics.

	Max BCG Integral	IJ Amp	RMS BCG	Low Freq Peak Amp	JK Amp	KL Amp
Weight	0.46	0.34	0.37	-	-	-
Height	0.41	-	0.38	0.30	-	-
IJ Amplitude	0.86	-	0.41	-	0.88	0.58

Table 6-3 Summary of correlation coefficients for all statistically significant ($p < 0.05$) correlations between BCG features, combined ECG-BCG features, subject demographics, and echocardiogram parameters.

	Max BCG Integral	Low Freq Peak Amp	SV_{est}*	LVM_{est}*
Stroke Volume	-	-	0.60	-
Left Ventricular Mass	0.46	0.43	-	0.61

* Estimates using multiple linear regression, incorporating BCG features and subject demographics.

test this theory on a larger number of subjects ($N = 92$), the time interval between a J-wave and the preceding and following L-wave was computed for each beat from each subject in the trial ($n = 7949$ beats). The mean ($\pm\sigma$) were computed for both sets of time intervals and the results were as follows: the time interval from the J-wave to the preceding L-wave was 653 ms (± 204 ms), and the interval from the J-wave to the following L-wave was 181 (± 26 ms). The standard deviation expressed as a percentage of the mean was nearly 33% for the preceding intervals, and less than 15% for the following intervals. This data demonstrates that these waves could not be related to diastole, but are most likely post-systolic events – possibly mechanical resonances of the body-scale system or vasculature within the thorax.

6.2.3. Correlation Analysis (Subject Demographics)

The statistically significant correlations between BCG features and subject demographics are summarized in Table 6-2. The IJ amplitude and RMS power were also found to be significantly higher for men compared to women ($p \ll 0.001$). For female subjects, the mean ($\pm\sigma$) BCG IJ amplitude was 3.56 N (± 1.06 N), and for male subjects was 5.56 N (± 1.74 N); the corresponding values for RMS power were 1.17 N_{RMS} (± 0.33 N_{RMS}) for females and 1.74 N_{RMS} (± 0.60 N_{RMS}) for males.

6.2.4. Correlation Analysis (Echocardiogram Parameters)

The significant correlations between BCG, and combined ECG-BCG, features and echocardiogram parameters are summarized in Table 6-3. For stroke volume, no linear

Table 6-4 Summary of results from multi-day intra-subject variability trial (n = 50 recordings, one subject).

	HR (bpm)	RMS BCG (N _{RMS})	IJ Amp (N)	JK Amp (N)	Max BCG Integral (g m/s)	IJ Int (ms)	JK Int (ms)	IJK Width (ms)
Mean	88.1	0.72	2.70	3.00	108.2	102.7	88.6	273.9
σ	9.0	0.09	0.35	0.40	15.3	10.6	2.2	19.3
Min	68.9	0.57	2.06	2.17	82.3	89.0	84.0	239.0
Max	107.0	0.95	3.50	4.03	140.2	125.0	94.0	312.0
SE (%)	10.3	12.6	13.0	13.4	14.2	10.3	2.4	7.1

correlation was found. However, a multiple linear regression analysis showed that a linear combination of height, weight, and BCG features (IJ amplitude, IJK width, and R-J interval), was correlated to stroke volume ($R^2 = 0.60$, F-statistic p-value < 0.01). For LVM, similar results were obtained using a linear combination of height, weight, maximum value of the BCG integral, and R-J interval ($R^2 = 0.60$, F-statistic p-value < 0.01).

The latter finding could be extremely significant for large screening applications of athletes for cardiac hypertrophy – enlarged cardiac muscle. Currently, the primary argument against screening every athlete before allowing participation is cost. Echocardiography is certainly too expensive; the cost-effectiveness of the ECG is a subject of debate in the literature. ECG screening requires a professional to attach electrodes to the subject and record a full 12-lead reading. However, a combination ECG and BCG scale, such as the one described here, would certainly be cost-effective, if it were capable of correlating parameters of the signals to hypertrophy. Future work should investigate the possibilities of using this system for estimating left ventricular mass – the preliminary data is encouraging.

6.2.5. Multi-Day Intra-Subject Variability

The extracted features are summarized in Table 6-4. Standard error (SE) is also shown, defined here as the ratio of the standard deviation to the mean for each parameter. The only parameters with a significant ($p < 0.05$) correlation to heart rate were the I-J interval ($R^2 = 0.30$) and the maximum value of the BCG integral ($R^2 = 0.36$). After normalizing the I-J intervals for heart rate using the slope of the correlation line (0.64 ms bpm^{-1}), the standard deviation decreased from 10.6 ms (SE = 10.3%) to 8.9 ms (SE = 8.7%); similarly, by normalizing the maximum integral of the BCG for heart rate using the slope of the correlation line ($1.02 \text{ g m/s bpm}^{-1}$), the standard deviation decreased from 15.3 g m/s (SE = 14.2%) to 12.3 g m/s (SE = 11.3%).

The ensemble averages for all 50 recordings are shown in Figure 6.8 for visual comparison. These averages have not been normalized in amplitude, but were aligned in time using the peak of the BCG J-wave. Note that the variability from $t = 700$ ms to the end of the window is due to changes in heart rate – for some of the ensemble averages, the start of the next beat interferes with the average. If the ECG R-waves were available, these interfering beats could be

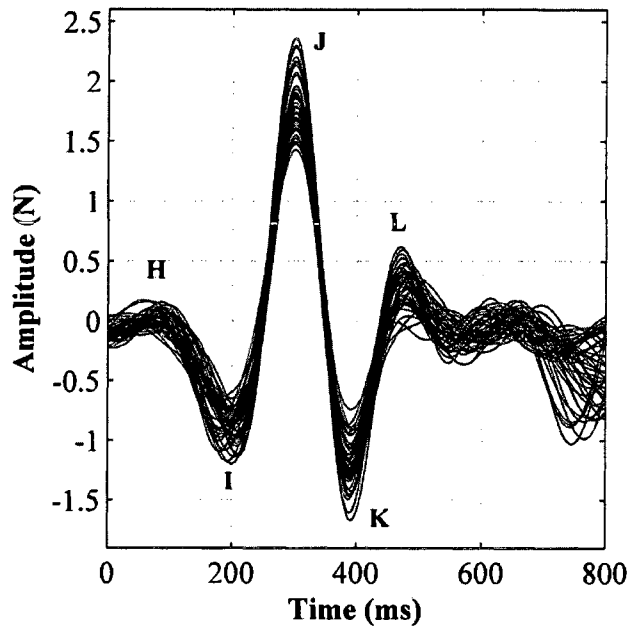


Figure 6.8 Ensemble averages for fifty recordings from the same subject taken at random times during the day for a three-week period. Amplitudes are not normalized, though the signals are aligned in time using the J-wave.

cancelled using the methods described in Chapter 4. However, for the PPG, the timing reference is not precise enough to allow this modified ensemble averaging to be successfully implemented.

6.2.6. Single-Day Intra-Subject Variability

The extracted features are summarized in Table 6-5. (Note that PP represents pulse pressure, the difference between systolic and diastolic blood pressure, in mmHg.) None of the

Table 6-5 Summary of results from single-day intra-subject variability trial ($n = 8$ recordings, one subject).

	HR (bpm)	PP (mmHg)	RMS BCG (N_{RMS})	IJ Amp (N)	JK Amp (N)	Max BCG Integral (g m/s)	IJ Int (ms)	JK Int (ms)	IJK Width (ms)	RJ Int (ms)
Mean	73.9	42.3	0.82	4.01	4.78	135.7	88.1	87.6	175.8	240.3
σ	2.4	4.6	0.054	0.58	0.48	14.9	2.8	1.6	3.5	10.9
Min	70.0	34.0	0.75	3.24	4.14	115.8	84.0	85.0	170.0	226.0
Max	76.5	48.0	0.90	4.76	5.31	156.9	92.0	90.0	182.0	256.0
SE (%)	3.2	10.8	6.6	14.4	10.1	11.0	3.2	1.8	2.0	4.5

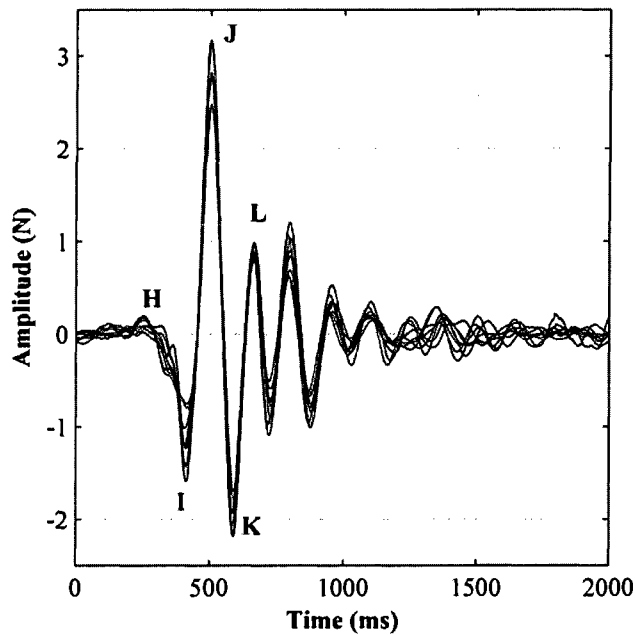


Figure 6.9 BCG pulse responses, estimated using methods described in Chapter 4, for eight recordings taken throughout the same day for one subject. The timing intervals and RMS power of the BCG signals showed minimal variability among the measurements.

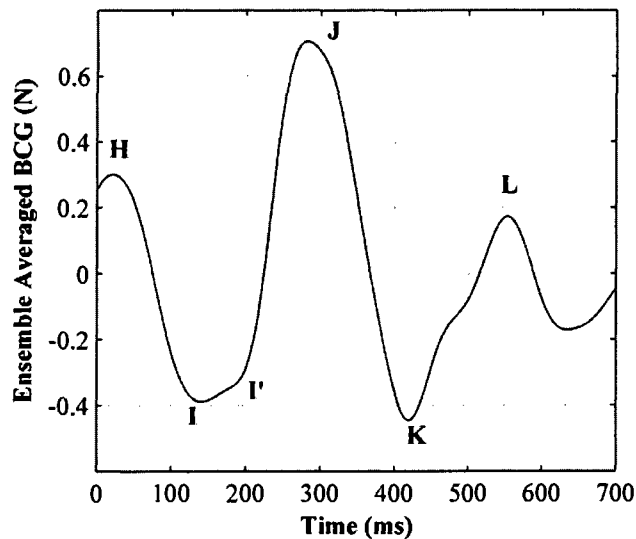


Figure 6.10 Ensemble averaged BCG from a subject with heart failure. The amplitude and RMS power of the BCG were significantly lower and the R-J interval was longer than for the normal population. Additionally, the beat has two I-waves, marked as *I* and *I'* in the figure.

BCG parameters were found to be correlated to blood pressure (systolic, diastolic, or pulse pressure). The standard errors for all parameters were relatively low, with IJ amplitude having the highest error: 14%. This was comparable to the variability in pulse pressure: 10.8%. The time intervals showed minimal variability among recordings, with the R-J interval having a standard error of less than 5%.

The RMS power of the BCG was also shown to have minimal standard error over all recordings: 6.6%. The modified ensemble averages for all eight recordings are shown in Figure 6.9. Here, since the ECG was available, the full BCG pulse responses were estimated, and the variability apparent in Figure 6.8 from 700–800 ms into the averages is substantially reduced. Again, the averages were not normalized in amplitude, but were aligned using the J-wave peak of the BCG.

6.3. Preliminary Data from Subjects with Cardiovascular Conditions

BCG recordings were taken at rest from three subjects with cardiovascular conditions, including heart failure, to provide some preliminary anecdotal data supporting the basic trends observed in the healthy population. Data from three subjects are analyzed and presented here. Figure 6.10 shows the ensemble averaged BCG from a subject

(Male, Age: 53, Height: 165.1 cm, Weight: 96 kg, Heart Rate: 77 bpm, normal blood pressure) with heart failure. Morphologically, the ensemble averaged signal looks abnormal – the I-wave is much wider than normal, and split into two valleys, and the J-wave peak is rounder. Quantitatively, the features related to BCG amplitude were much lower than normal. The IJ amplitude, 1.05 N, and the maximum value of the BCG integral, 41 g m/s, were both significantly lower than the average values for the normal population (4.06 N and 92.2 g m/s, respectively). The RMS power of the BCG, 0.31 N_{RMS} , was nearly half of the *minimum* value (0.55 N_{RMS}) measured for all healthy subjects in the trial. The R-J interval, 281 ms, was much higher than the average value for the normal population, 244.9 ms. These results suggest that this subject had significantly reduced contractility compared to the normal population.

Figure 6.11 shows the ensemble averaged BCG from another subject (Female, Age: 58, Height: 166.1 cm, Weight: 95 kg, Heart Rate: 98 bpm, Blood Pressure: 130/80 mmHg) with cardiomyopathy (deteriorated heart muscle), heart block and an implanted pacemaker. The IJ amplitude, 0.94 N, and maximum value of the BCG integral, 31.1 g m/s, were much lower than the average values for healthy subjects. The RMS power of the BCG, 0.26 N_{RMS} , was less than half of the minimum value measured for all healthy subjects. Surprisingly, the R-J interval (200 ms) was much lower than for the average population; however, the true

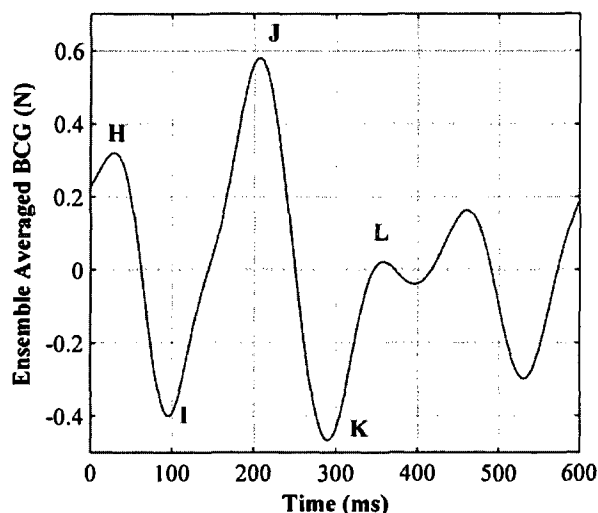


Figure 6.11 Ensemble averaged BCG beat from a subject with cardiomyopathy, heart block, and an implanted pacemaker. The amplitude and RMS power of the BCG were significantly lower than for the normal population, and the morphology of the beat was unusual.

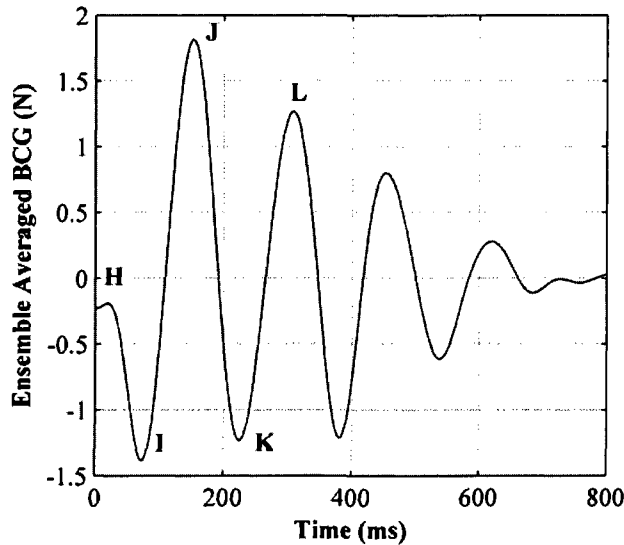


Figure 6.12 Ensemble averaged BCG taken from a subject with a 4.8 cm abdominal aortic aneurysm. The R-J interval and the IJK width are much shorter than the minimum values for all healthy subjects in the trials. Visually, the response seems to be much more resonant than the typical traces, suggesting that the mechanical properties of the vasculature may be related to the afterwaves of the signal.

definition of the R-J interval for *paced* beats may be quite different than for normal beats. The pacing pulse peak to J-wave peak interval was 308 ms, which is much longer than the R-J interval for normal subjects, consistent with a decreased contractile state of the heart.

Figure 6.12 shows an ensemble averaged BCG from a subject (Male, Age: 71, Height: 178 cm, Weight: 75 kg, Heart Rate: 64 bpm, Blood Pressure: 154/84 mmHg) with a 4.8 cm abdominal aortic

aneurysm. The amplitude features of the signal were normal for this subject. However, the timing features were not: the R-J interval, 152 ms, and the IJK width, 151 ms, were much lower than the minimum values for all subjects. Additionally, the BCG response seemed to be much more resonant than the typical traces, suggesting that the physical properties of the aorta may be related to the morphology of the BCG signal.

6.4. Conclusions

Normal standards were established at rest for healthy subjects for various time and frequency domain features of the BCG. For some of these features, results were available in the existing literature for comparison. The values found in this work were comparable to these previously reported results, demonstrating that, with an inexpensive and compact apparatus, high-fidelity BCG recordings can be obtained. Furthermore, since measuring the longitudinal signal from a standing or prone subject yields similar BCG results, this suggests that the effects of gravity on the BCG signal may be minimal. The intra-subject variability trials both confirmed that the measurements are repeatable, and that RMS power of the BCG and R-J interval are both features of the signal with minimal measurement error.

From the correlation analysis, the features of the BCG that are most relevant to absolute measurements were determined: IJ amplitude, IJK width, R-J interval, and the maximum value of the BCG integral. With these parameters, some relatively strong correlations were established to both stroke volume and LVM. The estimation of LVM from BCG parameters, in particular, is an exciting area for future investigation. The BCG is a measurement of contractile force, and it is not surprising that features of the signal would be correlated to the mass of ventricular muscle responsible for producing this force. One current and important medical problem is differentiating between physiological and pathological hypertrophy: it is possible that by supplementing the 12-lead ECG with a BCG measurement, a more specific diagnosis could be attained. Currently, the ECG measurements are used to estimate the LVM based on amplitude, since more muscle mass leads to a larger electrical signal measured at the surface. If the amplitude of the ECG was larger than the normal limit, but the integral of the BCG was smaller, this could indicate that the larger muscle mass was inefficient in its contractions due to the disarray of the myofibrils – this is the case for pathological hypertrophy.

Additionally, ensemble averaged BCGs were shown for three subjects with cardiovascular abnormalities. These preliminary data further suggested that the IJ amplitude, RMS power, maximum value of the integral, R-J interval and IJK width of the BCG contain useful hemodynamic information. Nevertheless, the strongest impact of the BCG on home monitoring will likely be in *trending*. The next chapter describes human subjects trials demonstrating that the BCG can accurately *trend* important cardiovascular parameters such as cardiac output.

7

Effects of Hemodynamic Changes on the BCG

When the music changes, so does the dance.
– African proverb

A central aim of this work is to provide an easy and effective home monitoring solution to patients with chronic cardiovascular diseases. For this goal, in addition to simple and robust instrumentation solutions, the ability of the system to automatically detect changes in the cardiovascular system is crucial – in particular, changes indicating worsening condition. In terms of hemodynamics, this translates to accurate estimation of changes in cardiac output or contractility.

To determine which features of the BCG signal would be most useful for tracking these cardiovascular parameters, the hemodynamics were modulated from rest using a variety of techniques, and the effects on the BCG were studied. The five most common drivers for hemodynamic changes are:

1. Pharmaceutical agents
2. Injury or shock
3. Arrhythmias
4. Maneuvers designed to test the cardiovascular system (e.g., Valsalva)
5. Exercise

Pharmaceutical interventions and the effects of injury or shock on the BCG were not investigated in this thesis due to the risks involved for healthy subjects; on the other hand, the effects of preexisting arrhythmias [92], the Valsalva maneuver [145], and exercise [11] were observed. The effects of arrhythmias, observed in only two subjects, provided preliminary data used to form hypotheses for two larger trials: one for testing the effects of the Valsalva maneuver, and a second for exercise recovery. For this second trial, the results were correlated to a gold standard clinical measurement (Doppler echocardiography), as discussed below.

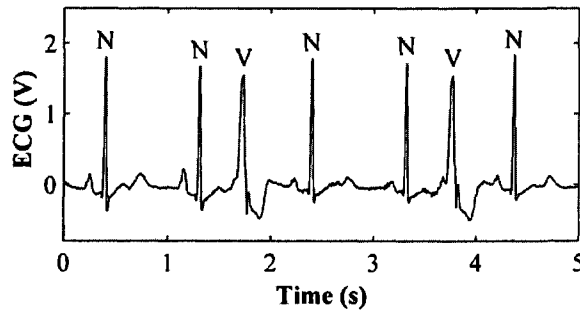


Figure 7.1 ECG recording showing normal ('N') and premature ventricular contraction ('V') beats.

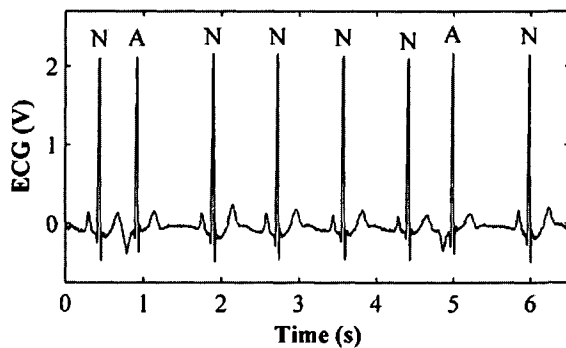


Figure 7.2 ECG recording showing normal ('N') and premature atrial contraction ('A') beats.

7.1. Effects of Arrhythmias on the BCG: Ectopic Beats

The effects of the two most common arrhythmias, premature ventricular contractions (PVCs) and premature atrial contractions (PACs), on the BCG are discussed in this section. These are two types of premature beats originating from ectopic foci in the ventricular or atrial chambers of the heart, respectively. To place these results in context, first the pathophysiology of these two arrhythmias, and their associated ECG waveforms, is discussed briefly below.

7.1.1. Pathophysiology of PVCs and PACs and the Associated ECG Waveforms

A group of myocytes that beats independently of the rhythm set by the sinoatrial (SA) node of the heart is referred to as an ectopic focus. The chamber of the heart housing this focus determines the type of ectopic beats exhibited by the heart: PVCs for ventricular foci and PACs for atrial foci [146].

In the ECG, PVCs manifest as wide QRS complexes occurring prematurely relative to the mean R-R interval for the trace, and without an associated P-wave. In addition, the amplitudes of the QRS complexes are usually larger than the surrounding normal beats. Frequently, a PVC beat is followed by a compensatory pause, although in some instances, where the PVC is 'interpolated,' it simply appears as an extra heartbeat in between two normal beats [146]. Figure 7.1 shows an example ECG trace with normal ('N') and PVC ('V') heartbeats. Note that these PVCs are not followed by a compensatory pause since they are interpolated.

PACs have prematurely occurring narrow QRS complexes and unusual P-wave morphology. The P-wave is distorted since the source of the atrial depolarization wave is the

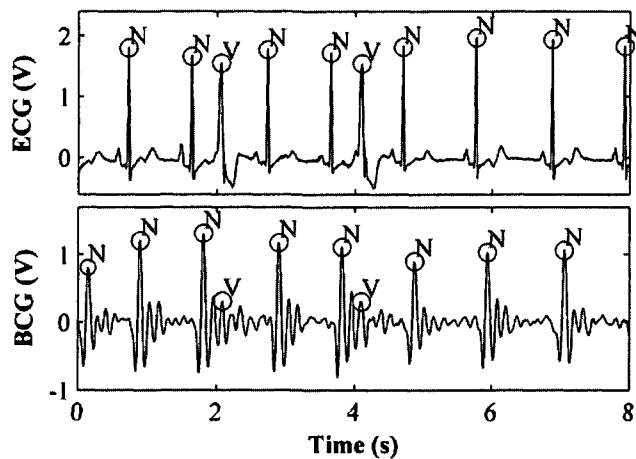


Figure 7.3 ECG and BCG recordings from a subject with PVCs. For both the ECG and BCG, the normal beats are annotated 'N' and the PVC beats 'V'. The BCG IJ amplitude of the PVC beats is lower than for the normal beats.

ectopic focus rather than the SA node. Usually, the SA node is depolarized by this premature beat, thus the PAC is followed by a compensatory pause. Figure 7.2 shows an example ECG recording, with normal ('N') and PAC ('A') beats. The SA node was depolarized in both of these PACs, thus both are followed by a compensatory pause.

The width of the QRS complex is indicative of the

depolarization mechanism of the ventricles: a healthy, effective, contraction results from the depolarization wave travelling rapidly down the Purkinje fibers, allowing a synchronized, powerful contraction of the ventricular myocytes. An ineffective contraction results when the depolarization is initiated independent of the Purkinje fibers, such as from an ectopic focus within the ventricle – the contractile efficiency of the ventricle is then compromised.

The volume of blood ejected by the ventricles in a PVC is significantly lower than for a normal beat for two reasons: first, since the contraction is premature, the ventricles will have less time to fill than normal (decreased preload); second, since the depolarization originates from an ectopic focus rather than the Purkinje fibers the strength of contraction will be relatively weak (transiently reduced contractility). For a PAC beat, the stroke volume can also be lower than normal, but depends only on the degree of prematurity since the ventricular muscles still contract in unison [10, 147].

7.1.2. *BCG Recordings from Subjects with Ectopic Beats*

Two subjects in the trials had premature beats: one (Age: 36) had PVCs and another (Age: 46) had PACs (Stanford IRB Protocol No. 6503). Figure 7.3 shows BCG and ECG traces for the subject with PVCs. As discussed earlier, the PVCs were diagnosed based on an early occurrence of a wide QRS complex without an associated P-wave. The BCG IJ-amplitude was much lower for these beats compared to the surrounding normal beats. Since this decreased amplitude was an incidental finding, with only two PVCs detected for all of the subjects

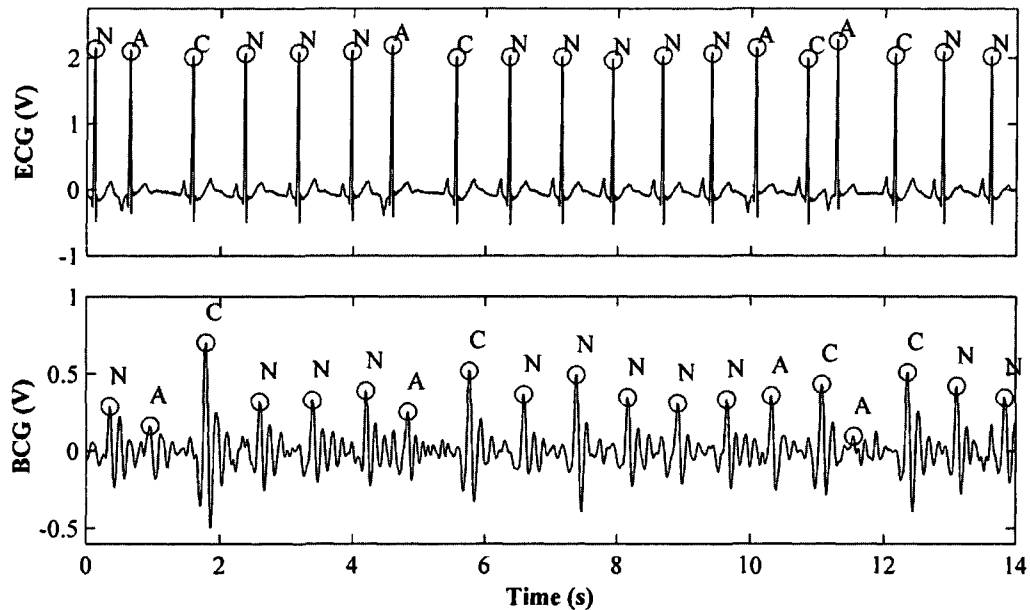


Figure 7.4 ECG and BC65G recordings from a subject with PACs. For both the ECG and BCG, the normal beats are annotated 'N', the PAC beats 'A', and the compensatory beat 'C'. The BCG J-amplitude of the PAC beats is lower than for the normal beats, and the amplitudes of the compensatory beats are higher.

studied, statistical significance was not determined. However, this preliminary data was used to form the hypothesis that BCG amplitude, or RMS power, could be related to cardiac output. Note that the beats following the premature events in this figure are not compensatory beats, since the PVCs did not depolarize the SA node.

Figure 7.4 shows ECG and BCG traces for the subject with PACs, diagnosed based on the early occurrence of morphologically unusual P-waves. For this analysis, 86 normal beats, 15 PAC beats, and 15 compensatory beats were used. These premature atrial impulses depolarized the SA node, resulting in a compensatory pause following the premature beat. Accordingly, the heartbeats in this figure are labeled normal ('N'), PAC ('A'), and compensatory ('C').

In Figure 7.5, the correlation between BCG amplitude (J-wave) and the preceding R-R interval for PAC beats is shown ($R^2 = 0.73$). This correlation is a direct result of the degree of prematurity affecting the diastolic time interval and preload. Similarly, it has been shown in the literature that, for ectopic beats, both stroke volume and pulse pressure are correlated to the R-R interval preceding the premature beat [10, 147].

It has also been shown that premature atrial beats of reduced output are followed by a compensatory pause, resulting in a heartbeat with increased output [148]. On the same plot

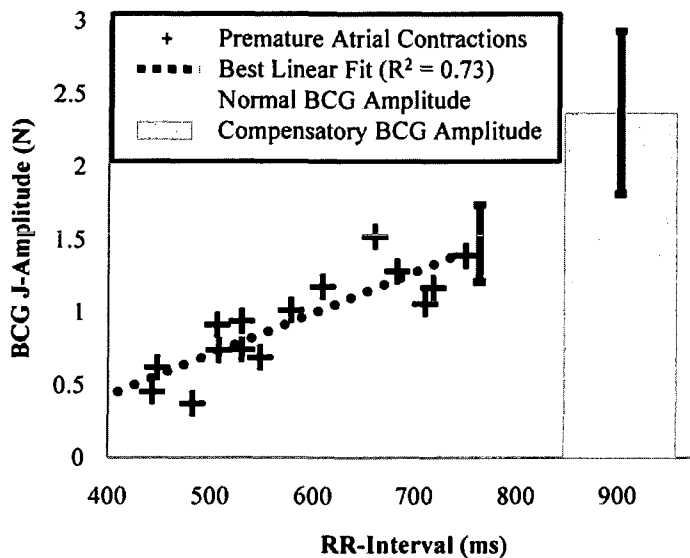


Figure 7.5 Correlation of BCG J-amplitude to the R-R interval preceding the premature beat, consistent with the literature: stroke volume was shown to be correlated with the preceding R-R interval due to the modulation of the diastolic time interval [10]. The bars show mean ($\pm\sigma$) normal and compensatory J-amplitudes; the x-location and width of the bars correspond to the mean ($\pm\sigma$) R-R intervals for these beats.

(Figure 7.5), the mean ($\pm\sigma$) BCG amplitudes (J-wave) for normal and compensatory beats are also given. The location and width of the bars for normal and compensatory beats indicate the mean ($\pm\sigma$) R-R intervals. The PAC amplitudes were significantly lower than for normal beats ($p \ll 0.001$) and the amplitudes of the compensatory beats following the PACs were significantly higher than for normal beats ($p \ll 0.001$).

7.2. Effects of the Valsalva Maneuver

7.2.1. Physiological Effects of the Valsalva Maneuver

The Valsalva maneuver involves a subject forcedly exhaling against a fixed pressure, or keeping the mouth and nose closed, for a period of time to transiently increase intrathoracic pressure [1]. This increase in pressure leads to a series of changes in heart rate, blood pressure, stroke volume, and cardiac contractility that have been studied extensively and are well documented in the existing literature [149-152].

It should be noted that there is no infallible method for standardizing the execution of the Valsalva maneuver. However, in this work, two parameters were used to establish some level of standardization: the duration of the strained period was set between 15 and 20 seconds, and each recording was inspected to ensure that the criterion for a normal Valsalva ratio was met. The Valsalva ratio is defined as the ratio of the longest to shortest R-R interval during the maneuver. Normally, this ratio should be greater than 1.5 [153]. The expected physiological effects for healthy subjects performing the maneuver are summarized below.

During the period of strain, venous return decreases as does cardiac output, resulting in a reflex increase in heart rate due to reduced parasympathetic drive. A simultaneous increase in sympathetic tone causes peripheral vasoconstriction and increased cardiac contractility to compensate for reduced output. When the strain is released by the subject, venous return suddenly increases, causing a transient overshoot in stroke volume and blood pressure. This overshoot is sensed by the baroreceptors, resulting in increased parasympathetic drive and reflex bradycardia for a few beats. The sympathetic tone is also reduced following release. However, since sympathetic changes are slower than parasympathetic, cardiac contractility remains elevated compared to rest for tens of seconds following release. Several researchers have studied hemodynamic changes induced by Valsalva using the echocardiogram, electrocardiogram (ECG), and impedance cardiogram.

For stroke volume, the results spanned a range of 24-52% increase after release compared to rest [149, 151]. The effects on contractility are more difficult to study directly. Consequently, the pre-ejection period (PEP) was proposed as an indirect measure of contractility since increased contractile state leads to a shortened isovolumetric contraction interval [154]. The PEP is defined as the time interval between electrical depolarization (ECG R-wave peak) and the opening of the aortic valve, which can be measured by echocardiography or impedance cardiography. For PEP, the reported results spanned a range of 20-30 ms decrease after Valsalva release compared to rest [150, 152].

7.2.2. *Expected Changes in the BCG Following Strain Release*

Previous work suggests that relative changes in BCG amplitude may be correlated to changes in stroke volume [80]. Additionally, since the peak of the BCG (J-wave) represents the greatest vertical force resulting from cardiac ejection, the time interval between the ECG R-wave and the BCG J-wave (R-J interval) will modulate with PEP changes. Subsequently, it is expected that following Valsalva release, (1) the BCG amplitude will increase significantly compared to rest, and (2) the R-J interval will decrease. The relative changes in these values should be consistent with the changes reported in literature for stroke volume and PEP.

7.2.3. *Study Details: Population and Procedure*

Fifteen healthy adults participated in this study (Stanford IRB Protocol 6503). The participants ranged from 55 to 143 kg in weight, 157 to 201 cm in height, and 20 to 35 years in age. After affixing ECG electrodes to each subject in a Lead II configuration, subjects were asked to stand still on the scale for 30 seconds for ECG and BCG recording. This was the averaging period for the resting segment. Next, subjects were instructed to perform a Valsalva

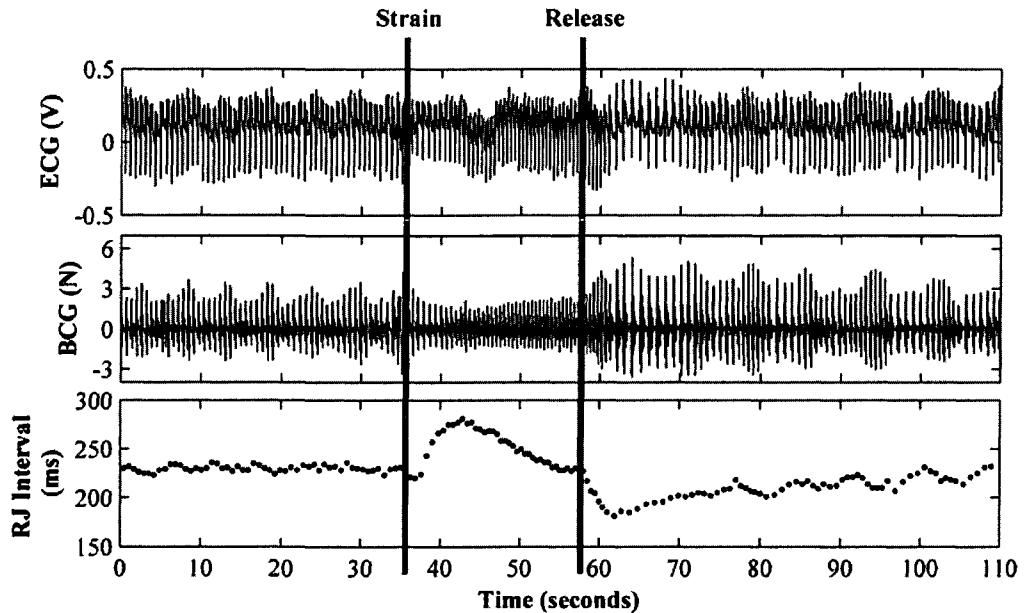


Figure 7.6 ECG and BCG time traces showing the response of one subject to the Valsalva maneuver. The BCG amplitude is reduced during the period of intrathoracic strain and then overshoots above the resting value after release. The time-series R-J interval plot is also shown and the response is remarkably similar to the expected pre-ejection period (PEP) responses reported in the literature. The Valsalva response suggests that changes in BCG amplitude are correlated to changes in stroke volume and that the R-J interval is modulated by changes in ventricular contractility.

maneuver for 15-20 seconds. Upon release, the subject remained still, and 15 seconds of data were averaged for post-release feature extraction.

7.2.4. *Digital Signal Processing and Feature Extraction*

The BCG and ECG signals were digitally band-pass filtered with passbands of 0.1 to 15 Hz and 2.5 to 40 Hz, respectively. A simple peak detection algorithm was used to find the R-wave and J-wave peaks, and the time elapsed between these peaks was computed as the R-J interval. For frequency analysis, the power spectra (estimated from the FFT) of the ensemble averaged BCG waveforms were computed. The area under the low frequency (0–5Hz) and high frequency (5–20 Hz) bands were calculated and the ratio of high to low frequency power before and after intrathoracic strain was compared.

7.2.5. *Example Results from One Subject: Time Traces and Ensemble Averages*

Example ECG and BCG traces for one subject are shown in Figure 7.6 to demonstrate the general trends observed from the subject population ($N = 15$ subjects). The time-series plot of the computed R-J interval is also provided. For this subject, a consistent BCG signal could be captured during the strain. The BCG amplitude increased and R-J interval decreased following

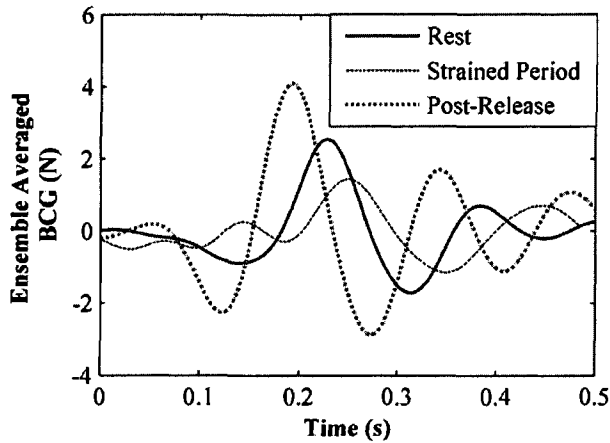


Figure 7.7 Ensemble averaged BCG waveforms from the resting, strained (Valsalva), and post-release periods of the traces shown in Figure 7.6. R-J interval increased during the strained segment and decreased after release when the sympathetic tone was elevated.

the release. The R-J interval time series was consistent with PEP results reported in a recent article. The ensemble averaged BCG waveforms for three segments (resting, strained (Valsalva), and post-release) of traces from this subject are shown in Figure 7.7. The increase in R-J interval during strain and subsequent decrease following release are shown, consistent with an increased inotropic state of the

ventricles.

Figure 7.8 shows the frequency response magnitude of the same three ensemble averages, also normalized to unity. The frequency content of the ensemble averaged BCG is shifted to higher frequencies for post-release than for the resting condition since the ventricular ejection force impulse is narrower. The ratio of high (> 5 Hz) to low (< 5 Hz) frequency power increase after release for this subject.

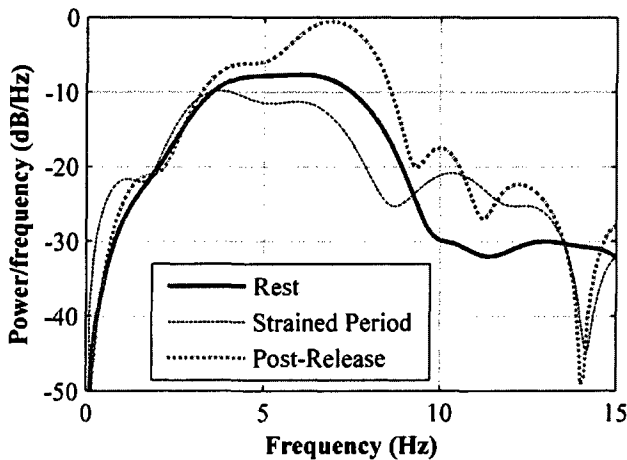


Figure 7.8 Periodogram-based power spectral density estimates for the ensemble averages shown in Figure 7.7. The high frequency content decreased during the period of strain when blood pressure decreased, and increased transiently following release when blood pressure was elevated.

7.2.6. Statistical Analysis for All Subjects

As expected, for many subjects the motion artifact in the strained period prevented reliable feature extraction. Consequently, the statistical analysis was limited to resting and post-release periods. The changes in the BCG amplitude, R-J interval, high frequency to low frequency power ratio, and heart rate for all subjects are

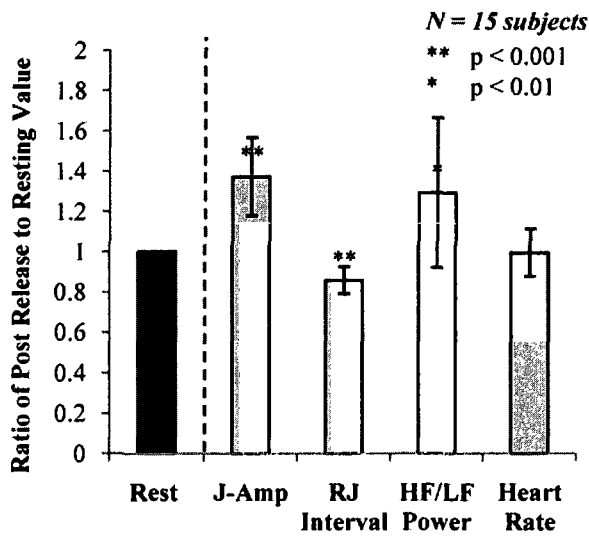


Figure 7.9 Ratio of post-release to resting values for all subjects (mean \pm standard deviation). A paired t-test was used to determine p-values (* indicates $p < 0.01$ and **, $p < 0.001$).

shown in Figure 7.9. Each parameter is normalized to the corresponding resting value, as indicated visually by the unity amplitude rest bar.

A paired t-test was used to determine statistical significance, and all parameters changed significantly after release compared to the resting values ($p < 0.01$) except heart rate. Note that heart rate did transiently decrease after release for a few beats but, when averaged over 15

seconds, there was no significant change from rest. Consequently, the other results (amplitude, R-J interval, and frequency response) were not simply a result of changing cardiac cycle length. For example, R-J interval changes did not correlate to R-R interval changes ($R^2 = 0.005$).

The BCG amplitude increased by an average ($\pm\sigma$) of 37% ($\pm 19\%$) for all subjects following release of strain. This range was consistent with the existing literature for Valsalva-induced stroke volume changes [149, 151]. The R-J interval decreased by 34 ms (± 17 ms), consistent with the ranges reported for PEP [150, 152]. The high frequency to low frequency power ratio increased by 29% ($\pm 37\%$). The R-J interval was the parameter with the least variance and most significant change for the paired tests ($p \ll 0.001$). To evaluate the beat-by-beat significance of this parameter, a Student's t-test was implemented comparing R-J intervals from all post-release BCG beats ($n = 236$ beats) to the intervals from resting beat ($n = 409$ beats): this difference was also highly significant ($p \ll 0.001$).

7.3. BCG Measurements during Exercise Recovery

The idea of estimating cardiac output from the BCG signal dates back to Starr, *et al.* in 1939 [9], and was further developed by several other researchers in the 1930s and 1940s [155, 156]. While the results of these studies were encouraging, the correlations were only

established at rest. Additionally, the systems used for BCG measurement were cumbersome, elaborate tables or beds requiring regular mechanical maintenance and an expert operator.

This section addresses the question, “Can cardiac output be accurately trended on a modified weighing scale using the BCG?” Specifically, the hypothesis was that changes in the root-mean-square (RMS) power of the BCG were correlated to changes in cardiac output. This hypothesis was tested by modulating cardiac output and using Doppler echocardiography measurements as the gold standard for comparison.

Exercise was chosen as the means for modulating cardiac output for three main reasons. First, exercise causes dramatic variations in cardiac output (up to 400% increases for healthy adults), allowing for a wide range of measurements using the new technique to be compared against the gold standard. Second, the risks of exercise are minimal compared to pharmaceutical options for cardiac output modulation. Finally, several studies have used exercise for modulating cardiac output in testing the performance of a new measurement method against a gold standard, allowing for fair comparisons to be made between this work and others from the literature. Such a comparison is provided in Table 7-1, which is limited to studies using healthy subjects only.

The method proposed in this work is less obtrusive and expensive than all of the other methods shown in Table 7-1, and is the only method that does not require a medical professional to perform the measurement. Nonetheless, three limitations of the BCG approach that are not captured by this table should be noted: first, the measurements cannot be taken *during* exercise; second, during longer recordings, postural shifting by the subject on the scale may lead to errors; and, third, the cardiac output measurements are relative rather than absolute. The first limitation is not shared by any of the other methods in Table 7-1. However, the second limitation can lead to significant errors in impedance cardiogram measurements, and must be controlled for optimal results. The latter limitation is also suffered by continuous blood pressure measurements since a calibration step is needed to acquire accurate absolute cardiac output measurements from the recordings.

In many instances, this third limitation is not a major obstacle – the absolute value of cardiac output may be less important than relative changes over time after a baseline measurement has been taken. For example, in monitoring heart failure patients at home, *changes* in cardiac output over time could direct therapeutic decisions, such as diuretic dosage, and signal the need for a follow-up clinical visit. Note that this particular application would

Table 7-1 Comparison of several studies on non-invasive cardiac output measurement for exercise and exercise recovery (healthy subjects)

Author (Year)	Method	“Gold” Standard	Number of Subjects	Number of Data Points	Correlation Coefficient (R ²)
<i>This Work [11]</i>	<i>Ballistocardiography</i>	<i>Doppler Echocardiography</i>	9	275	0.85
Houtman (1999) [17]	Continuous Blood Pressure	Gas Rebreathing	12	24	0.46
Sugawara (2003) [18]	Continuous Blood Pressure	Doppler Echocardiography	16	640	0.76
Antonutto (1995) [19]	Continuous Blood Pressure	Doppler Echocardiography	9	27	0.77
Christie (1987) [20]	Doppler Echocardiography	Fick (direct)	10	42	0.66
Wilmore (1982) [21]	Gas Rebreathing	Thermodilution	6	12	0.76
Liu (1997) [22]	Gas Rebreathing	Fick (direct)	9	37	0.77
Johnson (2000) [23]	Gas Rebreathing	Fick (direct)	6	96	0.90
Zhang (1986) [24]	Impedance Cardiography	Gas Rebreathing	10	78	0.91
Miyamoto (1981) [25]	Impedance Cardiography	Gas Rebreathing	6	19	0.83
Moore (1992) [26]	Impedance Cardiography	Gas Rebreathing	11	44	0.76
Hatcher (1986) [27]	Impedance Cardiography	Gas Rebreathing	60	230	0.56
Tordi (2004) [28]	Impedance Cardiography	Gas Rebreathing	8	40	0.82
Richard (2001) [29]	Impedance Cardiography	Fick (direct)	12	50	0.88

require an inexpensive and unobtrusive measurement method to be truly effective, further justifying the use of the BCG.

Of the previously reported methods shown in Table 7-1, the transthoracic impedance cardiogram (ICG) measurements have achieved the best statistical results based on number of subjects, data points, and correlation coefficients [24-29]. Notably, Zhang, *et al.* reported a correlation coefficient of 0.91 for 78 data points from 10 subjects exercising [24]. Unfortunately, Zhang, *et al.* do not address the agreement between the methods which is arguably more important than correlation itself [157]. The agreement between bathroom-scale-BCG and Doppler echocardiogram based cardiac output trending is computed in this section and compared to other works in the literature.

The statistical results of this work are superior to the two studies shown in Table 7-1 where Doppler echocardiography was used as the “gold” standard. It should be noted that all non-

Table 7-2 Characteristics and hemodynamic parameters for all subjects

Subject	Age	Ht (cm)	Wt (kg)	SBP (mmHg)	DBP (mmHg)	HR _{rest} (bpm)	SV _{rest} (mL)	CO _{rest} (L/min)
1-Fem	25	167	53.5	113	69	68	47	3.2
2-Fem	46	173	63.5	110	82	82	33	2.7
3-Fem	23	157	65.5	112	77	65	40	2.6
4-Male	24	163	63.5	120	77	85	46	3.9
5-Male	46	177	71	134	89	71	41	2.9
6-Male	31	179	95	146	95	84	47	4
7-Male	49	186	100	125	85	78	60	4.7
8-Male	21	165	54.5	121	76	63	44	2.8
9-Male	26	201	143	140	85	122	28	3.4
5-Male†	46	177	71	139	81	71	54	3.8
Mean	34	175	78	126	82	79	44	3.4
Stdev	12	13	28	13	7	17	9	0.7

† 2nd trial for same subject as “5-Male,” performed on a separate day.

invasive cardiac output measurements, including Doppler echocardiography, are susceptible to errors compared to invasive measurements such as thermodilution or Fick’s method. Doppler echocardiography was chosen in this work since it is used widely in clinical settings and it has been shown to have good agreement and correlation with thermodilution for both healthy and critically ill subjects [158-161]. Nevertheless, the errors inherent to the measurement should certainly be considered when interpreting the results of this work.

The results of this paper are comparable in terms of correlation and statistical power to all of the other studies to date in non-invasively trending cardiac output changes from subjects after exercise. Additionally, the proposed method has distinct practical advantages over any of the non-invasive alternatives: the measurement procedure is simple and unobtrusive, with nothing attached to the body or face, and the apparatus is compact and inexpensive.

7.3.1. Study Details: Subject Population

Nine healthy adults (six males, three females) participated in the study approved by the Stanford IRB (Protocol No. 6503). Their physical characteristics, age, height (*Ht*), and weight (*Wt*), as well as resting hemodynamic parameters, systolic (*SBP*) and diastolic (*DBP*) blood pressure, heart rate (*HR_{rest}*), stroke volume (*SV_{rest}*), and cardiac output (*CO_{rest}*) are shown in Table 7-2. The stroke volume and cardiac output were measured using Doppler echocardiography, as described below. Participants spanning a large range of ages (21-49

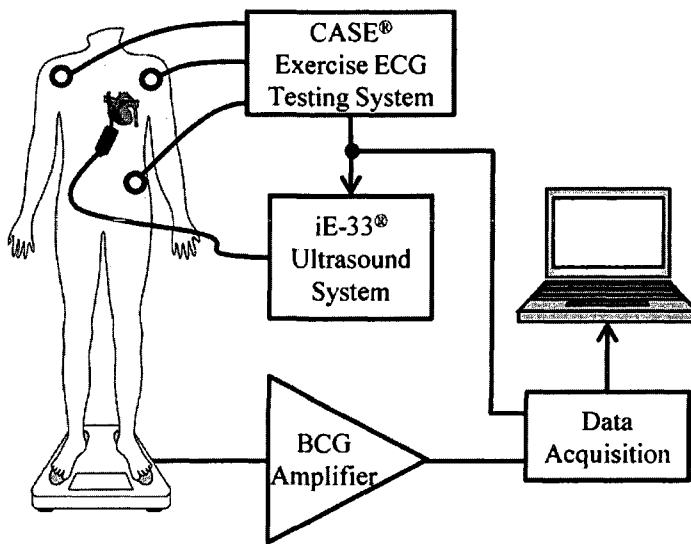


Figure 7.10 Block diagram depiction of measurement setup. The iE-33® Ultrasound System (Philips Healthcare, Andover, MA) was used to acquire Doppler ultrasound, and the CASE® Exercise ECG Testing System (GE Healthcare, Chalfont St. Giles, United Kingdom) was used to acquire the ECG.

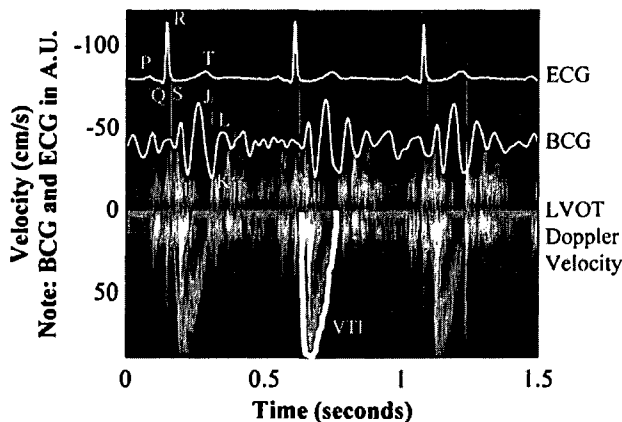


Figure 7.11 Image of sample ECG, BCG and Doppler ultrasound recordings taken from a subject at rest. Note that the ECG and BCG signals have been digitally band-pass filtered for this image, as described in the text. The P-T waves of the ECG and the I-L waves of the BCG are annotated. The velocity time integral (VTI) of the Doppler trace is used to calculate stroke volume.

years), weights (53.5-143 kg), and heights (157-201 cm) were selected. One subject, 5-Male in Table 7-2, had some premature atrial contractions (PACs) during the first trial and, as a result, volunteered to participate in a follow-up test. Other than these benign arrhythmias, the subject was in excellent cardiovascular health and, as a result, was not excluded from the study. The arrhythmic beats, however, were excluded from the analysis.

7.3.2. Materials and Methods

All tests were conducted at the Stanford Echocardiography Lab, part of Stanford Hospitals and Clinics. A standard patient room was used, equipped with a CASE® ECG Exercise Testing System (GE Healthcare, Chalfont St. Giles, United Kingdom), an iE-33® Ultrasound System (Philips

Healthcare, Andover, MA), and the modified InnerScan BC-534 bathroom scale (Tanita Corporation, Tokyo, Japan) and associated amplifier.

Figure 7.10 shows the measurement setup in block diagram form. The ECG was recorded in a Lead II configuration and the Doppler transducer was aimed at the left ventricular outflow tract (LVOT) of the heart. The iE-33[®] was configured in a Pulsed-wave mode at 1.6 MHz, with 70% of maximum power. The ECG and BCG signals were sampled at 1 kHz using a 12-bit data acquisition card (6024E, National Instruments, Austin, TX), then stored on a laptop computer using software (Matlab[®] Version 2007b, The Mathworks, Natick, MA). In addition, the sonographer stored the Doppler data on the iE-33[®] system. A time stamp was used to later synchronize the recorded BCG and ECG with the Doppler data. The three signals acquired simultaneously from one subject at rest are shown in Figure 7.11.

Two recordings were taken for each subject: one “rest recording” before exercise, and one “recovery recording” which started immediately after the subject completed exercise and was able to stand on the scale. The rest recording lasted thirty seconds. Then, each subject was asked to exercise on the treadmill using the Bruce protocol for 15 minutes [162]. Immediately after exercise, the subject stood still on the bathroom scale for 10 minutes while all signals were again simultaneously acquired.

Changes in cardiac output due to exercise, compared to rest, were obtained from the Doppler recordings. Changes in BCG RMS power were extracted from the BCG recordings. These changes were compared in terms of the correlation coefficient and agreement (Bland-Altman) for all subjects individually, and the group as a whole.

7.3.3. *Measuring Changes in Cardiac Output from Doppler Recordings*

For the Doppler echocardiogram measurements, the transducer was aimed by a professional sonographer (A. Paloma) at the left ventricular outflow tract (LVOT) of the heart. The sonographer was careful when positioning the probe to avoid applying force to the body and interfering with the BCG measurement.

To estimate cardiac output from the Doppler echocardiogram, first the diameter of the LVOT, D_{LVOT} , in centimeters, was estimated from the ultrasound image, and the LVOT area, A_{LVOT} , in square centimeters, was calculated:

$$A_{LVOT} = \pi \left(D_{LVOT} / 2 \right)^2 \quad (7.1)$$

The Doppler velocity curve for one beat was then traced and the velocity-time-integral, VTI , in centimeters, was calculated using the Xcelera software (Philips Healthcare, Andover, MA). The stroke volume, SV , in milliliters, was then computed using the following equation:

$$SV = VTI \times A_{LVOT} \quad (7.2)$$

Finally, the cardiac output, CO , in $L \min^{-1}$, was computed using the average R-R intervals from the ECG recordings, expressed in seconds, for the five beats surrounding the beat:

$$CO = SV \times \frac{60}{\sum_{n=-2}^2 RR_n(\text{seconds})} \quad (7.3)$$

where n is the index of the beat, with $n = 0$ indicating the beat of interest, and RR_n is the R-R interval between the n^{th} and the $(n-1)^{\text{th}}$ beats.

For the resting recording, an average beat was located within the ECG recording and used for the cardiac output measurement. For the recovery recordings, since many of the beats were corrupted by motion and respiration noise, only the beats determined to be usable by the professional sonographer were considered. This resulted in a total of 275 beats considered for all of the subjects. Percent changes in cardiac output compared to rest, $\Delta CO_i(\%)$, for each i^{th} beat, were calculated as follows:

$$\Delta CO_i(\%) = \left(\frac{CO_i - CO_{rest}}{CO_{rest}} \right) \times 100\% \quad (7.4)$$

where CO_{rest} was the cardiac output calculated at rest, and CO_i was the cardiac output calculated for each i^{th} beat.

7.3.4. *Measuring Changes in RMS Power from BCG Recordings*

The BCG signal was digitally low-pass filtered (FIR filter, Kaiser window, $N = 1000$, with a cutoff frequency of 15 Hz). After filtering, the BCG signal was downsampled by a factor of 10 to a sample rate of 100 Hz. For the resting measurements, the RMS power of the BCG was calculated using the entire recording, and is denoted $BCG_{RMS,rest}$ in the equations below.

For the exercise recovery measurements, the moving root-mean-square (RMS) power of the signal was calculated for each k^{th} sample using a sliding window of width 10 seconds. This window width was not the same as the width used for the resting data (30 seconds) for the following reason. For the resting data, the objective was to cancel any time-varying components, such that the best estimate of resting cardiac output could be obtained – hence the use of the entire 30 second recording. On the other hand, for the exercise recovery data, the objective was to precisely quantify time-varying components – hence the use of the shorter window of 10 seconds. Nevertheless, the choice of exercise recovery window width was not found to significantly influence the results.

The moving RMS power was calculated as follows:

$$BCG_{rms}[k] = \sqrt{\frac{1}{A} \sum_{i=0}^{A-1} BCG[k+i]^2}, \quad k = 1, \dots, N_{sample} - A \quad (7.5)$$

In this equation, A is the width of the sliding window in samples, and $BCG_{RMS}[k]$ is the moving RMS power of the BCG signal calculated at sample k . This moving average filter was implemented as follows: the signal was squared, then moving average filtered (FIR filter, rectangular window, $A = 1000$), and, finally, the square root of the moving average filter output was computed.

Percent changes in this moving RMS power, $\Delta BCG(\%)$, were calculated at a given point in time compared to the baseline value, taken at rest, as follows:

$$\Delta BCG(\%)[k] = \left(\frac{BCG_{rms}[k] - BCG_{rms,rest}}{BCG_{rms,rest}} \right) \times 100\% \quad (7.6)$$

7.3.5. *Data Analysis*

The following analysis was done first for each subject individually, then for the aggregate data from all subjects. The percent changes in cardiac output were plotted against percent changes in RMS power of the BCG, and the correlation coefficient was computed. A Student's t-test was applied to the data with a null hypothesis of no linear relationship between the two variables. The best least-squares regression line was fitted to the data, and the

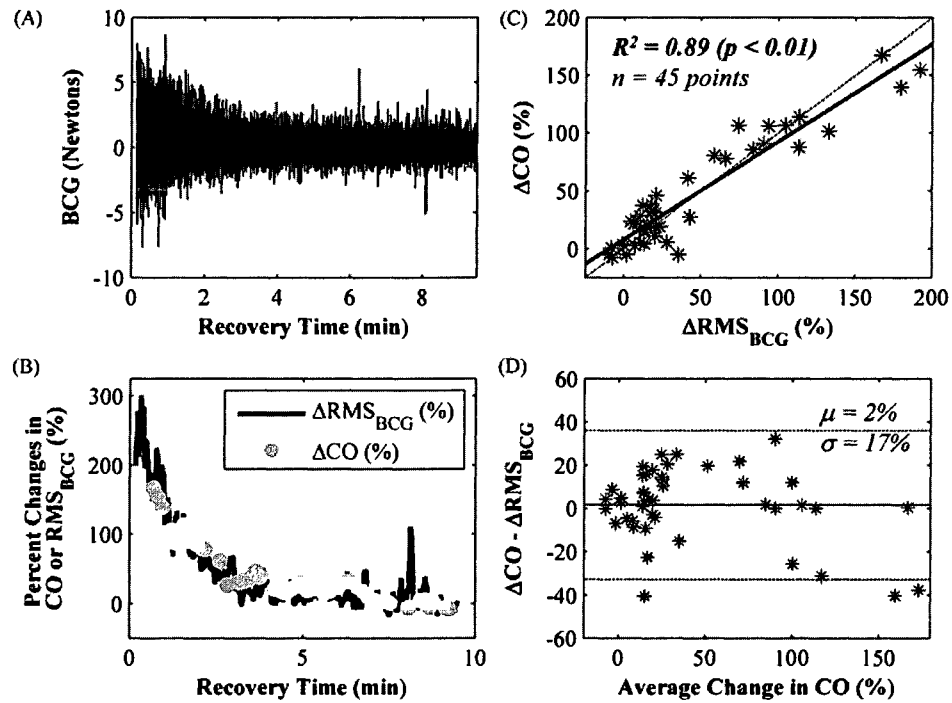


Figure 7.12 Demonstrative exercise recovery results from one subject. (A) Raw BCG waveform during recovery. The spikes in the waveform were caused by sudden movements of the subject on the scale. (B) Percentage change in RMS power (moving averaged over a ten second window) of the BCG waveform and cardiac output measured using Doppler echocardiography. (C) Correlation plot showing percentage change in cardiac output versus RMS power of the BCG. The correlation was high ($R^2 = 0.89$) and the null hypothesis of zero slope was rejected ($p < 0.01$). The slope of the regression line was 0.84 and the intercept was 8.1%. The equal value line (dashed line with unity slope) is also shown. (D) Bland-Altman plot showing agreement between the two methods. The mean difference was 2% with a standard deviation of 17%.

standardized residuals were computed. A Kolmogorov-Smirnov goodness-of-fit test was used to assess the normality of the standardized residuals. The result of this test was used to determine whether a linear fit was appropriate. The slope of the regression line was compared to unity to determine the agreement. Perfect agreement would result in a unity slope such that percent changes in RMS power of the BCG could be used to estimate percent changes in cardiac output directly. To further assess the agreement, methods described by Bland and Altman were applied to the data before and after calibration of the entire data set using the regression line slope [157].

As discussed below, the slope of the regression line correlating percent changes in RMS BCG to percent changes in cardiac output was not unity for the aggregate analysis, and was different from person to person. To determine if the slope of each subject's individually

analyzed data was related to subject characteristics, a multiple linear regression analysis was performed. The results from this analysis could be used in the future to calibrate each subject's data using basic characteristics without the need for a reference measurement such as Doppler ultrasound. Height, weight, age, blood pressure (systolic and diastolic), and resting heart rate were considered the independent variables and slope of the regression line was the dependent variable. The best least-squares linear combination of these independent variables mapping them to regression line slope was found, and the coefficient of multiple determination was computed.

7.3.6. *Results*

Figure 7.12 shows results from one subject recovering from exercise to illustrate general trends observed over the data set. Figure 7.12 (A) shows the raw BCG signal as a function of recovery time in minutes. The blank segment at the beginning of the trace represents the time during which the subject moved from the treadmill to the bathroom scale. During the recovery, there were instances when the subject moved unintentionally or shifted to be more comfortable. These instances resulted in the spikes that are apparently higher than the envelope of the decaying BCG amplitude. Data taken during these spikes were manually noted during the acquisition and removed from the analysis.

Figure 7.12 (B) shows the percentage change in the RMS power of the BCG signal on the same plot as the change in cardiac output measured by Doppler echocardiography. Figure 7.12 (C) is a correlation plot ($R^2 = 0.89$) showing the percentage change in cardiac output versus RMS power of the BCG. The null hypothesis of no linear relationship was rejected ($p < 0.01$). The regression line had a slope of 0.84 and intercept of 8.1%. Figure 7.12 (D) is a Bland-Altman plot showing the agreement of the two methods. The mean difference was 2% with a standard deviation of 17%.

Table 7-3 shows the correlation coefficient, slope, intercept, and standard deviation difference for the individually analyzed data from all subjects. The worst case and best case for each column are also noted based on the highest value being best for R^2 , lowest values best for intercept and standard deviation difference, and value closest to unity being best for slope. The standard deviation of the difference was calculated using calibrated data (with a scaling factor equal to the slope of the aggregate regression line, 0.67). The worst case in terms of correlation coefficient was the 201 cm tall, 143 kg male subject, and in terms of slope and intercept was the 186 cm tall, 100 kg male subject.

Table 7-3 Correlation coefficient, slope, intercept, and standard deviation difference data for individually analyzed data from all subjects (sorted by R^2)

Subject	Age	Wt (kg)	R^2	Slope	Interc. (%)	Stdev. Diff.‡ (%)
3-Fem	23	65.5	<u>0.96</u>	0.76	-27.2	22
6-Male	31	95	0.94	1.35	-20.5	26.7*
8-Male	21	54.5	0.9	0.69	-17.5	15.5
2-Fem	46	63.5	0.89	0.67	23.7	22.6
5-Male†	46	71	0.89	0.84	8.1	17.7
1-Fem	25	53.5	0.87	0.67	11.5	14.4
7-Male	49	100	0.86	0.62*	52.0*	<u>13.6</u>
4-Male	24	63.5	0.85	<u>0.98</u>	<u>4.6</u>	20
5-Male	46	71	0.82	0.93	-13.9	23.4
9-Male	26	143	0.79*	0.91	-10.7	20
Mean	34	78	0.88	0.84	1.01	19.6
Stdev	12	28	0.05	0.22	24.15	4.3

† 2nd trial for same subject as “5-Male”

‡ Standard deviation of $(\Delta RMS_{BCG} * 0.67 - \Delta CO)$

* Worst case

Best case

Figure 7.13 (A) shows the aggregate correlation for all subjects between percent changes in cardiac output measured by Doppler echocardiography and percent changes in the RMS power of the BCG signal. The total number of data points was 275 from 10 trials using 9 subjects. The line of equal value (dashed black line) is also plotted for comparison. The null hypothesis of no linear relationship was rejected ($p \ll 0.001$) and the correlation coefficient (R^2) for all data points was 0.85. The Kolmogorov-Smirnov test was applied to the standardized residuals, and normality could not be rejected ($p = 0.88$). Consequently, a linear fit was considered appropriate. The slope of the regression line (solid black line) was 0.67 and the intercept was 27%. The 95% prediction bands for the data are also shown in grey.

Figure 7.13 (B) shows the Bland-Altman plot with a mean difference of -0.5% and a standard deviation of 37%. To eliminate the effect of non-unity slope on the standard deviation difference, the RMS BCG data was calibrated by a single scaling operation (using the regression line slope) and the standard deviation difference was recalculated. After calibration, the standard deviation was 24%.

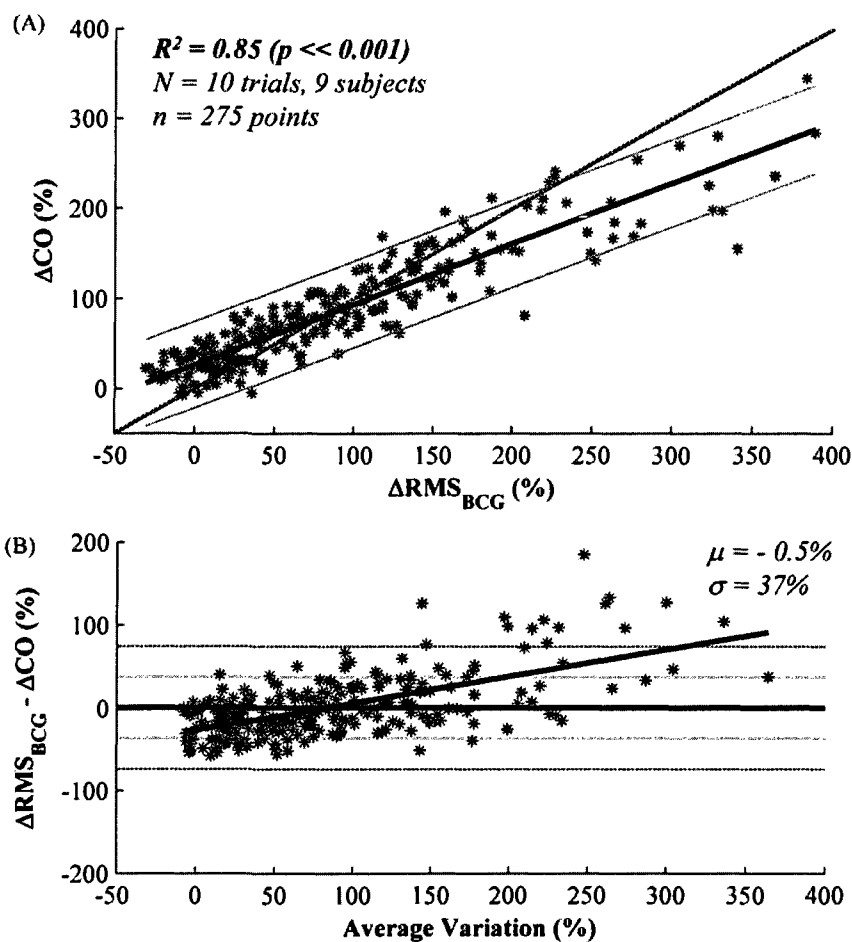


Figure 7.13 (A) Correlation plot showing percentage changes in cardiac output measured by Doppler echocardiography versus percent changes in the RMS power of the BCG ($R^2 = 0.85$, $n = 275$ data points, $p \ll 0.001$). The solid black line is the best least squares regression line for the data ($y = 0.67x + 27$) and the two parallel grey lines are the 95% prediction bands. The dashed black line shows the line of equal value. (B) Bland-Altman plot showing agreement of the methods (Mean Difference: -0.5% , Standard Deviation Difference: 37%). The percent changes in RMS BCG tended to exceed those of cardiac output measured by Doppler, resulting in an upward trend in this difference plot. This skews the data, causing an exaggerated standard deviation difference between the methods. When the data is calibrated based on the regression line slope by a single scaling operation, the standard deviation difference is 24% .

The results of the multiple linear regression analysis were that a linear combination of height, systolic blood pressure, and heart rate could be used to predict the slope of an individual's regression line ($R^2 = 0.83$, $p = 0.01$). This best fit was found with the following coefficients: -0.019 , 0.0193 , and 0.0087 , corresponding to height (cm), systolic blood pressure (mmHg), and heart rate (bpm). Slope of the RMS BCG power-cardiac output correlation for each individual was thus shown to have a decreasing relationship with height, and increasing

relationship with systolic blood pressure and heart rate. No linear dependence was found between this slope and body weight.

7.3.7. Discussion

The correlation coefficients were consistently high (Range: 0.79 to 0.96) when the data were correlated for each individual separately. The lowest correlation coefficient for individually analyzed data was for the heaviest participant (143 kg), and the slope that deviated most from unity was for the second heaviest participant (100 kg). While there was no linear dependence found between slope and body weight, this suggests that high body weight may still have a confounding effect on the accuracy of the method.

It is possible that these larger individuals had more difficulty remaining still on the scale during recovery. Another possibility is that these individuals had higher respiration rates or tidal volumes following exercise, leading to more pronounced respiratory artifacts in the BCG signals. Respiration causes amplitude modulation of the BCG signal which cannot be removed by linear filtering techniques.

For the aggregate data, a high correlation was demonstrated between percent changes in the RMS power of the BCG signal and cardiac output measured by Doppler echocardiography. The correlation coefficient, 0.85, compares favorably to other values reported in the literature for alternate methods (Range: 0.46 to 0.91).

The Bland-Altman plot results indicate that the percent changes in RMS power of the BCG signal showed minimal bias (0.5%) in predicting percent changes in cardiac output. The standard deviation of the difference between the methods was found to be 24% over a measurement range of -3% to 350% changes in cardiac output, corresponding to a 95% confidence prediction interval of $\pm 48\%$ change in cardiac output. Using the average resting cardiac output for the subjects in the trial (3.4 L min^{-1}) this corresponds to a prediction interval of $\pm 1.6 \text{ L min}^{-1}$. Note that in exercising conditions, two factors will always cause this interval to be larger than it would be at rest: first, the range of cardiac outputs studied is much larger than at rest and, second, the measurement noise is always greater than at rest since the levels of motion and respiration are elevated.

To illustrate how, in an exercise trial, the prediction interval for this study would provide accurate results, the following hypothetical case is provided. If a subject's RMS BCG power at rest corresponded to a cardiac output of 3.4 L min^{-1} , and the RMS BCG power tripled due to exercise, it could be predicted with 95% confidence that the cardiac output increased to $10.2 \text{ L min}^{-1} \pm 1.6 \text{ L min}^{-1}$. To the best of the authors' knowledge, the three lowest prediction intervals

reported in the literature for non-invasive exercise or exercise recovery cardiac output estimation studies were 2.35 L min⁻¹ [28], 3.47 L min⁻¹ [29], and 3.9 L min⁻¹ [17], all of which are higher than the corresponding interval found in this work (1.6 L min⁻¹).

The slope of the regression line was less than unity for the aggregate data, indicating that changes in the RMS BCG signal exceeded those in cardiac output measured by Doppler echocardiography. This was likely due to high levels of involuntary motion and respiratory artifact present during the recovery. While, as mentioned before, excessive artifacts causing large spikes in the data were removed manually, more subtle artifacts were still present in the data. For example, the motion of the chest while breathing heavily after the exercise was a source of interference that was likely much lower in amplitude at rest. Additionally, it is more difficult to stand still after exercise than while at rest, with involuntary swaying and leg twitching corrupting the measurement. Motion and respiration would both tend to increase the measured RMS power of the BCG signal, resulting in a less than unity regression line slope (exaggerated RMS BCG change compared to actual cardiac output change).

The importance of the multiple linear regression analysis in reducing the slope error of the individual regression lines is yet to be determined, and will require future studies. However, the preliminary results are very encouraging based on the statistics of the model ($R^2 > 0.8$ and F-test p-value < 0.01). In future work, each subject's height, systolic blood pressure, resting heart rate, and weight will be used to predict the slope of the regression line correlating BCG RMS power and cardiac output changes. The predicted slope will be compared against the measured slope to quantify the accuracy of the model.

7.4. Conclusions

This chapter focuses on demonstrating that robust estimation of hemodynamic changes is possible with standing BCG measurements. Furthermore, for estimating cardiac output changes, a reference signal, such as the ECG, is not needed for signal averaging, reducing the complexity of the apparatus and measurement procedure. Accordingly, the method is significantly less obtrusive compared to the competing technologies. While the cardiac output measurements are relative rather than absolute, in many instances such relative changes can be sufficient for directing therapy decisions. One important example is for monitoring heart failure outpatients at home.

One limitation of the exercise recovery study is that the repeatability of the method has not yet been explored. Thus, future work should focus on quantifying the reproducibility of the method. Multiple trials with the same subject should be performed to determine the inter-

measurement variability. In this study, the variability of the results due to measurement errors must be statistically differentiated from variability due to physiological differences—one subject may recover quite differently from the same level of exercise on two separate days. An additional area of future work would be in expanding the trials to include subjects with various cardiovascular diseases.

It should be noted that although the measurements were taken continuously from a standing subject for ten minutes of recovery time, in many instances shorter measurements would suffice. A tremendous amount of information can be gained by comparing only the cardiac output measured immediately after exertion to that taken at rest. For example, patients with early signs of heart failure may have normal resting cardiac output, but lower than normal cardiac output after exercise. This can be evaluated using the bathroom scale by measuring BCG before and immediately after exercise. The simplicity of the method combined with the practicality of the device could allow relative cardiac output changes to be measured quickly and reliably in the clinic or the home.

8

Conclusions and Future Directions

Prediction is very difficult, especially of the future.

– Niels Bohr

You are young, my son, and, as the years go by, time will change and even reverse many of your present opinions. Refrain therefore awhile from setting yourself up as a judge of the highest matters.

– Plato

8.1. Conclusions

The work described in this thesis establishes the groundwork for augmenting the care of heart failure patients in the home. With the modified scale, bodyweight measurements could be supplemented by relative changes in cardiac output – a key parameter used clinically for monitoring cardiovascular health. To prove that improved outcomes can be achieved, future work would include a longitudinal study of substantial size and duration. To show a significant result statistically, this trial would likely require several tens to hundreds of heart failure patients monitored over a period of at least one to two years. Due to these practical limitations, this was considered to be beyond the scope of this work. Instead, the focus was to usher in such a trial by conducting initial studies on healthy subjects and conquering the engineering obstacles.

The most important study, described in Chapter 7, established the correlation between changes in RMS power of the BCG and changes in cardiac output. This provides the basis for how serial measurements taken at home could be interpreted. An initial calibration of the device in the clinic prior to discharge would relate the absolute RMS power of the BCG to cardiac output measured via Doppler echocardiography or catheterization. Then, the changes in the RMS power over time, measured on the scale at home, could indicate impending decompensation and direct therapeutic interventions. Since cardiac output changes reflect degraded cardiac function, while increased bodyweight indicates increased fluid in response to degraded function, an earlier warning of decompensation may be gained. Furthermore, the combination of the two measurements could provide a more specific assessment of the hemodynamic profile.

The most challenging technical obstacle was preserving accurate measurement of BCG features in unsupervised settings; namely, in the home. In such settings, myriad sources of interference and noise can affect the fidelity of the measurements. Inventing new methods for mitigating or eliminating these sources of interference and noise was of paramount importance in this work, and should be instrumental for acquiring robust measurements in the home in future clinical trials.

These methods involved the use of multiple sensors and signal-fusion algorithms to enable robust and repeatable physiological measurements. The sensors were fully characterized and novel electronic circuits were designed to ensure that the signals could be acquired without distortion, and the electronic noise could be minimized.

For the ECG, the novel two-electrode transimpedance amplifier achieved the best co-optimization of power consumption and noise reduction of any ECG amplifier disclosed in the literature. With only 11 μW of power consumption, a total input referred noise current of 23 pA_{pp} was achieved. Additionally, integrative current feedback to the electrode enabled signal acquisition with only two electrodes contacting the body. As a result, ECGs were acquired using the handlebar electrodes of the HBF-500 scale (Omron Healthcare Inc., Bannockburn, IL) for nearly 100 subjects with no instances of amplifier saturation. Furthermore, the R-waves were sufficiently well-defined such that a simple, automated beat detection algorithm implemented in software was successfully used for triggered averaging of the simultaneously-acquired BCGs.

For the BCG, a lock-in amplifier was used to reduce electronic noise. By exciting the strain gauges with a square wave and synchronously demodulating the resulting differential bridge output, the flicker noise region of the input stage was bypassed. This approach reduced the electronic noise floor of the system by 7.7 dB. In future implementations, where the external interferences are reduced, this increased headroom could be crucial in measuring subtle features of the signal.

New methods for reducing external interferences – motion artifacts and floor vibrations – on the BCG signal were conceived and developed. These solutions involved the use of auxiliary sensors and signal-fusion algorithms for detecting the presence of motion and eliminating the effects of floor vibrations in the measurements. For motion artifact detection, EMG signals from the feet were shown to correlate to motion-induced BCG noise. The noise was estimated using an improved algorithm for BCG signal estimation, leveraging the timing information of a simultaneously acquired ECG. For floor vibrations, a seismic sensor was

positioned next to the scale and an adaptive algorithm was used to eliminate the effects of these vibrations in the measured BCG signals. The vibrations were reduced by more than 10 dB, such that robust measurements were demonstrated aboard an idling transit bus.

The technology described in this dissertation could also be used in a variety of settings other than home monitoring of heart failure patients. Some of these potential applications are described below, in addition to other possible methods for improving the robustness of the measurements, and future studies of correlations between BCG features and diagnostically relevant parameters.

8.2. Future Directions

As described earlier, perhaps the most logical next step for this research is the execution of a clinical trial with heart failure patients to determine whether an earlier warning of decompensation can be obtained. Scales could be provided to heart failure patients upon discharge from the hospital, and their BCG and ECG signals could be recorded daily in addition to body weight for an extended period of time (one to two years). As a portion of these patients' condition worsens, and they are re-hospitalized, the BCG/ECG features with the strongest predictive value can be determined statistically based on the outcome.

8.3. Final Remarks

The technology developed and discussed in this work could significantly improve home monitoring of cardiovascular diseases, and advance our understanding of basic physiology by providing a platform for easy and unobtrusive measurements of important cardiovascular parameters. The rapidly growing need for inexpensive health care solutions in the developed world today, coupled with the exploding population of people with cardiovascular disease, defined the main objectives of this research: finding a simple novel and low-cost solution for unobtrusively monitoring cardiovascular parameters in the home. The hope is that this solution can be used by healthy and diseased people to improve the quality of their lives.

Glossary of Key Acronyms and Symbols

Acronym/Symbol Name	Description
A_{cl}	Closed-Loop Gain or Transfer Function
ADC	Analog-to-Digital Converter
AIC	Akaike Information Criterion
A_{LVOT}	Area of the LVOT
A_{op}	Operational Amplifier Open-Loop Transfer Function
ASIC	Application Specific Integrated Circuit
A_v	Voltage Gain
BCG	Ballistocardiogram
BNC	Bayonet Neill-Concelman Connector
bpm	Beats per Minute
CAD	Coronary Artery Disease
CMRR	Common-Mode-Rejection Ratio
CO	Cardiac Output
CRT	Cathode Ray Tube
Δ	Delay
DBP	Diastolic Blood Pressure
DIP	Dual in-Line
D_{LVOT}	Diameter of the LVOT
ε	Error
ECG	Electrocardiogram
EDV	End Diastolic Volume
EEG	Electroencephalogram
EMFi	ElectroMechanical Film
EMG	Electromyogram
e_{ni}	Input-Referred Voltage Noise Density
EOG	Electrooculogram
ESV	End Systolic Volume
f_c	Cutoff (-3 dB) Frequency
FFT	Fast Fourier Transform

f_{hpf}	High-Pass Filter Cutoff (-3 dB) Frequency
FIR	Finite Impulse Response
f_{lpf}	Low-Pass Filter Cutoff (-3 dB) Frequency
F_{ni}	Input Referred Force Noise Density
f_{osc}	Oscillator Frequency
f_{res}	Resonant Frequency
GBWP	Gain-Bandwidth Product
HR	Heart Rate
Ht	Height
IC	Integrated Circuit
ICG	Impedance Cardiogram
IJ Amplitude	BCG I-Wave Amplitude Minus BCG J-Wave Amplitude
IJK Complex	Main Complex of BCG – Ventricular Contraction
J-Wave	Main Ballistocardiogram Peak
K	Spring Constant
KCG	Kinetocardiogram
LMS	Least-Mean Squares
LVM	Left Ventricular Mass
LVOT	Left Ventricular Outflow Tract
m	Mass
μ	Mean, or Adaptive Filter Learning Rate
M	Misadjustment
ML	Maximum Likelihood
MSE	Mean Square Error
NMRI	Nuclear Magnetic Resonance Imaging
NSR	Noise-to-Signal Ratio
PAC	Premature Atrial Contraction
PCB	Printed Circuit Board
PCG	Phonocardiogram
PCWP	Pulmonary Capillary Wedge Pressure
PEP	Pre-Ejection Period
PPG	Photoplethysmogram
PSD	Power Spectral Density

PV Loop	Pressure-Volume Loop
PVC	Premature Ventricular Contraction
Q	Quality Factor
Q-I Interval	Interval Between ECG Q-Wave and BCG I-Wave
Q-J Interval	Interval Between ECG Q-Wave and BCG J-Wave
QRS Complex	Main Complex of ECG – Ventricular Depolarization
R	Autocorrelation Matrix
R^2	Correlation Coefficient
R_E	Electrode-to-Skin Interface Resistance
R-J Interval	Interval Between ECG R-Wave and BCG J-Wave
R-R Interval	Interval Between Successive R-Waves
R-Wave	Main Electrocardiogram Peak
RMS	Root Mean Square
σ	Standard Deviation
SA Node	Sinoatrial Node – Pacemaker of the Heart
SBP	Systolic Blood Pressure
SCG	Seismocardiogram
SCSB	Static Charge-Sensitive Bed
SNR	Signal-to-Noise Ratio
SSE	Sum of the Square Errors
SV	Stroke Volume
t	Time
τ	Time Constant
TA-4	Mini-XLR 4-Pin Audio Connector
THD	Total Harmonic Distortion
V_{DM}	Differential-Mode Voltage
VTI	Ventricular Time Interval
Wt	Weight
XLR	3-Pin Audio Connector
$Z_{in,DM}$	Differential-Mode Input Impedance

References

- [1] R. Berne and M. Levy, *Cardiovascular Physiology*, 8th ed. St. Louis: Mosby, 2001.
- [2] A. Despopoulos and S. Silbernagl, *Color Atlas of Physiology*, 5 ed. Stuttgart: Thieme, 2001.
- [3] P. Horowitz and W. Hill, *The Art of Electronics*, 2nd ed. Cambridge: Cambridge University Press, 1989.
- [4] K. Tavakolian, F. M. Zadeh, Y. Chuo, A. Vaseghi, and B. Kaminska, "Development of a Novel Contactless Mechanocardiograph Device," *International Journal of Telemedicine and Applications*, pp. 1-5, 2008.
- [5] M. H. Hayes, *Statistical Digital Signal Processing and Modeling*. New York, NY: John Wiley & Sons Inc., 1996.
- [6] E. Ferrara and B. Widrow, "Multichannel adaptive filtering for signal enhancement," *Circuits and Systems, IEEE Transactions on*, vol. 28, pp. 606-610, 1981.
- [7] T. E. Owan and M. M. Redfield, "Epidemiology of Diastolic Heart Failure," *Progress in Cardiovascular Diseases*, vol. 47, pp. 320-332, 2005.
- [8] B. Widrow, J. R. Glover, Jr., J. M. McCool, J. Kaunitz, C. S. Williams, R. H. Hearn, J. R. Zeidler, Eugene Dong, Jr., and R. C. Goodlin, "Adaptive noise cancelling: Principles and applications," *Proceedings of the IEEE*, vol. 63, pp. 1692-1716, 1975.
- [9] I. Starr, A. J. Rawson, H. A. Schroeder, and N. R. Joseph, "Studies on The Estimation of Cardiac Output in Man, and of Abnormalities in Cardiac Function, From The Heart's Recoil and The Blood's Impacts; The Ballistocardiogram," *The American Journal of Physiology*, vol. 127, pp. 1-28, August 1 1939.
- [10] H. Benjelloun, R. Itti, L. Philippe, J.-M. Lorgeton, and M. Brochier, "Beat-to-beat assessment of left ventricular ejection in atrial fibrillation," *Eur J Nuc Med and Mol Imaging*, vol. 8, pp. 206-210, 1982.
- [11] O. T. Inan, M. Etemadi, A. Paloma, L. Giovangrandi, and G. T. A. Kovacs, "Non-Invasive Cardiac Output Trending During Exercise Recovery on a Bathroom-Scale-Based Ballistocardiograph," *Physiological Measurement*, vol. 30, pp. 261-274, 2009.
- [12] K. L. Grady, K. Dracup, G. Kennedy, D. K. Moser, M. Piano, L. W. Stevenson, and J. B. Young, "Team Management of Patients With Heart Failure : A Statement for Healthcare Professionals From the Cardiovascular Nursing Council of the American Heart Association," *Circulation*, vol. 102, pp. 2443-2456, 2000.

- [13] A. D. Droitcour, "Non-contact measurement of heart and respiration rates with a single-chip microwave doppler radar," in *Electrical Engineering*, vol. Ph.D. Stanford: Stanford Univeristy, 2006.
- [14] A. Akhbardeh, S. Junnila, M. Koivuluoma, T. Koivistoinen, and A. Varri, "Evaluation of heart condition based on ballistocardiogram classification using compactly supported wavelet transforms and neural networks," in *Control Applications, 2005. CCA 2005. Proceedings of 2005 IEEE Conference on*, 2005, pp. 843-848.
- [15] R. Coppola, R. Tabor, and M. S. Buchsbaum, "Signal to noise ratio and response variability measurements in single trial evoked potentials," *Electroencephalography and Clinical Neurophysiology*, vol. 44, pp. 214-222, 1978.
- [16] N. Bershad and A. Rockmore, "On estimating signal-to-noise ratio using the sample correlation coefficient (Corresp.)," *Information Theory, IEEE Transactions on*, vol. 20, pp. 112-113, 1974.
- [17] S. Houtman, B. Oeseburg, and M. T. E. Hopman, "Non-invasive cardiac output assessment during moderate exercise: pulse contour compared with CO2 rebreathing," *Clinical Physiology*, vol. 19, pp. 230-237, 1999.
- [18] J. Sugawara, T. Tanabe, M. Miyachi, K. Yamamoto, K. Takahashi, M. Iemitsu, T. Otsuki, S. Homma, S. Maeda, R. Ajisaka, and M. Matsuda, "Non-invasive assessment of cardiac output during exercise in healthy young humans: comparison between Modelflow method and Doppler echocardiography method," *Acta Physiologica Scandinavica*, vol. 179, pp. 361-366, 2003.
- [19] G. Antonutto, M. Girardis, D. Tuniz, and P. E. di Prampero, "Noninvasive assessment of cardiac output from arterial pressure profiles during exercise," *Eur J Appl Physiol*, vol. 72, pp. 18-24, 1995.
- [20] J. Christie, L. Sheldahl, F. Tristani, K. Sagar, M. Ptacin, and S. Wann, "Determination of stroke volume and cardiac output during exercise: comparison of two-dimensional and Doppler echocardiography, Fick oximetry, and thermodilution," *Circulation*, vol. 76, pp. 539-547, 1987.
- [21] J. H. Wilmore, P. A. Farrell, A. C. Norton, R. W. Cote, 3rd, E. F. Coyle, G. A. Ewy, L. P. Temkin, and J. E. Billing, "An automated, indirect assessment of cardiac output during rest and exercise," *J Appl Physiol*, vol. 52, pp. 1493-1497, 1982.
- [22] Y. Liu, E. Menold, A. Dullenkopf, Rei, S. necker, W. Lormes, M. Lehmann, and J. M. Steinacker, "Validation of the acetylene rebreathing method for measurement of

- cardiac output at rest and during high-intensity exercise," *Clinical Physiology*, vol. 17, pp. 171-182, 1997.
- [23] B. D. Johnson, K. C. Beck, D. N. Proctor, J. Miller, N. M. Dietz, and M. J. Joyner, "Cardiac output during exercise by the open circuit acetylene washin method: comparison with direct Fick," *J Appl Physiol*, vol. 88, pp. 1650-1658, 2000.
- [24] Y. Zhang, M. Qu, J. G. Webster, W. J. Tompkins, B. A. Ward, and D. R. Bassett, "Cardiac Output Monitoring by Impedance Cardiography During Treadmill Exercise," *Biomedical Engineering, IEEE Transactions on*, vol. BME-33, pp. 1037-1042, 1986.
- [25] Y. Miyamoto, M. Takahashi, T. Tamura, T. Nakamura, T. Hiura, and M. Mikami, "Continuous determination of cardiac output during exercise by the use of impedance plethysmography," *Medical and Biological Engineering and Computing*, vol. 19, pp. 638-644, 1981.
- [26] R. Moore, R. Sansores, V. Guimond, and R. Abboud, "Evaluation of cardiac output by thoracic electrical bioimpedance during exercise in normal subjects," *Chest*, vol. 102, pp. 448-455, 1992.
- [27] D. D. Hatcher and O. D. Srb, "Comparison of two noninvasive techniques for estimating cardiac output during exercise," *J Appl Physiol*, vol. 61, pp. 155-159, 1986.
- [28] N. Tordi, L. Mourot, B. Matusheski, and R. L. Hughson, "Measurements of cardiac output during constant exercises: comparison of two non-invasive techniques," *Int J Sports Med*, vol. 25, pp. 145-9, 2004.
- [29] R. Richard, E. Lonsdorfer-Wolf, A. Charloux, S. Doutreleau, M. Buchheit, M. Oswald-Mammosser, E. Lampert, B. Mettauer, B. Geny, and J. Lonsdorfer, "Non-invasive cardiac output evaluation during a maximal progressive exercise test, using a new impedance cardiograph device," *European Journal of Applied Physiology*, vol. 85, pp. 202-207, 2001.
- [30] J. Quail, "Leading the Weigh; Scales are Gaining Momentum, Thanks to Advances in Technology and Design," in *HFN The Weekly Newspaper for the Home Furnishing Network*, 2001.
- [31] G. Morago, "Introducing Bathroom Scales That Do More Than Carry Your Weight," in *Los Angeles Times Los Angeles*, 2001.
- [32] A. C. Guyton, *Textbook of Medical Physiology*, 11 ed. Philadelphia: Elsevier Saunders, 2006.

- [33] J. J. V. McMurray and M. A. Pfeffer, "Heart failure," *The Lancet*, vol. 365, pp. 1877-1889.
- [34] D. Lloyd-Jones, R. Adams, M. Carnethon, G. De Simone, T. B. Ferguson, K. Flegal, E. Ford, K. Furie, A. Go, K. Greenlund, N. Haase, S. Hailpern, M. Ho, V. Howard, B. Kissela, S. Kittner, D. Lackland, L. Lisabeth, A. Marelli, M. McDermott, J. Meigs, D. Mozaffarian, G. Nichol, C. O'Donnell, V. Roger, W. Rosamond, R. Sacco, P. Sorlie, R. Stafford, J. Steinberger, T. Thom, S. Wasserthiel-Smoller, N. Wong, J. Wylie-Rosett, Y. Hong, f. t. A. H. A. S. Committee, and Stroke Statistics Subcommittee, "Heart Disease and Stroke Statistics--2009 Update: A Report From the American Heart Association Statistics Committee and Stroke Statistics Subcommittee," *Circulation*, vol. 119, pp. e21-181, 2009.
- [35] "Morbidity & Mortality: 2007 Chart Book on Cardiovascular, Lung, and Blood Diseases," NHLBI, Ed., 2007, p. 23.
- [36] H.-C. Kung, D. L. Hoyert, J. Xu, and S. L. Murphy, "National Vital Statistics Reports, Deaths: Final Data for 2005," Center for Disease Control and Prevention, 2008.
- [37] V. L. Roger, S. A. Weston, M. M. Redfield, J. P. Hellermann-Homan, J. Killian, B. P. Yawn, and S. J. Jacobsen, "Trends in Heart Failure Incidence and Survival in a Community-Based Population," *JAMA*, vol. 292, pp. 344-350, 2004.
- [38] W. Rosamond, K. Flegal, K. Furie, A. Go, K. Greenlund, N. Haase, S. M. Hailpern, M. Ho, V. Howard, B. Kissela, S. Kittner, D. Lloyd-Jones, M. McDermott, J. Meigs, C. Moy, G. Nichol, C. O'Donnell, V. Roger, P. Sorlie, J. Steinberger, T. Thom, M. Wilson, and Y. Hong, "Heart disease and stroke statistics--2008 update: a report from the American Heart Association Statistics Committee and Stroke Statistics Subcommittee," *Circulation*, vol. 117, pp. e25-146, Jan 29 2008.
- [39] "Heart and Stroke Statistical Update (Dallas, TX)," *American Heart Association*, 1999.
- [40] W. J. Remme and K. Swedberg, "Task Force for the Diagnosis and Treatment of Chronic Heart Failure: Guidelines for the diagnosis and treatment of chronic heart failure," *Eur Heart J*, vol. 22, pp. 1527-1560, 2001.
- [41] L. R. Goldberg, J. D. Piette, M. N. Walsh, T. A. Frank, B. E. Jaski, A. L. Smith, R. Rodriguez, D. M. Mancini, L. A. Hopton, E. J. Orav, and E. Loh, "Randomized trial of a daily electronic home monitoring system in patients with advanced heart failure:

- the Weight Monitoring in Heart Failure (WHARF) trial," *American Heart Journal*, vol. 146, pp. 705-712, 2003.
- [42] S. I. Chaudhry, Y. Wang, J. Concato, T. M. Gill, and H. M. Krumholz, "Patterns of Weight Change Preceding Hospitalization for Heart Failure," *Circulation*, vol. 116, pp. 1549-1554, 2007.
- [43] S. D. Anker, A. Negassa, A. J. S. Coats, R. Afzal, P. A. Poole-Wilson, J. N. Cohn, and S. Yusuf, "Prognostic importance of weight loss in chronic heart failure and the effect of treatment with angiotensin-converting-enzyme inhibitors: an observational study," *The Lancet*, vol. 361, pp. 1077-1083, 2003.
- [44] E. E. Wolfel, "Can We Predict and Prevent the Onset of Acute Decompensated Heart Failure?," *Circulation*, vol. 116, pp. 1526-1529, 2007.
- [45] S. D. Anker and A. J. S. Coats, "Cardiac Cachexia," *Chest*, vol. 115, pp. 836-847, 1999.
- [46] J. R. Teerlink, "Learning the Points of COMPASS-HF: Assessing Implantable Hemodynamic Monitoring in Heart Failure Patients," *J Am Coll Cardiol*, vol. 51, pp. 1080-1082, 2008.
- [47] M. Packer, W. T. Abraham, M. R. Mehra, C. W. Yancy, C. E. Lawless, J. E. Mitchell, F. W. Smart, R. Bijou, C. M. O'Connor, B. M. Massie, I. L. Pina, B. H. Greenberg, J. B. Young, D. P. Fishbein, P. J. Hauptman, R. C. Bourge, J. E. Strobeck, S. Murali, D. Schocken, J. R. Teerlink, W. C. Levy, R. J. Trupp, and M. A. Silver, "Utility of Impedance Cardiography for the Identification of Short-Term Risk of Clinical Decompensation in Stable Patients With Chronic Heart Failure," *Journal of the American College of Cardiology*, vol. 47, pp. 2245-2252, 2006.
- [48] C.-M. Yu, L. Wang, E. Chau, R. H.-W. Chan, S.-L. Kong, M.-O. Tang, J. Christensen, R. W. Stadler, and C.-P. Lau, "Intrathoracic Impedance Monitoring in Patients With Heart Failure: Correlation With Fluid Status and Feasibility of Early Warning Preceding Hospitalization," *Circulation*, vol. 112, pp. 841-848, 2005.
- [49] W. T. Abraham, B. Foreman, R. Fishel, G. Haas, and B. Moe, "Fluid accumulation status trial (FAST)," *Heart Rhythm*, vol. 2, pp. S65-S66, 2005.
- [50] K. C. Bilchick, B. Fetis, R. Djoukeng, S. Gross Fisher, R. D. Fletcher, S. N. Singh, E. Nevo, and R. D. Berger, "Prognostic value of heart rate variability in chronic congestive heart failure (Veterans Affairs' Survival Trial of Antiarrhythmic Therapy

- in Congestive Heart Failure)," *The American Journal of Cardiology*, vol. 90, pp. 24-28, 2002.
- [51] P. B. Adamson, A. L. Smith, W. T. Abraham, K. J. Kleckner, R. W. Stadler, A. Shih, and M. M. Rhodes, "Continuous Autonomic Assessment in Patients With Symptomatic Heart Failure: Prognostic Value of Heart Rate Variability Measured by an Implanted Cardiac Resynchronization Device," *Circulation*, vol. 110, pp. 2389-2394, 2004.
- [52] R. C. Bourge, W. T. Abraham, P. B. Adamson, M. F. Aaron, J. M. Aranda Jr, A. Magalski, M. R. Zile, A. L. Smith, F. W. Smart, M. A. O'Shaughnessy, M. L. Jessup, B. Sparks, D. L. Naftel, and L. W. Stevenson, "Randomized Controlled Trial of an Implantable Continuous Hemodynamic Monitor in Patients With Advanced Heart Failure: The COMPASS-HF Study," *Journal of the American College of Cardiology*, vol. 51, pp. 1073-1079, 2008.
- [53] J. Ritzema, I. C. Melton, A. M. Richards, I. G. Crozier, C. Frampton, R. N. Doughty, J. Whiting, S. Kar, N. Eigler, H. Krum, W. T. Abraham, and R. W. Troughton, "Direct Left Atrial Pressure Monitoring in Ambulatory Heart Failure Patients: Initial Experience With a New Permanent Implantable Device," *Circulation*, vol. 116, pp. 2952-2959, 2007.
- [54] R. P. P. W. G. Kubicek, D. A. Witsoe,, "Impedance Cardiography as a Noninvasive Method of Monitoring Cardiac Function and Other Parameters of the Cardiovascular System," *Annals of the New York Academy of Sciences*, vol. 170, pp. 724-732, 1970.
- [55] D. Bernstein and H. Lemmens, "Stroke volume equation for impedance cardiography," *Medical and Biological Engineering and Computing*, vol. 43, pp. 443-450, 2005.
- [56] J. P. Piccini and P. Hranitzky, "Diagnostic monitoring strategies in heart failure management," *American Heart Journal*, vol. 153, pp. 12-17, 2007.
- [57] P. G. Katona and F. Jih, "Respiratory sinus arrhythmia: noninvasive measure of parasympathetic cardiac control," *J Appl Physiol*, vol. 39, pp. 801-805, 1975.
- [58] H. R. Brown, V. de Lalla, M. A. Epstein, and M. J. Hoffman, *Clinical ballistocardiography*. New York: Macmillan, 1952.
- [59] J. W. Gordon, "Certain Molar Movements of the Human Body produced by the Circulation of the Blood," *Journal of Anatomy and Physiology*, vol. 11, pp. 533-536, 1877.

- [60] Y. Henderson, "The Mass-Movements of the Circulation as Shown by a Recoil Curve," *Am J Physiol*, vol. 14, pp. 287-298, 1905.
- [61] C. G. Douglas, J. S. Haldane, Y. Henderson, E. C. Schneider, G. B. Webb, and J. Richards, "Physiological Observations Made on Pike's Peak, Colorado, with Special Reference to Adaptation to Low Barometric Pressures," *Philosophical Transactions of the Royal Society of London, Series B, Containing Papers of a Biological Character*, vol. 203, pp. 185-318, 1913.
- [62] R. S. Gubner, M. Rodstein, and H. E. Ungerleider, "Ballistocardiography: An Appraisal of Technic, Physiologic Principles, and Clinical Value," *Circulation*, vol. 7, pp. 268-286, 1953.
- [63] J. L. Nickerson and H. J. Curtis, "The Design of the Ballistocardiograph," *Am J Physiol*, vol. 142, pp. 1-11, August 1 1944.
- [64] V. E. Krahl, "The Electric Strain Gauge Ballistocardiograph," *Am Heart J*, vol. 39, pp. 161-173, 1950.
- [65] M. B. Rappaport, H. B. Sprague, and W. B. Thompson, "Ballistocardiography: I. Physical Considerations," *Circulation*, vol. 7, pp. 229-246, 1953.
- [66] "Trail-Blazing in Cardiac Research: The Starr-Type Horizontal Ballistocardiograph for the Direct Measurement of Cardiac Output," *Advertisement in Circulation*, vol. 5, p. xxxix, 1952.
- [67] W. Dock and F. Taubman, "Some technics for recording the ballistocardiogram directly from the body," *Am J Med*, vol. 7, pp. 751-5, illust, Dec 1949.
- [68] L. Pordy, K. Chesky, A. M. Master, R. C. Taymor, and M. Moser, "The dual displacement and velocity ballistocardiograph apparatus," *American Heart Journal*, vol. 44, pp. 248-256, 1952.
- [69] R. L. Fulton, N. O. Rothermich, and W. Bergen, "The Usefulness and Reliability of the Dock Ballistocardiograph in Clinical Medicine," *Annals of Internal Medicine*, vol. 55, p. 258, 1961.
- [70] R. A. Helm and A. Iglauer, "A statistical comparison of normal ballistocardiograms recorded with a high-frequency table and with various instruments which record body motion directly," *American Heart Journal*, vol. 46, pp. 321-328, 1953.
- [71] R. Gubner, "Selective Synchronous Recording of the Ballistocardiogram and Electrocardiogram on a Single Channel," *Circulation*, vol. 4, pp. 239-241, 1951.

- [72] W. R. Scarborough, F. W. Davis, B. M. Baker, R. E. Mason, and M. L. Singewald, "A review of ballistocardiography," *American Heart Journal*, vol. 44, pp. 910-946, 1952.
- [73] I. Starr, "The relation of the ballistocardiogram to cardiac function," *The American Journal of Cardiology*, vol. 2, pp. 737-747, 1958.
- [74] W. R. Scarborough, R. E. Mason, F. W. Davis, M. L. Singewald, B. M. Baker, and S. A. Lore, "A ballistocardiographic and electrocardiographic study of 328 patients with coronary artery disease; Comparison with results from a similar study of apparently normal persons," *American Heart Journal*, vol. 44, pp. 645-670, 1952.
- [75] I. Starr and R. L. Mayock, "On the Significance of Abnormal Forms of the Ballistocardiogram," *Am J Med Sci*, vol. 215, pp. 631-650, 1948.
- [76] I. Starr and F. C. Wood, "Studies with the Ballistocardiograph in Acute Cardiac Infarction and Chronic Angina Pectoris," *Am Heart J*, vol. 25, pp. 81-101, 1943.
- [77] B. Berman, J. R. Braunstein, and J. McGuire, "The Effect of Meals on the Electrocardiogram and the Ballistocardiogram in Patients with Angina Pectoris," *Circulation*, vol. 1, pp. 1017-1025, 1950.
- [78] H. R. Brown, JR., M. J. Hoffman, and V. De Lalla, JR., "Ballistocardiographic Findings in Patients with Symptoms of Angina Pectoris," *Circulation*, vol. 1, pp. 132-140, 1950.
- [79] M. Moser, L. Porady, K. Chesky, R. C. Taymor, and A. M. Master, "The Ballistocardiogram in Myocardial Infarction: A Study of One Hundred Cases," *Circulation*, vol. 6, pp. 402-407, 1952.
- [80] H. Mandelbaum and R. A. Mandelbaum, "Studies Utilizing the Portable Electromagnetic Ballistocardiograph: V. The Importance of the Light Exercise Test in Clinical Ballistocardiography," *Circulation*, vol. 9, pp. 388-399, 1954.
- [81] K. Chesky, M. Moser, R. C. Taymor, A. M. Master, and L. Porady, "Clinical evaluation of the ballistocardiogram : II. Heart disease--Hypertension, angina pectoris, and myocardial infarction," *American Heart Journal*, vol. 42, pp. 328-333, 1951.
- [82] H. L. Taylor, W. F. Maloney, and A. Keys, "Factors affecting the low-frequency, critically-damped ballistocardiogram, with special reference to age, body size, and body composition," *American Heart Journal*, vol. 48, pp. 864-880, 1954.
- [83] J. A. Schack, O. Tannenbaum, L. Friedfeld, and H. Vesell, "The Ballistocardiogram in Persons Over Eighty-Five Years of Age," *Am J Med*, vol. 14, p. 525, 1953.

- [84] I. Starr and E. A. Hildreth, "The Effect of Aging and of the Development of Disease on the Ballistocardiogram: A Study of Eighty Subjects, Originally Healthy, Followed from Ten to Fourteen Years," *Circulation*, vol. 5, pp. 481-495, 1952.
- [85] E. E. Eddleman, W. K. Harrison, D. H. Jackson, and H. L. Taylor, "A critical appraisal of ballistocardiography," *The American Journal of Cardiology*, vol. 29, pp. 120-122, 1972.
- [86] I. Starr and F. C. Wood, "Twenty-Year Studies with the Ballistocardiograph: The Relation between the Amplitude of the First Record of "Healthy" Adults and Eventual Mortality and Morbidity from Heart Disease," *Circulation*, vol. 23, pp. 714-732, 1961.
- [87] J. Alihanka, K. Vaahtoranta, and I. Saarikivi, "A new method for long-term monitoring of the ballistocardiogram, heart rate, and respiration," *American journal of physiology*, vol. 240, p. R384, 1981.
- [88] T. Koivistoinen, S. Junnila, A. Varri, and T. Koobi, "A new method for measuring the ballistocardiogram using EMFi sensors in a normal chair," in *Engineering in Medicine and Biology Society, 2004. IEMBS '04. 26th Annual International Conference of the IEEE*, 2004, pp. 2026-2029.
- [89] K. Yamakoshi, M. Kuroda, S. Tanaka, I. Yamaguchi, and A. Kawarada, "Non-conscious and automatic acquisition of body and excreta weight together with ballistocardiogram in a lavatory," in *Engineering in Medicine and Biology Society, 1996. Bridging Disciplines for Biomedicine. Proceedings of the 18th Annual International Conference of the IEEE*, 1996, pp. 67-68 vol.1.
- [90] W. P. S. McKay, P. H. Gregson, B. W.S. McKay, and J. Militzer, "Sternal acceleration ballistocardiography and arterial pressure wave analysis to determine stroke volume," *Clinical & Investigative Medicine*, vol. 22, p. 4, 1999.
- [91] J. Williams, "Bridge Circuits - Marrying Gain and Balance," *Linear Technology Application Note*, vol. AN43, pp. 1-46, 1990.
- [92] O. T. Inan, M. Etemadi, R. M. Wiard, L. Giovangrandi, and G. T. A. Kovacs, "Robust Ballistocardiogram Acquisition for Home Monitoring," *Physiological Measurement*, vol. 30, pp. 169-185, 2009.
- [93] S. H. Woodward, N. J. Arsenault, K. Voelker, T. Nguyen, J. Lynch, G. Leskin, and J. Sheikh, "Estimating heart rate and RSA from the mattress-recorded kinetocardiogram," *Psychophysiology*, vol. 44, pp. 635-638, 2007.

- [94] P. Castiglioni, A. Faini, G. Parati, and M. Di Rienzo, "Wearable Seismocardiography," in *Engineering in Medicine and Biology Society, 2007. EMBS 2007. 29th Annual International Conference of the IEEE*, 2007, pp. 3954-3957.
- [95] K. Tavakolian, A. Vaseghi, and B. Kaminska, "Improvement of ballistocardiogram processing by inclusion of respiration information," *Physiological Measurement*, vol. 29, pp. 771-781, 2008.
- [96] J. Alihanka, K. Vaahtoranta, and I. Saarikivi, "A new method for long-term monitoring of the ballistocardiogram, heart rate, and respiration," *Am J Physiol Regul Integr Comp Physiol*, vol. 240, pp. R384-392, 1981.
- [97] A. Lindqvist, K. Pihlajamaki, J. Jalonen, V. Laaksonen, and J. Alihanka, "Static-charge-sensitive bed ballistocardiography in cardiovascular monitoring," *Clinical Physiology*, vol. 16, pp. 23-40, 1995.
- [98] M. Paajanen, J. Lekkala, and K. Kirjavainen, "ElectroMechanical Film (EMFi) -- a new multipurpose electret material," *Sensors and Actuators A: Physical*, vol. 84, pp. 95-102, 2000.
- [99] U. K. Sepponen, "Method and apparatus for measuring physical condition," 1995.
- [100] B. S. Lipman and E. Massie, *Clinical Scalar Electrocardiography*. Chicago: Year Book Medical Publishers Inc., 1965.
- [101] J. G. Webster, "Medical Instrumentation: Application and Design," 3rd ed New York: John Wiley & Sons, 1998.
- [102] J. Pan and W. J. Tompkins, "A Real-Time QRS Detection Algorithm," *Biomedical Engineering, IEEE Transactions on*, vol. BME-32, pp. 230-236, 1985.
- [103] I. I. Christov and I. K. Daskalov, "Filtering of electromyogram artifacts from the electrocardiogram," *Medical Engineering & Physics*, vol. 21, pp. 731-736, 1999.
- [104] H. de Talhouet and J. G. Webster, "The origin of skin-stretch-caused motion artifacts under electrodes," *Physiological Measurement*, vol. 17, pp. 81-93, 1996.
- [105] J. Alametsa, A. Varri, M. Koivuluoma, and L. Barna, "The potential of EMFi sensors in heart activity monitoring," in *2nd OpenECG Workshop "Integration of the ECG into the EHR & Interoperability of ECG Device Systems"* Berlin, Germany, 2004.
- [106] R. Gonzalez-Landaeta, O. Casas, and R. Pallas-Areny, "Heart rate detection from an electronic weighing scale," *Physiological Measurement*, vol. 29, pp. 979-988, 2008.
- [107] M. J. Burke and D. T. Gleeson, "A micropower dry-electrode ECG preamplifier," *Biomedical Engineering, IEEE Transactions on*, vol. 47, pp. 155-162, 2000.

- [108] E. M. Spinelli and M. A. Mayosky, "AC coupled three op-amp biopotential amplifier with active DC suppression," *Biomedical Engineering, IEEE Transactions on*, vol. 47, pp. 1616-1619, 2000.
- [109] A. MettingVanRijn, A. Peper, and C. Grimbergen, "Amplifiers for bioelectric events: A design with a minimal number of parts," *Medical and Biological Engineering and Computing*, vol. 32, pp. 305-310, 1994.
- [110] C.-N. Chien and F.-S. Jaw, "Miniature ultra-low-power biopotential amplifier for portable [sic] applications," *Biomedical Engineering - Applications, Basis & Communications*, vol. 17, 2005.
- [111] A. Putra, T. H. Teo, and S. Rajinder, "Ultra Low-Power Low-Voltage Integrated Preamplifier Using Class-AB Op-Amp for Biomedical Sensor Application," in *Integrated Circuits, 2007. ISIC '07. International Symposium on*, 2007, pp. 216-219.
- [112] K. Lasanen and J. Kostamovaara, "A 1-V analog CMOS front-end for detecting QRS complexes in a cardiac signal," *Circuits and Systems I: Regular Papers, IEEE Transactions on*, vol. 52, pp. 2584-2594, 2005.
- [113] M. Shojaei-Baghini, R. K. Lal, and D. K. Sharma, "A Low-Power and Compact Analog CMOS Processing Chip for Portable ECG Recorders," in *IEEE A.S.S.C.C.*, 2005, pp. 473-476.
- [114] R. F. Yazicioglu, P. Merken, R. Puers, and C. Van Hoof, "A 60/spl mu/W 60 nV/Hz Readout Front-End for Portable Biopotential Acquisition Systems," in *Solid-State Circuits Conference, 2006. ISSCC 2006. Digest of Technical Papers. IEEE International*, 2006, pp. 109-118.
- [115] W. Honglei and X. Yong-Ping, "A low-voltage low-noise CMOS instrumentation amplifier for portable medical monitoring systems," in *IEEE-NEWCAS Conference, 2005. The 3rd International*, 2005, pp. 295-298.
- [116] Y. Chih-Jen, C. Wen-Yaw, and C. Mely Chen, "Micro-power low-offset instrumentation amplifier IC design for biomedical system applications," *Circuits and Systems I: Regular Papers, IEEE Transactions on*, vol. 51, pp. 691-699, 2004.
- [117] G. A. Hanasusanto and Z. Yuanjin, "A Chopper Stabilized Pre-amplifier for Biomedical Signal Acquisition," in *Integrated Circuits, 2007. ISIC '07. International Symposium on*, 2007, pp. 200-203.

- [118] K. A. Ng and P. K. Chan, "A CMOS analog front-end IC for portable EEG/ECG monitoring applications," *Circuits and Systems I: Regular Papers, IEEE Transactions on*, vol. 52, pp. 2335-2347, 2005.
- [119] R. R. Harrison, "A Versatile Integrated Circuit for the Acquisition of Biopotentials," in *IEEE CICC*, 2007.
- [120] E. Company-Bosch and E. Hartmann, "ECG Front-End Design is Simplified with MicroConverter," in *Analog Dialogue*. vol. 37, 2003, pp. 1-5.
- [121] S. Grimnes, "Impedance measurement of individual skin surface electrodes," *Medical and Biological Engineering and Computing*, vol. 21, pp. 750-755, 1983.
- [122] J. Rosell, J. Colominas, P. Riu, R. Pallas-Areny, and J. G. Webster, "Skin impedance from 1 Hz to 1 MHz," *IEEE Trans Biomed Eng*, vol. 35, 1988.
- [123] H. Schwerdt, L. Bette, R. Grillmaier, W. Hoffmann, H. Schieffer, and H. Stanger, "Design and evaluation of a new computer-based force vectorballistocardiograph," *Medical and Biological Engineering and Computing*, vol. 25, pp. 453-458, 1987.
- [124] O. Postolache, P. S. Girao, and G. Postolache, "New Approach on Cardiac Autonomic Control Estimation Based on BCG Processing," in *Electrical and Computer Engineering, 2007. CCECE 2007. Canadian Conference on*, 2007, pp. 876-879.
- [125] L. Bacharova, O. V. Baum, G. A. Muromtseva, L. A. Popov, V. B. Rozanov, V. I. Voloshin, O. M. Voroshnin, and E. A. Zhavoronkova, "Body mass index and the relationship between QRS amplitude and left ventricular mass in hypertensive patients and patients with metabolic syndrome," *Journal of Electrocardiology*, vol. 41, pp. 637-637, 2008.
- [126] S. Y. Tan, G. Engel, J. Myers, M. Sandri, and V. F. Froelicher, "The Prognostic Value of T Wave Amplitude in Lead aVR in Males " *Annals of Noninvasive Electrocardiology*, vol. 13, pp. 113-119, 2008.
- [127] P. Celka and B. Kilner, "Carmeli's S index assesses motion and muscle artefact reduction in rowers' electrocardiograms," *Physiological Measurement*, vol. 27, pp. 737-755, 2006.
- [128] L. Sornmo and P. Laguna, *Bioelectrical Signal Processing in Cardiac and Neurological Applications*. Amsterdam: Elsevier Academic Press, 2005.
- [129] C. E. Davila and M. S. Mobin, "Weighted averaging of evoked potentials," *Biomedical Engineering, IEEE Transactions on*, vol. 39, pp. 338-345, 1992.

- [130] C. Li, C. Zheng, and C. Tai, "Detection of ECG characteristic points using wavelet transforms," *Biomedical Engineering, IEEE Transactions on*, vol. 42, pp. 21-28, 1995.
- [131] P. S. Hamilton and W. J. Tompkins, "Adaptive matched filtering for QRS detection," in *Engineering in Medicine and Biology Society, 1988. Proceedings of the Annual International Conference of the IEEE*, 1988, pp. 147-148 vol.1.
- [132] I. Starr and C. K. Friedland, "On the Cause of the Respiratory Variation of the Ballistocardiogram, with a Note on Sinus Arrhythmia," *J Clin Invest*, vol. 25, pp. 53-64, 1946.
- [133] O. T. Inan, M. Etemadi, R. M. Wiard, L. Giovangrandi, and G. Kovacs, "Evaluating the Foot Electromyogram Signal as a Noise Reference for a Bathroom Scale Ballistocardiogram Recorder," in *Computer-Based Medical Systems, 2008. CBMS '08. 21st IEEE International Symposium on*, 2008, pp. 70-74.
- [134] O. T. Inan, M. Etemadi, B. Widrow, and G. T. A. Kovacs, "Adaptive cancellation of floor vibrations in standing ballistocardiogram recordings using a seismic sensor as a noise reference," *IEEE Trans Biomed Eng*, In Press.
- [135] B. Widrow and S. D. Stearns, *Adaptive signal processing*: Prentice-Hall, Inc., 1985.
- [136] J. Alametsa, E. Rauhala, E. Huupponen, A. Saastamoinen, A. Varri, A. Joutsen, J. Hasan, and S.-L. Himanen, "Automatic detection of spiking events in EMFi sheet during sleep," *Medical Engineering & Physics*, vol. 28, p. 267, 2006.
- [137] J. M. Kortelainen and J. Virkkala, "FFT averaging of multichannel BCG signals from bed mattress sensor to improve estimation of heart beat interval," in *Engineering in Medicine and Biology Society, 2007. EMBS 2007. 29th Annual International Conference of the IEEE*, 2007, pp. 6685-6688.
- [138] C. K. Battye, D. C. Deuchar, R. E. George, R. D. Moore, and P. J. Winter, "A Simple, Calibrated, Ultra-low Frequency Ballistocardiograph," *Med. & Biol. Engng.*, vol. 4, pp. 543-554, 1966.
- [139] C. B. Henderson, "The Abnormal Ballistocardiogram in Mitral Stenosis: The Relationship of the Abnormal Waves to Right Ventricular Ejection and to the Mean Pulmonary Artery Pressure," *Circulation*, vol. 12, pp. 858-868, 1955.
- [140] W. R. Scarborough, S. A. Talbot, J. R. Braunstein, M. B. Rappaport, W. Dock, W. F. Hamilton, J. E. Smith, J. L. Nickerson, and I. Starr, "Proposals for Ballistocardiographic Nomenclature and Conventions: Revised and Extended: Report

- of Committee on Ballistocardiographic Terminology," *Circulation*, vol. 14, pp. 435-450, 1956.
- [141] J. E. Smith and S. Bryan, "The Low Frequency Velocity Measurement Ballistocardiograph," *Circulation*, vol. 5, pp. 892-902, 1952.
- [142] J. Alametsa, J. Viik, J. Alakare, A. Varri, and A. Palomaki, "Ballistocardiography in sitting and horizontal positions," *Physiological Measurement*, vol. 29, pp. 1071-1087, 2008.
- [143] D. C. Deuchar, S. A. Talbot, and W. R. Scarborough, "Some Observations on the Relation of the High-Frequency Bed Ballistocardiogram to that Obtained from an Aperiodic Bed," *Circulation*, vol. 11, pp. 228-239, 1955.
- [144] O. Tannenbaum, J. A. Schack, and H. Vesell, "Relationship between Ballistocardiographic Forces and Certain Events in the Cardiac Cycle," *Circulation*, vol. 6, pp. 586-592, 1952.
- [145] O. T. Inan, M. Etemadi, R. M. Wiard, G. T. A. Kovacs, and L. Giovannardi, "Non-invasive measurement of Valsalva-induced hemodynamic changes on a bathroom scale Ballistocardiograph," in *Engineering in Medicine and Biology Society, 2008. EMBS 2008. 30th Annual International Conference of the IEEE*, 2008, pp. 674-677.
- [146] E. K. Chung, *Electrocardiography: Practical Applications with Vectorial Principles*, 3rd ed. Norwalk, CT: Appleton-Century-Crofts, 1985.
- [147] M. A. Watanabe, J. E. Marine, R. Sheldon, and M. E. Josephson, "Effects of Ventricular Premature Stimulus Coupling Interval on Blood Pressure and Heart Rate Turbulence," *Circulation*, vol. 106, pp. 325-330, 2002.
- [148] E. K. Chung, *Principles of Cardiac Arrhythmias*, 4th ed. Baltimore, MD: Williams & Wilkins, 1989.
- [149] K. Lu, J. W. Clark, Jr., F. H. Ghorbel, D. L. Ware, and A. Bidani, "A human cardiopulmonary system model applied to the analysis of the Valsalva maneuver," *Am J Physiol Heart Circ Physiol*, vol. 281, pp. H2661-2679, 2001.
- [150] V. V. Ermishkin, E. V. Lukoshkova, E.-Y. Bersenev, M. A. Saidova, V. N. Shitov, O. L. Vinogradova, and V. M. Khayutin, "Beat-by-beat changes in pre-ejection period during functional tests evaluated by impedance aortography: a step to a left ventricular contractility monitoring," in *13th International Conference on Electrical Bioimpedance and the 8th Conference on Electrical Impedance Tomography*, Graz, Austria, 2007, pp. 655-658.

- [151] J. C. Greenfield, JR., R. L. Cox, R. R. Hernandez, C. Thomas, and F. W. Schoonmaker, "Pressure-Flow Studies in Man During the Valsalva Maneuver with Observations on the Mechanical Properties of the Ascending Aorta," *Circulation*, vol. 35, pp. 653-661, 1967.
- [152] J. P. Blackburn, C. M. Conway, R. M. Davies, G. E. H. Enderby, A. W. Edridge, J. M. Leigh, M. J. Lindop, G. D. Phillips, D. A. P. Strickland, R. Tennant, and H. Knight, "Valsalva responses and systolic time intervals during anaesthesia and induced hypotension," *Br. J. Anaesth.*, vol. 45, pp. 704-710, 1973.
- [153] A. B. Levin, "A simple test of cardiac function based upon the heart rate changes induced by the valsalva maneuver," *The American Journal of Cardiology*, vol. 18, pp. 90-99, 1966.
- [154] R. Lewis, S. Rittogers, W. Froester, and H. Boudoulas, "A critical review of the systolic time intervals," *Circulation*, vol. 56, pp. 146-158, 1977.
- [155] J. L. Nickerson, J. V. Warren, and E. S. Brannon, "The cardiac output in man: Studies with the low frequency, critically-damped ballistocardiograph, and the method of right atrial catheterization," *J Clin Invest*, vol. 26, pp. 1-10, 1947.
- [156] A. Cournand, H. A. Ranges, and R. L. Riley, "Comparison of results of the normal ballistocardiogram and a direct Fick method in measuring the cardiac output in man," *J Clin Invest*, vol. 21, pp. 287-294, 1942.
- [157] J. M. Bland and D. G. Altman, "Statistical methods for assessing agreement between two methods of clinical measurement," *Lancet*, vol. 1, pp. 307-310, 1986.
- [158] C. L. Colebourn, V. Barber, J. B. Salmon, and J. D. Young, "The accuracy of diagnostic and haemodynamic data obtained by transthoracic echocardiography in critically ill adults: a systematic review," *J Inten Care Soc*, vol. 9, 2008.
- [159] A. Evangelista, D. Garcia-Dorado, H. G. Del Castillo, T. Gonzalez-Alujas, and J. Soler-Soler, "Cardiac index quantification by Doppler ultrasound in patients without left ventricular outflow tract abnormalities," *Journal of the American College of Cardiology*, vol. 25, pp. 710-716, 1995.
- [160] A. S. McLean, A. Needham, D. Stewart, and R. Parkin, "Estimation of cardiac output by noninvasive echocardiographic techniques in the critically ill subject," *Anaesth Intensive Care*, vol. 25, pp. 250-4, 1997.

- [161] B. W. B. Janerot Sjöberg, "Cardiac output determined by ultrasound-Doppler: clinical applications," *Clinical Physiology and Functional Imaging*, vol. 10, pp. 463-473, 1990.
- [162] R. A. Bruce and T. R. Hornsten, "Exercise stress testing in evaluation of patients with ischemic heart disease," *Progress in Cardiovascular Diseases*, vol. 11, pp. 371-390, 1969.